On the Synthesis and Characterisation of Magnetic Metal and Metal oxide Nanostructures

Thesis submitted to

COCHIN UNIVERSITY OF SCIENCE AND TECHNOLOGY

in partial fulfilment of the requirements

for the award of the degree of

DOCTOR OF PHILOSOPHY

Vijutha Sunny

Department of Physics
Cochin University of Science and Technology
Kochi - 682 022, Kerala
INDIA

March 2010

On the Synthesis and Characterisation of Magnetic Metal and Metal oxide Nanostructures

Ph. D. Thesis

Author

Vijutha Sunny
Thekknedathe (H)
Viju Nivas
Vyttila P.O.
Kochi - 682 019
Kerala, INDIA
e-mail: vijutha@gmail.com
Ph: +91 0484 2304976

$T23$

Supervising Guide

Prof. M R Anantharaman
Department of Physics
Cochin University of Science and Technology
Kochi - 682 022
Kerala, INDIA
e-mail: mraiyer@gmail.com
Ph:+91 0484 2577404
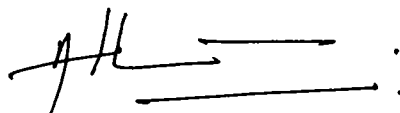
March 2010

Cover Page Illustration
Front Page: HRTEM image of cobalt-carbon nano onion core-shell nanostructure
Back Page: Optical microscope image of latex-ferrite composite film

Certificate

Certified that this thesis entitled *"On the synthesis and characterisation of magnetic metal and metal oxide nanostructures"* submitted by **Vijutha Sunny** is an authentic record of research work carried out by her under my supervision at the Department of Physics in partial fulfilment of the requirement for the award of degree of Doctor of Philosophy of the Cochin University of Science and Technology and the work embodied in this thesis has not been included in any other thesis submitted previously for the award of any other degree.

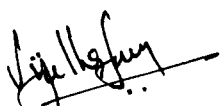22nd March 2010
Kochi - 682 022

Prof. M R Anantharaman
(Supervising guide)
Head of the Department
Department of Physics
Cochin University of Science
and Technology

Declaration

I hereby declare that the work presented in this thesis entitled *"On the synthesis and characterisation of magnetic metal and metal oxide nanostructures"* is based on the original research work carried out by me under the guidance and supervision of **Prof. M R Anantharaman**, Head, Department of Physics, Cochin University of Science and Technology, Kochi - 682 022 and no part of the work reported in this thesis has been presented for the award of any other degree from any other institution.

22nd March 2010

Kochi - 682 022

Vijutha Sunny

Acknowledgements

---

*Personally, at this juncture I prefer recognizing all those to whom my success is more rightfully attributed. Some are too close to me while others just strangers. But all of them alike, in one way or the other contributed for the successful completion of this work. **I thank you all.***

Of particularly outstanding value has been the guidance of my research supervisor, Prof. M R Anantharaman, without which this work would not have been possible. I am extremely grateful for the excellent guidance, creative suggestions and constant support he has rendered on me over the entire period of my doctoral studies. Sir... I remember your patience and concern shown to me. I treasure at the depth of my heart, the advices, constructive criticism and care, which really is the force that drive me on whenever I damp out.

I acknowledge the guidance and encouragements provided by Prof. Philip Kurian (Controller of examinations/Department of Polymer Science and Rubber Technology, CUSAT), my project investigator, which helped me to imbibe experimental skills and a passion for research especially in polymeric materials.

I am indebted to Dr. P Mohanan (Department of Electronics, CUSAT), for his sincere guidance and suggestions which helped me a lot in getting ideas on microwave measurement techniques. I also remember the suggestions given by Prof. RPRC Iyar (IIT Bombay) at this instance.

I am thankful to all former heads of the Department of Physics - Prof. K P Vijayakumar, Prof. V C Kuriakose, Dr. T Ramesh Babu and Prof. Godfey Louis for their support. Special thanks are due to Prof. C Sudha Kartha and Dr. S Jayelakshmi for their fruitful suggestions and care. I remember the support of my doctoral committee member Dr. Jacob Philip at various stages of my research carrier.

I am grateful to all teaching/non-teaching staff of the Department of Physics as well as Department of Polymer Science and Rubber Technology, Electronics, Chemistry and Instrumentation.

The helping hands from different research laboratories around the world are greatly acknowledged. Without their constant support, this work would have

science-society relationships. Yes! it is none other than MAGLAB. I thank all my seniors, colleagues, their family and all those associated with Magnetics Laboratory for helping me to move ahead and tackle different situations.

The path laid by Dr. K A Malini (chechi), Dr. Sindu S, Dr. Mohammed, Dr.Mathew George, Dr. Prema K H and Dr. Jamal EMA helped me to pursue my work polymer composites at ease. I recollect the memories of those good old days with Dr. Saravanan S, Dr. Swapna S Nair, Dr. Santhosh D Shenoy and Dr. Asha Mary John. I cherish the sweet memories with Sajeevetan, Sagar, Hysen, Tom chetan, Babu sir, Smitha Joby, Rajeev, Sanoj, Binumon, Dineshan, Blesson, Manu, Jaleel, Aparna, Tinu, Anjali and Lakshmi. Sweet moments with Ramkumar, Sethulekshmi, Smitha, Navaneeth, Neeraj, Akhila and Anand were really great.

My special thanks are due to my dear colleagues who were always around me as a soothing breeze and a helping hand. They have now become part and parcel of my life. Reena, Veena, Senoy, Narayanan, Geetha and Vinaya. You are always an answer to my "?" and my constant motivator giving wings to my thoughts. Thank you all...my ever sweet friends.

At this juncture, I remember all my teachers at Kendiya Vidyalaya-Cochin Port Trust, Sacred Heart College-Thevara and St. Joseph B.Ed. Training College-Ernakulam; and all the enlightening advices I got from my Church.

Prayers and encouragemnts from my grandparents (Amma-Appa), uncles, aunts and cousins are countless. Your well wishes always motivate me. Words are not worth for the love and support that I get from my brother and family. Viju-Veena, I love you a lot. The innocent smile of my niece Cristom and the newly arrived tiny tots, is a real boost. The constant support I get from my father make me accomplish the impossible. Appacha... you are the perfect dad in this world. I remember my mother, who taught me to believe in myself and fight the odds. Ammachi... I always feel your presence around me. It is your perspiration, dream and prayers that I have completed this work. I dedicate this thesis to you.

Lord Almighty... showering blessings on me... I bow before Thy love

Vijutha Sunny

Contents

Preface

Materials in the nanoregime exhibit superlative physical, chemical and mechanical properties when compared to their micron sized cousins. In nanostructured materials it is necessary that one of the dimensions fall in the 10-100 nm range. The enhanced properties exhibited by material in the nanoregime arise because of the quantum size effects. This is a phenomenon taking place because of the quantum confinement and this in turn gives rise to modified optical, magnetic, electrical or mechanical properties. The dawn of the millennium witnessed tremendous research activities in the area of nanostructured materials which probably has propelled this brand new technology as the technology of the 21st century. Thus, nanoscience and nanotechnology is here to stay and contribute to making new devices and help remove obsolescence. This is an interdisciplinary science where chemistry meets physics, physics meets material science and material science meets physics, chemistry or biology.

When the size of a material reduces to finer levels, they become highly reactive and are prone to oxidation. They are thus rendered useless as far as applications are concerned. Hence passivation of these ultrafine particles is a viable solution. Embedding nanoparticles in appropriate matrices not only protect these particles from oxidation but also result in nanocomposites. These nanocomposites are important from an application point of view as well as from a fundamental perspective.

From time immemorial the ferromagnetic properties of iron, cobalt and nickel were well known to mankind and many devices are made based on these materials. However, with the advent of nanoscience, fine particles of these materials are

synthesized and the modified magnetic properties of these are being exploited for different applications. However, along with these prospects there are limitations as well. They become reactive converting themselves to their nonmagnetic oxide states. These 3d-transition metals, if prepared in the nanoregime and encapsulated with an appropriate organic or inorganic material like carbon, gold or silica, gets converted to very useful materials for applications in recording media, nanoscale optics, nanoelectronics, biomedicine and so on. Carbon encapsulated ferromagnetic metal particles are found to be useful for diverse applications in medicine, recording media, aerospace materials and tribology, owing to their biocompatibility and resistance to oxidation.

Ferrites are ferromagnetic oxides of iron which find numerable applications. The nano forms of ferrites are also sought after. In the nanoregime they display superparamagnetic and single domain characteristics and they are also thought as useful materials for magnetic refrigeration. Incorporation of nanosized ferrites in matrices like natural/synthetic rubber will lead to nanocomposites whose combined dielectric and magnetic properties can be made use of for different applications. From a fundamental point of view, composites containing various loadings of ferrites are important and are candidate materials for the study of ferrimagnetism at the nanolevel. From an application point of view, they are flexible and can be moulded into any shape.

Encapsulating nanoparticles with carbon is increasingly being tried because carbon is chemically inert. These passivated ferromagnetic metal carbon core shell nanostructures possess high thermal stability, monodispersability and provision for attaching functional groups which make them ideal for potential drug delivery and drug targeting. Thus, a protective layer of carbon, either amorphous or graphitic can serve this purpose of attaining the desired properties due to the core-shell hybrid nanostructures. Such materials based on hybrid carbon nanostructures can be used for making supercapacitors, flexible batteries, nano brushes and nanoscale devices like molecular switches, transistors, actuators etc.

Carbon nanotubes, fullerenes and carbon black suspension are promising candidates for optical limiting applications. Optical limiters display a decreasing transmittance as a function of laser intensity, fluence or irradiance. These nanostructures are investigated for arresting the high intense laser beams thereby pre-

venting human eye and highly sensitive devices like sensors for high intense radiation. Metal nanoparticles such as gold and silver are identified as strong optical limiting materials. Their properties depend on size, shape and the dielectric environment. Recently, optical limiting is reported in magnetic metal nanoparticles systems. Hence there lies enormous scope in unveiling the hidden non-linear optical properties of magnetic metal carbon nanostructures.

The proliferation of microwave based communication system (radar systems, satellite communications, defence applications, mobile phones and other portable wireless devices) has increased the problems related to environmental pollution and interferences. This can be minimized by developing an electromagnetic wave absorber which can minimize the transmission as well as reflection of the incident wave. The electromagnetic wave absorbing property of a material is mainly determined by the matching between complex dielectric permittivity and magnetic permeability. Microwave absorbers and stealth materials are engineered keeping in view of their microwave absorption, weight, thickness, mechanical strength, environmental resistance and cost. The material parameters which satisfy this requirement can either be magnetic metals or their magnetic oxides in the nanoscale. Such a study in the nano regime is new and there lie plenty of opportunities to manipulate the dimensions and structures for probing the microwave absorbing properties.

Carbon rich materials like carbon nano fibres, carbon nano coils and carbon nanotubes provide mobile charge carriers or conducting channels imparting electromagnetic interference shielding capabilities. The deciding factors when materials are in the nanoregime, are the Snoek's limit and the skin depth. Carbon coated magnetic materials are good candidates for microwave absorbers. Moreover, the percolation threshold value for electrical conductivity of nanosized carbon fillers in a composite is quite low when compared to their micron sized counterparts. Metal carbon nanostructures like α-Fe/C(a), Fe-B/C(a), $Fe_{1.4}Co_{0.6}B$/C(a) or magnetic metal filled carbon nanotubes are reported to give good microwave absorbing properties. The enhancement of microwave absorption in metal/polyaniline nanocomposites by dual dielectric relaxation is also reported in literature. This has motivated the group to investigate the microwave properties of magnetic metal carbon nanostructures fabricated by cost effective and

scalable preparation techniques. The reflection loss of the metal-carbon nanocomposite can be simulated for different thicknesses of the material by a single layer metal backed absorber model, thereby investigating the possibility of these materials as microwave absorbers. Thus, the microwave absorbing properties of these materials are interesting and need in-depth investigations both from a fundamental and applied perspective.

An ideal microwave absorber is characterized by a reflection loss of less than -20 dB. Magnetic elastomers can play an important role here in realizing these microwave absorbers with additional functionalities like elasticity and mouldability aided by light weight. Moreover, the dielectric and magnetic properties of the nanocomposites can be tailored by using the right amount of the filler. Tuning the imaginary part of magnetic permeability improves impedance matching, broadens the range of operating frequencies, increases attenuation and reduces the thickness of absorber layer. This can be achieved by using appropriate fillers with optimum magnetic permeability.

Ferrites are chemically stable and are non-corrosive with high electrical resistance. So they are also good candidates for microwave applications. The inherent drawback of ceramic ferrites is that they are not easily machinable to obtain complex shapes. Plastic or elastomeric magnets on the other hand have several advantages since they are flexible, easily machinable and mouldable having light weight as well. Flexible microwave absorbers are thought to be ingenious new generation materials having potential applications. So appropriate amount of nanosized ferrites when incorporated in flexible matrices like rubber give rise to rubber ferrite composites (RFCs). These RFCs can be moulded into any shapes and thus gaskets or shields can be fabricated.

Natural rubber is a low cost material abundantly available in the state of Kerala and its processing technique is a well developed and matured technology. Nickel ferrite as filler fits into the requirement of having the appropriate permeability, low loss and low dc conductivity. High resisitivity ($\sim 10^{14}$ times that of metal) ensures low eddy current loss in the high frequency regime. Further, the Curie temperature of nickel ferrite is ~ 858 K which makes them ideal for high temperature applications. Low coercivity and high saturation magnetization of nickel ferrite are also significant for obtaining good absorption properties.

Metals are good reflectors and they are good conductors as well. But there is a need to minimize the reflection and reduce the eddy current loss. This could be achieved by reducing the size of the particles well below their respective skin depth. Once the grains of magnetic metals are below the size of their skin depth, they can be used as microwave absorbing material since they possess higher Snoek's limit. Thus flexible composite sheets with nanosized ferromagnets (Fe, Co, Ni) as fillers can be good microwave absorbers. Measurement of complex dielectric permittivity and magnetic permeability in various frequency bands are important in determining the microwave absorbing properties. Evaluation of attenuation constant and reflection loss in the S and X-band is necessary for modelling the absorbing properties and determining the optimum thickness for maximum absorption. These material parameters were measured and reflection loss was evaluated by employing cavity perturbation technique using a vector network analyser. For this a full-fledged experimental set-up for characterizing the microwave properties was made operational.

For any investigation in material science, synthesis and optimization of the process parameters are very important. Their characterization using various analytical techniques is also important.

Thus main objectives of the work can be listed as follows

- Synthesize magnetic metal nanoparticles of iron, cobalt and nickel by employing both bottom up and top down approach

- Passivate 3d-transition magnetic metal nanoparticles with organic coating and study the evolution of magnetic metal carbon hybrid nanostructures

- Study the magnetic and optical limiting properties of passivated magnetic metal nanoparticles

- Synthesize, characterize and evaluate the magnetic as well as dielectric properties of magnetic metal oxide nanoparticles obtained by employing both bottom up as well as top down approach

- Incorporate magnetic metal oxide nanoparticles in a natural rubber matrix to obtain flexible RFCs and study their cure, physicomechanical, dielectric and magnetic properties

- Incorporate magnetic metal nanoparticles obtained via high energy ball milling in a natural rubber matrix to obtain flexible magnetic material and hence compare their properties

- Fabricate an experimental set up for measuring complex dielectric permittivity and complex magnetic permeability at microwave frequencies

- Investigate the microwave properties of the metal carbon hybrid structures and magnetic rubber composites thereby tune their microwave absorbing properties

- Employ the surface impedance equation to simulate the optimum composite composition for minimum thickness and reflection loss

- Correlate the results

The thesis consists of nine chapters. The division of chapters with a brief outline of the contents is as follows

Chapter 1 gives an introduction to nanoscience and technology. A brief outlook on magnetism and magnetic materials and carbon nanostructures is presented. A note on polymer and polymer nanocomposites with emphasis on natural rubber is also provided. The significance of passivating highly reactive magnetic metals and the importance of composites are also discussed. Finally the motivation and objectives of the work are outlined.

Chapter 2 describes the experimental techniques and analytical tools employed in the synthesis and characterization of nanostructured magnetic materials. The rubber process methodology for developing the magnetic rubber composite sheets are also discussed in detail.

Chapter 3 discusses the synthesis techniques for producing passivated iron nanoparticles. The structural, magnetic and microwave absorbing properties of these hybrid nanostructures are analysed and correlated.

Chapter 4 includes the details of synthesis and characterization of carbon encapsulated with cobalt nanoparticles. The evolution of carbon nano onions over the magnetic metal particles are presented with supporting evidences. The potential of these structures as optical limiters is also identified through open aperture z-scan experiments.

In **Chapter 5**, the results on the investigations carried out on passivated nickel nanoparticles are highlighted. The structure, morphology and magnetic properties are studied in detail. The evolution of nickel carbon hybrid structures and their microwave absorbing properties are also dealt in detail.

Nanosized nickel ferrite particles are prepared via both bottom-up and top-down approaches and are discussed in **Chapter 6**. The structural changes occurring with high energy ball milling is evaluated. The effect of high energy ball milling on the magnetic and dielectric properties of ultrafine nickel ferrite particles are also depicted.

Chapter 7 essentially discusses the cure and physicomechanical properties of nickel ferrite nanoparticles incorporated in natural rubber matrix. Structural, physicomechanical, dielectric and magnetic properties of these flexible magnetic composites are investigated. By tuning the complex dielectric permittivity and complex magnetic permeability of the composite, the microwave absorbing properties are varied. The minimum reflection loss corresponding to optimum thickness of the composite sample is simulated by employing the single layer metal backed absorber model.

Chapter 8 mainly focuses on the properties of magnetic metal nanoparticle (Fe, Co, Ni) incorporated in a natural rubber matrix. The cure, mechanical, dielectric and magnetic properties of these flexible magnetic metal-rubber composite sheets are analyzed. The microwave properties of samples were examined in the S and X-band and the reflection loss were simulated for optimizing the thickness and bandwidth.

Chapter 9 gives the summary of findings of investigations carried out on magnetic metals, metal oxides and their composites and discusses the scope for future work emanating from the present study.

The following publications/intellectual property rights has resulted out of this investigation.

Patents

1. Metal Encapsulated With Carbon Nano Onion And Method Thereof. **Vijutha Sunny** and MR Anantharaman, Indian Complete Patent Appl. No.: 294/CHE/2008

Peer reviewed journal publications

1. Synthesis and properties of highly stable nickel/carbon core/shell nanostructures. **Vijutha Sunny**, D Sakthi Kumar, Yasuhiko Yoshida, Magdalena Makarewicz, Wojciech Tabiś and MR Anantharaman. Carbon 48 (2010) 1643-1651.

2. Nickel/carbon hybrid nanostructures as microwave absorbers. **Vijutha Sunny**, Wojciech Tabiś, D Sakthi Kumar, Yasuhiko Yoshida, P Mohanan and MR Anantharaman. Materials Letters (2010) doi: 10.1016/ j.matlet. 2010.02.010.

3. A flexible microwave absorber based on nickel ferrite nanocomposites. **Vijutha Sunny**, Philip Kurian, P Mohanan, PA Joy and MR Anantharaman. Journal of Alloys and Compounds 489 (2010) 297-303.

4. Cure kinetics and sorption characteristics of neoprene-based rubber ferrite composites, Prema KH, Philip Kurian, MR Anantharaman and **Vijutha Sunny**, International Journal of Polymeric Materials. 59 (2010) 173-183.

5. Enhanced microwave absorption in nickel-filled multiwall carbon nanotubes in the S band. TN Narayanan, **Vijutha Sunny**, MM Shaijumon, PM Ajayan, and MR Anantharaman. Electrochemical and Solid-State Letters. 12(4) (2009) K21-K24
Cited by Virtual Journal of Nanoscience and Technology. 19 (2009) 4.

6. Evidence for intergranular tunnelling in polyaniline passivated α- Fe nanoparticles. **Vijutha Sunny**, TN Narayanan, US Sajeev, PA Joy, D Sakthi Kumar, Yasuhiko Yoshida and MR Anantharaman, Nanotechnology. 17 (2006) 4765-4772.

Manuscript under review

1. Microwave absorbing properties of ferromagnetic metal/ natural rubber nanocomposites. **Vijutha Sunny**, Philip Kurian, P Mohanan, PA Joy and MR Anantharaman. Composite Science and Technology (Under review).

2. On the magnetic and magneto-optical properties of aqueous ferrouids of non-interacting SPIONs for magnetic hyperthermia. AP Reena Mary, TN Narayanan, **Vijutha Sunny**, D Sakthikumar, Yasuhiko Yoshida and MR Anantharaman. Journal of Magnetism and Magnetic Materials (Under Review).

Conference Proceedings

1. Encapsulated nickel nanoparticles: preparation and characterization. **Vijutha Sunny**, D Sakthi Kumar, Yasuhiko Yoshida, Magdalena Makarewicz, Wojciech Tabiś and MR Anantharaman, International Conference on Materials for Advanced Technologies (ICMAT-2009) Singapore, 28 June to 3 July, 2009 (Oral).

2. Microwave absorbing properties of natural rubber-nickel ferrite composites at high frequencies. **Vijutha Sunny**, P Mohanan, Philip Kurian and MR Anantharaman, INDO-US Workshop On Advanced Magnetic Materials and Their Applications, 1-4 March 2009. IIT Bombay, India.

3. On the microwave wave absorption of rubber ferrite nanocomposites containing precipitated silica. **Vijutha Sunny**, P Mohanan, Philip Kurian. MR Anantharaman, Cochin Nano 2009, 3-6 January 2009. Cochin, India.

4. Magneto-Optical dichroism studies on hydrocarbon based iron oxide ferrofluid thin films. Reena Mary AP, **Vijutha Sunny** and MR Anantharaman, Cochin Nano 2009, 3-6 January 2009, Cochin, India.

5. Dielectric measurements in the S-Band on silica containing rubber ferrite composites. **Vijutha Sunny**, P Mohanan, Philip Kurian, MR Anantharaman. International Conference on Magnetic Materials and their Applications for 21st Century (MMA2), 21-23rd October, 2008, National Physical Laboratory, New Delhi, India.

6. A Smart Magnetorheological nanocomposite based on iron and natural rubber. MP Vasudevan Nambudiri, **Vijutha Sunny**, Prema KH, TN Narayanan, Rajeev R Ashokan, V Natarajan, Philip Kurian and MR Anantharaman. New Horizons on Theoretical and Experimental Physics (NHTEP-2007), 8th-10th October, 2007, CUSAT, Kochi, India.

7. Effect of high energy ball milling on the magnetic properties of α-Fe. **Vijutha Sunny**, US Sajeev, PA Joy and MR Anantharaman. National Conference on Current Trends in Materials Science (CTMS-07), 25th-27th March, 2007, Charal Mount, Kuriannur, Kerala, India.

8. Effect of precipitated silica on rheometric, physicomechanical and dielectric properties of rubber ferrite composites based on nickel ferrite and natural rubber. **Vijutha Sunny**, Philip Kurian and MR Anantharaman. International Conference on Smart Electroceramics (NCSE). 8th-9th March, 2007, Thrissur, Kerala, India.

9. Investigations on the cure characteristics of carbon black and precipitated silica loaded rubber ferrite composites based on natural rubber and nickel ferrite. **Vijutha Sunny**, Philip Kurian and MR Anantharaman. International Conference on Materials for the Millennium (MatCon 2007). March 1st-3rd 2007, CUSAT. Kochi, India.

10. Structural organisation of Fe_3O_4 nanoparticles in rubber latex. **Vijutha Sunny**, Philip Kurian and MR Anantharaman. International Conference on Nanomaterials and its Applications, February 4th - 6th 2007, NIT-Trichy, India.

11. Dielectric and mechanical properties of rubber ferrite composites based on nickel ferrite and natural rubber. **Vijutha Sunny**, Philip Kurian and MR Anantharaman. Indian National Science Academy and Hungarian Academy of Sciences, Workshop on Condensed Matter Research: Magnetism, 4th December 2006, University of Hyderabad, Hyderabad, India.

12. Structural and magnetic characterization of oleic acid coated cobalt nanoparticles synthesized by a novel route. **Vijutha Sunny**, PA Joy, D Sakthi Kumar, Yasuhiko Yoshida and MR Anantharaman. 4th International Symposium on Bioscience and Nanotechnology, 7th November - 8th Nov 2006, Okinawa, Japan.

13. Evidence for the occurrence of inter granular tunnelling in passivated ultrafine α-Fe nanoparticles. **Vijutha Sunny**, TN Narayanan, US Sajeev, PA Joy, MR Anantharaman, International Seminar on Optoelectronic Materials and Thin Films Opto Electronic Materials for Advanced Technology International Conference (OMTAT) October. 24th-27th 2005, Kochi, India.

Chapter 1

Introduction

The growth of material science during the last few decades is always synonymous with the developments in nanoscience and nanotechnology. Such are the advances made in nanoscience and nanotechnology during the last two decades that the immediate fruits of this new branch of science is being made available to mankind on a day to day basis. Not a single day breaks in without the news of any one new device based on nanoscience and nanotechnology or a discovery of a novel technique or a new phenomenon! The vast and fast developments made in areas like spintronics, multiferroic materials, metamaterials, nano drug delivery system, biomimetic materials, magnetocaloric materials, to name a few, are a 'living' testimony to the above statement.

Earlier, scientists thought that properties could be tailored and modified by playing with the composition of the materials. The amount of impurities in a chemical compound decided the electrical, magnetic or optical properties of the material. The historic statement made by Richard Feynman that "There's Plenty of Room at the Bottom", has been proven beyond doubt that size and shape matters a lot in deciding many useful properties of a material. Quantum mechanically speaking, the properties of a particular material is largely determined by the length scale to which charged particles are confined.

Physicists say that, with respect to confinement, we can classify structures as 3D, 2D, 1D or 0D or the corresponding structures as bulk, quantum wells, quantum wires or quantum dots. In classical systems, the flow of electrons are

impeded by dislocations, defects and grain boundaries. This in turn is decided by the mean free path of electrons.

However, if one can fabricate nanostructures confining to 2D, 1D or 0D and when the mean free path of electrons are greater than the confined length scales, new phenomenon like quantum mechanical tunnelling, band gap engineering, Coulomb blockade, or surface plasmon resonance occurs and new transport mechanisms decide the overall properties. If the length scales can be tailored by fabricating new nanostructures, materials with novel properties can be prepared. Such materials can be hybrid structures or heterostructures with multifunctional properties. The direct incorporation of these 0D and 1D nano architectures in existing materials to improve properties is often referred to as incremental nanotechnology. The self assembly of these nanostructured building blocks into 2D and 3D architectures may yield entirely new devices and functionalities referred to as evolutionary nanotechnology.

In material science, synthesis and properties of thermally and chemically stable materials assumes significance. The cost effectiveness of the synthesis route is another deciding factor which determines scaling and mass production. Thus, hybrid structures in the form of core-shell configuration and heterostructures capable of imparting multifunctional properties are of interest both from an application point of view as well as from a fundamental perspective. If the hybrid structures are magnetic, there are many parameters which determine the overall magnetic properties. For example, interacting and non-interacting particles differ substantially in a magnetic nanostructure and they in turn determine the anisotropy, magnetic moment etc.

Metal nanoparticles are revisited because they are ideal templates for investigating magnetism at the nanoregime. However, nano forms of metals must be embedded in inert matrices to provide passivation and ensure thermal and chemical stability. However, passivation of metal nanoparticles with monolayer atomic coating on magnetic metal particles also gives rise to new phenomenon like surface spin, freezing of spins, spin clusters and superparamagnetism. From a fundamental point of view, these are factors that decide the overall properties of nano magnetic entities. From an applied perspective ultrafine particles, especially, metal particles embedded in carbon structures are ideal material for

sensing, tribological applications, nonlinear optical applications and as microwave absorbers. So synthesis and evaluation of properties of such heterostructures employing low tech techniques are of utmost importance for any investigation in material science.

Nanocomposites which are flexible are alternative materials for many useful applications such as microwave absorbing layers and gaskets. However, flexible matrices like natural rubber are necessary and appropriate recipe for mixing magnetic nanoparticles in natural rubber is to be worked out. This requires elaborate trial runs and optimization. This investigation is an attempt to delve into the fundamental aspects of different mechanisms that decide the various properties of materials at the nanolevel and also to synthesize and characterization of nanoparticles of magnetic materials and their composites. In this context, it is customary to give a general outline on the different aspects of magnetism and a brief note on their theoretical aspects.

1.1   Magnetic materials and magnetism

Magnets have become an integral part in almost all human endeavours. Oxides and semiconductors containing transition metal elements and some rare earths as dopants or constituents show magnetic behavior if the spin of the magnetic ions are aligned. High resistivity (low loss) ferrimagnets find a plethora of applications in passive microwave components such as isolators, circulators, phase shifters and miniature antennas operating at wide range of frequencies and as magnetic recording media using their novel physical properties.

Magnetic materials [1-4] are objects that attract or repel each other depending on their relative orientations. The development of magnetism has been a fascinating one, which dates back to tens of centuries. The earliest observations of magnetism can be traced back to the Greek philosopher Thales in B.C. 600. But only during 1600, the understanding of magnetism began which paved the way for the modern treatment of magnetism. William Gilbert, Hans Christian Oested, Michael Faraday, William Sturgeon, Emil G Warburg, Pierre Curie, Paul Langevin, Louis Eugène Félix Néel and Pierre-Ernest Weiss were milestone contributors in the saga of modern magnetism.

The first recognized magnet was lodestone (magnetite or Fe_3O_4). This was followed by magnetic carbon steel and alnico magnets in 1930s. Boosted by the 2nd world war, hard magnets ($BaFe_{12}O_{19}$ or $SrFe_{12}O_{19}$) experienced considerable developments. 1960s and the era that followed witnessed substantial developments in magnetic materials containing samarium cobalt and yttirium cobalt. Moreover, neodymium-iron-boron, developed in the 1980s, spot a good combination of high saturation magnetization and good resistance to demagnetization, but had relatively low Curie temperature (585 K) and high cost. Metallic soft magnetic materials which could not be used at high frequencies due to eddy current loss, were soon replaced by a variety of soft ferrites. The present era is witnessing drastic developments of nanochemistry that is well equipped with the capability of producing variety of magnetic nanostructures. Supramolecular assemblies, multifunctional supramolecules, magnetic metal nanostructures, spin glass structures, magnetic quantum dots, ferromagnetic/antiferromagnetic coupled systems and magnetic semiconducting hybrid structures [5, 6] are a few to list. These are proposed as potential building blocks of storage as read devices. Magnetic metal particles are particularly interesting nanoscale systems because of the ease with which they can be synthesized and modified chemically.

There are several important parameters related to magnetic materials. For example, magnetic flux density or magnetic induction 'B', is the net magnetic response of a medium to an applied field 'H'. It is measured in Tesla (T) in SI units and Gauss (G) in cgs units. The relationship is given by the following equation: In cgs units $B = H + 4\pi M$ and in SI units

$$B = \mu_o(H - M) \tag{1.1}$$

where 'H' is magnetic field strength generated by currents and magnetic poles (A/m in SI units and Oersteds in cgs units). 'M' is magnetization and μ_o is the permeability of free space (4×10^{-7} H/m). Magnetization is defined as the magnetic moment 'm' per unit volume 'V', thus $M = m/V$. It is measured as A/m in SI units and emu/cm^3 in cgs units. In general, magnetization 'M' of a material is dependent on the magnetic field 'H' applied on it. Therefore, magnetic susceptibility χ, a magnetic parameter giving an indication of the response of a

material to an applied magnetic field, has been used. Magnetic susceptibility is defined as the ratio of magnetization 'M' to the applied field 'H',

$$\chi = \frac{M}{H} \tag{1.2}$$

Here χ can be expressed in terms of B as follows:

$$B = \mu_o(1 + \chi)H \tag{1.3}$$

One can define magnetic permeability $\mu = 1 + \chi$ and thus

$$B = \mu_0 \mu H \tag{1.4}$$

Magnetic Moments : A magnet in a field has a potential energy, 'E_p', relative to the parallel position given by E_p=-mH. The origin of atomic magnetic moments is the incomplete cancellation of electronic magnetic moments. Electron spin and orbital motion both have magnetic moments associated with them. But in most atoms the electronic moments are so oriented that they cancel giving no net atomic magnetic moment, leading to diamagnetism. If the cancellation of electronic moments is incomplete then the atom has a net magnetic moment. These 'magnetic atoms' can display para-, ferro-, antiferro- or ferrimagnetic ordering depending upon the strength and type of magnetic interactions and external parameters such as temperature. The magnetic moments of atoms, molecules or formula units are often quoted in terms of the Bohr magneton μ_B, which is equal to the magnetic moment due to electron spin

$$\mu_B = \frac{eh}{4\pi m} = 9.27 \times 10^{-24} J/T \tag{1.5}$$

Here 'e' and 'm' denotes the charge and mass of an electron. 'h' the Plank's constant.

1.2 Classification of magnetic materials

The orbital and spin motions of electrons and their interactions decide the overall magnetism of a substance. Although as surprising as it may sound, all matter is magnetic to varying degrees [1, 2, 4]. The magnetic behavior of materials can

be classified according to the values of magnetic susceptibility, χ and magnetic permeability, μ as: vacuum ($\chi = 0$, $\mu = 1$), diamagnetic ($\chi =$ small and negative, $\mu \leq 1$), paramagnetic ($\chi =$ small and positive, $\mu \geq 1$), antiferromagnetic ($\chi =$ small and positive, $\mu \geq 1$), ferromagnetic ($\chi =$ large and positive, $\mu \gg 1$) and ferrimagnetic ($\chi =$ large and positive, $\mu \gg 1$).

Diamagnetism is a fundamental property of all matter. The atoms (with no unpaired electrons) have no net magnetic moment when there is no applied field. Under the influence of an applied field 'H', the spinning electrons precess and this motion, which is a type of electric current, produces a magnetization 'M' in an opposite direction to that of 'H'. The diamagnetic effect is often masked by larger paramagnetic or ferromagnetic term. Here the susceptibility is independent of temperature. Rare gases (He, Ne, Ar), most of the polyatomic gases (H_2, N_2), elements like C (diamond), Si, Ge, GaAs, GaN and most of the organic compounds are a few examples to list.

Electronic paramagnetism arises from atoms, molecules and lattice defects, possessing an odd number of electrons (unpaired) causing a nonzero total spin. There are several theories of paramagnetism, which are valid for specific types of materials. The Langevin model, which is true for materials with non-interacting localized electrons, states that each atom has a magnetic moment, which is randomly oriented as a result of thermal agitation. The application of a magnetic field creates a slight allignment of these moments and hence a low magnetization in the same direction as the applied field. As the temperature increases, thermal agitation will increase and it will become harder to align the atomic magnetic moments and hence the susceptibility decreases. This behaviour is known as the Curie's law and is given by $\chi = \frac{C}{T}$, where C is a material constant called the Curie's constant. Materials which obey this law are materials in which the magnetic moments are localized at the atomic or ionic sites and there is no interaction between neighbouring magnetic moments. Hydrated salts of transition metals (like $CuSO_4 \cdot 5H_2O$), are examples of this type of behaviour as the transition metal ions, which have a magnetic moment, are surrounded by a number of non-magnetic ions/atoms, which prevent interaction between neighbouring magnetic moments. Salts and oxides of rare earths, rare earth elements (although

many of them become ferromagnetic at low temperatures) and metals like Cu are also strongly paramagnetic.

In fact the Curie's law is a special case of the more general Curie-Weiss law, $\chi = \frac{C}{T-\theta}$, which includes a temperature constant (θ) and derived from Weiss theory, proposed for ferromagnetic materials, that incorporates the interaction between magnetic moments. In this equation, θ can either be positive, negative or zero. Clearly when $\theta = 0$, Curie-Weiss law is Curie's law. When $\theta \neq 0$, there exist an interaction between neighbouring magnetic moments and the material is paramagnetic only above a certain transition temperature. If $\theta > 0$, the material is ferromagnetic below the transition temperature. Here is referred to as Curie temperature, T_C. If $\theta < 0$, then the material is antiferromagnetic below the transition temperature (Nèel temperature, T_N), however the value of θ does not relate to T_N). It is important to note that this equation is only valid when the material is in a paramagnetic state. It is also not valid for many metals as the electrons contributing to the magnetic moment are not localized. However, the law does apply to some metals, e.g. the rare-earths, where the 4f electrons, that create the magnetic moment, are closely bound.

The Pauli model of paramagnetism [4] is true for materials where the electrons are free and interact to form a conduction band. This is valid for most of the paramagnetic metals. In this model, the conduction electrons are considered essentially to be free, and under an applied field an imbalance between electrons with opposite spin is set up leading to a low magnetization in the same direction as the applied field.

Ferromagnetism is only possible when atoms are arranged in a lattice and the atomic magnetic moments can interact to align them parallel to each other. This effect is explained in classical theory by the presence of a molecular field within the ferromagnetic material, which was first postulated by Weiss in 1907. This field is sufficient to magnetize the material to saturation. In quantum mechanics, the Heisenberg model of ferromagnetism describes the parallel alignment of magnetic moments in terms of an exchange interaction between neighbouring moments.

Weiss postulated the presence of magnetic domains within the material, which are regions where the atomic magnetic moments are aligned. The movement of these domains determines how the material responds to a magnetic field and as a

consequence, the susceptibility is a function of applied magnetic field. Therefore, ferromagnetic materials are usually compared in terms of saturation magnetization (magnetization when all domains are aligned) rather than susceptibility.

In the periodic table of elements, only Fe, Co and Ni are ferromagnetic at and above room temperature. As ferromagnetic material is heated, the thermal agitation causes the degree of alignment of the atomic magnetic moments to decrease, reducing their saturation magnetization. Eventually the thermal agitation becomes so great that the material becomes paramagnetic; the temperature of this transition is the Curie temperature, $'T_C'$. Above T_C, the susceptibility varies according to the Curie-Weiss law.
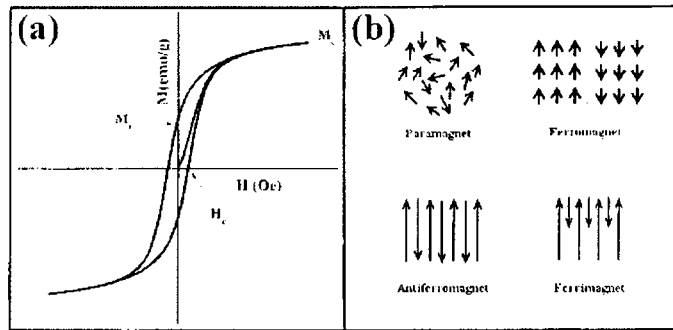
Figure 1.1: (a) Typical hysteresis curve and (b) Arrangement of atomic spins dictates magnetic properties

Ferromagnets will tend to stay magnetized to some extent after being subjected to an external magnetic field. This tendency to 'remember their magnetic history' is called hysteresis. The fraction of the saturation magnetization which is retained when the driving field is removed is called the remanence or remanent magnetization $'M_r'$ of the material, and is an important factor in permanent magnets. Typical curve of M vs H called magnetization curve or hysteresis curve are characterized by phenomena like saturation magnetization and hysteresis (Figure 1.1a). At higher values of H, the magnetization M becomes constant at its saturation value of $'M_s'$. After saturation, a decrease in H to zero does not reduce M to zero which is termed as hysteresis. The reverse field applied to cause M to zero, is the coercive field or coercivity of the material $'H_c'$.

In the periodic table, the only element exhibiting antiferromagnetism at room

temperature is chromium. Antiferromagnetic materials, are very similar to ferromagnetic materials but the exchange interaction between neighbouring atoms leads to the anti-parallel alignment of the atomic magnetic moments. Therefore, the magnetic field cancels out and the material appears to behave in the same way as a paramagnetic material. Like ferromagnetic materials, these materials become paramagnetic above a transition temperature, known as the Nèel temperature, $'T_N'$ (Cr: T_N =310 K).

Ferrimagnetism is only observed in compounds, which have more complex crystal structures than pure elements. Within these materials, the exchange interactions lead to parallel alignment of atoms in some of the crystal sites and anti-parallel alignment of others. The material breaks down into magnetic domains, just like a ferromagnetic material and the magnetic behaviour is also very similar, although ferrimagnetic materials usually have lower saturation magnetization. 3d-transition metal oxides and their compounds with spinel, magnetoplumbite and garnet structure, all fall in the class of ferrimagnetic materials. Figure 1.1b shows the arrangements of atomic spins in different magnetic materials. In all of the above mentioned magnetic materials, different types of magnetic interactions take place which are discussed below.

1.3   Magnetic interactions

Each magnetic moment of the substance is subjected to a magnetic dipolar interaction with each other [1]. Two magnetic dipoles $'m_1'$ and $'m_2'$ separated by a distance $'r'$ have an energy equal to

$$E = \frac{\mu_0}{4\pi r^3} \left[m_1.m_2 - \frac{3}{r^2}(m_1.r)(m_2.r) \right] \tag{1.6}$$

which therefore depends on their degree of mutual alignment. The dipolar interaction is much weaker than the exchange interaction among near neighbour moments, and become dominant only at large distances. The magnetic dipolar interactions are found to be too weak to account for the ordering of most magnetic materials with higher ordering temperatures.

J. Frenkel made the assumption that the origin of strong ferromagnetic interactions is due to what are called as exchange interactions. It is a characteristic

quantum effect having no parallel in classical physics. Various types of exchange interactions are present in solids [1]. Direct exchange interaction is operative between the adjacent atoms/ions without the need of any intermediary and leads to a strong magnetic coupling while indirect exchange or superexchange interactions take place between non neighbouring magnetic ions mediated by a nonmagnetic ion which is placed in between the magnetic ions in the case of ionic solids. Superexchange interaction involves the oxygen orbitals as well as metal atom (in ferrites) and it is a second order process derived from second order perturbation theory. Superexchange interactions could occur in ferromagnetic materials but less common than the usual antiferromagnetic or ferrimagnetic superexchange. The ferromagnetism of Fe, Co and Ni can be attributed to direct exchange. In metals, the exchange interactions between magnetic ions can be mediated by the conduction electrons. A localized spin magnetic moment polarizes the conduction electrons and this polarization in turn couples to a neighbouring localized magnetic moment at a distance 'r' away. The interaction is called RKKY interaction or itinerant exchange after the discoverers of this effect: Ruderman, Kittel, Kasuya and Yosida. The interaction is long range and has an oscillatory dependence on the separation between the magnetic moments. The resulting interaction can be either ferro or antiferromagnetic depending on the separation between the ions. In some oxides, it is possible to have a ferromagnetic exchange interaction which occurs between the magnetic ions showing a mixed valency. The ferromagnetic alignment is due to the double exchange mechanism. Zener proposed this exchange mechanism to account for the interaction between adjacent ions of parallel spins. Zener's mechanism of double exchange forms a positive interaction which is a contributing factor to the observed ferromagnetic interaction in materials like perovskite mixed manganates like $LaCaMnO_3$, $LaSrMnO_3$ etc. It has been found that spin orbit interaction results in exchange interactions in a similar manner to that of the oxygen atom in superexchange. There is an exchange interaction between the excited state of one ion and the ground state of the other ion. The excited state is produced by the spin-orbit interaction in one of the magnetic ions. This is known as anisotropic exchange interaction or also as the Dzyaloshinsky-Moriya interaction. The form of interaction is such that it tries to force the spins to be at right angles in a plane so that orientation will

ensure that the energy is negative. Its effect is therefore to cant the spins by a small angle. The effect is known as weak ferromagnetism. It is found in α-Fe_2O_3, $MnCO_2$, $CoCO_3$ etc.

1.4 Magnetic anisotropy

One factor which may strongly affect the shape of the hysteresis loop is magnetic anisotropy. This term simply means that the magnetic properties depend on the direction in which they are measured. There are several kinds of anisotropies like crystalline or magnetocrystalline anisotropy, shape anisotropy, stress anisotropy, exchange anisotropy and anisotropy induced by magnetic annealing, plastic deformation and irradiation.

Magnetocrystalline anisotropy: In a crystalline magnetic material the magnetic properties will vary depending on the crystallographic direction in which the magnetic dipoles are aligned. A crystal can magnetize more easily in certain direction called easy axes than the others which are called hard axes. Figure 1.2 demonstrates this effect for a single crystal of (a) magnetite and (b) cobalt.

From the magnetization curves for single crystal of magnetite, it can be seen that, along the $< 111 >$ direction, a very small magnitude of the magnetic field is required to produce a large magnetization; in other words it is 'easy' to magnetize magnetite crystal along $< 111 >$ direction, while it is 'hard' to do so along the other directions. The hexagonal crystal structure of Co can be magnetized easily in the $< 0001 >$ direction (i.e. along the c-axis), but has hard directions of magnetization in the $< 10\bar{1}0 >$ type directions, which lie in the basal plane (90° from the easy direction). A measure of the magnetocrystalline anisotropy in the easy direction of magnetization is the anisotropy field H_a, which is the field required to rotate all the moments by 90° as one unit in a saturated single crystal. The anisotropy is caused by the coupling of the electron orbitals to the lattice, and in the easy direction of magnetization, this coupling is such that these orbitals are in the lowest energy state.
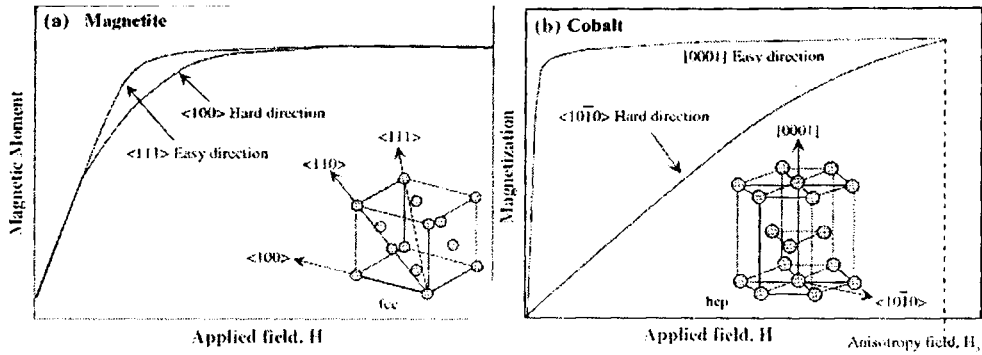
Figure 1.2: Magneocrystalline anisotropy in (a) cubic-like spinel structure (magnetite-Fe_3O_4) and (b) hexagonal structure such as in cobalt with H_a being the anisotropy field

The easy direction of magnetization for a permanent magnet, based on ferrite or the rare earth alloys, must be uniaxial, however, it is also possible to have materials with multiple easy axes or where the easy direction can lie anywhere on a certain plane or on the surface of a cone. The fact that a permanent magnet has uniaxial anisotropy means that, it is difficult to demagnetize as it is resistant to rotation of the direction of magnetization.

Shape anisotropy: Consider a polycrystalline specimen having no preferred orientation of its grains and therefore no crystal anisotropy. If spherical in shape, the same applied field will magnetize it to the same extent in any direction. If non spherical, it will be easier to magnetize along a long axis than short axis. This phenomenon is known as shape anisotropy. This is so because the demagnetizing field (the internal field which tends to demagnetize the magnet) is less along a short direction, because the induced poles at the surface are farther apart. For a spherical sample there is no spherical anisotropy. The magnetostatic energy density for an elliospidally shaped sample magnetized along one of its principal axes is given by

$$E = \frac{1}{2}\mu_0 N_d M^2 V \tag{1.7}$$

where $'N_d'$ is the tensor and represents the demagnetized factor (which is calculated from the ratio of the axis) while $'V'$ is the volume of the sample and $'M'$ is the saturation magnetization of the sample.

Induced anisotropy: Induced anisotropy is not intrinsic to the material but produced by a treatment which has directional characteristics. Both the magnitude and easy axis can be altered by appropriate treatment. The degree and direction of possible orientation is possible via casting, rolling and wire drawing in polycrystalline alloys.

Surface anisotropy: In small magnetic nanoparticles, a major source of anisotropy results from surface effects. The surface anisotropy is caused by the breaking of the symmetry and their reduction of the nearest neighbour coordination. The protective shell or ligand molecules which cover the small particles play an important role as well leading to a change of the electronic environment on the particle surface

1.5 Magnetic properties of small particles

1.5.1 Single and multi-domain particles

A permanent magnet creates a magnetic field in space, which carries energy. This energy can be minimized by creating oppositely facing domains in the material, so that the external field is decreased. The boundary between domains carries energy, but this is less than the energy benefit obtained. When the dimensions of a magnetic particle get close to the domain wall size, it may be more energetically favourable for the particle to form a single domain.

The critical size between a single- or multi-domain particle can be estimated by considering the two situations depicted in Figure 1.3a, b. The energy of a single-domain particle (E_{sd})

$$E_{sd} = \frac{1}{2}\mu_0 N M_{sat}^2 \frac{4}{3}\pi R^3 \tag{1.8}$$

just has the magnetostatic energy of a spherical particle with radius 'R', saturation magnetisation M_{sat} and demagnetisation factor 'N'. The energy of a two domain particle (E_{md}) includes the domain wall energy as well.

$$E_{md} = \gamma \pi R^2 + \alpha \frac{1}{2}\mu_0 N M_{sat}^2 \frac{4}{3}\pi R^3 \tag{1.9}$$

with 'γ' the domain wall energy per surface area.

The exact magnetostatic energy of a two-domain particle is not easily derivable, therefore it is written as a fraction α of the single-domain case. Since the two-domain particle has a lower stray field, the magnetostatic two-domain energy is less than the single-domain energy and $\alpha < 1$. It is obvious that $\alpha > 0$ (appropriate $\alpha = \frac{1}{2}$).

The critical domain diameter D_{do} is found when the energies of the single- and multi-domain configuration are equal, $E_{sd} = E_{md}$. This results in

$$D_{do} = \frac{6\gamma}{2(1-\alpha)\mu_0 N M_{sat}^2} = \frac{18\gamma}{\mu_0 M_{sat}^2} \tag{1.10}$$

Thus, spherical particles with a diameter below D_{do} consist of a single magnetic domain, larger particles consist of multiple domains. Below a critical size, a particle contains only one domain. The width of a domain depends on the balance between the exchange energy (prefers wide wall) and magnetocrystalline anisotropy (prefers narrow wall).

(a)   (b)

(c)   (d)   (e)
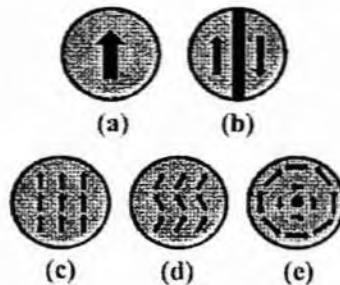
Figure 1.3: Magnetization of (a) a single domain particle, and (b) the simplest multi-domain particle. Magnetization modes of a single domain: (c) homogeneous rotation, (d) buckling and (e) curling. The centre of the curling mode is pointing out of (or into) the plane

1.5.2 Coercivity of single domain particles

Figure 1.3(c-e) shows the most basic modes. A typical single domain particle will have all its spins pointing in the same direction, homogeneous rotation (Figure 1.3c). When an external magnetic field is applied, these spins rotate in unison to become parallel to the field and minimize the Zeeman energy. This behaviour is also termed coherent or homogeneous rotation. There may be, however, an anisotropy barrier to be overcome. The external field needed, H_{sw}, to rotate the

magnetisation of a spherical particle from opposite to parallel to the field, can be estimated using Stoner-Wohlfarth[4] theory given by

$$H_{sw} = \frac{2K}{\mu_0 M_{sat}} \qquad (1.11)$$

Magnetization reversal by fanning mechanism is relevant in chains of particles or highly elongated particles. In a chain, the M_s vector of each particle interacts with its neighbours via the magnetic dipolar interaction. Thus the dipoles line up, north to south, and like to remain in alignment, hence causing an anisotropy even if no others exist. This has been called an interaction anisotropy. An applied field in the opposite direction tends to reorient these dipoles, but the reorientation may occur either coherently or incoherently. The incoherent alignment is called fanning. With buckling or fanning (Figure 1.3d), magnetization is homogeneously varying along one direction. In the figure, it is varying upwards, and fluctuations to the left and right cancel each other, thereby decreasing the total stray field. Buckling often occurs in thin rods.

Curling or vortex (Figure 1.3e) is an interesting mode, where the stray field is reduced to a minimum by circular symmetry. It has also small exchange energy, but for the centre; their opposed spins are just next to each other, forcing the magnetization to rotate out of plane. This mode is found primarily in thin disks, with possible applications in data storage; this vortex state has a centre magnetization either into the paper or out of it.

1.5.3 Superparamagnetic limit

When the size of a particle is very small, they will be single domain and thermal energy $k_B T$ may be enough to overcome the anisotropy barrier KV. Here k_B is the Boltzmann's constant, 'K' is the anisotropy constant and 'T' the temperature. This results in the magnetization being rotated spontaneously every once in a while. With no external field, this yields an average magnetization of zero, with the averaging done either over time or over multiple particles. When an external field is present, the particle does have an averaged magnetization parallel to the field. This phenomenon is called superparamagnetism. 'D_{th}' is the diameter, below which this occurs, the superparamagnetic limit. The approach of thermally activated switching of a single-domain particle is called the Néel-Brown model.

The average time τ_m, it takes for the thermal energy to flip the magnetization can be expressed using the Arrhenius-Nèel law given by

$$\tau_m = \tau_0 e^{\frac{KV}{k_B T}} \tag{1.12}$$

with τ_0 the resonance relaxation time of the spin system, which is generally around the order of 10^{-10}s. The fluctuations therefore slow down (τ_m increases) as the sample is cooled and the system appears static when τ_m becomes much longer than the measuring time 't' of the particular laboratory experiment technique which one is using. This equation can also be understood directly by recognizing the Boltzmann-factor.
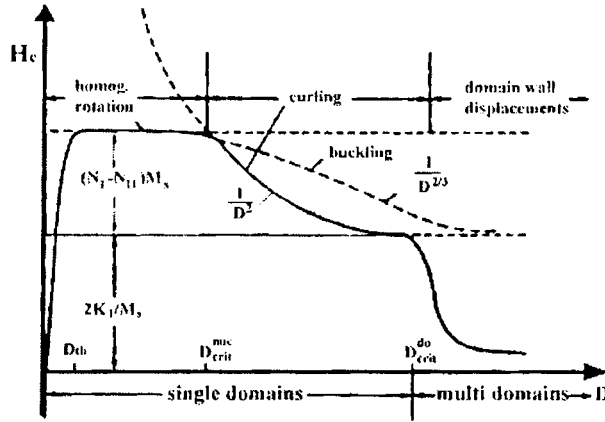
Figure 1.4: A schematic graph of the coercivity field as a function of diameter. The different size regime can be recognized

For a given time span τ_m, the critical diameter is

$$D_{th} = \sqrt[3]{\frac{6k_B T}{\pi K} \ln \frac{\tau_m}{\tau_0}} \tag{1.13}$$

Of a particle of this diameter has a stable magnetization for time span of just τ_m. The value τ_m is, of course, application dependent. In superparamagnetic beads for biomedical applications, a second is appropriate while for hard disc, τ_m of the order of few tens of years is desirable.

So far we have seen three regimes, multidomain (bulk; $D > D_{do}$), single domain ($D_{th} < D < D_{do}$) and superparamagnetic ($D < D_{th}$). 'D_{do}' is the critical domain diameter, below which the energy of a domain wall is too large to reduce

the stray field. But there are other options for reduction, besides creating multiple domains. This is what happens in the curling and buckling magnetization modes: the magnetization varies continuously over the geometry. The exchange energy resulting from slightly nonparallel spins is kept small, while spins are canceling each other's field over a larger area.

Multidomain particles decrease the field by forming domains, while single domain particles have a high field, originating from magnetocrystalline and shape anisotropy. Below the superparamagnetic limit D_{th}, the coercive field decreases because thermal energy is enough to overcome the barrier.

1.6 Magnetic metal and metal oxide nanoparticles

Magnetic materials are always a fascination to researchers owing to their potential use in communication, data storage, biomedicine and defence applications [2, 7, 8]. Over the last few years the magnetic properties of ferri/ferro magnetic nanostructures (nanoparticles, nanowires, nanorods or self assembled nanostructures) have been widely studied, as they present an interest both for fundamental physics and for applications [6, 9]. The general requirements would often be of magnetic particles displaying a large magnetic susceptibility, while keeping inter particle interactions low so that they do not agglomerate. Metals like iron, cobalt and nickel are ferromagnetic at room temperature. However, their magnetic properties will vary from the bulk metal is broken into finer and finer pieces. The magnetic properties of nanometals can be very different, manifesting softer magnetism or single domain magnetism with a much greater coercivity. If small enough, they can also test the superparamagnetic limit of matter. Several approaches have been applied to synthesize magnetic metal nanoparticles, including thermal and sonochemical decomposition of organometallic precursors, high-temperature reduction of metal salts, or reduction with reverse micelles [10 13], however, control of shape is very important. Only few anisotropic magnetic nanoparticles have been developed so far [14 16]. Some research groups have employed laser ablation methods [17, 18] and prepared magnetic nanoparticles (Co, Ni, Fe) of 40-500 atoms. However, these nanoparticles were not stable in air

due to oxidation and aggregation because their surfaces were not passivated by other organic or inorganic molecules (bare nanoparticles).

Last decade scientists explored the structure and transport properties of ferrite materials. Now the properties of these are investigated in the nanoregime. Appropriate processing techniques and controlled microstructures play a significant role in formulating ferrite devices. The other important factor is characteristic modification by means of substitution or doping. Metal oxide nanomaterials are prepared in a great number using novel routes like co-precipitation, sonochemical, microwave plasma, ball milling, sol-gel, polyol process, reverse micelle and hydrothermal methods [6, 9–13, 19, 20]. These methods produce nanometer range particles when compared to the ceramic methods leading to drastic changes in their properties. Magnetic metal oxides can be broadly classified as spinel, garnet or magnetoplumbite. Details of ferrites with spinel structure are discussed in Chapter 6.

1.7   Carbon nanostructures-an overview

Carbon is undoubtedly one of the most important elements known to man. It is the 4th most abundant element in the solar system, 6th most abundant element in the universe and the 19th most abundant element in the earth's crust. There are more compounds of carbon, about 16 million, than of any other elements except hydrogen. Electronic structure of carbon atom is $1s^2 2s^2 2p^2$ in its ground state with two unpaired 2p electrons and the 2s and 2p wave function normally hybridized to form 4 degenerate sp^3 orbitals. Carbon has two naturally occurring stable allotropes: ^{12}C (98.89%) and ^{13}C (1.11%). The radioactive isotope ^{11}C, are formed by thermal neutron irradiation of Li or Al nitride [21, 22].

Modern 'nanotechnology revolution' was undoubtedly catalyzed by the mid-1980s serendipitous discovery of carbon nanoclusters known as fullerenes or C_{60} (caged molecules uniquely formed from carbon) for which the 1996 Nobel Prize in Chemistry was awarded to Richard Smalley, Robert Curl, and Sir Harold Kroto [23]. Later in 1989, first large-scale synthesis of fullerenes was wisely discovered by Huffman and Krätschmer [24], which provided a macroscopic quantity of C_{60} confirming the proposed icosohedral structure. This was followed by a

stream of discoveries and inventions related to carbon nanostructures. Versatile methods for the preparation of carbon nanostructures with different morphology (nanoparticles, nanorods or nanotubes) have been developed as they can act as multifunctional device component. They are capable of creating a variety of nanoscale structures such as spheres, tubules, onions, ribbons, rods etc [25 35]. Out of these, carbon nanotubes have received and continue to receive significant attention due to their potential applications, but the field of multilayer fullerenes or carbon nano onions (CNO) still remains in its infancy. The main reason for this is the expensive and impractical preparation processes involved together with low yields and uncontrollable size.

Carbon nanotube, the most widely studied 1D nanomaterial, was first discovered by Iijima in 1991 [36], consist of a graphitic sheets of sp^2 hybridized carbon atoms [21, 22] rolled in to a tubular array. The diameters of CNTs range from 1 nm to > 30 nm, with aspect ratios (length:width) ranging from 100 to greater than 1×10^6. Their tensile strength is ca. 20 times greater than steel - a property attributed to extremely strong sp^2 bonding between neighboring hexagonal units. Based on empirical data and theoretical predictions [6, 22], the catalytic ability of the metal/alloys for SWNT growth follows the order: Ni/Mo > Ni/Cr > Ni/Co > Ni/Pt > Ni/Rh > Ni/Fe > Ni > Fe/Mo > Fe/Cr > Fe/Co > Fe/Pt > Fe/Rh > Fe > Ni/Mo > Fe/Mo > Co/Mo > Co > Pt > Cu.

Soon after this in 1992, D Urgate [25] discovered carbon onions (concentric spherical graphitic shells) during his experiments with the irradiation of nanoparticles filled with gold and lanthanide oxides. Subsequent works revealed that carbon onions can be prepared from a diversity of carbon rich materials [6, 21, 37–40]. Carbon nano onions (CNOs) are made of concentric fullerene-like shells and range from double-, triple- or multilayered structures. A number of methods to produce CNO have been demonstrated, including arc discharge, high-energy electron beam irradiation, high-temperature nanodiamond annealing, plasma-enhanced chemical vapor deposition and implantation of carbon ions onto metal particles [25, 41 44]. Multiwalled CNOs are usually the byproducts of multiwalled CNTs. They have empty cavity in the middle, offering the potential to be filled with other nanoparticles forming core shell structures with interesting properties.

1.8 Core shell nanoparticles

Some of the exciting breakthroughs in nanoscience and nanotechnology are the development of flexible batteries, nanotweezers, nano brushes, hydrogen storage devices, catalysts [45–48] etc. By particle engineering, well defined morphologies or hybrid systems with required properties (metallic, semiconducting, magnetic and dielectric) could be achieved with nanometer core within the shell material [22, 39, 40, 49 55]. Shell protection is absolutely necessary for nanomaterials especially metal nanoparticles due to the following important reasons: (a) the shell can alter the surface charge, reactivity and functionality of the metal core thereby enhancing the stability and dispersibility of the colloidal materials; (b) by choosing a suitable shell-forming material, one can incorporate magnetic, optical and catalytic properties into the composite material; (c) encasing the core particle (especially metal) in a shell invariably protects it from physical and chemical changes; and (d) core-shells exhibit improved physical and chemical characteristics as compared to their single component counterparts. The different types of core shell systems include metal/metal oxide core/shell structure, bimetallic core/shell system, semiconductor core/shell system and polymer coated core/shell system [56, 57].

Since the first report of graphitic encapsulation of materials by Ruff *et al.* [28] in 1993, it offers the possibility to investigate the properties of low dimensional material in a closed environment. This would greatly change the chemical and physical properties of the materials providing interesting applications. Magnetic metal nanoparticles as core with carbon layers as shell can prevent the rapid oxidation of bare metal nanoparticles. Various techniques have been developed for synthesizing metal-filled carbon nanoclusters, such as carbon arc technique, wet chemical methods [6, 22, 24-31]. Catalytic pyrolysis method is of great promise due to low costs, ready availability or raw materials and simple processing techniques [58]. Although several groups have successfully obtained metal-filled carbon nanotubes or nanoparticles by catalytic method and several reaction models have been proposed, the catalytic mechanism and the nature of the encapsulated materials are not still clear. The shell protection imparts certain functional properties to the nanomaterial hence providing tremendous applications for these

materials in nanoscale optics, nanoelectronics, as well as in magnetic, catalytic, chemical and biological fields [59, 60]. Graphene nanocomposites are being used for electrochemical cell electrodes. For lithium ion batteries, the binder or matrix material is preferably amorphous polymeric carbon. Metal carbon hybrid nanostructures can also be thought of as electrode for supercapacitor applications. The studies show that carbon nanostructured materials can be used in energy generation as well as in energy storage applications. CNOs or hyperfullerenes are also being investigated theoretically as well as experimentally for utilizing the fantastic properties exhibited by these nanostructures. Ingenious fabrication techniques can make use of these nanostructures for creating new materials for nanoelectronics, diagnostics or sensing devices. Tribology [37, 38] is another area wherein these nanostructures can be exploited. Moreover, multifunctional materials can be fabricated by engineering nanocomposite properties using these nanostructures.

1.9 Natural rubber based magnetic nanocomposites

Natural rubber (NR) or cis 1,4 polyisoprene, has been identified in about 2000 plant species, but only the species *Hevea brasiliensis* is of commercial significance. From the tree, rubber is collected in the form of latex by tapping rubber is separated from the latex by coagulation usually by acidification. The resultant coagulum is then processed into different marketable forms of NR. Their molecular weight ranges from 200,000 to 600,000 with a relatively broad weight distribution [61]. Rubber separated from latex contains more than 90% of hydrocarbon; cis-1,4 polyisoprene in admixture with naturally occurring resins, proteins, sugars etc. NR is characterized with low hysteresis, high resilience and low water absorption. High tensile strength and elongation at break are the major attractive features of NR over synthetic rubbers [62]. Poor resistance to sunlight, oxygen and ozone are the drawbacks over synthetic rubbers, but it is inexpensive. NR is a versatile and adaptable material which find application in transport and engineering applications such as automobile tyres, aero tyre, off shore and aerospace industries, civil engineering, railways, vibration engineering etc.

Discovery of reinforcement of NR by particulate fillers is almost a century old. Although NR exhibits very good strength even without reinforcement, it was reinforced with unique composition of Jordanian silica sand with different particle size. Recently work are on modify the structure and properties of NR reinforced with nanofillers [63–65].

Polymers are inherently nonmagnetic materials. As early as in 1955, it has been seen that their properties could be modified by incorporation of magnetic fillers in plastic or rubber [66], though their magnetic properties are generally considered to be inferior to cast or sintered magnets. This is principally related to the relatively low permeability values associated with such composites as opposed to magnetic permeability of cast or sintered materials. However, polymer composites possess numerous advantages. The polymeric binder coats the magnetic particles and acts as an insulator suppressing eddy current losses. Polymer based magnets can be manufactured by conventional polymer processing techniques [62, 67, 68], allowing them to be moulded into complex shapes and sizes, with higher production rates, lower cost and better uniformity and reproducibility.

Incorporation of magnetic materials in a polymeric matrix offers wide possibilities for the nanostructures in applications where mechanical, dielectric and magnetic properties are equally important. Since NR is easily available and an inexpensive material, composites based on magnetic materials (both ferrites and ferromagnets) are extensively studied. The incorporation of filler particles modifies their dielectric as well as magnetic properties of the composites. Thus by appropriate manipulation of the filler amount in the composite, the phyiscomechanical, dielectric as well as magnetic properties can be tailored [67, 68]. These magentodielectric composites also find applications in areas where flexible magnetic materials are required. One of the other significant aspects is their microwave absorbing property.

1.10   Electromagnetic wave absorbers

The self propagating electromagnetic (EM) waves possess electric and magnetic components that oscillate at right angles to each other and to the direction of

propagation and are in phase with each other. In 1985, Federal Communication Commission in US defined the ISM (Industrial, Scientific and Medical) frequency bands with specific bandwidth (BW), allowing unlicensed spread spectrum communication. Three of the ISM bands are at frequency 500 MHz (BW $\sim$ 2.6 MHz), 2.44 GHz (BW$\sim$83.5 MHz) and 5 GHz (BW$\sim$300 MHz). 2.4 GHz band is available worldwide having more bandwidth, supporting higher data rate and multiple adjacent channels in the band, thus offering good balance of equipment performance and cost. 2.4 GHz is ideal for WLAN, high speed unlicensed data link. IEEE8020011b, Bluetooth and home RF operate in this band. It is less crowded, has global allocation and associated technique is cost effective. Hence studies on the wave absorbing properties in the S-band (2-4 GHz) become more significant.

The characteristics of materials that influence the EM wave are their complex permittivity, complex permeability, dielectric loss tangent, magnetic loss tangent and wave impedance. The basic requirements of a microwave absorbing material are high attenuation, small external surface reflection, low weight, stability of structure and properties. Microwave absorbing materials find applications in antenna techniques and production, for protection of humans and other biological objects form harmful action of EM waves, in military applications for anti-radar camouflage, for improving the EM compatibility between different electromagnetic devices [69–73]. The basic principle of microwave absorbing material development includes selection of suitable matrix fillers. The effectiveness of absorption composite structure is one which possesses low reflection, minimum transmission and maximum absorption at the same time.

An electromagnetic wave may be attenuated in three ways: i) by absorption due to the thickness of the shield, ii) by reflection at the surfaces, and iii) by multiple internal reflections [74, 75]. Reflection, requires the existence of mobile charge carriers (electrons or holes) which interact with the electromagnetic radiation. Thus, the shield tends to be electrically conducting, though a high conductivity is not required for shielding. For example, a volume resistivity of the order of 1 Ohm.cm is typically sufficient. The reflection loss is a function of the ratio electrical conductivity relative to copper and relative magnetic permeability. The reflection loss decreases with increasing frequency. Absorption,

requires electric and/or magnetic dipoles which interact with the electromagnetic fields. The electric dipoles may be provided by materials having high dielectric permittivity or magnetic permeability. The absorption loss is a function of the product of electrical conductivity relative to copper and relative magnetic permeability. Unlike reflection where the loss decreases with increasing frequency, the absorption loss increases with increasing frequency. The absorption loss is proportional to the thickness of the shield. Silver, copper, gold and aluminum are excellent for reflection, due to their high conductivity. Supermalloy are excellent for absorption, due to their high magnetic permeability [74]. The third mechanism of attenuation is multiple reflections (at various surfaces or interfaces in the shield). This mechanism requires the presence of a large surface area or interface area in the shield. For instance, a porous or foam material has a large surface area, and composite material containing fillers have a large interface area in the shield. The loss due to multiple reflections can be neglected when the distance between the reflecting surfaces or interfaces is large when compared to the skin depth which is the distance that electromagnetic radiation can be penetrate at certain high frequency.

The reflection loss of an absorber material with a metal backing can be evaluated from their dielectric permittivity and magnetic permeability values of the absorber layer medium for a known thickness in a specific frequency band. It is expressed in decibels (dB). An ideal absorber material should have a reflection loss over -20 dB. In other words, about 99.9% of the incident energy is lost when passing through the absorber material.

Nanocomposites based on ferro/ferri magnetic materials are light-weight and inexpensive materials that can prevent medical, military, and aircraft systems from EM interference (EMI) which can result in damages ranging from data jamming to burn out of sensitive equipment. Flexible composites can be developed by incorporating these magneto-dielectric fillers in appropriate ratio into natural rubber matrix.

1.11 Nonlinear optical properties of materials

Nonlinear optics deals with various new optical effects and novel phenomena arising from interactions of intense coherent optical radiations with matter. In the pre-laser era nonlinear optical effects could not be experimentally observed since the field strength of conventional sources was too small to perturb the atomic and interatomic fields. The assumptions of linearity of an optical medium where, the optical properties such as refractive index and absorption coefficients are independent of light intensity, the frequency of light cannot be altered by its passage through the medium, and light cannot interact with light. Irradiation of a medium with high intensity laser radiation is in principle equivalent to the application of large electric field to the material. The nonlinear behavior exhibited by media are (a) change in refractive index and consequently change in the speed of light as it propagates through a nonlinear medium, (b) light can alter its frequency as it passes through a nonlinear optical medium, and (c) light can control light; photon can be made to interact. A brief introduction on the general theory of nonlinear optical property is provided below for the sake of continuity.

When a molecule is subjected to strong laser radiation, the molecule's polarization is being driven beyond the linear regime. The modified nonlinear polarization P_m (which is a function of applied field and leads to nonlinear effects) is expressed as $P_m = \alpha' E + \beta' E^2 + \gamma' E^3 + ...$ where α' is the linear polarization of the molecule or atom, β' is the first molecular hyperpolarisatbility (second order nonlinear term), γ' is the third order nonlinear term and E the electric field acting on the molecule. Usually, $\alpha' >> \beta'$ or γ'. With increasing field strength, nonlinear effects become observable due to the presence of higher powers of E and the equation gets generalized to $P_m = \epsilon_o[\chi^{(1)} E + \chi^{(2)} E^2 + \chi^{(3)} E^3 + ...]$, where $\chi^{(1)}$ is the first order susceptibility and $\chi^{(n)}$ is the nth order nonlinear optical susceptibility.

Thus, the optical characteristics of a medium such as dielectric permittivity or refractive index, which depend on susceptibility, also become a function of the electric field strength E. The optical nonlinearity is thus the property of the medium through which light travels, rather than a property of light itself. If the

incident light has the form $E = E_0 cos(\varpi t)$, then we have

$$P_m = \epsilon_o[\chi^{(1)}E_o \cos(\varpi t) + \chi^{(2)}E_o^2 \cos^2(\varpi t) + \chi^{(3)}E_o^3 \cos^3(\varpi t) + ...] \qquad (1.14)$$

Using the trigonometric relations: $\cos^2(\varpi t) = [1 + \cos(2\varpi t)]/2$ and $\cos^3(\varpi t) = [\cos(3\varpi t) + 3\cos(\varpi t)]/4$, the above relation becomes

$$P_m = (1/2)\epsilon_o\chi^{(2)}E_o^2 + \epsilon_o[\chi^{(1)} + (3/4)\chi^{(3)}E_o^2]E_o \cos(\varpi t)+$$

$$(1/2)\epsilon_0\chi^{(2)}E_o^2 \cos^2(2\varpi t) + (1/4)\epsilon_0\chi^{(3)}E_o^3 \cos(3\varpi t) + ... \qquad (1.15)$$

The first term is a constant term which gives rise to a DC field across the medium, the effect of which is of comparatively little importance. The second term follows the external polarization and is called first or fundamental harmonic of polarization. The third oscillates at a frequency $2\varpi t$ and is called the second harmonic of polarization, the fourth is called the third harmonic of polarization and so on. These higher harmonics of dielectric polarization results from the nonlinearity of the medium leading to various optical nonlinear phenomena.

In general, depending on the order of the nonlinearity, effects like second harmonic generation ($\chi^{(2)}$ process whereby two photons of the frequency interact together to form a single photon of frequency 2ϖ), Pockel's effect ($\chi^{(2)}$ process where the refractive index of a material varies linearly with an applied DC electric field), optical Kerr effect ($\chi^{(3)}$ process whereby the refractive index of a medium varies linearly with the intensity of an applied electromagnetic radiation field), etc can take place. However, due to phase matching restrictions, all allowed nonlinear phenomena will not occur simultaneously in a given nonlinear medium.

For a third order nonlinear medium (like isotropic solutions), the real and imaginary components of $\chi^{(3)}$ are related to the nonlinear refraction and nonlinear absorption respectively through the expressions: $Re\chi^{(3)} = 10^{-6}cn_o^2n_2/(480\pi^2)$ and $Im\chi^{(3)} = 10^{-7}c^2n_o^2\beta/(96\pi^2\varpi)$, where c (cm/s) is the velocity of light, n_o is the refractive index, ϖ(Hz) is the laser radiation frequency, β(cm/W) is the nonlinear absorption coefficient and n_2 (cm^2/W) is the nonlinear refractive index. The refractive index and absorption coefficient of the medium are given by

$$n = n_o + n_2 I$$

$$\alpha = \alpha_o + \beta I \tag{1.16}$$

where 'I' is the laser intensity, α_o is the linear absorption coefficient, and β is the nonlinear absorption coefficient. The propagation equation for light travelling in the z direction through a third order nonlinear medium can then be written as

$$\frac{dI}{dz} = -(\alpha_0 + \beta I)I \tag{1.17}$$

Depending on the sign of n_2 and β, the modification in the refractive index will give rise to self focusing or defocusing effects while that in the absorption coefficient will lead to induced transmission or absorption.

Various organic and hybrid nanostructures are identified for nonlinear optical applications [76]. Nanostructured materials are found to be interesting candidates, since their optical properties are highly dependent on the size of these structure. Noble metals like Cu, Ag and Au as well as magnetic metals like Fe, Co, Ni and their nanostructures are being investigated recently. Carbon nanostructures are well studied for their optical limiting properties, especially carbon black, carbon nanotube, fullerene and nanowire [77-81].

Optical Limiting: Controlling the intensity of light in a predetermined and predictable manner is a fundamental and important requirement with applications ranging from optical communication to optical computing. This can be used to switch, limit, amplify or modulate the amplitude of an optical signal via dynamic or passive methods.

Over the last few decades, many scientists have sought the so-called optical limiting materials that exhibit 'nonlinear extinction', i.e. strongly attenuate intense, potentially dangerous laser beams, while readily transmitting low-intensity ambient light. Up to now, a number of organic and inorganic materials, including phthalocyanines, porphyrins, fullerenes, carbon nanotubes, inorganic nanoparticles, metal complexes and clusters [79-84] have found to show a strong nonlinear extinction effect for practical optical limiters. There are a variety of nonlinear optical phenomena that can be used to construct an optical limiter. These include two photon/multi photon, excited state and free carrier absorption, nonlinear refractive processes such as self focusing and photo refraction and optically induced scattering.

Two photon absorption (TPA) is an instantaneous non-linearity that involves the absorption of a photon from an electromagnetic field to promote an electron from its initial state to a virtual intermediate state, followed by the absorption of a second photon that takes the electron to its final real state. Since the intermediate state for such transition are virtual, energy need not be conserved in the intermediate state but only in the final state. For TPA, the material response is of the order of an optical cycle and is therefore independent of the optical pulse length for a fixed intensity. The device will respond virtually instantaneously to the pulse. On the other hand, because of the low value of TPA co-efficient β (where $\beta = (\frac{3\varpi}{2}\epsilon_0 c^2 n_0^2)Im(\chi^{(3)})$ with ϖ=circular frequency of the optical field, n_o—the linear index of refraction and c=the speed of light in vacuum), in usual materials, high intensities are required to realize significant TPA in them. Since the intensity is essentially the energy density divided by the pulse duration, short pulses are required to achieve limiting with TPA for energy densities that may be enough to damage an optical sensor. Thus, TPA acting alone is not a practical approach to device protection for nano second and longer threat pulses.

Reverse saturable absorption (RSA) or excited state absorption generally arises in a system when an excited state absorbs stronger than the ground state. The process can be understood by considering a system that is modelled using three vibronically broadened electronic energy levels. Let the cross section for absorption from the ground state 1 is σ_1 and σ_2 is the cross section for absorption from the excited state 2 to the second excited state 3. The lifetime of the first excited state is σ_2 (seconds). As light is absorbed by the material, the first excited state begins to become populated and contributes to the total absorption cross section. If σ_2 is smaller than σ_1, the material becomes transparent and bleaches. Such materials are known as saturable absorber. If σ_2 is larger than σ_1, then the total absorption increases and the material is known as reverse saturable absorber. Reverse saturable absorbers are good optical limiters.

Once charge carriers are optically generated in a semiconductor, whether by single photon or two-photon absorption, these electrons (holes) can be promoted to states higher (lower) in the conduction (valence) band by absorbing addition photons. This process is often photon assisted, although depending on the details of the band structure and the frequency of the optical excitation it may also be

direct. The photon-assisted phenomenon is referred to as free carrier absorption and it is analogous to the excited state absorption in a molecular system. It is clearly an accumulative nonlinearity, since it depends upon the buildup of carrier population in the band as the incident optical pulse energy is absorbed.

Optical limiters based on self-focusing and defocusing form another class of promising device. The mechanism for these devices may arise from the real part of $\chi^{(3)}$ or from nonlinear refraction associated with carrier generation by either linear or two photon absorption in a semiconductor. Both self focusing and defocusing limiters operate by refracting light away from the sensor as opposed to simply absorbing the incident radiation. Compared to strictly absorbing devices, these limiters can therefore potentially yield a larger dynamic range before damage to the limiter itself happens.

Scattering is caused by light interacting with small centers that can be physical particles or simply the interfaces between the groups of non-excited and excited molecules. Scattering can be highly directional or fairly uniform depending on the size of the scattering centers. It is observed that if an optical signal induces scattering centers in a medium, the transmission of the medium measured in a given solid angle will decrease. Hence, optical scattering can be used in optical limiters for sensor application. Scattering are of two types. When particles are much smaller that the wavelength of light or where the particles are nonabsorbing, Rayleigh scattering occurs. For particles where the size is either comparable or larger than the wavelength of light, Mie scattering occurs. The essential point is that as the size of the scattering particle increases, a larger percentage of the scattered radiation is forward scattered. Hence, limiting based on Mie scattering will be less effective than Rayleigh scattering [85, 86].

1.12   Motivation of the present work

Having discussed some of the issues pertaining to both fundamental and applied aspects in the introduction, it is necessary that these nanostructures are prepared in laboratory itself. Simple and cost effective methods are necessary for the preparation of such nanostructures. Moreover, history of the sample preparation is highly essential for the proper and error free interpretation of results. So

emphasis was laid in synthesizing magnetic metal-carbon nanostructures. In order to look at the size effects on different properties, both top-down as well as bottom-up approaches were adopted.

Magnetic metal nanoparticles are candidate materials for studying various phenomena like surface spin, spin clusters or superparamagnetism. Because of their large surface to volume ratio, majority of the atoms will be on the surface and this determines the overall properties of materials in the nanoregime. So one of the motivations of the present investigation is to synthesize pure metal nanoparticles employing both top-down as well as self assembly techniques. Metallic particles in the nanoregime are to be passivated to prevent oxidation. Carbon is an ideal candidate for achieving this objective. Coating of carbon on metal particles could be attempted by the pyrolysis of organic coating over metal nanoparticles. Since 3d-transition metals namely Fe, Co and Ni are known for their ferromagnetism, iron-carbon, cobalt-carbon and nickel-carbon hybrid nanostructures are to be fabricated. This is yet another objective of this study.

Magnetic metal particles with reduced size and when embedded in carbon matrices are believed to be good microwave absorbers. This is because of size dependent Snoek's limit, higher skin depths and higher magnetic permeability values. So the evaluation of their dielectric permittivity and magnetic permeability is necessary in various frequency bands. After evaluation of the real and imaginary part of complex dielectric permittivity and complex magnetic permeability of the material, they are to be modelled based on surface impedance equation and the minimum thickness are to be found out for maximum absorption. Hence, evaluation of microwave absorbing properties of these nanostructures is another motivation of the present study.

Different forms of carbon are known for their non-linear optical properties and also for their optical limiting properties. Metal nanoparticles are also being investigated to great detail in this regard. However a combination of cobalt-carbon nano onion is never investigated for their optical limiting properties. It was thought that such a study would be novel and probably would throw light on various mechanisms leading to nonlinear properties vis-a-vis saturable absorption, two photon absorption, three photon absorption, scattering etc. This forms another objective of this work.

Flexible magnetic nanocomposites are in great demand since they can be moulded into complex shape and can be made into gaskets. Nano nickel ferrites or magnetic metals, if impregnated in matrices like natural rubber will result in magnetic rubber nanocomposites and will be good microwave absorbers because rubber can impart the required dielectric properties while ferrite imparts magnetic permeability to the composite.

The **main objectives** can thus be summarized in a nutshell as follows.

- Synthesize magnetic metal nanoparticles of iron, cobalt and nickel by employing both bottom up and top down approach

- Passivate 3d-transition magnetic metal nanoparticles with organic coating and study the evolution of magnetic metal carbon hybrid nanostructures

- Study the magnetic and optical limiting properties of passivated magnetic metal nanoparticles

- Synthesize, characterize and evaluate the magnetic as well as dielectric properties of magnetic metal oxide nanoparticles obtained by employing both bottom up as well as top down approach

- Incorporate magnetic metal oxide nanoparticles in a natural rubber matrix to obtain flexible RFCs and study their cure, physicomechanical, dielectric and magnetic properties

- Incorporate magnetic metal nanoparticles obtained via high energy ball milling in natural rubber to obtain flexible magnetic material and hence compare their properties

- Fabricate an experimental set up for measuring complex dielectric permittivity and complex magnetic permeability at microwave frequencies

- Investigate the microwave properties of the metal carbon hybrid structures and magnetic rubber composites thereby tune their microwave absorbing properties

- Employ the surface impedance equation to simulate the optimum composite composition for minimum thickness and reflection loss

- Correlate the results

Chapter 2

Experimental Techniques

The swift developments in material science demands ingenious synthesis methodologies along with the simultaneous characterization of intermediate stages employing sophisticated characterization/analytical tools specific for low dimensions. The first part of this chapter describes the synthesis methodologies adopted in the present study. Conventional, modified as well as novel techniques were employed for the preparation of magnetic metal and metal oxide nanostructures. Rubber process methodology for developing the magnetic rubber composite is also discussed in detail. These magnetic nanostructures were characterized using sophisticated analytical tools namely X-ray diffraction, scanning electron microscopy, transmission electron microscopy, energy dispersive X-ray spectroscopy, Fourier transform infrared spectroscopy, inductively coupled plasma analysis, Raman spectroscopy, UV-Vis-NIR spectroscopy and thermal gravimetry. Details of magnetic characterization tools like vibrating sample magnetometer, superconducting quantum interference device magnetometer and zero field cool-field cooled measurements are also mentioned. Experimental setup for the determination of dielectric, microwave and nonlinear optical properties of materials are explained in the latter section of this chapter.

2.1 Synthesis of metal/metal oxide nanoparticles

Recently magnetic nanoparticles are extensively being investigated due to their wide and important applications in medicine, electronic industry and many other

fields. The main difficulty encountered is the synthesis of monodispersed nanoparticles. Nanoparticle synthesis methodology can be broadly classified into two, namely, physical and chemical [6, 87]. Physical methods include inert gas evaporation technique, sputtering, sonication, laser pyrolysis, high energy ball milling [17, 18, 87 91]. Meanwhile chemical methods often used are sol-gel process, UV irradiation, thermal decomposition of metal carbonyls, inverse micelle technique, electrode deposition, reduction of metal salts by borohydride derivatives [92 101] etc. In the present work the nanoparticles were prepared by both top-down as well as bottom-up approaches and the details of which are described below.

2.1.1 Borohydride reduction of metal salts

A well-known and successful means to produce stable metal nanoparticles with narrow size distributions is reduction of their corresponding metal salts. Reducing agents such as $NaBEt_3H$, $LiBEt_3H$ and $NaBH_4$ have been commonly used to yield nano powders [92 95]. It is found that the structure of the products strongly depends on the reaction conditions like types of solvents, presence of oxygen and water, pH, concentration etc. In aqueous solution in the presence of small amounts of oxygen, the following reaction mechanism is proposed:

$$2M^{2+} + 4(BH_4)^- + 9H_2O \longrightarrow M_2B + 12.5H_2 + 3B(OH)_3$$

$$4M_2B + 3O_2 \longrightarrow 8M + 2B_2O_3 \qquad (2.1)$$
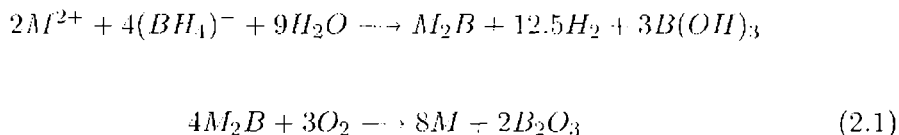
where M denotes metal (Fe, Co, Ni etc). An excess of oxygen can oxidize the metal to its oxide derivatives. In nonaqueous solutions, the nonaqueous solvent behaves as a ligand (L) and the reaction is as shown.

$$M^{2+} + 2NaBH_4 + nL \longrightarrow (L)_n M(BH_4)_2 + 2Na^+$$

$$(L)_n M(BH_4)_2 \longrightarrow M + H_2 + B_2H_6 + nL \qquad (2.2)$$
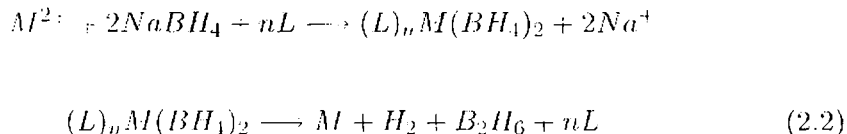
The particle size can be tuned by varying the concentration of the solution, which promises wide variation of size of the nanoparticles.

2.1.2 Sol-gel method

Sol-gel process [99 101] is widely used for the synthesis of metal oxide nanoparticles. In this process, inorganic metal salts like nitrates, chlorides or sulphates are dissolved in an organic solvent to form the sol which is allowed to undergo gelation forming highly porous gel. Chemical reaction in the first stage of the process leads to the formation of a network of metal hydroxides. Gelation takes place when all the hydroxide species are linked in a single network like structure. This gel is a thick and porous solid structure surrounding the interconnecting pores and is a polymer of hydroxides, formed in three dimensions. By heating, the solvent can be removed completely and highly porous and ultrafine metal hydroxide powder can be obtained. Metal oxides are formed from this ultrafine metal hydroxide powder by heat treatment [102–104].

In certain cases heating the gel in an open container exposed to atmospheric air to a temperature of around 373 K can result the combustion of the gel assisted by the organic material remaining in the gel. Metal oxide powder of nanometer size is readily formed in such reactions. Such a process is generally called a sol-gel combustion process. A variety of organic combustion agents are used for the automatic combustion of the gel. Urea, citric acid, ethylene glycol or diethylene glycol are some of the commonly used combustion agents. But normally, metal oxides are synthesized by calcinating the gel in temperature controlled furnaces for specified time durations at temperatures ranging from 573 to 1273 K depending on the nature of metal oxide to be formed.

2.1.3 Ceramic method

Ferrites are widely synthesized via the conventional double sintering ceramic technique [105 107] which involves high temperature sintering. Initially ferric oxide is prepared by decomposing freshly precipitated ferrous oxalate dyhidrate (FOD). FOD in turn is prepared by co-precipitation of ferrous sulphate with oxalic acid. Appropriate amount of metal precursors, necessary for the synthesis of the mixed ferrites are weighed according to molecular weight considerations. These metal oxides or carbonates together with the required amount of ferric oxide are mixed thoroughly in an agate mortar to produce a homogeneous mixture of fine particles. The process of mixing is carried out in an acetone medium to ensure

uniformity. This homogeneous mixture is pre-fired at around 773 K for 5 h in a furnace at ambient conditions. The pre-sintered sample is then crushed into powder form and finally sintered at around 1273 K for 12 h. They were then allowed to cool to room temperature.

2.1.4 High energy ball milling

Mechanical attrition is a simple and relatively inexpensive technique, widely used for alloying, mixing and reduction of grain size of powder samples [88, 89]. Fritsch planetary micro mill - 'Pulverisette 7' high energy ball milling (HEBM) unit (Figure 2.1) employed in this study consists of two grinding vials symmetrically held on a rotating base. These vials are filled with equal number of balls, both made of tungsten carbide. Equal amounts of samples were added into each of the vials. Atmospheric contamination is minimized by sealing the vial with flexible 'O' ring after the powder has been loaded. Usually an organic fluid is used to avoid contamination from the milling tools and also to minimize the wear. The grinding vials are made to rotate on their own axis while simultaneously rotating through an arc around the central axis. The grinding balls and the material in the grinding vial are thus acted upon by the centrifugal forces, which constantly change in direction and intensity, resulting in efficient, fast grinding process. The grinding vials and the supporting disc rotate in opposite directions, so that the centrifugal forces alternatively act in the same and opposite directions. This results in a frictional effect. The grinding balls running along the inner wall of the grinding bowl cause impact effect. The balls impacting against the opposite wall of the grinding bowl gives energy which is many times higher than for traditional mills. This results in excellent grinding performance within a short duration of time.

Parameters that determine the quality of powders are type of mill, milling atmosphere, milling media, intensity of milling, ball to powder weight ratio, milling time and milling temperature, all affects the particle size of the resulting sample [108]. In this study, tungsten carbide balls and vials were used maintaining the balls to powder ratio at 10:1 with a rotation speed of 550 rpm in toluene medium. Care was taken to cool the system by giving a break of 30 min after every half an hour of milling.
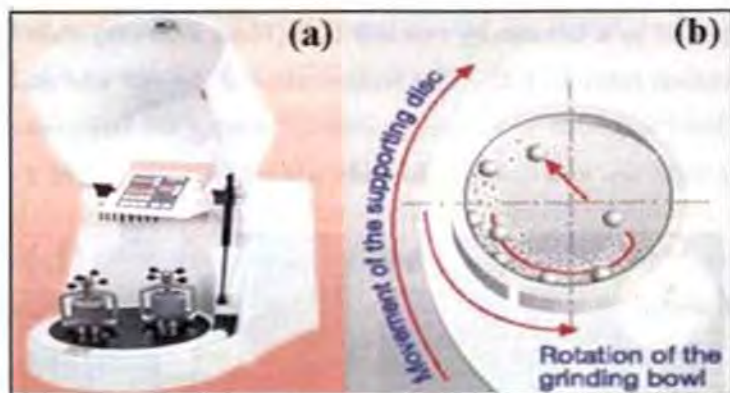
Figure 2.1: (a) Fritsch Planetary micromill - 'Pulverisette 7', and (b) Rotation of the bowl and balls around the central axis

2.2 Synthesis of magnetic rubber nanocomposites

Synthesis of magnetic rubber nanocomposites involves careful selection of compounding recipe and a step by step procedure of mixing, aging, moulding and curing the compounds. Specific test procedures [109–111], are used to measure almost all of the physical properties of the rubber composites.

2.2.1 Compounding

Compounding involves incorporation of fillers into the rubber matrix according to a specific recipe (details in Chapter 7). Mixing was carried out in a Brabender Plasticorder (model: PL 3S) torque rheometer [112–115]. The heart of the torque rheometer is a jacketed mixing chamber of volume $\sim$40 cm^3 (Figure 2.2) with horizontal rotors connected to a shaft.

A dc thyrister controlled drive is used to control the speed of rotation of the rotors. The temperature of the mixing chamber can be varied up to 573 K which can be controlled and measured with the aid of a temperature controller and a recorder. After selecting the temperature and rotor speed, the rubber is charged into the mixing chamber. When the nerve of the rubber disappears, compounding ingredients are added as per the sequence given in ASTM D 3182 (1982). Mixing was carried out at 343 K at 50 rpm speed. This is followed by the homogenization

of the compound in a laboratory two roll mill (15cm x 33 cm) shown in Figure 2.2b at a friction ratio 1: 1.25. The temperature of the roll was maintained at 333 K and the compound was homogenized by passing the compound six times through the tight nip and finally made into a sheet at a nip gap of 3 mm.
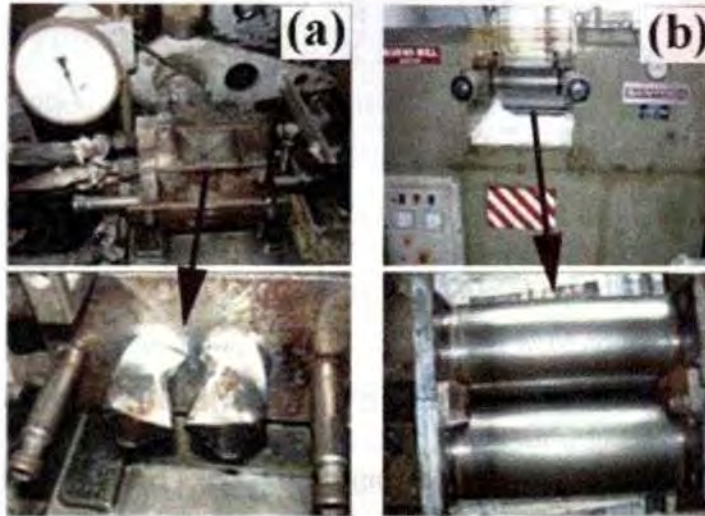
Figure 2.2: (a) Brabender Plasticorder and (b) Two roll micromill

2.2.2 Cure characteristics

After aging the composite for 24 h, cure characteristics of the mixed compounds were determined using a rubber processing analyser (RPA 2000-Alpha technology) shown in Figure 2.3a. It is an advanced dynamic mechanical and rheological test instrument designed to measure the properties of polymers and rubber compounds to investigate the physicomechanical properties of polymers before, after or during the process of curing.

RPA measures the viscoelastic properties of rubber compounds providing comprehensive data on key parameters such as processability and cure characteristics. It is a microprocessor controlled rotorless cure meter with a quick temperature control mechanism and well defined homogeneous temperature distribution in the test chamber. It uses two directly heated low mass biconical dies. The required starting temperature for the test is set and controlled by heating

and/or forced air cooling. The temperature can be varied during the test or maintained at a constant value within ± 0.5 K.

RPA is equipped with a direct drive servo motor system that can vary the oscillation angle and frequency. A circular shaped test specimen is kept in the lower half of the cavity, which is oscillated through a small deformation angle. The frequency of oscillation is maintained at 50 cycles/min. The torque is transmitted through the sample from the oscillating lower die to a highly sensitive torque transducer positioned in the upper die. The measurements made by the torque transducer are fed into the system computer. The selected sample properties are calculated and the results are displayed and the data is available for further analysis. Figure 2.3c shows the sample obtained after test from RPA.

In the present study, cure characteristics of the rubber composites were determined at a temperature of 423 K by measuring modulus and torque against time at a pre-programmed strain. Different cure parameters obtained are as follows [62, 116].

- Minimum torque, (D_{min}) : Torque obtained by the mix after homogenizing at the test temperature and before the onset of cure.

- Maximum torque (D_{max}): Maximum torque recorded at the completion of cure.

- Optimum cure time (t_{90}): This is the time taken for obtaining 90% of the maximum torque

- Scorch time (t_{10}): It is the time taken for two unit rise above minimum torque (i.e.; about 10% vulcanisation)

- Cure rate index (CRI): Cure rate index is calculated using the relation CRI = 100 / (t_{90}-t_{10})

2.2.3 Moulding

The test specimens for determining the physical properties were prepared in a standard mould by compression moulding on an electrically heated hydraulic press (Figure 2.3b) having 45 cm x 45 cm platens at a pressure of 140 kg/cm^2 to their respective cure times (t_{90}). After completing the cure, pressure was released and the sheet was stripped out from the mould and suddenly cooled by immersing

in cold water. Samples were matured for 24 h prior to testing. The photograph of moulded rubber composite is shown in Figure 2.3d.
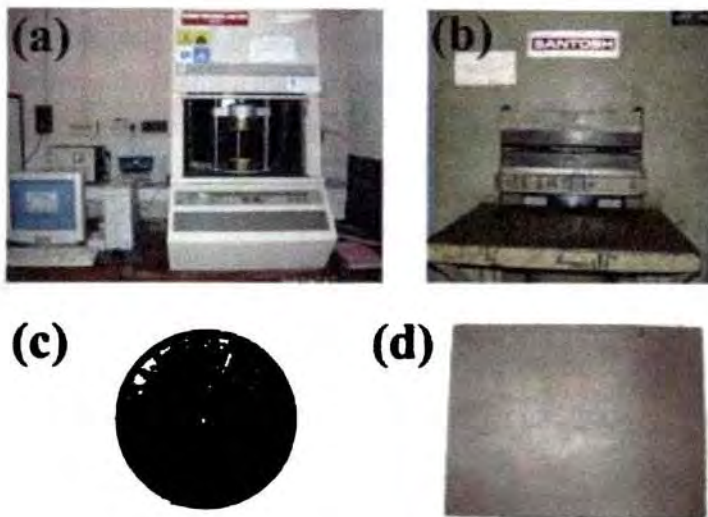
Figure 2.3: (a) Rubber process analyzer, (b) hydraulic press, and (c, d) moulded rubber nanocomposites

2.3 Mechanical properties of rubber composites

2.3.1 Stress-strain properties

Tensile strength, modulus and elongation at break are some of the most important indications of the strength of a composite material. These are determined using a universal testing machine (UTM) model : Shimadzu-SPL 10 kN as shown in Figure 2.4.

It has a stationary part carrying one grip and a movable part carrying the second grip. Stress-strain measurements were carried out as per ASTM D 412-98a(2002) at 296 ± 1 K and 65 ± 5 % relative humidity. Dumbbell shaped test specimens (Figure 2.4c) were punched out from the compression moulded sheets along the mill grain direction using a standard die (Type D). The sample is held between the two grips on the UTM and a uniform rate of grip separation of 500 ± 50 mm/min was applied. The tensile strength. elongation at break and modulus at different elongations were recorded and evaluated after each measurement

by the microprocessor.
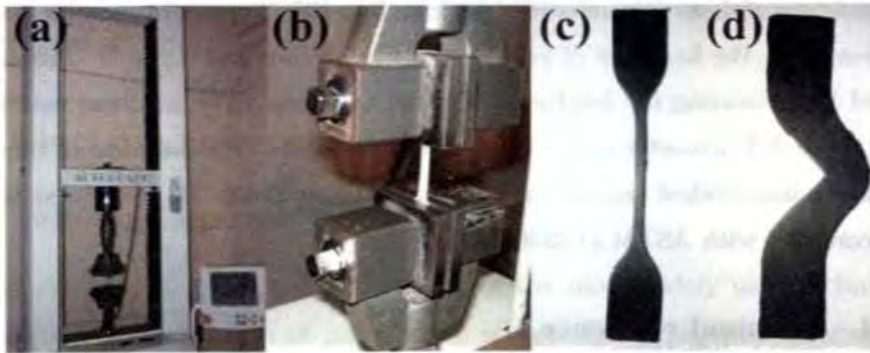
Figure 2.4: (a, b) Universal testing machine, (c) tensile test specimen, and (d) tear test specimen

2.3.2 Tear strength

Tear of a rubber is a mechanical rupture process initiated and propagated at a site of high stress concentration caused by a cut, defect or localized deformation. In a tear test, the force is not applied evenly, but concentrated onto a deliberate flaw or sharp discontinuity and the force to continuously create a new surface is measured. Tear strength of the samples were measured as per ASTM D 624(2000) using standard test specimens (Figure 2.4d) with 90° angle on one side and tab ends (Type-C die), which were punched out from the moulded sheets along the mill grain direction. The test was carried out in a UTM.

2.3.3 Hardness

Hardness can generally be defined as the resistance of a material to deform. This gives a measure of elastic modulus at low strain of the sample and can be measured by determining its resistance to indentation by a rigid indenter. Durometer hardness tester is used for measuring the relative hardness of soft materials. It consists of a pressure foot, an indenter and a dial gauge. The indenter is spring loaded and the point of the indenter protrudes through the opening in the base. Several instruments are used to measure the hardness of materials ranging from soft sponge to ebonite type materials. The most commonly used durometers are Type A and Type D. The basic difference between these two is the shape and

dimension of the indenter. The hardness numbers derived from either scale are just numbers without any units ranging from 0 to 100. Type A Durometer is used for measuring the hardness of relatively soft materials and Type D Durometer is used for measuring the hardness of harder materials. The hardness measured using Type A Durometer is expressed in Shore A unit. The hardness of the mechanically unstretched samples was tested by using Zwick 3114 hardness tester in accordance with ASTM D 2240(2003).

2.3.4 Rebound resilience

Rebound resilience is a very basic form of dynamic test in which the test piece is subjected to one half cycle of deformation only. The strain is applied by impacting the test piece with an indenter which is free to rebound after the impact. Rebound resilience is defined as the ratio of the energy of the indenter after impact to its energy before impact expressed as percentage. Resilience of the samples was measured according to the ASTM D 2632(2001) with vertical rebound resiliometer.

2.4 Powder X-ray diffraction

X-ray diffraction (XRD) pattern of samples were recorded using an X-ray diffractometer (Rigaku Dmax-C) with CuKα radiation (λ=1.5418Å). From the diffraction patterns, parameters like relative intensity (I/I$_0$) of the crystallographic planes, their interatomic spacing 'd' and average crystallite size 'D' are determined. Assuming cubic symmetry lattice parameter 'a' is evaluated using the relations [117, 118]

$$\frac{1}{d^2} = \frac{h^2 + k^2 + l^2}{a^2} \tag{2.3}$$

where 'h', 'k' and 'l' are the Miller indices.

The average crystallite size is evaluated from the measured width of their diffraction curves by using Debye-Scherrer's formula.

$$D = \frac{0.9\lambda}{\beta cos\theta} \tag{2.4}$$

where λ is the wavelength of CuKα radiation, β is the full width at half maximum of the diffraction peak and θ is the glancing angle (or the complement of the angle of incidence)

2.5   Electron microscopy

2.5.1   Scanning electron microscopy

Scanning electron microscopy (SEM) is one of the most widely used techniques used for the characterisation of micro/nano structures. It provides information about the morphology and microstructures of materials. The resolution of SEM approaches a few nanometers and the instrument operates in the range of 10-30 kV. SEM is carried out by scanning an electron beam over the sample's surface and detecting the yield of low energy electrons (secondary electrons) and high energy electrons (backscattered) according to the position of the primary beam. The secondary electrons which are responsible for the topological contrast provide mainly information about the surface morphology. The backscattered electrons which are responsible for the atomic number contrast carry information on the samples composition [119]. In new generation SEM, field emission gun provides the electron beam and the resolution is as high as 1 nm. FESEM JSM-6335 scanning electron microscope was employed to check the morphology of our samples.

2.5.2   Transmission electron microscopy

Transmission electron microscopy (TEM) is a straight forward technique to determine the size and shape of the nanostructured materials. In TEM, electrons accelerated to 100 keV or higher are projected onto a thin specimen by means of a condenser lens system, and penetrated into the sample [120]. It uses transmitted and diffracted electrons to generate a two dimensional projection of the sample.

The principal contrast in this projection or image is provided by diffracted electrons. In bright field image the transmitted electrons generate bright regions while the diffracted electrons produce dark regions whereas in dark field image, the diffracted electrons preferentially form the image. One can switch between imaging the sample and viewing its diffraction pattern by changing the strength

of the intermediate lens. TEM offers high magnification ranging from 50 to 10^6 and provide both image and diffraction information from a single sample. The magnification or resolution of TEM is given by

$$L = \frac{h}{\sqrt{2mqV}} \qquad (2.5)$$

where $'m'$ and $'q'$ are the electron mass and charge, $'h'$ the Planck's constant and $'V'$ is the potential difference through which the electrons are accelerated. The schematic of a transmission electron microscope is shown in Figure 2.5.
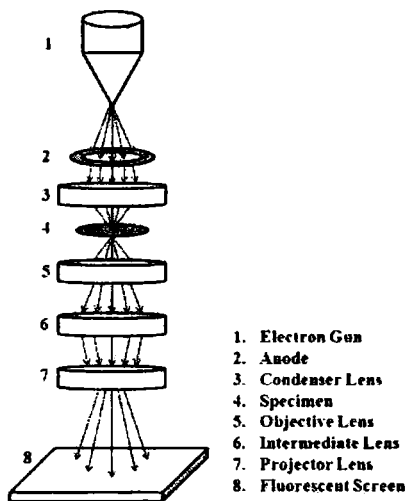
Figure 2.5: Schematic of transmission electron microscope

It consists of an emission source (tungsten filament or a lanthanum hexaboride source) coupled with three stages of lensing namely; condenser lenses, objective lenses and projector lenses. The condenser lenses are responsible for primary beam formation, whilst the objective lenses focus the beam down onto the sample itself. The projector lenses are used to expand the beam onto the phosphor screen or other imaging device, such as film. The magnification of the TEM is due to the ratio of the distances between the specimen and the objective lens's image plane. Imaging systems in a TEM consist of a phosphor screen, which may be made of fine (10-100 μm) particulate zinc sulphide, for direct observation by the operator. Optionally, an image recording system such as film based or doped YAG screen coupled CCD's is attached. High resolution transmission electron microscope

(HRTEM) [121] can generate lattice images of the crystalline material allowing the direct characterization of the samples atomic structure. The resolution of the HRTEM is 1 nm or smaller. However, the most difficult aspect of the TEM technique is the preparation of samples. Joel JEM-2200 FS TEM was used here for carrying out the different electron microscopic studies.

2.6 Energy dispersive X-ray spectroscopy

Energy dispersive X-ray spectroscopy (EDS) is an analytical technique which utilizes X-rays that are emitted from the specimen when bombarded by the electron beam to identify the elemental composition of the specimen. To explain further, when the sample is bombarded by the electron beam of the SEM/TEM, electrons are ejected from the atoms on the specimens surface. A resulting electron vacancy is filled by an electron from a higher shell, and an X-ray is emitted to balance the energy difference between the two electrons. The EDS X-ray detector measures the number of emitted X-rays versus their energy. The energy of the X-ray is characteristic of the element from which the X-ray was emitted. A spectrum of the energy versus relative counts of the detected X-rays is obtained and evaluated for qualitative and quantitative determinations of the elements present [122].

2.7 ICP-atomic electron spectroscopy

Elemental analysis of the samples (up to the parts per million levels) was carried out with the help of inductively coupled plasma-atomic electron spectroscopy (ICP-AES, model: Thermo Electron Corporation, IRIS INTREPID II XSP). In this method, a plasma or gas consisting of ions. electrons and neutral particles are formed from an Argon gas. The plasma is used to atomize and ionize the elements in a sample. The resulting ions are then passed through a series of apertures (cones) into the high vacuum mass analyzer. The elements are identified by their mass-to-charge ratio (m/e) and the intensity of a specific peak in the mass spectrum is proportional to the amount of that element in the original sample [123].

2.8   Spectroscopic analysis

2.8.1   Fourier transform infrared spectroscopy

Infrared spectroscopy is a useful technique for characterizing materials and obtaining information on the molecular structure, dynamics and environment of a compound. Vibrational motion of chemical bonds occurs in the infrared region of the energy beam. Fourier Transform Infrared (FTIR) spectroscopy exploits this phenomenon.
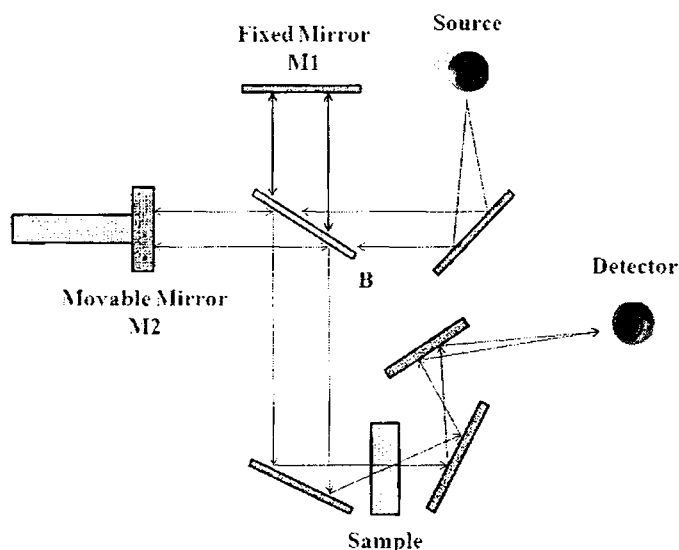
Figure 2.6: Schematic of FTIR spectrometer

When a sample is exposed to IR radiation, this energy couples with the energy of the sample and if the impinging IR energy is in resonance with the energy of the chemical bond in the sample, the intensity of the beam is measured before and after it interacts with the sample [124]. In an FTIR spectrum, the absorption or transmittance peaks correspond to the frequencies of vibrations between the bonds of the atoms making up the material. FTIR spectrophotometer (model: Thermo Nicolete Avatar DTGS) was used in our study. FTIR spectrometry uses the technique of Michelson interferometry, as illustrated in Figure 2.6.

A beam of radiation from the source is focused on a beam splitter, where half of the beam is reflected to a fixed mirror and other half of the beam is

transmitted to a moving mirror which reflects the beam back to the beam splitter from where it travels, recombines with the original half beam, to the detector. The IR intensity variation with optical path difference (interferogram) is the Fourier transform of the (broadband) incident radiation. The IR absorption spectrum can be obtained by measuring an interferogram with and without a sample in the beam and transforming the interferograms into spectra.

2.8.2 Raman spectroscopy

Raman spectroscopy, a technique which measures the energies of vibrational transitions in molecules, is a widely used tool to study and distinguish between different types of carbon nanostructures [125]. Raman spectroscopy measures the difference in energy between a source and the light scattered off from a sample. This energy difference corresponds to vibrational transitions in the molecules, specifically vibrations which change the polarizability of the molecules. When radiation hits a molecule, depending on the molecule and wavelength, much of the radiation may be absorbed and emitted in various ways. A small fraction of the radiation is scattered, most of it at the same wavelength as the incoming radiation (Rayleigh scattering). A very small fraction of the incoming radiation is scattered at a different wavelength due to Raman scattering. The difference in energy corresponds to vibrational transitions in the molecule. When a photon of radiation impinges on a molecule, it is absorbed, bringing the molecule to a virtual state, which does not necessarily correspond to any particular electronic or vibrational states. This is why Raman works with different source wavelengths. The energy is almost immediately released as a new photon, usually at the same wavelength as the incoming light. However, if the energy was absorbed from the ground vibrational state, but leaves the particle in a higher vibrational state, the scattered light will have a Stokes shift from the original light. Anti-Stokes shift can occur if the molecule was in an excited vibrational state before absorbing the energy, but these shifts are less likely because of the small probability of finding a molecule in an excited vibrational state. The intensity of anti-Stokes lines on a Raman spectrum goes up as the temperature is increased because this increases the number of molecules in an excited vibrational state. Raman lines correspond

to vibrations which change the polarizability, unlike infrared absorption lines, which are due to a change in dipole moment.

The basic components of a Raman spectrometer are a source, a sample, and a detector. The source is often a near-infrared laser, such as a Diode laser or Niobium YAG laser. Liquid samples may be dissolved in many solvents, including water. Solid samples, such as polymers, can be used, and are often ground into a powder before the spectrum is taken. Because the Raleigh scattering line is much more intense than the Raman lines, a notch filter, which filters a very small range of wavelengths, is often used after the sample. The instrument might have a grating to select a wavelength before the detector and then scan through the wavelength range over time, or it may have a detector that collects many frequencies at one time and decomposes them using a Fourier transform. Since the signal is relatively small (about 0.001% of the incoming radiation), the source used must be powerful, and is often a laser. The wavelength of the source is not the important parameter, as it is in infrared spectrometry. Instead, the change in frequency of the scattered light, or the Raman shift, is the important information [126]. This means that glass cuvettes can be used to hold the sample. Micro-Raman (model: S2000 Raman spectrometer) and FT Raman (model: BRUKER RFS100/S, Germany)were used in the present study.

2.8.3   UV-Vis-NIR spectroscopy

UV-Vis-NIR spectroscopy uses light in the visible, near ultraviolet and infrared region. In this region of electromagnetic spectrum, molecules undergo electronic transitions. A UV-Vis-NIR spectrophotometer (Figure 2.7) measures the intensity of light passing through a sample 'I' and compares it to the intensity of light before it passes through the sample 'I_o'. The ratio 'I/I_o' is called the transmittance expressed in percentage (%T). The absorbance 'A' is based on the trasmittance given by [127] A = -log(%T). Over a short period of time, the spectrophotometer scans all the component wavelengths. The absorption coefficient is calculated from the spectrum by dividing the 'αd' (fluence) value by the thickness 'd' of the sample and it is plotted against the photon energy. The intercept of the plot gives the band gap of the material.
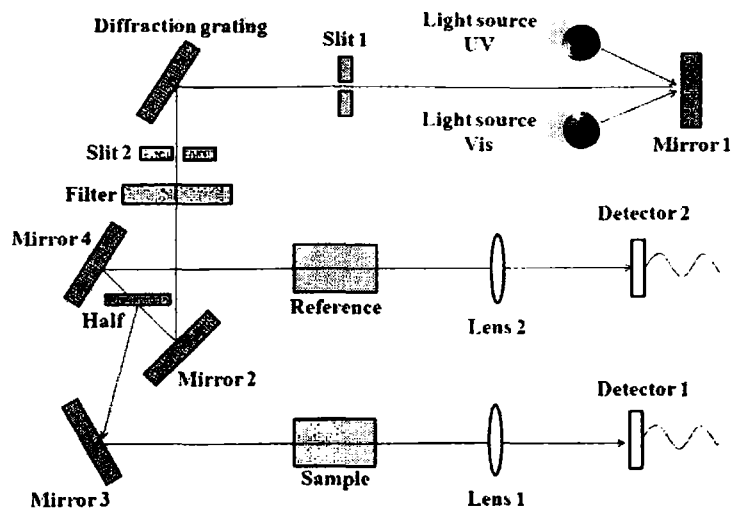
Figure 2.7: Schematic of UV-Vis-NIR spectrophotometer

2.9 Thermal analysis using TG/DTA

In thermo gravimetric (TG) analysis, the mass of the sample is recorded continuously as a function of temperature as it is heated or cooled at a controlled rate [42]. A plot of mass as a function of temperature (thermogram) provides both quantitative and qualitative information. The apparatus required for thermo gravimetric analysis include a sensitive recording analytical balance, a furnace, a furnace temperature controller and programmer and a recorder that provides a plot of sample mass as a function of temperature. Often an auxiliary equipment to provide an inert atmosphere for the sample is also needed. Changes in the mass of the sample occur as a result of rapture and/or formation of various physical and chemical bonds at elevated temperature that led to the evolution of volatile products or formation of reaction products. Thus. the TG analysis curve gives information regarding the thermodynamics and kinetics of various chemical reactions, reaction mechanisms, and intermediate and final reaction products.

Differential thermal analysis (DTA) involves heating or cooling a test sample and an inert reference under identical conditions. while recording any temperature difference between the reference and sample. This differential temperature is then plotted against time, or against temperature. Changes in the sample which

leads to the absorption or evolution of heat can be detected relative to the inert reference. Differential temperatures can also arise between two inert samples when their response to the applied heat treatment is not identical. DTA can therefore be used to study thermal properties and phase changes which do not lead to a change in enthalpy. The baseline of the DTA curve should then exhibit discontinuities at the transition temperatures and the slope of the curve at any point will depend on the microstructural constitution at that temperature. Phase transitions, dehydration, reduction and some decomposition reactions produce endothermic effects whereas crystallization, oxidation and some decompositions reactions produce exothermic effects. In the present study TG/DTA analysis was carried in Perkin Elmer, Diamond TG/DTA operated from room temperature to 1073 K in the nitrogen atmosphere with a heating rate of 10 K/min.

2.10   Magnetic characterization

The principle aim of magnetometry is to measure the magnetization (either intrinsic or induced by an applied field) of a material. This can be achieved in a number of ways utilizing various magnetic phenomena. Magnetometers are categorized into two. (a) Measuring the force acting on a sample in an inhomogeneous magnetic field (magnetic balance or magnetic pendulum) (b) Measuring the magnetic field produced by a sample (vibrating sample magnetometer or superconducting quantum interference device)

2.10.1   Vibrating sample magnetometer

A vibrating sample magnetometer (VSM) operates on Faraday's Law of induction (changing magnetic field produces an electric field). This electric field can be measured and provides information about the changing magnetic field. Using VSM, the hysteresis loop parameters like saturation magnetization, coercive field, remanence and squareness ratio are determined. Photograph and the corresponding schematic of a VSM is shown in Figure 2.8.
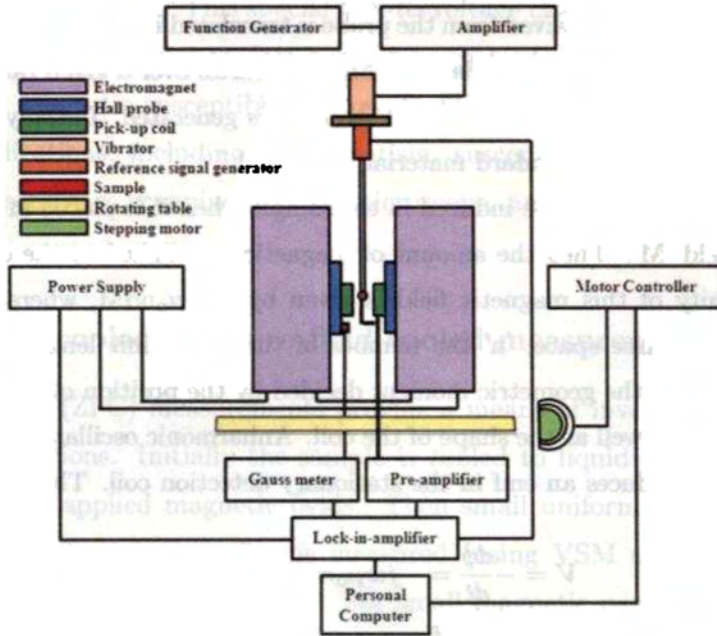
Figure 2.8: Vibrating Sample Magnetometer: Model EG & G Par 4500

In a VSM, the sample to be studied is placed in a magnetic field which will magnetize the sample by aligning the magnetic domains or the individual magnetic spins with the field. Stronger the applied field, larger the magnetization. The magnetic dipole moment of the sample will create a magnetic field around the sample, sometimes called the magnetic stray field. As the sample is moved up and down, this magnetic stray field change as a function of time and can be sensed by a set of pick-up coils. A transducer converts a sinusoidal ac drive signal provided by a circuit located in the console in to a sinusoidal vertical vibration of the sample rod and the sample is thus made to undergo a sinusoidal motion in a uniform magnetic field. Coils mounted on the pole pieces of the magnet, picks up the signal resulting from the sample motion.

The alternating magnetic field will cause an electric field in the pick up coil as according to Faraday's law of induction, the current will be proportional to the magnetization of the sample. Greater the magnetization, greater is the induced current. This induction current is amplified by a transimpedence amplifier and a lock-in amplifier. Various components of VSM are interfaced via a computer using controlling and monitoring software. For a particular field strength, the

corresponding signal received from the probe is translated into a value of magnetic moment of the sample. When the constant field varies over a given range, a plot of magnetization versus magnetic field strength is generated. Initially the loops are calibrated using a standard material like nickel.

Let a dipole moment be induced in the sample when it is placed in a uniform magnetic field 'M'. Then the amount of magnetic flux linked to the coil placed in the vicinity of this magnetic field is given by $\phi = \mu_o n\alpha M$, where μ_o is the permeability of free space, 'n' the number of turns per unit length of the coil and α represents the geometric moment decided by the position of moment with respect to coil as well as the shape of the coil. Anharmonic oscillator of the type, $Z = Z_o + Ae^{j\varpi t}$, induces an emf in the stationary detection coil. The induced emf is given by

$$V = -\frac{d\phi}{dt} = -j\varpi\mu_0 nMA(\frac{\partial\alpha}{\partial z})e^{j\varpi t} \qquad (2.6)$$

If amplitude of vibration 'A', frequency ϖ and $\partial\alpha/\partial z$ are constant over the sample zone then induced voltage is proportional to the magnetic moment of the sample. A cryogenic setup attached to the sample permits low temperature measurements. This is the basic idea behind VSM [128–130].

2.10.2   SQUID magnetometer

Superconducting quantum interference device (SQUID) magnetometer is a very sensitive magnetometer capable of measuring extremely small magnetic fields typically of the order of 10^{-17} T [131]. They are based on superconducting loops containing Josephson junctions. Noise levels in a SQUID are extremely low. A Josephson junction is made up of two superconductors, separated by an insulating layer so thin that electrons can pass through it. A SQUID consists of tiny loops of superconductors employing Josephson junctions to achieve superposition: each electron moves simultaneously in both directions. Because the current is moving in two opposite directions, the electrons have the ability to perform as qubits (that theoretically could be used to enable quantum computing). The direct current superconducting SQUID consists of two Josephson junctions connected in parallel. When the SQUID is biased with a current greater than the critical current, the voltage across the SQUID is modulated with the flux treading the SQUID at a period of one flux quantum, $\phi_o \equiv$ h/2e. Therefore, the SQUID is a

flux-to-voltage transducer. This special flux-to-voltage characteristic has enabled researchers to use the device to detect small magnetic field, current, voltage, inductance and magnetic susceptibility. Low-T_c SQUID has been used in a wide range of applications, including biomagnetism, susceptometers, nondestructive evaluation, geophysics scanning SQUID microscope, and nuclear magnetic resonance [132].

2.10.3 Field cooled and zero field cooled measurements

Zero field cooled (ZFC) measurements provide a means of investigating various magnetic interactions. Initially the sample is cooled to liquid helium temperatures under zero applied magnetic fields. Then small uniform external filed is applied and the net magnetization is measured (using VSM or SQUID) while heating the sample at a constant rate. For small magnetic particles, this curve has a characteristics shape. As the particle cools in a zero applied magnetic field, they will tend to magnetize along the preferred crystal directions in the lattice, thus minimizing the magneto-crystalline energy. Since the orientation of each crystallite varies, the net moment of the systems will be zero. Even when a small external field is applied, the moments will remain locked into the preferred crystal directions, as seen in the low temperature portion of the ZFC curve. As the temperature increases more thermal energy is available to disturb the system. Therefore more moments will align with the external field direction in order to minimize the Zeeman energy term. In other words, thermal vibration is providing the activation energy required for the Zeeman interaction. Eventually the net moment of the system reaches a maximum where the greatest population of moments has aligned with the external field. The peak temperature is called blocking temperature (T_B) which depends on particle volume. As temperature rises above T_B, thermal vibrations become strong enough to overcome the Zeeman interaction and thus randomize the moments [132].

Field cooled (FC) measurements proceed in a similar manner to ZFC except that the constant external field is applied while cooling and heating. The net moment is usually measured while heating. However, the FC curve will diverge from the ZFC curve at a point near the blocking temperature. This divergence occurs because the spins from each particle will tend to align with the easy

crystalline axis that is closest to the applied field direction and remain frozen in that direction at low temperature. It is important to note that ZFC and FC measurements are non equilibrium measurements [133, 134]. Care must be taken to ensure same heating rate during the measurements in order to properly compare the measurements. In the present investigation, FC-ZFC modes of the VSM were employed for the measurements. In the ZFC mode, the sample was cooled in the absence of a field and the magnetization was measured during warming by applying a nominal field of 100 or 200 Oe. In the FC mode, the sample was cooled in presence of a field and the magnetization was measured during warming, under the field of 100 or 200 Oe.

2.11   Dielectric measurements in the radio frequency range

The samples for dielectric measurement were pressed by applying a pressure of 5 tones to get compact cylindrical pellets with 12 mm diameter and ~ 2 mm thickness. The capacitance, loss factor, dielectric constant and ac conductivity were measured in the frequency range 100 kHz to 8 MHz at different temperatures (300 K to 390 K in steps of 10 K). The sample temperature is controlled by a temperature controller and the temperature on the sample is sensed by an Iron-Constantan (Fe-K) thermocouple on the sample. The schematic design of the home made dielectric cell [135] employed for the electrical measurements is shown in Figure 2.9. The cell is made up of mild steel with a cylindrical stem having provisions for fixing various attachments such as electrical connections and vacuum gauges. It is connected to a rotary pump which maintains a pressure of 10^{-2} torr inside the chamber. The inner diameter of the cell is about 18 cm. and has a length of 30 cm. The sample holder is fixed at the bottom of a one-end closed metallic tube to be embedded to the top flange.
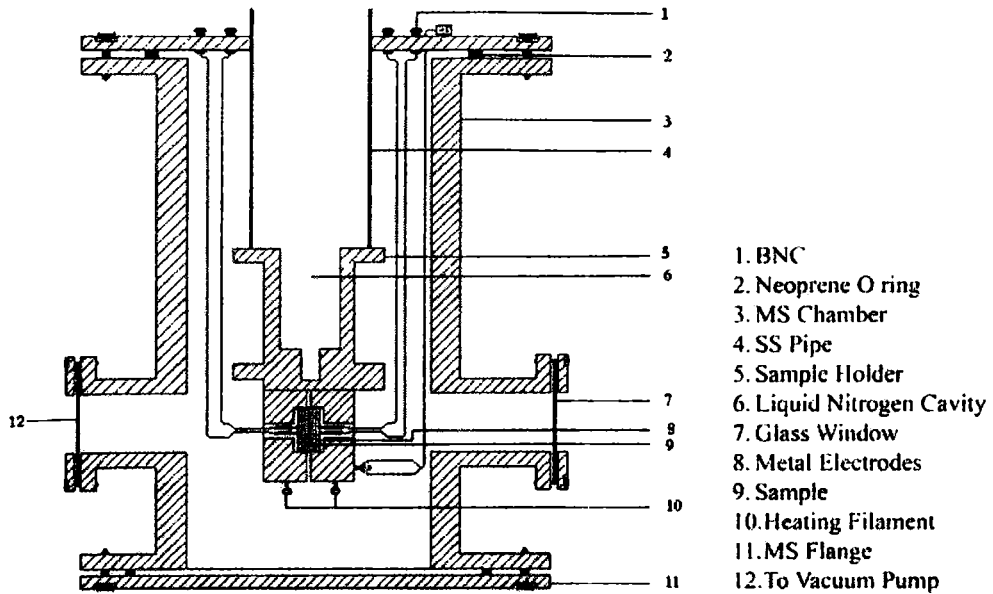
	1. BNC
	2. Neoprene O ring
	3. MS Chamber
	4. SS Pipe
	5. Sample Holder
	6. Liquid Nitrogen Cavity
	7. Glass Window
	8. Metal Electrodes
	9. Sample
	10. Heating Filament
	11. MS Flange
	12. To Vacuum Pump

Figure 2.9: Cell for the dielectric and conductivity measurements

For carrying out the electrical conductivity and dielectric permittivity measurements, pellets are mounted on the sample holder consisting of two copper disc electrodes in between which the pelletized sample is loaded. The sample holder is then heated using a temperature-controlled heater. The dielectric constant measurements of the samples at different frequencies were carried out using a Hewlett Packard 4285A LCR meter which is automated and controlled by a virtual instrumentation package LabVIEW (Version 8). The relative dielectric permittivity of the sample (hereafter termed as the dielectric permittivity ϵ) can be calculated using the equation.

$$\epsilon_r = \frac{Cd}{\epsilon_0 A} \tag{2.7}$$

where $'d'$ is the thickness of the pellet, $'C'$ is the capacitance measured by LCR meter, $'A'$ is the area of sandwiched structure and ϵ_0' is the absolute permittivity of free space. The theory involved for the evaluation of ac conductivity from dielectric constant values may be summarized as follows. Any capacitor when charged under an ac voltage will have a loss current due to ohmic resistance or

impedance by heat absorption. The ac conductivity is given by the relation [51]

$$\sigma_{ac} = \frac{J}{E} \tag{2.8}$$

Here $'J'$ is the current density and $'E'$ is the field density. But we know that the electric field vector

$$E = \frac{D}{\epsilon} \tag{2.9}$$

where $'D'$ is the displacement vector of the dipole charges and ϵ is the complex permittivity of the material. Also, the electric field intensity for a parallel plate capacitor is the ratio of potential difference between the plates of the capacitor and the inter plate distance.

$$E = \frac{V}{d} \tag{2.10}$$

Here $'V'$ is the potential difference between the plates of the capacitor, $'d'$ is the inter plate distance. Since the current density $J = \frac{dq}{dt}$ and $'q'$ is given by $\frac{Q}{A} = \frac{V\epsilon}{d}$, where $'Q'$ is the charge in Coulomb due to a potential difference of $'V'$ volts between the two plates of the capacitor. Hence

$$J = \frac{dq}{dt} = \frac{d}{dt}[\frac{V\epsilon}{d}] = \frac{\epsilon}{d}\frac{dV}{dt} \tag{2.11}$$

$$J == \frac{\epsilon}{d}\frac{dV}{dt} = \frac{\epsilon}{d} \cdot Vj\varpi \tag{2.12}$$

Substituting for $'E'$ and $'J'$ from the above equations we get

$$\sigma_{ac} = \frac{J}{E} = \epsilon j\varpi \tag{2.13}$$

Considering ϵ as a complex entity of the form $\epsilon^* \approx \epsilon' - j\epsilon''$ and neglecting the imaginary term in the conductivity we have

$$\sigma_{ac} = \varpi\epsilon'' \tag{2.14}$$

But the loss factor or dissipation factor in any dielectric is given by the relation

$$\tan\delta = \frac{\epsilon''(\varpi)}{\epsilon'(\varpi)} \tag{2.15}$$

Hence from the dielectric loss and dielectric permittivity, ac conductivity can be evaluated using the relation

$$\sigma_{ac} = 2\pi f \tan \delta \epsilon_0 \epsilon' \qquad (2.16)$$

where 'f' is the frequency of the applied field and tan is the loss factor [136]

2.12 Permittivity and permeability measurements at microwave frequencies

Broadband measurements for complex permittivity and permeability determination are required for characterization of substances in civil engineering, electronics, agriculture, and wood industry. The well-known Nicolson-Ross-Weir method is a transmission-reflection technique [137–139], which noniteratively determines ϵ and μ using measurements of complex scattering parameters(or S-parameter). This method has encountered some modifications over time because the derived equations are algebraically unstable when the values of reflection scattering parameters (S11 and S22) approach zero and phase uncertainty of these parameters greatly increases when the sample thickness is a multiple of half-wavelengths. Cavity perturbation technique is another method for the determination of ϵ and μ. The earliest treatment of cavity-perturbation theory was given by Bethe and Schwinger [140]. Following them, many researchers [141–144] have reviewed and studied the cavity-perturbation technique. It is a simple technique that gives accurate results with less amount of sample requirement.

2.12.1 Cavity perturbation technique

Cavity perturbation theory of resonant cavities was first proposed by Bethe and Schwinger [140] in 1943. It is based on the change in the resonant frequency and quality factor of the cavity with insertion of a sample into it at the position of electric field maximum or magnetic field maximum, depending upon the nature of the parameter to be studied.

Cavity is a cylindrical or rectangular box made of a non-magnetic metal with dimensions appropriately chosen to have resonance of electromagnetic waves in the frequency range of interest and connected to a vector network analyzer

through coaxial cables. The length 'l', breadth 'a' and height 'b' of a cavity are so chosen to have a pre-determined TE mode to sustain in the cavity. We have used rectangular cavities of dimensions 34.5 cm x 7.2 cm x 3.4 cm and 14.1 cm x 2.3 cm x 1.1 cm in the S and X-band respectively. Samples whose complex dielectric permittivity and magnetic permeability to be measured are usually made in the form of thin rods of very small volume in comparison to the volume of the cavity and inserted through a non-radiating hole (or slot) made on the cavity wall generally along the broad side along the length. Cavity perturbation technique is a relatively simple, non-destructive and contact-less method. Volume of the sample inserted must be very small so as to produce a negligible effect on the field configuration in the cavity. A schematic representation of the cavity is shown in Figure 2.10.
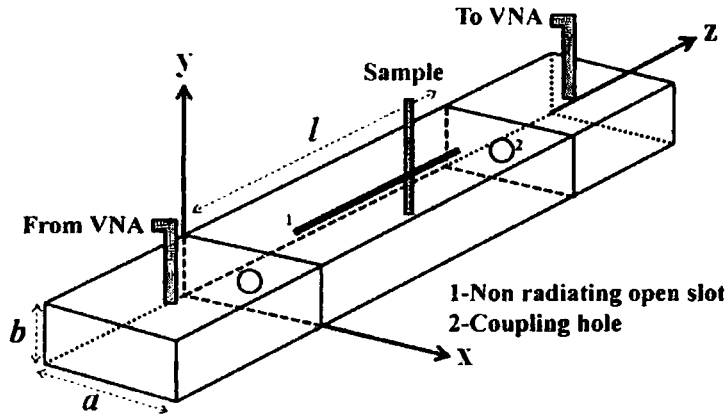
Figure 2.10: Schematic representation of a cavity resonator

Real and imaginary part of complex dielectric permittivity for the material inserted in a rectangular cavity is given by [144-147],

$$\epsilon' = \frac{V_c(f_c - f_s)}{2V_s f_s} + 1 \qquad (2.17)$$

$$\epsilon'' = \frac{V_c}{4V_s}[\frac{1}{Q_s} - \frac{1}{Q_c}] \qquad (2.18)$$

where V_s and V_c are the volume of the material and cavity, respectively. f_s and f_c are the resonance frequencies with and without the material while Q_s and Q_c are the corresponding quality factors of the cavity, given by

$$Q_s = \frac{f_s}{f_c - f_s} \qquad (2.19)$$

$$Q_c = \frac{f_c}{f_c - f_s} \qquad (2.20)$$

The real and imaginary parts of the complex permeability can be obtained from the relation [17]

$$\mu' = 1 + \frac{(\lambda_g^2 + 4a^2)}{8a^2} \frac{(f_c - f_s)}{f_s} \frac{V_c}{V_s} \qquad (2.21)$$

$$\mu'' = \frac{(\lambda_g^2 + 4a^2)}{16a^2} (\frac{1}{Q_s} - \frac{1}{Q_c}) \frac{V_c}{V_s} \qquad (2.22)$$

where λ_g is the guided wavelength. For TE_{10n} mode, $\lambda_g = \frac{2l}{p}$ where $'l'$ is the length of the cavity and p = 1, 2, 3, 4... Also $'a'$ is the breadth of the cavity (a = 3.4 cm for S-band and a = 1 cm for X-band). Measurements were carried out using a vector network analyzer in the S (Rohde & Schwarz-ZVB4) and X-band (HP-8510C).

Initially full two port calibration was performed via Through-Open-Short-Match (TOSM) method and experiments were carried out on standard samples. Interlaboratory calibrations were also performed to ascertain the authenticity of the measurement setup.

2.13 Measurement of nonlinear optical properties using z-scan technique

The nonlinear properties of materials can be explored by employing the z-scan technique which will throw light to different aspects of fundamental as well as application physics. The third order nonlinear susceptibility $\chi^{(3)}$, which is responsible for the third harmonic generation or optical phase conjugation, is of great interest. In media with inversion symmetry (gases, liquids, non-crystalline material), third order nonlinearity is the lowest order nonlinearity allowed under the electric-dipole approximation. Third harmonic generation, phase conjugation, saturation, self-focusing, optical Kerr effect and two photon absorption are all attributed to this optical nonlinearity [148-150].

The nonlinear refractive index $'n_2'$ and the two photon absorption coefficient β, are the parameters normally used to characterize these self action non-linear

optical behaviour. Several experimental techniques have been developed to measure the magnitude and dynamics of third order nonlinearities. Degenerate four wave mixing (DFWM) and beam distortion measurements (z-scan) are some of them. DFWM directly measures the third order non-linear susceptibility and usually involves complicated set-up. The fact that the setup includes temporal and spatial overlapping of three separate beams, permits increased flexibility, such as the possibility of measuring different tensor components of $\chi^{(3)}$, and a straightforward study of temporal behaviour.

Initially z-scan was used to investigate nonlinear susceptibility of transparent bulk materials, but now this technique has been extended to wide variety of samples, particularly absorbing media, especially semiconductor or metal crystallites of nanometer size embedded in dielectric media. There are two types of z-scan technique, namely the open aperture and the closed aperture z-scan.

z-scan setup is relatively simple and this technique utilizes the self-focusing effects of the propagating beam to measure the nonlinear refractive index. To extract β, the nonlinear transmittance method is employed, which measures the nonlinear transmittance of the laser medium as a function of the lasers intensity. Moreover, it is a highly sensitive single beam technique to determine the nonlinear refractive index and nonlinear absorption coefficient. In this method the sample is translated in the z-direction along the axis of a focused Gaussian beam, and the far field intensity is measured as a function of sample position. Analysis of the intensity versus sample position, z-scan curve, gives the real and imaginary parts of the third order susceptibility. In this technique, the optical effects can be measured by translating a sample in and out of the focal region of an incident laser beam. Consequent increase or decrease in the maximum intensity incident on the sample, produce wave front distortions created by nonlinear optical effects in sample being observed. By varying the size of an aperture kept in front of the detector, one makes the z-scan transmittance more sensitive or less sensitive to either the real or imaginary parts of the nonlinear response of the material, i.e.; $'n_2'$ or β, respectively.
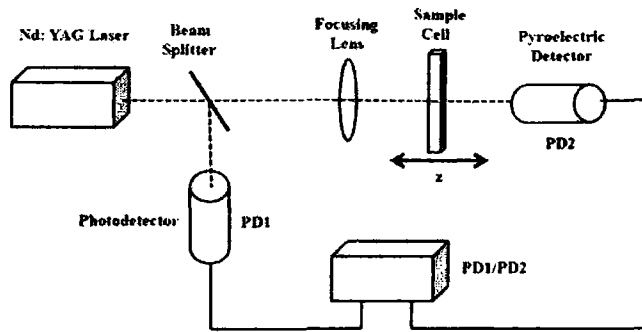
Figure 2.11: Schematic of Z-scan experiment

The schematic of the experimental setup is given in Figure 2.11. A lens initially focuses the laser beam with a Gaussian profile. The sample, thickness of which is kept less than the Rayleigh range, is then moved along the axial direction of the focused beam, in such a way that it moves away from the lens, passing through the focal point. At the focal point, the sample experiences the maximum pump intensity, which will progressively decrease in either direction of motion from the lens. A suitable light detector is placed in the far field and the transmitted intensity is measured as a function of the position of the sample, to obtain the open aperture z-scan curve. An aperture of suitable 'S' value is placed closely in front of the detector, and the experiment is repeated to obtain the closed aperture z-scan. The absorptive nonlinearity is first determined from the open aperture data, and then the refractive nonlinearity is determined from the closed aperture data.

Chapter 3

On the synthesis and microwave absorbing properties of highly stable iron-carbon nanostructures

Currently there is a great interest towards the development of nanoparticles with multiple functions or properties not obtainable in individual particles. Elemental iron being highly magnetic and metallic is a candidate material for various applications. This chapter discusses the synthesis of highly stable iron nanoparticles embedded in a carbon matrix prepared by a modified synthesis technique. The structure, morphology and grain size were analysed using powder X-ray diffraction, scanning electron microscopy and transmission electron microscopy. The elemental mapping and Raman spectrum confirmed the passivation of iron nanoparticles. Magnetic behavior of the nanocomposite were also investigated which showed that the iron-carbon nanostructures possess a saturation magnetization of 113 emu/g. Investigation of their microwave absorbing properties in the S and X-bands revealed a reflection loss minimum of -18 dB at 3.2 GHz suggesting their applicability as electromagnetic wave absorbers.

3.1 Introduction

Among all elements, iron has the highest room temperature magnetization (216 emu/g) and a Curie temperature of 1043 K [2], making it ideal for various applications. Moreover, iron is a soft magnetic material with low magnetocrystalline anisotropy. Hence, larger iron particles were superparamagnetic with a higher magnetic moment when compared to other magnetic metals like cobalt. Recently, functional nanoscale structures of iron are identified as promising candidates for biological labelling, diagnosis, catalysis and sensors [146, 151–153]. They also play a vital role in the production of clean fuels and carbon nanotubes.

Elemental iron at nanoscales is prone to oxidation and this is regarded as a drawback as far as applications are concerned. One way to overcome this is by passivating iron with inert materials like carbon, silica or gold. Passivated iron nanoparticles have been synthesized by employing different chemical and physical methods [88, 154, 155]. It is found that iron oxides were usually formed over iron nanoparticles. Iron nanoparticles with fcc or bcc structure have been synthesized depending on the techniques used. In 1991 Suslick *et al.* [156] obtained amorphous iron via sonochemical approach. Later, many studies on coating amorphous iron by long chain carboxylic acids and alcohols were reported [157, 158].

Furthermore, iron possesses higher Snoek's limit [159] when compared to both hard and soft ferrites. But at high frequencies of the order of giga hertz (GHz), permeability attenuates due to eddy current loss [160]. Passivation of iron nanoparticles with carbon would be appropriate in this regard, since metal in carbon matrix would modify the effective complex dielectric permittivity and magnetic permeability which plays a significant role in determining the performance characteristics of a microwave absorbing material. If particle size is less than the skin depth [161], eddy current losses can be minimized thereby improving the impedance matching condition.

Precipitation or growth of carbon layers/structures on metal surfaces usually involves techniques like high pressure chemical vapor deposition [22, 43, 44, 162] or arc methods [24, 41, 42, 163–165] which require complicated experimental setups. Jinping Huo et al has reported the pyrolysis of hydrocarbon leading to the formation of carbon passivated Fe and Fe_3C nanoparticles [166]. It is

found that most of the synthesis methods result in the formation of iron oxide or iron carbide which eventually reduces the magnetic properties of the composite. In this study, highly stable crystalline iron nanoparticles passivated in carbon matrix were synthesized by a simple and economic method. They were thoroughly characterized and microwave absorbing properties were investigated.

3.2 Experimental

3.2.1 Synthesis

Amorphous iron nanoparticles were prepared by employing a borohydride reduction method [167]. 5 ml oleic acid ($C_{18}H_{34}O_2$, AR grade, Merck Ltd, Mumbai) was mixed with 0.1 M iron sulphate ($FeSO_4.6H_2O$, AR grade, Merck Ltd, Mumbai) in 500 ml distilled water and stirred at a constant rate for 30 min at a temperature of 333 K. To this solution, 0.2 M sodium borohydride ($NaBH_4$, AR grade, purity >95%, Merck Ltd, Mumbai) in 500 ml of distilled water was added dropwise, which reduced iron ions to iron particles. Oleic acid present in the solution acts as the surfactant, coating over the surface of the iron nanoparticles [168, 169]. The hydrophilic COO^- group of oleic acid attaches to the elemental iron particles precipitated in the solution, while the carbon tail remains pointed outwards, thus preventing agglomeration of iron particles. The oily black precipitate was magnetically separated and washed twice with hot distilled water to remove the unreacted precursors, byproducts and excess of surfactant. The mixture was centrifuged and the resulting slurry was dried in hot air oven for 5 h at 333 K. The so obtained oleic acid coated iron nanoparticles were labelled as FeA. FeA was subjected to thermal analysis and then heat treated under different conditions by varying the temperature and annealing atmosphere. The obtained samples were stored at normal laboratory conditions for further characterization.

3.2.2 Characterization

Thermogravimetric analysis (TGA) was carried out in a Perkin Elmer Pyrex Diamond 6 instrument in a nitrogen atmosphere at a heating rate of 10 K/min from 323 K to 1073 K. X-ray diffraction (XRD) of the samples was recorded in a Rigaku Dmax-2C X-ray diffractometer using Cu Kα radiation (λ=1.5418 A). Scanning

electron microscopy (SEM) was carried out in a JEOL Model JSM - 6390LV microscope to obtain high resolution surface images of the powder samples. X-ray line scans and mapping was performed with energy dispersive spectrum (JEOL Model JED - 2300) attached to the scanning electron microscope. A JEOL JEM 2200 FS transmission electron microscope (TEM) with an accelerating voltage of 200 kV was used to determine the morphology and particle size of the samples. Fourier Transform (FT) Raman spectrometer (BRUKER RFS100/S, Germany) equipped with an Nd-Yttrium Aluminium Garnet (YAG) laser (excitation wavelength, 1064 nm) and a Germanium target was employed for characterizing the formed iron-carbon nanostructures. The microwave absorbing properties of the samples were determined by measuring the complex relative dielectric permittivity ($\epsilon = \epsilon' - j\epsilon''$) and relative magnetic permeability ($\mu = \mu' - j\mu''$) via cavity perturbation techniques [100] using a vector network analyzer in the S (2-4 GHz, Rohde and Schwarz-ZVB4) and X-band (8-12 GHz, Agilent-8510C).

3.3 Thermal analysis

Elemental iron particles can exist in three different phases (bcc, fcc and hcp) depending on the temperature and synthesis parameters. It is known that the arrangement of iron atoms in the preferred crystalline orientation depends on the local carbon concentration [170, 171] as well.
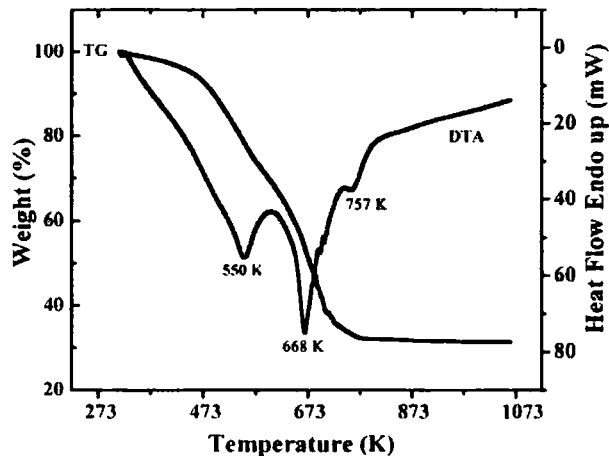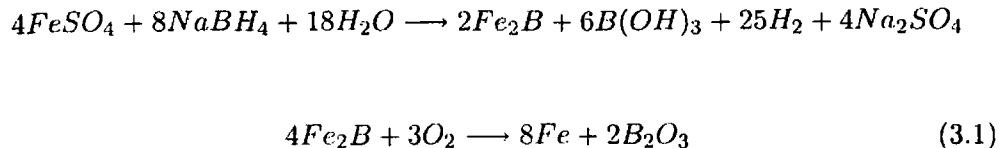

Figure 3.1: Thermogravimetric analysis of FeA

In this study, iron nanoparticles were precipitated by the borohydride reduction of iron sulphate following the well established chemical reaction [167] given by

$$4FeSO_4 + 8NaBH_4 + 18H_2O \longrightarrow 2Fe_2B + 6B(OH)_3 + 25H_2 + 4Na_2SO_4$$

$$4Fe_2B + 3O_2 \longrightarrow 8Fe + 2B_2O_3 \tag{3.1}$$

TGA curve of iron nanoparticles *in situ* coated with oleic acid (FeA) is shown in Figure 3.1. With increase in temperature, the weight loss occurs at different stages. Intense exothermic peaks are found in the differential thermal anlaysis (DTA) curve. This indicates that multilayer of oleic acid molecules are coated over the surface of iron particles. Initially the outer layer of oleic acid molecules gets desorbed (at ~ 550 K). They are bound to the primary or inner layers through hydrophobic interactions with the alkyl chains of their COO^- groups. At higher temperatures ($\sim$573-773 K), strongly bonded inner layers of oleic acid molecules decompose [172]. Thus carboxylation followed by carbonization of carbon rich oleic acid in FeA occurs.

3.4   Structure and morphology

The XRD pattern of FeA and FeA heat treated at different temperatures and annealing atmospheres are depicted in Figure 3.2. No distinguishable peaks of either iron or iron oxide are observed in the XRD pattern of FeA (Figure 3.2a). FeA annealed in vacuum (10^{-5} mBar) at 673 K (Fe400V) too did not result in the formation of any crystalline phase of either iron or iron oxide (Figure 3.2b). This suggests the requirement of higher annealing temperatures for the formation of crystalline iron particles. Hence FeA was heated in air at 873 K for 1 h (Fe600A). This resulted in the complete oxidation of iron forming Fe_2O_3 (ICDD file no. 85-1436) and Fe_3O_4 (ICDD file no. 85-0987), indicated by 'S' and '*' in Figure 3.2c.
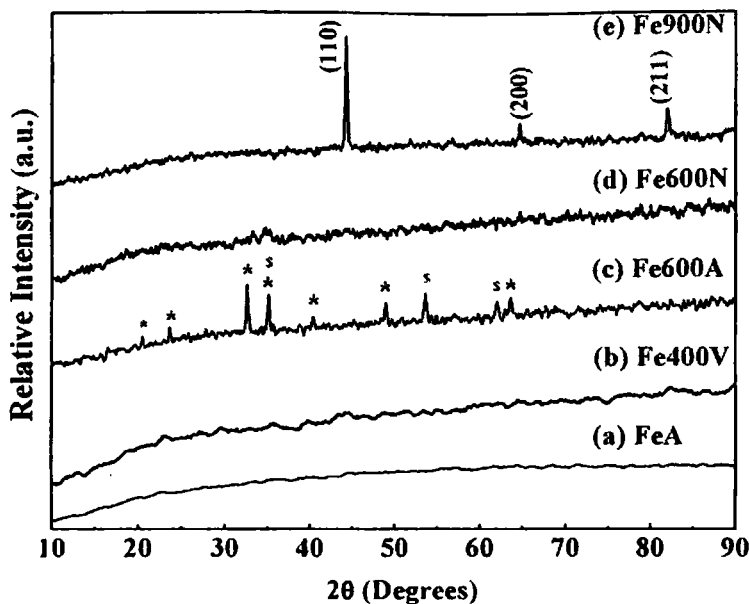
Figure 3.2: X-ray diffraction pattern of (a) FeA, (b) Fe400V, (c) Fe600A, (d) Fe600N and (e) Fe900N

Further annealing was carried out in nitrogen atmosphere (gas flow rate maintained at 5 l/h) at 873 K (Fe600N) and 1173 K (Fe900N). Crystalline phases of neither iron nor iron oxide were observed in Fe600N (Figure 3.2d). Crystalline peaks at 44.29°, 64.67° and 82.01° corresponding to (110), (200) and (211) planes of phase pure body centered cubic iron (α-Fe) was observed in the XRD pattern of Fe900N (Figure 3.2e) which matched well with the standard card (ICDD file no. 85-1410). Absence of oxide contamination in the XRD pattern suggests the effectiveness of the synthesis method employed to obtain polycrystalline iron nanoparticles. The grain size was estimated to be 31 nm using the Debye Scherrer's formula [118] while the lattice constant was found to be 2.88 Å in agreement with the reported value [173].

SEM images and corresponding energy dispersive spectra (EDS) of FeA and Fe900N are shown in Figure 3.3. There is a clear indication of incorporation of iron nanoparticles inside the oleic acid matrix in FeA (Figure 3.3a).
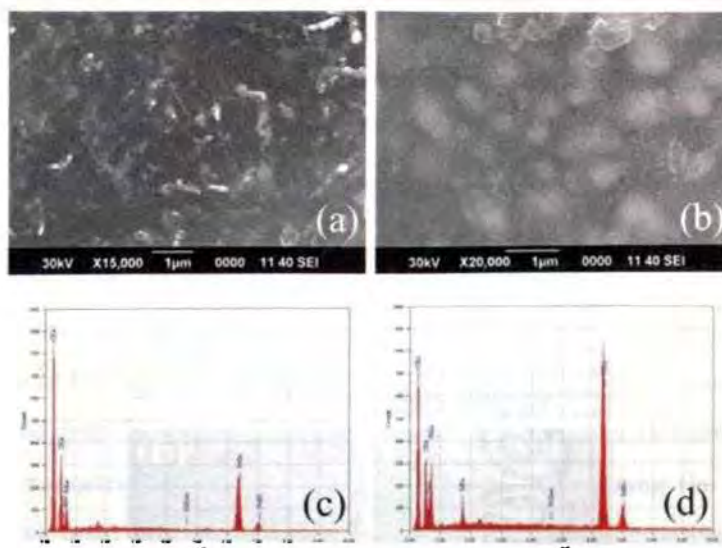
Figure 3.3: Scanning electron microscopy images of (a) FeA and (b) Fe900N. Energy dispersive spectrum of (c) FeA and (d) Fe900N

The COO^- group of oleic acid gets attached to the surface of iron particle as soon as they are formed in the solution. Thus, the oleic acid coated iron nanoparticles remain as spherical clusters forming chain like structures, due to strong intermolecular forces (like van der Waal's attraction or magnetic dipole-dipole interactions). Since iron nanoparticles are *in situ* coated with oleic acid, the particle growth is impeded. Upon heat treatment, FeA undergoes pyrolysis; as indicated in Figure 3.3b, Fe900N has an entirely different morphology. At elevated temperatures, the organic coating undergoes pyrolysis [166]. There is an increase in grain size and formation of microporous structures in Fe900N. From the EDS (Figure 3.3c-d), the iron to carbon mass ratio was determined and found to increase from 0.25 (FeA) to 0.74 (Fe900N) upon annealing. This increase in iron content is due to crystallization of amorphous iron and removal of molecular fragments or radicals of carbon, hydrogen or oxygen from the organic surfactant [174]. Moreover, the carbon atoms precipitate over the surface of iron particles, which serve as nucleation centres or catalyst for the formation of iron-carbon nanostructures [166].

The TEM image and elemental mapping of Fe900N are depicted in Figure 3.4. The average grain size of iron nanoparticles embedded in carbon matrix is 29 nm

with a distribution ranging from 15-40 nm. The bright field image and elemental mapping corresponding to iron and carbon in Fe900N confirms the passivation of spherical iron nanoparticles in the carbon matrix.
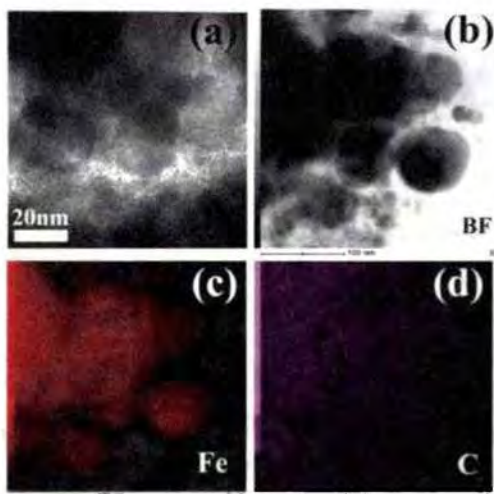
Figure 3.4: (a) TEM image, (b) bright field image, (c) iron mapping and (d) carbon mapping of Fe900N
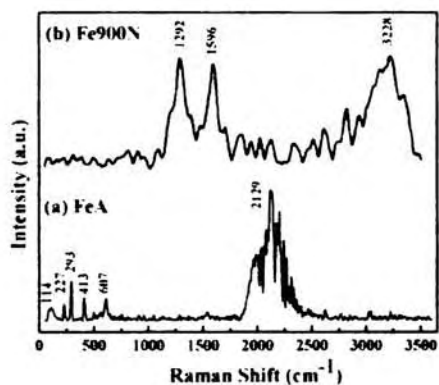
Figure 3.5: Raman spectrum for FeA and Fe900N

Information regarding the structure of carbon in the iron-carbon composite was determined from room temperature FT Raman spectrum ($\lambda_{ex}= 1064$ nm) depicted in Figure 3.5. An intense peak near 2129 cm^{-1} is typical of alkyl groups. Vibrations corresponding to δC-C aliphatic chains are indicated by the peaks in

the range 250-400 cm^{-1} and X metal-O bonds are inferred by peaks between 150 and 450^{-1}, as clearly seen in the Raman spectrum of FeA [125]. These peaks are absent in the Raman spectrum of Fe900N, where prominent peaks at 1592 cm^{-1} and 1292 cm^{-1} characteristic of G (sp^2 hybridized carbon of highly ordered graphitic carbon) and D-bands (related to the disordered carbon structure) are observed [175]. Also, a broad peak corresponding to the second overtone of G-band is observed at 3228 cm^{-1}; this is indicative of the graphitization of carbon forming around the iron nanoparticles. A shift from the typical Raman peaks of highly ordered graphitic carbon is indicative of high defect densities present in the iron-carbon nanostructures. These are significant for enhancing the permittivity by creating polarization centers, thereby enhancing the microwave absorbing properties [176].

3.5   Magnetic properties

Figure 3.6a depicts the room temperature magnetization curves of FeA and Fe600N while Figure 3.6b shows the magnetization curves of Fe900N. The saturation magnetization (M_s), coercivity (H_c) and remanence (M_r) of passivated iron nanoparticles were determined from the M-H curves. Reduced value of magnetization of FeA (M_s=16 emu/g, H_c=215 Oe, M_r=3 emu/g) is a consequence of finite size effects [2] of iron nanoparticles and due to the presence of nonmagnetic oleic acid surfactant. Short range atomic ordering, disordered surface spins and microstructural defects emanating from the grain boundaries account for the reduction in magnetization of the amorphous iron particles. It is to be noted that the samples annealed at 873 K in nitrogen did not show any noticeable change in the magnetization parameters (M_s=17.6 emu/g, 245 Oe, M_r=3 emu/g), consistent with the XRD results. Upon annealing at 1173 K, there is a marked change in the same parameters (M_s=113 emu/g, H_c=94.6 Oe, M_r=4.6 emu/g). The moments are found to almost saturate at 10 kOe with a maximum magnetization of 113 emu/g.
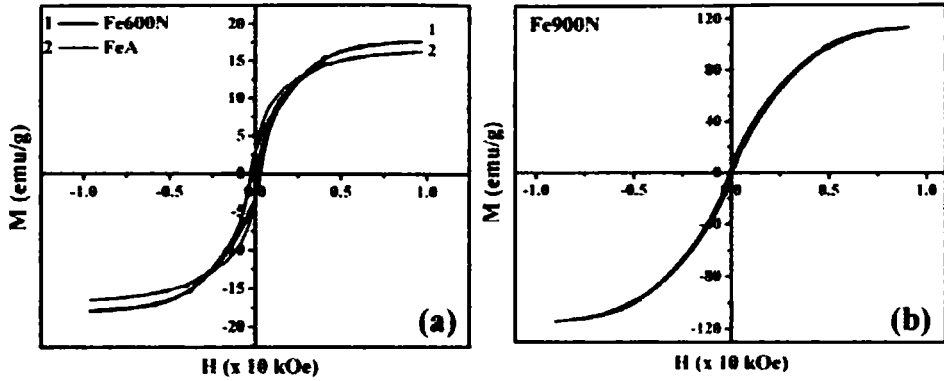
Figure 3.6: Room temperature M-H curves of (a) FeA and Fe600N (b) Fe900N

The saturation magnetization of pure iron in bulk form is 216 emu/g and that of iron oxide is 93 emu/g [2, 177]. The effective magnetisation of iron nanoparticles in this composite is 151 emu/g. The enhanced value of magnetization observed in nanocrystalline iron-carbon composite, which is $\sim$ 52% of the bulk value, demonstrates the effectiveness of the synthesis method adopted. Coercivity, which depends mainly on the magnetocrystalline anisotropy is found to decrease due to the increase in grain size of iron particles in the system [2].

3.6 Microwave absorbing property

3.6.1 Complex dielectric permittivity and complex magnetic permeability

The complex relative dielectric permittivity ($\epsilon = \epsilon' - j\epsilon''$)and complex relative magnetic permeability ($\mu = \mu' - j\mu''$) of Fe900N were investigated in the S and X-bands. According to transmission line theory, when an electromagnetic wave is transmitted through a medium, the reflectivity depends on ϵ, μ, and thickness of the absorber material at a particular operating frequency. Hence, determining these parameters is adequate for understanding the applicability of iron-carbon nanostructures as microwave absorbers. The experimental details of measurements are provided in Chapter 2. The variation of real and imaginary component of ϵ and μ values in the S and X-bands are depicted in Figure 3.7 and 3.8 respectively.

The real part of dielectric permittivity (ϵ') is found to be ~ 14 while the magnetic permeability (μ') is ~ 1.5. The higher value of ϵ' in iron embedded carbon nanostructures can be ascribed to the interfacial polarization of free charges [178] of conductive iron particles dispersed in a nonconducting carbon matrix. High electrical conductivities of metals increase the eddy current loss and ultimately reduces their permeability at high frequencies.

Figure 3.7: Frequency dependence of (a) complex dielectric permittivity and (b) complex magnetic permeability in the S-band

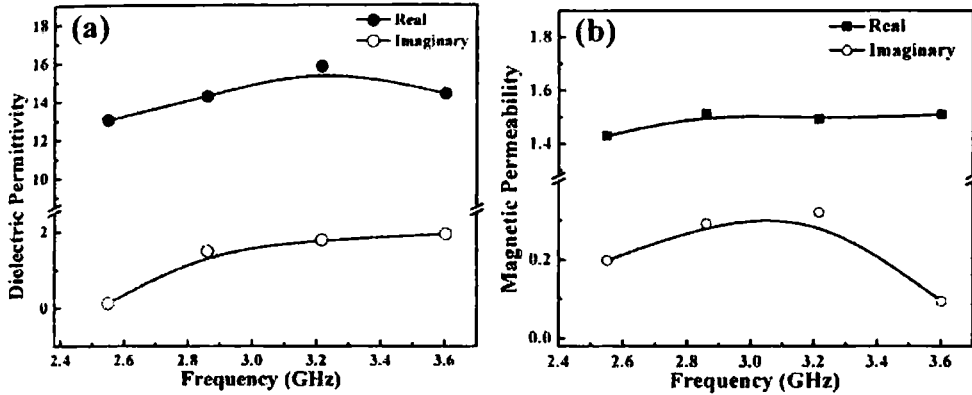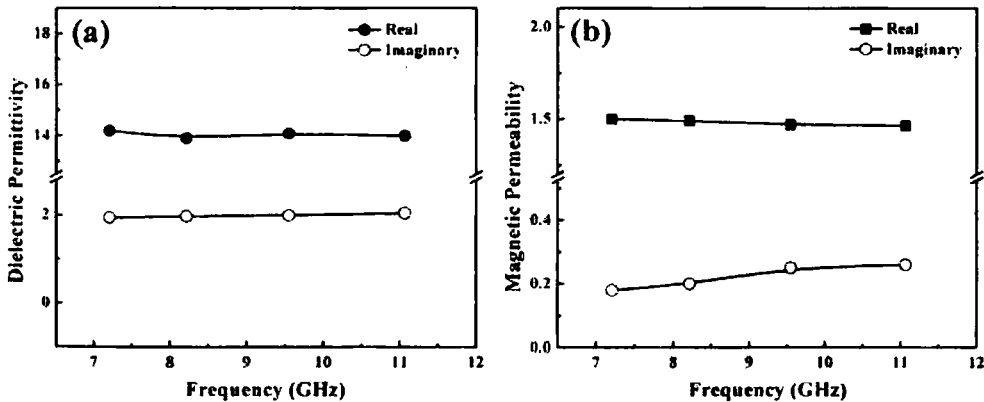**Figure 3.8:** Frequency dependence of (a) Complex dielectric permittivity and (b) Complex magnetic permeability in the X-band

Hence, reducing the size of metal particles below their skin depth will suppress the eddy current loss. Moreover, metals like iron possess high saturation magnetization that leads to higher Snoek's limit. Iron particles in the iron-carbon

composite possess grain size far less than their skin depth (~ 1 μm)[161], which reduce the eddy current effects. The permeability of a material is directly related to square of saturation magnetization and inversely related to its coercivity [179, 180]. Here, Fe900N possess high saturation magnetization and low coercivity, and hence give good permeability values at high frequencies.

3.6.2 Reflection loss

The electromagnetic wave energy can be completely absorbed and dissipated in the form of heat via the magnetic as well as dielectric losses. The effectiveness of an absorber can be quantified from its attenuation constant and reflection loss (RL). For a good absorber, the wave entering the material should be completely attenuated. The attenuation constant is evaluated from the measured value of complex dielectric permittivity and magnetic permeability given by

$$\alpha = \frac{\sqrt{2}\pi f}{c}\sqrt{(\mu''\epsilon'' - \mu'\epsilon') + \sqrt{(\mu''\epsilon'' - \mu'\epsilon')^2 + (\epsilon'\mu'' + \epsilon''\mu')^2}} \qquad (3.2)$$

where $'f'$ is the frequency and $'c'$ is the velocity of light.

RL is governed by the impedance matching criterion [181]. To obtain low reflection, impedance matching has to be satisfied i.e; μ'/ϵ' should be close to unity. But for most of the magnetic materials, μ' is less than ϵ' at high frequencies constraining the choice of ideal absorber material for the frequency of interest. Improving microwave permeability is difficult and hence lower values of ϵ'', higher values of μ'' and appropriate values of μ' and ϵ' are sort after to develop a good microwave absorbing material. The RL (in decibels) as a function of input frequency and absorber thickness, can be evaluated from the measured material parameters as

$$RL(dB) = 20\log|\frac{(Z_{in} - 1)}{(Z_{in} + 1)}| \qquad (3.3)$$

For a single layer absorber backed with a metal, the normalized input impedance is given by

$$Z_{in} = \sqrt{(\mu_r/\epsilon_r)}\tanh[j\frac{2\pi fd}{c}\sqrt{(\mu_r\epsilon_r)}] \qquad (3.4)$$

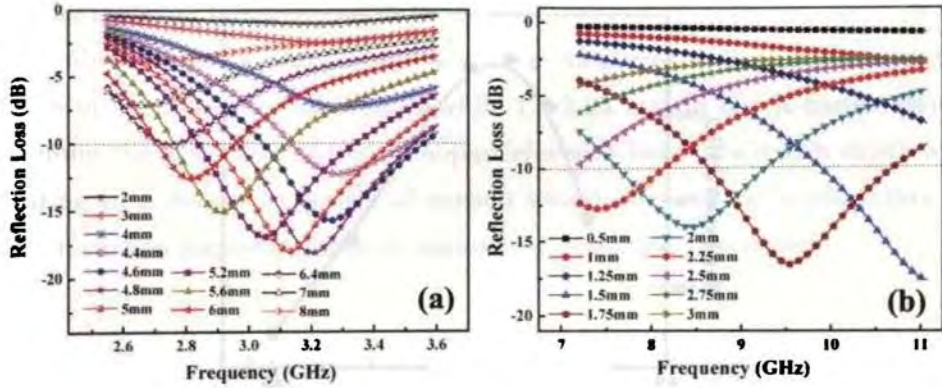where d is the thickness of the absorber layer.

Figure 3.9: Variation of reflection loss with frequency for Fe900N (a) S-band, and (b) X-band

The RL for Fe900N at different layer thicknesses (2-8 mm) was simulated from the material parameters in the S-band (Figure 3.9a). A minimum RL of -18 dB at 3.2 GHz with an absorber thickness of 4.8 mm is obtained. Similarly the RL were evaluated in the X-band. Fe900N gave a RL over -10 dB for an absorber layer thickness of 1.5-2.25 mm (Figure 3.9b). These results are quite encouraging since at higher frequencies the absorber thickness was minimized which is one of the requirements of an ideal wave absorber. Moreover, it is to be noted that with increase in layer thickness, the minimum RL is found to shift towards lower frequency. This is in accordance with the quarter wave principle [182, 183]. When the electromagnetic wave is incident on an absorber backed by metal plate, a part of it is reflected for the air-absorber interface while some part is reflected from the absorber-metal interface. These two reflected waves are out of phase by 180° and cancel each other at the air absorber interface when the quarter wave thickness criteria is satisfied [183] i.e.;

$$t = \frac{c}{4f} \frac{1}{\sqrt{\mu'\epsilon'}} (1 + \frac{1}{8} \tan^2 \delta_\mu)^{-1} \tag{3.5}$$

where $\tan \delta_\mu = \frac{\mu''}{\mu'}$, the magnetic loss. Since $t \alpha \frac{1}{f}$, above criterion is satisfied at increased sample thickness for lower frequencies.
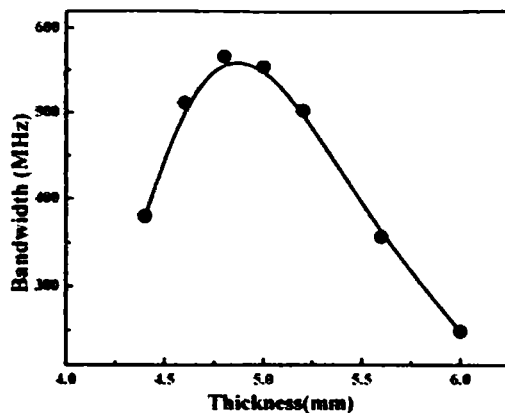
Figure 3.10: Variation of bandwidth with absorber thickness for Fe900N in the S-band

The dependence of bandwidth (in the S-band) for a reflection loss over -10 dB (90% loss) with absorber thickness is plotted in Figure 3.10. From our studies it can be proposed that the iron-carbon nanostructures possess a bandwidth of 450 MHz with an optimum thickness of 4.5-5.4 mm in the operating frequency range 2.8-3.4 GHz. The thickness is much small ($\sim$2 mm) in the X-band with a higher bandwidth of 1.5 GHz. Further studies are underway to tailor the ϵ and μ by varying the iron-carbon ratio in the composites. By doing so, we hope to widen the bandwidth as well as enhance the microwave absorbing capability of the composites.

3.7 Conclusion

Obtaining stable and crystalline iron particles in the nanoregime was considered a difficult task. Here we have demonstrated the synthesis of highly stable iron nanoparticles passivated within carbon structures by optimizing the experimental conditions. Raman spectroscopy together with elemental mapping revealed the formation of defective carbon nanostructures. This reduced the saturation magnetization in the iron-carbon nanostructure when compared to the bulk value of bcc Fe. The size of the metal particles in the composites could be restricted below their skin depth thereby reducing the eddy current effects. The applicability of iron carbon nanostructures for high frequency devices were also looked into. The permittivity as well as permeability were analysed to evaluate the reflection

loss of the material in the S and X-band. Reflection loss minimum over -10 dB could be obtained in the entire frequency range measured with an absorber layer thickness of 4.6-6 mm in the S-band while 1.5-2.25 mm in the X-band. Hence maintaining the grain size of iron nanoparticles well below their skin depth and passivating in a dielectric matrix of carbon would increase the applicability of these iron-carbon nanostructures as microwave absorbing materials.

Chapter 4

Synthesis of carbon nano onions by a novel and cost effective method and evaluation of its structural, magnetic, microwave absorbing and optical limiting properties

Multifunctional properties can be imparted to magnetic metal nanoparticles by forming hybrid nanostructures. This chapter discusses the major findings on the studies carried out on passivated cobalt nanostructures synthesized by a modified chemical processes. The properties of cobalt can be enhanced by embedding them within graphitic layers. This provides passivation as well as possibilities for applications. Unlike available literature reports, cobalt nanoparticles within graphitic layers were prepared by a simple scalable two step process. Graphitic layers were found to evolve over the surface of cobalt nanoparticles during thermal treatment by the decomposition of organic molecules surrounding the metal nanoparticles which serve as a catalyst. These were analyzed employing techniques like powder X-ray diffraction, transmission electron microscopy, micro-Raman spectroscopy and vibrating sample magnetometry. The microwave absorbing properties as well

as the nonlinear optical limiting properties of cobalt carbon nanostructures were also investigated.

4.1 Introduction

Though carbon nanostructures existed earlier, research in carbon nanomaterials received a fillip immediately after the discovery of fullerene (C_{60}) molecule [23, 36]. In the early 1990s research on fullerenes (C_{60}) were accelerated by the production of adequate amount of material using high pressure arc discharge method, first demonstrated by Krastchmer et al [24]. Filling the cavities of carbon nanostructures like carbon nanotubes (CNTs), carbon nano fibres, carbon nano onions (CNOs) with magnetic nano particles is exciting and expected to give rise to interesting materials with immense scope for applications [59]. They display interesting and unique properties for applications in optical limiting, catalysis, gas storage, additives for aerospace applications, magnetic metal based composite coatings, solar cells, light-emitting devices, fuel-cell electrodes etc [60, 184, 185].

With nanometer-scale quasi-spherical shape, perfectly arranged outer shell and stability, CNOs are attractive materials for studies for tribological applications [37]. Their advantage over graphite is that they have no edges where chemical attack can occur while maintaining the thermal stability of graphite. If magnetic properties can be incorporated to these structures, their applications are immense. The encapsulated magnetic nanomaterials can find applications in magnetic inks, magnetic recording media, toner for xerography and ferrofluids for biomedical applications [59, 60]. The carbon coating protects the magnetic nanoparticles against environmental degradation [186]. Moreover, carbon coatings can impart biocompatibility and stability in many organic and inorganic media. Therefore, carbon-coated magnetic nanoparticles have been recognized as interesting candidates for many bio-engineering applications including biosensors, drug delivery and magnetic contrast agents for magnetic resonance imaging [152, 153, 187].

Ultrafine elemental cobalt, which is ferromagnetic, readily oxidizes upon exposure to air, resulting in the formation of antiferromagnetic cobalt oxide layer [188]. Bulk cobalt possess a large room temperature saturation magnetization

of 162 emu/g. Major efforts are on in encasing these magnetic metal nanoparticles in a chemically inert oxygen-impermeable layer/matrix like gold, silica or carbon [49-54]. In some cases organic compounds, surfactant and polymers are also being tried. This approach also prevents unavoidable agglomeration which reduces their surface energy. Besides being a protective coating, they act as a means for attaching complex structures to biological systems like DNA, antibodies, proteins and cells in order to target them to specific sites. Cobalt carbon nanoparticles are reported as materials of great potential for *in vivo* tumor thermal ablation, bacteria killing, and various other biomedical applications [187]. Thus the other aspect of this method is that it will facilitate the passivation of otherwise highly reactive cobalt nanoparticles tuning the physical, mechanical and optical properties. Controlling the size of the magnetic nanoparticles and the thickness of the encapsulating graphitic layer is crucial for the design of devices. A survey of literature points towards the fact that the organic capping material and metal precursor governs the temperature of graphitization as well as size of nanostructures.

Since the discovery of carbon nano structures, lot of efforts has gone into in reducing the synthesis temperature of ordered carbon nano structures. Typical temperatures for graphitic carbon production by direct current arc discharge method are >1200 K. To date, various techniques are in vogue for synthesizing carbon-coated magnetic nanoparticles, such as conventional arc-discharge, modified arc-discharge and ion-beam sputtering methods [24–31]. Thermal transformation of carbonaceous compounds under pressure leading to structural reorganization of carbon residues formed is also reported [32, 33]. Pressure, temperature or the duration of heat treatment are also significant parameters which modifies the properties. Cobalt filled carbon nanoparticles or nanotubes are being studied by several groups [189–191]. However, all the above studies were based on the materials prepared by the conventional arc or modified arc method. In this work we have tried to develop a modified approach for obtaining cobalt embedded in CNOs employing simple and inexpensive techniques.

Metal carbon nanostructures are ideal optical limiting (OL) materials too. Carbon black, fullerene , or CNT suspensions have been extensively investigated in this regard and are considered as benchmark OL materials [77-84]. Metal

nanowires (Co, Cu, Ni, Pd, Pt or Ag) have shown broadband optical limiting properties comparable to materials like CNT which are dominated by nonlinear scattering [34]. However, not much literature exists on the nonlinear optical properties of magnetic metal nanoparticles probably because of their reactive nature and high work functions. Passivation of metal nanoparticles with an inert material like carbon can enhance their thermal stability and offers resistance to laser damages. These nanostructures have an added advantage of being a potential optical limiting candidate thereby enhancing the nonlinear optical properties. These materials should possess sensitive broadband response to long and short pulses, high linear transmission throughout the sensor bandwidth, resistance to laser-induced damages and invariably have high stability. Moreover, these cobalt-carbon nanostructures can be candidates as microwave absorbers once the metal core size is well below their skin depth [192]. Layered graphitic shells can tune the dielectric properties thereby improving the impedance matching criteria [181].

4.2 Experimental

4.2.1 Synthesis

Cobalt nanoparticles were prepared by the borohydride reduction of cobalt salts in the presence of stabilizing surfactant, which is a modified procedure of previously reported method [6]. 0.2 M sodium borohydride ($NaBH_4$, AR grade, purity >95%, Merck Ltd, Mumbai) was added dropwise to a solution of 0.1 M cobaltous sulphate ($CoSO_4.6H_2O$, AR grade, purity >98%, CDH (P) Ltd, New Delhi) containing 5 ml of oleic acid ($C_{18}H_{34}O_2$, Merck Ltd, Mumbai) at 353 K. The mixture was thoroughly stirred keeping the reaction temperature at 353 K for 1 h. A black precipitate was obtained which was magnetically separated, washed with acetone and dried in a hot air oven at 373 K for 3 h to obtain oleic acid coated cobalt nanoparticles. The sample was labelled as Co-S. The same reaction procedure was adopted with cobalt chloride as metal precursor. The resulting product was labelled as Co-Cl. These samples were thoroughly characterized. Co-S was heat treated in air for 12 h at 573 K (Co300), 873 K (Co600) and 1073 K (Co800) and were further investigated using various analytical tools.

4.2.2 Characterization

Transmission electron microscope (TEM) with an accelerating voltage of 200 kV (JEOL JEM 2200 FS) was used to characterize the morphology and particle size of the synthesized nanostructures. Micro-Raman spectroscopy, which is widely used to probe the quality of carbon structures, was carried out using S2000 Raman spectroscopy equipped with an argon laser (λ_{ex}= 514.5 nm). The structural analysis was carried out in a powder X-ray diffractometer (Rigaku Dmax-C) using CuKα radiation (λ=1.5406 Å) [118] with a scanning rate of 5°/min in the 2θ range 20-80°. Room temperature magnetic measurements were carried out using a vibrating sample magnetometer (EG&G PAR 4500). Complex dielectric permittivity and magnetic permeability were determined with the help of a vector network analyzer in the S (2-4 GHz, Rohde & Schwarz-ZVB4) and X-band (8-12 GHz, Agilent-8510C) by employing the cavity perturbation technique. The nonlinear optical applications were probed via an open aperture z-scan measurement technique.

4.3 Morphology

The TEM images and histogram showing the size distribution of oleic acid coated cobalt nanoparticles prepared from sulphate and chloride precursors are depicted in Figure 4.1 and 4.2 respectively. The dark regions indicate the formation of cobalt nanoparticles with spherical morphology. The average grain size of Co in Co-Cl is found to be ~26 nm, which is higher than the average grain size of Co-S (12 nm). Oleic acid coating of ~2 nm thickness was found for Co-S. The length of an oleic acid molecule is 2 nm and hence the observed thickness for oleic acid in Co-S suggests that a monolayer of oleic acid is being coated over the metal surface. However, this is not the case with Co-Cl samples. Here the particles are nonuniformly coated with the surfactant. This result indicates that the size of cobalt nanoparticle as well as the surfactant thickness varies significantly with the type of metal precursor used, which is directly related to the rate of reaction [193].
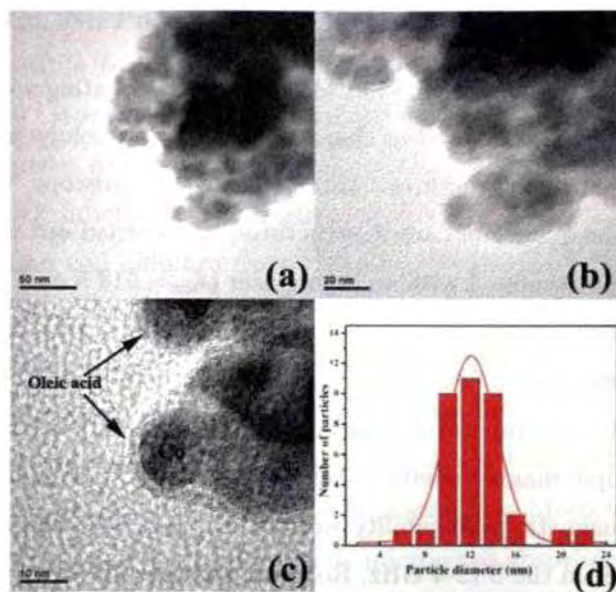
Figure 4.1: (a-c) Transmission electron microscope image of Co-S. (d) Histogram showing the particle size distribution of Co-S
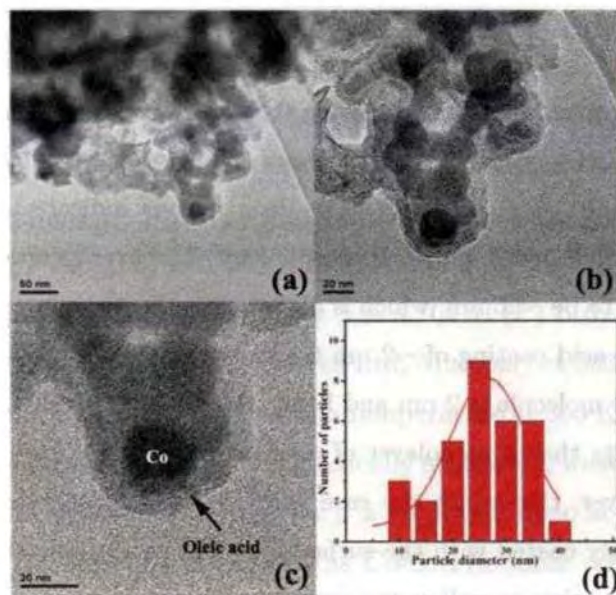

Figure 4.2: (a-c) Transmission electron microscope image of Co-Cl. (d) Histogram showing the grain size distribution of Co-Cl

The energy dispersive spectra of Co-S and Co-Cl (Figure 4.3) indicates the formation of elemental cobalt. It is to be noted that there are traces of chlorine contamination in Co-Cl emanating from the trapped NaCl, a byproduct formed during the precipitation of cobalt nanoparticles, from the cobaltous chloride precursors. These could not be washed off thoroughly since this lead to the removal of oleic acid coating. Such impurities were absent in the EDS spectrum of Co-S establishing the effectiveness of the sulphate precursor route.
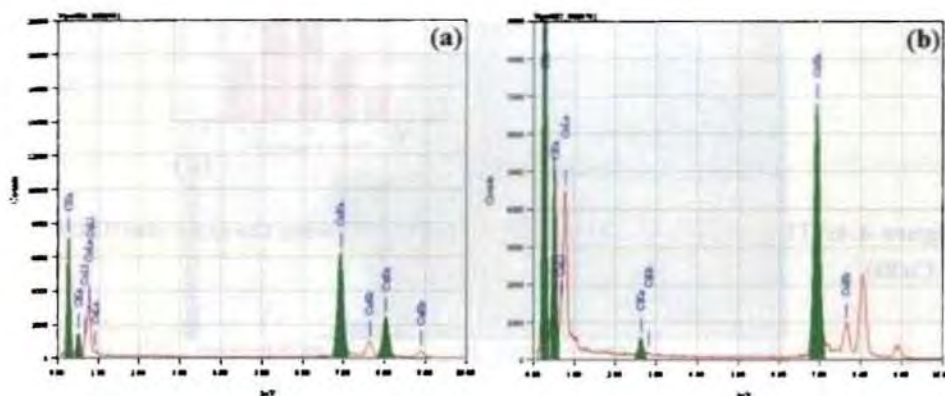
Figure 4.3: Energy dispersive spectra of (a) Co-S and (b) Co-Cl

Further, investigations were carried out on Co-S by heat treating at different temperatures (573, 873 and 1073 K). They were extensively analysed using transmission electron microscopy, selected images of which are depicted in Figure 4.4. The cobalt particles of average grain size of 13 nm, are found to be uniformly coated with an organic layer leaving behind no bare metal nanoparticles preventing oxidation by exposure to environmental oxygen. Moreover, it can also be seen that there is no noticeable grain growth taking place by heating at 573 K. The thickness of the coating was found to be ~ 2.2-3.8 nm, which prevents agglomeration or coalescence of cobalt nanoparticles.

Figure 4.4: TEM of (a-c) Co300, and (d) histogram showing the grain size distribution of Co300

Figure 4.5: (a,b) TEM and (c, d) HRTEM of Co600

TEM and HRTEM images of Co600 are depicted in Figure 4.5. Annealing at a temperature of 873 K caused the neighbouring cobalt grains to coalesce forming 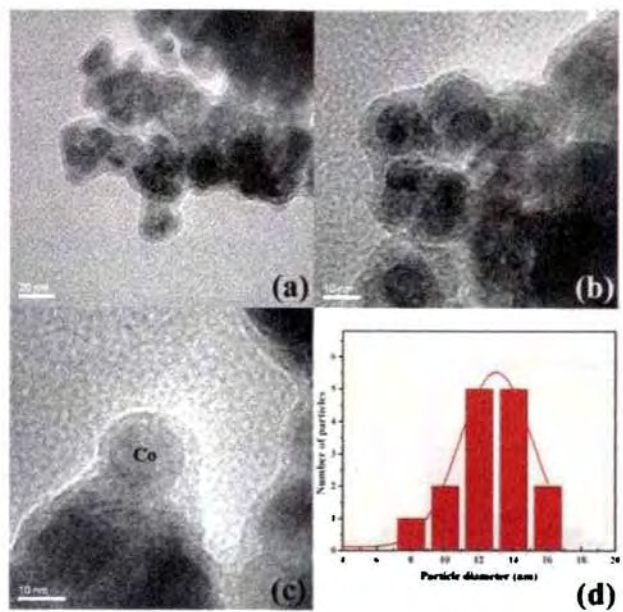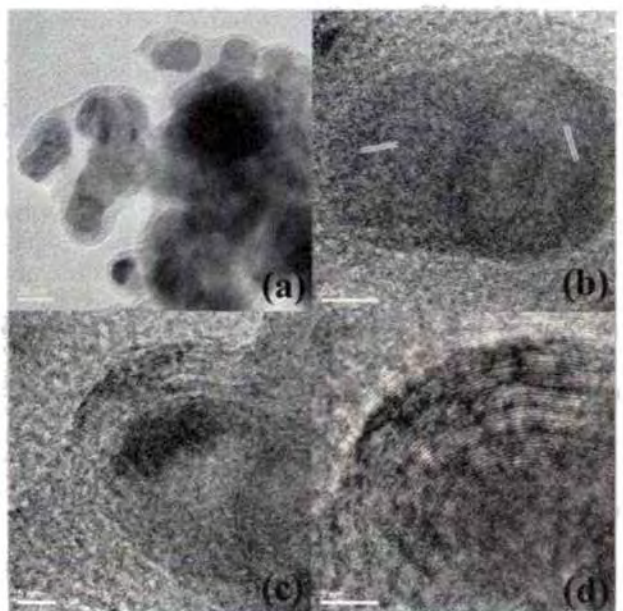larger grains. TEM image clearly showed lattice fringes of Co core corresponding to the (111) plane of fcc cobalt (marked in Figure 4.5b). The average grain size is found to increase to ~19 nm (Figure 4.5d). Thus, annealing enhanced the crystallinity of cobalt nanoparticles along with an increase in their grain size. High resolution TEM image focused on the outer surface of the particles (Figure 4.5c,d) establishes the formation of graphite layers (with interlayer spacing of ~0.34 nm) surrounding the cobalt grain. Atleast ~43 atomic layers are visible over cobalt nanoparticles.
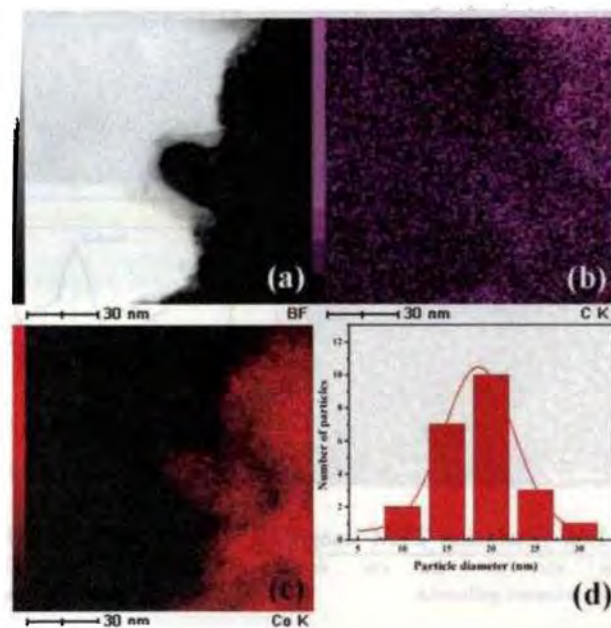
Figure 4.6: (a) Bright field image, (b) carbon mapping, (c) cobalt mapping, and (d) histogram showing the particle size distribution of cobalt in Co600

It may be noted here that the formation of concentric graphitic layers of carbon or CNOs at relatively low temperatures by employing cost effective and scalable experimental techniques is reported for the first time [194]. It was found that the coating thickness as well as the number of graphitic layer over cobalt particles, all depends not only on the initial thickness of organic layer coating but also on the geometry of the particles [195]. Since the initial cobalt core

possesses spherical morphology, concentric graphitic shells are formed. Formation of graphitic shells instead of carbon nano tubes are observed earlier during carbon deficient conditions in CVD [43, 44].

The sample was further subjected to elemental mapping. The bright field image and elemental mapping corresponding to carbon and cobalt further confirms the formation of carbon coated cobalt nanostructures and are shown in Figure 4.6a-c.
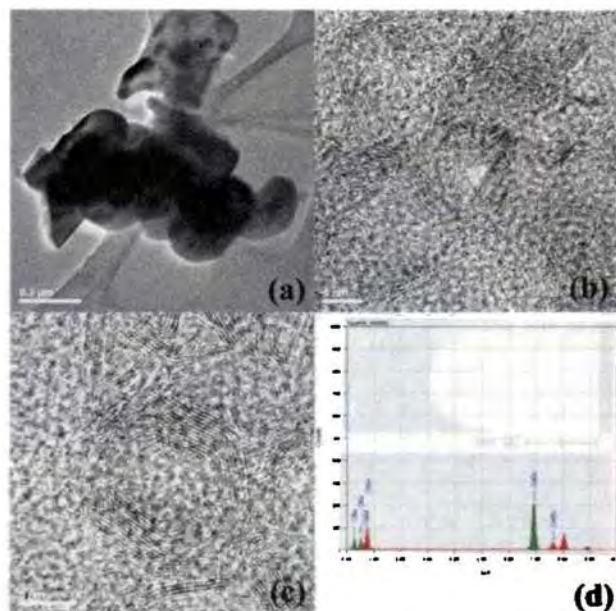
Figure 4.7: a) Low resolution TEM image, (b, c) HRTEM, and (d) EDS pattern of Co800

Further, these hybrid nanostructures were heated to 1073 K and characterized using TEM (Figure 4.7). It was interesting to note the dominance of the evolved graphitic structures over cobalt particles. The presence of cobalt was further verified from the energy dispersive spectra of Co800 (Figure 4.7d).

4.4 Micro-Raman spectroscopy analysis

Micro-Raman spectra of Co-S, Co300, Co600 and Co800 are depicted in Figure 4.8a. It clearly indicates the evolution of carbonaceous structure formed upon

heat treatment. The peak near 1600 cm^{-1} known as the graphitic or G-band, the characteristic E$_{2g}$ mode, is related to the stretching vibration of sp^2 carbon-carbon bond within the ordered graphitic layers of CNO. The disorder induced Raman breathing mode, D-band at ~ 1300 cm^{-1}, assigned to disordered carbon species, are associated with the vibrations of carbon atoms with dangling bonds at the curvatures or defects. Thus, the D-band is also used as a proof of disruption of the aromatic system of π-electrons in the nano-onions framework due to the sp^3 states of carbon. One can observe the signatures of multilayer structure of graphitic carbon with fingerprint peaks at ~1290 and 1595 cm^{-1} in Co300, Co600 and Co800, while they are absent in Co-S as expected. This observation has additional support from TEM results. It is clear that the carbon layers are being evolved over cobalt particles by the pyrolysis of carbon rich oleic acid coating. The metal particles act as catalyst for the precipitation of carbon layers [162, 166, 196].
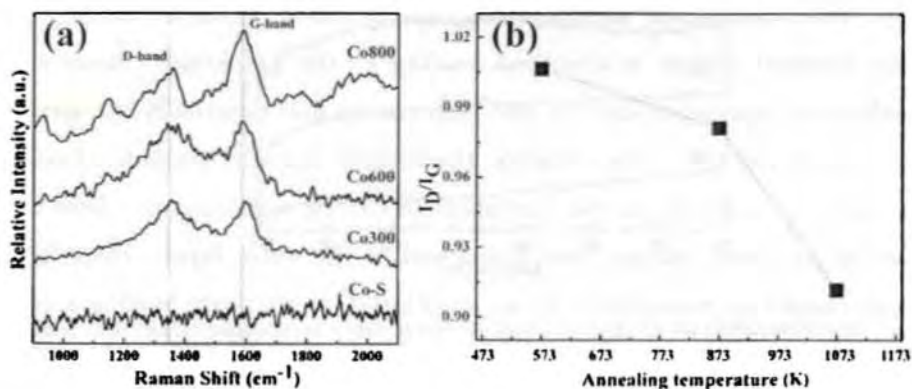
Figure 4.8: (a) Micro-Raman spectrum Cobalt carbon nanostructures (b) Variation of I$_D$/I$_G$ with temperature treatment

The ratio of the intensity of the D-band (I$_D$) to that of the G-band (I$_G$) for the samples annealed at different temperatures are shown in Figure 4.8b. I$_D$/I$_G$ decreased from 1.01 to 0.91 suggesting an increase in the graphitization of carbon layers formed in the composite. That is, the Raman intensity of the sp^2 carbon related mode has surpassed the sp^3 mode. This point towards the rise in the abundance of graphitic carbon with increase in annealing temperatures. The absence of any shoulder peak for the G-band confirms no lattice distortion in the

carbon layers formed [197].

Mechanism of growth: The mechanism leading to the growth of carbon nano onions assume importance because of their multifaceted properties and evolution of various carbon nano structures during the process. The mechanism can be properly elucidated by carefully analyzing the structure of cobalt-carbon nanostructures. It is well known that the explosion of carbon rich materials leads to carbon nanostructures [21, 22. 172, 191, 198–200]. Usually this process occurs at high temperature and under adequate pressure. Various transition metals accelerate graphitization of carbon by the solution precipitation mechanism [200, 201]. This results in the rupture of C-C bond by the catalytic transition metal particles. The carbon atom dissolves in the metal particle, diffuse and precipitates as graphite at the particle surface [202].

Formation of onion like structure requires a high degree of graphite like order. In the present system carbon rich organic surfactant (oleic acid) undergoes pyrolysis. They decompose precipitating carbon nanostructures. At high temperatures, thermal energy is absorbed leading to the breakage of some of the C-C bonds with high defect density and high energy and eventually the structure collapses. To reduce the surface energy, the broken domains tends to close from inside to outside resulting in the formation of carbon nano onions. Due to the lower radius and lower energy level contained at the outer layers, these broken C domains cannot be converted into an associated crystal form leaving a carbon nano sheath by amorphous carbon. Addition of layers results from a precipitation of C previously dissolved by the metal. If the solubility of C is low, it prevents this possibility. Annealing provides additional thermal energy that makes the structural rearrangement possible long after the initial deposition process. There are reports of energy transfer from the electron beam and catalytic effects from metal in the carbon onion formation around Pd clusters [55]. The driving force for graphitization would be the free energy difference between the initial and final form of carbon.

Here, cobalt particles act as a nucleation center for the growth of carbon nanostructures. The decomposition of organic compound into molecular fragments and their transformation or precipitation forming carbon nanomaterial is promoted by the transition metal catalysts, cobalt. Hence a metal mediated

graphitization occurs. It is observed that the amorphous carbon in contact with Co fully crystallize between 773-873 K [21, 22]. Carbon atoms dissolve onto the metal and upon supersaturation, graphite precipitates outwardly at the interfaces. Metallic cobalt simply acts as a template for carbon nano onion formation.

4.5 Structural analysis using X-ray diffraction

The structure of cobalt nanoparticles thus formed is further investigated by analyzing the XRD pattern of Co-S, Co300, Co600 and Co800 and are depicted Figure 4.9.
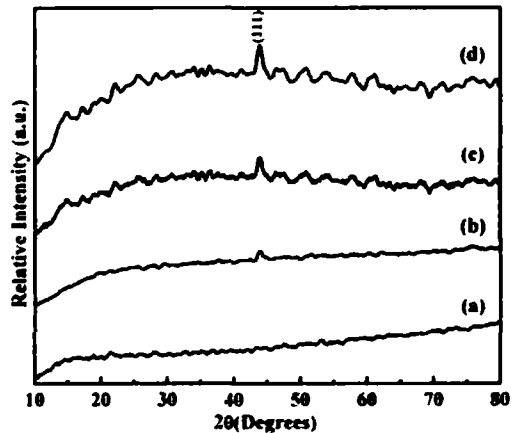
Figure 4.9: XRD patterns of Co-S at different annealing (in air) temperatures (a) Co-S, (b) Co300, (c) Co600, and (d) Co800

Co-S show an amorphous nature, but when heat treated at 573, 873 and 1073 K broad peaks at $2\theta = 44.2^o$ corresponding to (111) plane of fcc cobalt emerges (ICDD file no. 15-0806). It is to be noted that other planes of Co are not prominent in the XRD pattern, and the elemental cobalt is confirmed from EDS analysis. Signatures of cobalt oxide (CoO or Co_3O_4) are absent in the XRD pattern which confirms the effectiveness of the passivation of cobalt core within the graphitic carbon shells or CNOs. The lattice constant is found to be 3.57 Å which is in line with the ICDD values.

4.6 Magnetic properties

The determination of the saturation magnetization (M_s) of the fine particles is one way of securing information about their magnetic characteristics. The room temperature hysteresis loops of amorphous cobalt (Co-S and Co-Cl) are depicted in Figure 4.10a. A saturation magnetization of 5.4 emu/g and 4.4 emu/g with a remenance of 0.94 emu/g and 0.64 emu/g are obtained for Co-Cl and Co-S respectively. Slightly higher M_s for Co-Cl when compared to that of Co-S may be due to the larger grain size of Co-Cl (25 nm) when compared to Co-S(12 nm), as observed from the TEM images.
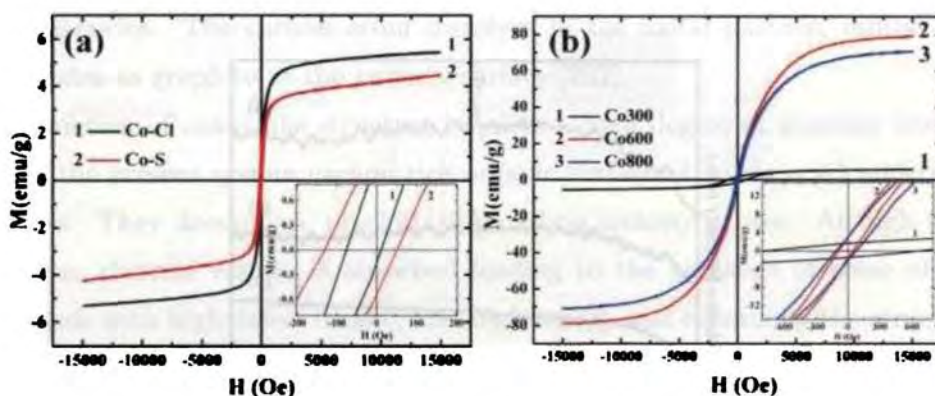
Figure 4.10: (a) M-H curves of Co-Cl and Co-S (b) M-H curves of Co300, Co600, Co800 (Inset: enlarged view showing coercivity)

The saturation magnetization for bulk cobalt is ~162 emu/g [2, 4]. Although oleic acid coating protects the core, it affects the magnetic properties of the nanocrystalline cobalt through the contribution of surface anisotropy and inter-particle interaction. In the nanoregime, as the surface to volume ratio increases, the saturation magnetization is found to decrease. Several factors determine the magnetic properties of nanocomposite. Disordered surface spins, non-magnetic surface coating and amorphous nature of cobalt particles in the system are the main factors for reduced magnetization.

Cobalt has an inherently high magnetocrystalline anisotropy resulting in high coercivity [2]. This also leads to a lower value of superparamagnetic size lim-its. The magnetization saturates at 15 kOe for both the samples. Upon heat

treatment, cobalt particles undergo crystallization and the magnetic properties undergoes drastic changes [203]. When Co-S is heated at 573 K(Co300), the coercivity is found to increase from 43 Oe to 717 Oe whereas there is only a marginal increase in M_s. For Co600, M_s drastically increases to 78 emu/g from $\sim$5 emu/g with a coercivity of 62 Oe. These observations show that there is a strong relation between the magnetic properties and heat treatment on the nanomaterials. Generally, it is known that the coercivity increases as the single domain grain size increases. When the size of the grain attains a value at which it becomes multidomain, the coercivity starts decreasing [2]. Moreover the enhancement of coercivity may be attributed to the variation of both particle size and ordering of the particles with annealing [31]. On heat treatment, the crystallinity increases as evident from XRD and HRTEM. The particle size also increases which accounts for the decrease of H_c.
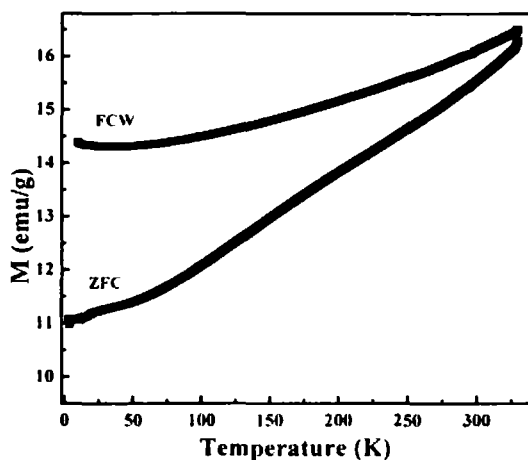

Figure 4.11: ZFC-FC curve for Co600

Further, vibrating sample magnetometer was employed to study the variation of magnetization with temperature in Co600. The ZFC-FC curves depicted in Figure 4.11 shows the absence of any superparamagnetic blocking in the temperature range measured (4-340 K).

4.7 Optical limiting property using z-scan technique

The optical limiting properties of cobalt-carbon nanostructures were evaluated using the traditional open aperture z-scan measurements. A frequency doubled Q-switched Nd:YAG laser (Minilite, Continuum) having a nominal pulse width of 5 ns at 532 nm wavelength was used for the measurements. The sample was dispersed in ethanol by sonicating for 10 min and was taken in a 1 mm glass cuvette mounted on a stepper motor controlled linear translation stage. The laser beam was focused using a plano-convex lens and the focal spot radius ϖ_o was around 17 μm. The laser propagation direction was taken as the z-axis. The sample was translated in the z-direction in small steps, and the transmitted energy was measured at each z position, using a pyroelectric laser energy detector (Laser Probe Inc.). The experiment was completely automated in a linux platform.

The Co300 and Co600 samples were dispersed in ethanol with concentrations such that their linear transmission was 50% at the laser wavelength, when taken in the 1 mm glass cuvette. The samples show a decrease in the transmittance at higher input intensities. The obtained z-scan curves fit well to a two-photon process, in which the net transmission 'T', of the sample is given by

$$T = (\frac{(1-R)^2 exp(-\alpha_0 L)}{\sqrt{\pi}q_0}) \int_{-\infty}^{+\infty} \ln[\sqrt{1 + q_0 exp(-t^2)}]dt \qquad (4.1)$$

where 'L' and 'R' are the sample length and surface reflectivity respectively, and α_0 is the linear absorption coefficient. Here 'q_0' is given by $\beta(1-R)I_z L_{eff}$, where β is the two-photon absorption coefficient, and 'I_z' is the intensity of the laser beam at position z. 'L_{eff}' is the effective sample thickness given by $[1 - exp(-\alpha_0 L)]/\alpha_0$. The obtained z-scan curves alongwith the theoretical fit to the experimental data are presented in Figure 4.12.

Both samples exhibit good optical limiting properties. The two photon absorption coefficients (β_1) were evaluated to be 1.8×10^{-10} m/W and 1.2×10^{-10} m/W for Co300 and Co600 samples respectively.
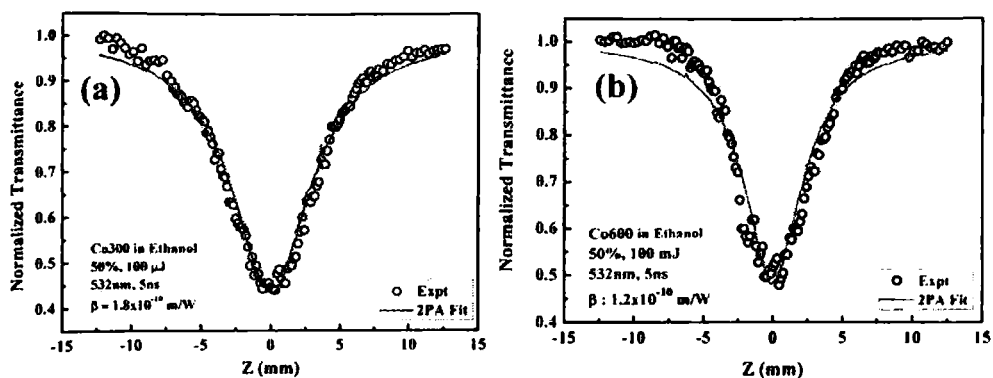
Figure 4.12: Optical limiting property of (a) Co300 and (b) Co600

The origin of this nonlinearity can be explained from the absorption spectra of the samples. The optical absorption spectrum of cobalt-carbon nanostructures (Co300 and Co600) dispersed in ethanol recorded in the range 200-1000 nm is depicted in Figure 4.13. The spectrum shows broad absorption peak at around 300 nm and is characteristic of $\pi - \pi^*$ electron transition in the polyaromatic system of curved graphitic layers [39]. Weak optical absorption of these nanostructures is due to the higher value of work function and first ionization potential of cobalt. The broad absorption band in the range 240-330 nm (band gap $\sim$4eV) is emanating from the carbonaceous structures formed around the cobalt nanoparticles. Reports reveal the variation of band gap of carbon nanostructures is in the range of 0.25 eV to 5.5 eV [21, 22, 40].

From the optical absorption spectrum, it can be seen that the samples have a strong absorption at 266 nm, which is the two-photon absorption level corresponding to the excitation wavelength of 532 nm. Considering the fact that there is a small residual absorption at 532 nm and that the samples are prepared in a concentration such that 50% of the incident photons are absorbed, the optical nonlinearity could be predominantly from a two-step excited state absorption rather than a pure two-photon absorption. The two-photon absorption coefficient evaluated thus can be termed as an effective two photon absorption coefficient.
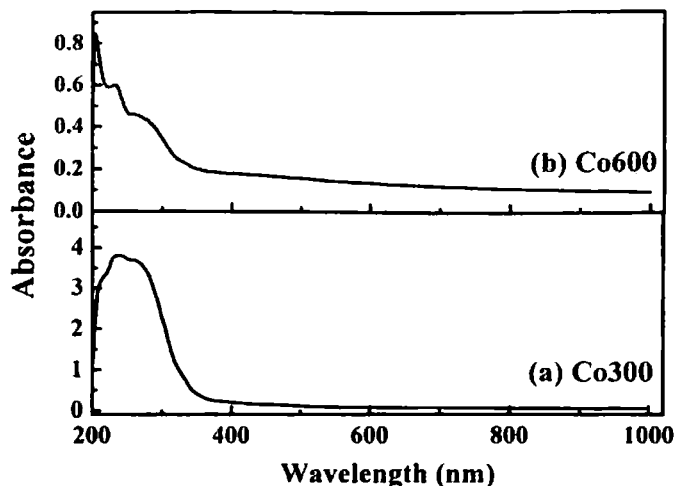
Figure 4.13: UV-vis NIR spectrum of (a) Co300 and (b) Co600

Nonlinear scattering, free carrier absorption, two/multi-photon absorption and reverse saturable absorption are the main mechanisms attributed to the optical limiting effects in nanomaterials [79–84]. It is a cumulative effect, rather than a contribution from one mechanism alone. The particle size, morphology, aggregation state, the local environment or the host matrix, all contribute to the limiting phenomenon. Pan *et al.* [34] has studied the optical limiting properties of nickel and cobalt [204] and found that nonlinear scattering, resulting from a photoionisation of metal atoms and subsequent expansion of the microplasmas in the suspension produces the optical limiting effects. Moreover, the laser parameters like wavelength, pulse duration or repetition rate of the laser source, plays a crucial role in the process.

From initial studies, it can be inferred that cobalt carbon nanostructures are good optical limiters. Further studies on their nonlinear refractive index and fabrication of devices based on these nanostructures can be carried out.

4.8 Microwave absorbing property

Extensive use of electronic gadgets in communication devices for domestic, military as well as industrial purposes using microwave frequencies has caused environmental pollution that causes health hazards and interference problems. One

way of sorting out this issue is to develop a microwave absorbing material in a scalable and cost effective manner. The cobalt carbon nanostructures are one such candidate that would tune the dielectric and magnetic properties thereby manipulate the microwave absorbing properties.

Cobalt nanoparticles embedded within carbon nano onions (Co600) were investigated for their microwave absorbing properties in the S and X-bands by measuring their complex dielectric permittivity and complex magnetic permeability using cavity perturbation technique. The details of measurements are explained in Chapter 2. Cobalt carbon nanostructures (Co600) was pressed into rectangular rod like pellets of dimension 1 mm x 2 mm x 4 cm with 1% poly vinyl alcohol added as binder. This was dried and subjected to microwave measurements.

Figure 4.14 and 4.15 depicts the variation of complex dielectric permittivity and magnetic permeability of Co600 in the S and X-band respectively. $\epsilon^{'}$ is found to be more or less $\sim$20 while $\epsilon^{''}$ is found to increase from 0.25 to 1.15 in the S-band with frequency, where as these parameters are almost constant in the X-band ($\epsilon^{'} \sim 18, \epsilon^{''} \sim 1.5$).
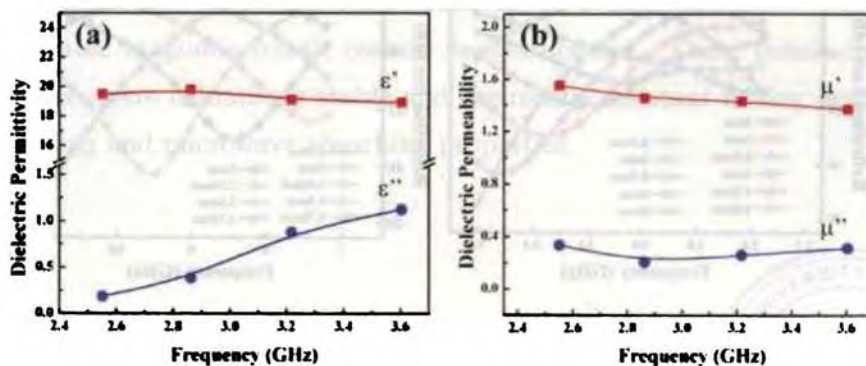
Figure 4.14: Variation of (a) complex dielectric permittivity and (b) complex magnetic permeability for Co600 in the S-band
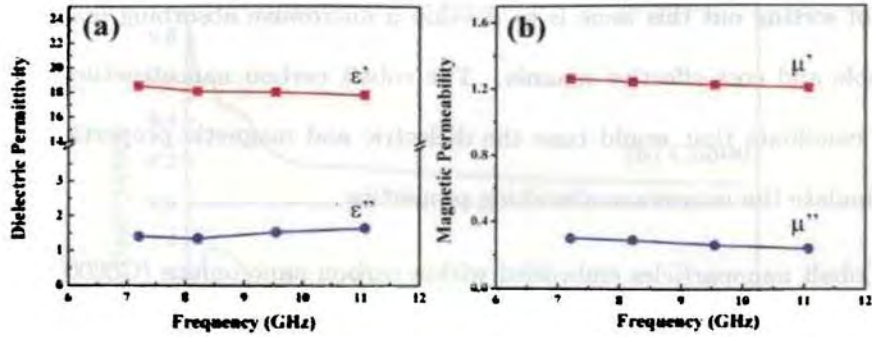
Figure 4.15: Variation of (a) complex dielectric permittivity and (b) complex magnetic permeability for Co600 in the X-band

The layered carbon structures formed over the cobalt particles causes a capacitive effect that increases the dielectric permittivity of the composite. With increase in frequency, the capacitive effect gradually vanishes. The nanocrystalline cobalt particles on the other hand improve the permeability values of Co600. Permeability values are found to reduce with increase in frequency. It is found that μ' is ~ 1.5 while μ'' is ~ 0.3 in the S-band whereas in the X-band $\mu' \sim 1.25$ and $\mu'' \sim 0.25$. Thus from the measured values of permittivity and permeability, the reflection loss of Co600 was simulated using the single layer absorber model [181] using Equation 3.3.
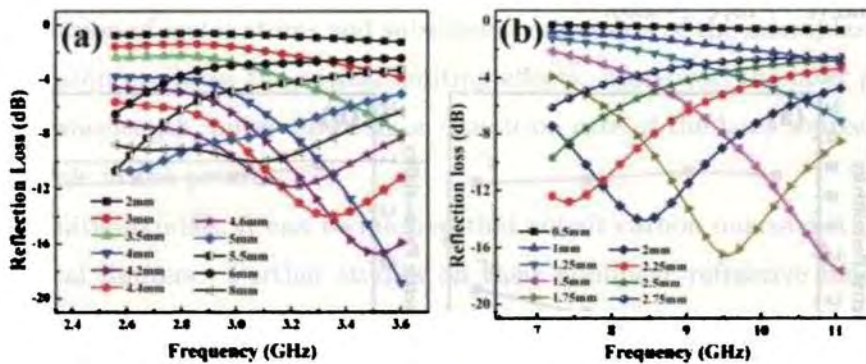
Figure 4.16: Reflection loss simulated for different absorber layer thickness of Co600 in the (a) S-band and (b) X-band

From these studies it can be seen that the reflection loss decreases with in-

creasing frequency (Figure 4.16) in accordance with the conventional theories [75, 181]. Also for increased thicknesses, the reflection loss minimum shifted to lower frequencies. A minimum reflection loss over -10 dB was obtained for a thickness of 4.2-4.6 mm in the S-band while this thickness is lowered to 1.5-2.25 mm in the X-band. This suggests the effectiveness of the cobalt-carbon nanostructures for the development of microwave absorbing materials.

4.9 Conclusion

Production of metal nanoparticles by bottom-up solution phase approach offers several advantages including easiness of surface modification, control of size, functionalization, prevention from agglomeration and oxidation. Stable cobalt nanostructures passivated by oleic acid was initially prepared by a controlled borohydride reduction technique. Effect of particle size and surfactant thickness with change in cobalt metal precursor were also looked into. Cobalt particles were formed in metallic form with no traces of cobalt compounds. Oxygen impermeable stealth, which is a prerequisite for use of these metal nanoparticles for several applications, was fabricated successfully. This was done by the heat treatment of oleic acid coated cobalt particles which lead to the evolution of carbon nano onions. The structure and morphology of the composites were extensively investigated using TEM, Raman spectroscopy and XRD studies. Room temperature magnetic properties of these nanoparticles determined using vibrating sample magnetometry revealed the effectiveness of the method developed for obtaining stable magnetic cobalt carbon nanostructures. These cobalt-carbon nanostructures were oxidatively stable and chemically resistant having desirable optical limiting and microwave absorbing properties.

Chapter 5

Preparation and characterization of highly stable nickel/carbon core/shell nanostructures

Magnetic metal nanoparticles attracted the attention of material scientists and are considered as ideal templates for the fabrication of novel magnetic nanostructures. Nickel/carbon core/shell nanostructure is one such candidate that imparts multifunctional properties to the system. A simple and cost effective technique for obtaining highly stable carbon coated nickel nanostructures at relatively low reaction temperatures is worked out. Thermogravimetric analysis of the precursors were carried out to optimize the annealing temperatures. Powder X-ray diffraction, transmission electron microscopy and Raman spectroscopy were used to characterize the metal nanostructures. The magnetic properties were extensively investigated using DC as well as SQUID magnetometry. The complex dielectric permittivity and magnetic permeability of nickel carbon nanostructures at different microwave frequencies (2-4 and 8-12 GHz) were measured using cavity perturbation technique. Their reflection losses were evaluated for different thicknesses using metal backed single layer absorber model. The synthesis, characterization and their various properties are presented in this chapter.

5.1   Introduction

Multifunctional magnetic nanostructures are increasingly being investigated because of their immense application potential in magnetic recording media, medical diagnostics, solid fuels, spintronics and telecommunication [1, 6, 152, 162, 205]. The catalytic activity of metal nanoparticles is also exploited in the synthesis of carbon materials. Though magnetism of 3d-transition metals like iron, cobalt and nickel is well understood at the bulk level, their nanocounterparts are interesting because, at the nanolevel, they exhibit altogether different physical, mechanical, optical, chemical and electrical properties [88, 206 208]. Such studies assume importance as they are ideal templates for exploring magnetism at the nanolevel.

Stable nickel nanoparticles are promising candidates as they find applications in magnetic recording, catalysis, solid lubricants, conducting and magnetic materials, and also in pressure cells and hydrogen storage devices [37, 60, 184, 185]. Nanostructured nickel fabricated in the form of tubes or wires possesses multifunctional properties and were found useful for diverse applications [209].

The proliferation of electronic devices using electromagnetic (EM) waves in the giga hertz (GHz) regime is a source of EM interference and is a subject of concern to environmental protection agencies [210-212]. Microwave absorbers and stealth materials are being engineered keeping in view of their microwave absorption, weight, thickness, mechanical strength, environmental resistance and cost of production [100]. Metallic magnetic materials have large saturation magnetization and higher Snoek's limit when compared to both hard and soft ferrites [159, 192]. Weak magnetocrystalline anisotropy and attenuation of permeability due to eddy current limits their use in the gigahertz frequencies [159, 160]. However, composites containing magnetic metal particles can modify the dielectric permittivity and magnetic permeability once particle size is less than their skin depth [161] and this reduces eddy current losses. Large surface area together with the required aspect ratio aided with the formation of interconnected networks in carbon or metal carbon nanostructures enhance their microwave absorbing properties [146, 213, 214]. However, for stability and also for broad band utilization of these nanostructures as microwave absorbers, a graphite or carbon coating is usually provided. Hence, dielectric permittivity and magnetic permeability are to

be evaluated and reflection loss need to be modelled at different frequencies using surface impedance equation for determining the optimum thickness for maximum absorption to ascertain their suitability for application.

Passivation of nickel with carbon often necessitates employment of methods like high pressure/temperature chemical vapor deposition, arc discharge process or sputtering [25–34]. Since, nanoparticles have large surface to volume ratio they are highly reactive and unstable. This makes preparation of nickel nanoparticles a difficult task. Mechanical milling, co-precipitation, reverse micelle technique, sol-gel method, microemulsion technique, sonochemical method, laser ablation and radiolysis are a few to list [6, 9-13, 17–22, 88, 155, 215]. Among the various solution-phase methods for obtaining nickel nanoparticles, reduction of nickel salts by reducing agents like sodium borohydride, hydrazine, polyols and amines are employed [216-218]. Strong reducing agents like sodium borohydride can be made use to synthesize metal nanoparticles within a short reaction period achieving narrow grain size distribution.

A number of strategies for passivating nickel nanoparticles are reported in literature. Nickel/nickel oxide core/shell structures have proved to keep the core nickel protected from oxidation [49]. *In situ* synthesis of magnetic metal nanoparticles in matrices like SiO_2 have resulted in stable magnetic composites [50, 215]. Production of carbon/graphite encapsulated metal nanoparticle has also been reported by several groups [51, 53, 54, 152, 166, 191, 198, 218-221]. Encapsulation of metal in carbon cages is a better choice when compared to materials like silica or polymer. This is because carbon exhibits higher chemical as well as thermal stability when compared to silica or other polymer cages when subjected to vigorous conditions (like acidic, basic, corrosive, oxidizing/reducing environments and high temperature or pressure). Furthermore, carbon is an ideal candidate for surface coating due to its biocompatibility [152, 162, 205] and ease of functionalization [222]. Carbon coated magnetic particles are being used for tagging catalytically active species on their surface [53, 198]. This facilitates the separation of expensive catalysts for further use. High production cost and relatively low yield of most of these methods has limited their large scale production. Developing an easy and cost effective synthesis technique for producing carbon encapsulated magnetic metal nanoparticles is still a challenge for researchers.

Methods like arc discharge, magnetron sputtering, ion beam sputtering, chemical vapour deposition, spray methods and pyrolysis of organometallic compounds [51, 53, 54, 152, 165, 166, 191, 198, 205, 220, 221] are being adopted for coating carbon over metal nanoparticles. Carbon encapsulated nickel and iron nanoparticles were successfully prepared by Jieshan Qiu *et al.* [219, 220] by modified arc discharge techniques. These particles had diameter ranging from a few nanometers to less than 55 nm, effectively passivated by several layers of carbon/graphite. A simpler method of passivating nickel is always thought of as a viable alternative of obtaining nickel/carbon nanostructures. In the present study, we report the synthesis and properties of highly stable nickel/carbon core/shell nanostructure by a simple and cost effective method.

5.2 Experimental

5.2.1 Synthesis

Nickel nanoparticles were prepared by a modified borohydride reduction method [216, 217]. Aqueous solution of 0.1 M nickel chloride hexahydrate ($NiCl_2.6H_2O$, AR grade, purity >98%, CDH (P) Ltd, New Delhi) in 500 ml distilled water was thoroughly mixed with 5 ml oleic acid ($C_{18}H_{34}O_2$, Merck Ltd, Mumbai) under vigorous stirring for 30 min at 333 K. To this, 500 ml 0.2 M sodium borohydride ($NaBH_4$, AR grade, purity >95%, Merck Ltd, Mumbai) solution was added dropwise. Nickel ions were reduced to nickel particles as evident from the colour change of the solution from light green to black. The grain size was controlled by confining the reaction in micro-emulsion of oil (oleic acid) in water. Oleic acid, which acts as the surfactant, gets coated over the surface of nickel nanoparticles terminating the agglomeration of nanoparticles. The oily black precipitate was magnetically separated and washed twice with distilled water to remove the unreacted precursors, byproducts and excess of surfactants. It was then centrifuged and the resulting slurry was dried in an hot air oven for 5 h at 333 K. The sample was labelled as NiA. TGA was carried out on NiA and hence the annealing temperature was optimized which was found to be 873 K in high purity nitrogen gas flow (flow rate maintained at 5 l/h) for 12 h. The sample was cooled to room temperature and the obtained powder was labelled as Ni@C.

Ni@C was aged for one year and then heated at 573 K in air for 2 h. This sample was labelled as Ni@C-1.

5.2.2   Characterization

TGA was carried out in a Perkin Elmer Pyrex diamond 6 instrument in a nitrogen atmosphere at a heating rate of 10 K/min from 323 to 1073 K. XRD was performed with a Rigaku Dmax-2C X-ray diffractometer using Cu Kα radiation (λ=1.5418 Å). A JEOL JEM 2200 FS electron microscope using an accelerating voltage of 200 kV was used to examine the morphology and particle size of the samples. The percentage of elemental nickel in the composite was found out using inductively coupled plasma atomic emission spectroscopy (ICP-AES, Model: Thermo Electron IRIS INTREPID II XSP DUO). FT Raman spectrometer (Model: BRUKER RFS100/S, Germany) equipped with an Nd-Yttrium Aluminium Garnet (YAG) laser (λ_{ex}=1064 nm) and a Germanium target was used for characterizing the carbon structures. The Raman laser power used was 50 mW with a resolution of 4 cm^{-1}. Magnetic properties were studied from the magnetization versus applied field (M-H) curves measured at different temperatures using Lakeshore 7225 DC magnetometer. The magnetic properties were also investigated using SQUID (MPMS-5S XL, Quantum Design) magnetometer equipped with a superconducting magnet which can produce a field of 1 T. The microwave absorbing properties were determined by measuring complex dielectric permittivity and magnetic permeability by using a vector network analyzer in the S (Rohde and Schwarz-ZVB4) and X-band (HP-8510C) employing cavity perturbation techniques [100]. Ni@C powder was pelletized to get rectangular rods of dimension $\sim$ 4 cm x 2 mm x 1 mm with 1% polyvinyl alcohol added as binder.

5.3   Thermal analysis

Nickel nanoparticles synthesized by sodium borohydride reduction method were *in situ* coated with oleic acid and subjected to TGA in the temperature range of 323-1073 K (Figure 5.1).
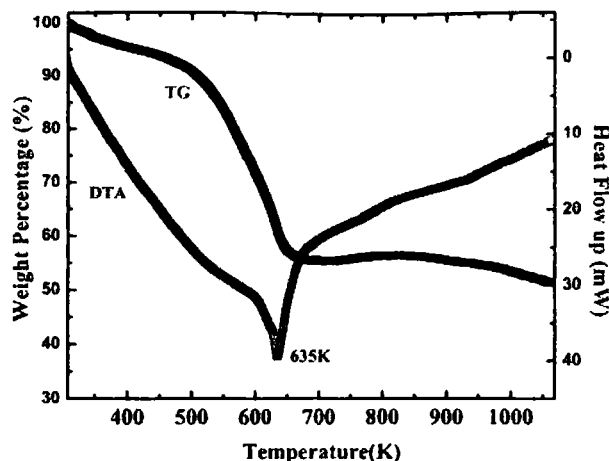
Figure 5.1: TGA /DTA curves of NiA taken in the temperature range 323 to 1073 K

Rapid weight loss ($\sim$44.5 wt.%) observed from 373 to 673 K is attributed to the desorption of oleic acid present on the surface of nickel nanoparticles. An endothermic peak at $\sim$635 K depicted in the differential thermal analysis (DTA) curve indicates the boiling point of oleic acid. A small increase in weight percentage from 673 to 873 K points towards the possible carbonization occurring around nickel nanoparticles from the radicals decomposed from carbon rich surfactant. The annealing temperature was optimized and fixed at 873 K.

5.4 Structure and morphology

XRD pattern of NiA, Ni@C and Ni@C-1 are shown in Figure 5.2a-c. A broad peak, emanating from the short range ordering, centered at around 2θ=44.5^o in NiA (Figure 5.2a) indicates the formation of amorphous nickel with face centered cubic structure (ICDD file no. 04-0850) [196, 222–224]. The peak around 21.2^o can be attributed to the amorphous carbon rich oleic acid layers, which completely disappear upon heat treatment [216, 217]. The peaks at 31.4^o and 45.2^o (Figure 5.2a-c) corresponds to (200) and (220) planes of sodium chloride (ICDD file no. 77-2064) impurity trapped in the slurry (indicated by '*'). This could not be washed off completely as this led to the removal of oleic acid from the precipitate, leaving behind bare nickel which is highly unstable. Thus, the wash-

ing protocol was optimized which decided the amount of carbon rich substance in the composite.
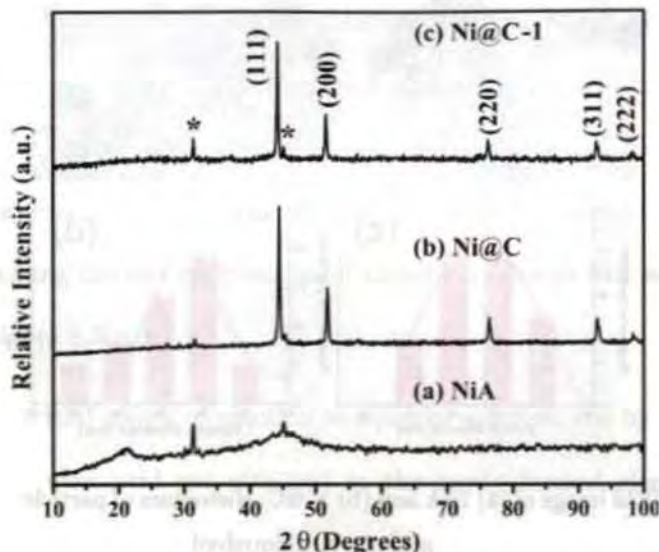
Figure 5.2: X-Ray diffraction pattern of (a) NiA, (b) Ni@C, and (c) Ni@C-1

XRD pattern of Ni@C (Figure 5.2b) show well defined peaks corresponding to (111), (200), (220), (311) and (222) planes of face centered cubic **nickel [224]**. Lattice constant was found to be 3.529 Å which is close to the literature value of bulk nickel (3.532 Å). There were no detectable impurities arising from nickel oxide, nickel carbide or nickel boride in the composite. The grain size was estimated from the XRD line broadening measurements by employing Debye Scherrer's formula [118]. The analysis of prominent peaks gave an average grain size of 31 nm. It is clearly seen that during annealing prominent peaks emerge which is attributed to the increase in grain size and improved crystallinity.

The sample (Ni@C) was aged for one year by exposing in air at normal laboratory conditions. It was then heated at 573 K in air for 2 h and then subjected to XRD studies. Prominent peaks (Figure 5.2c) of fcc nickel without any observable oxide contamination confirmed the strong oxidation resistance ability of passivated nickel nanoparticles.

Figure 5.3: TEM image of (a) NiA and (b) Ni@C. Histogram of particle size distribution of (c) NiA. and (d) Ni@C
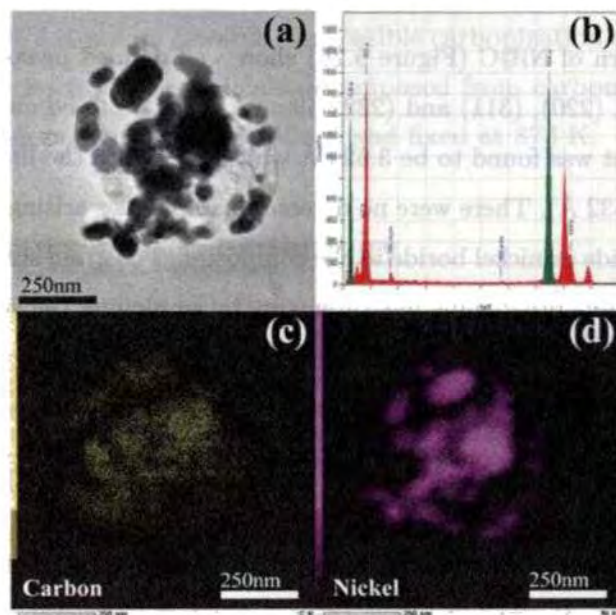
Figure 5.4: (a) TEM. (b) energy dispersive spectra. (c) Carbon mapping. and (d) Nickel mapping of Ni@C

Figure 5.3(a,b) depicts the TEM images of NiA and Ni@C. Passivation of nickel nanoparticles in oleic acid matrix is evidenced from the dark and light regions (Figure 5.3a). The diameter of nickel particles in NiA is in the range 10-25 nm with an average size of ∼17 nm. Examining the TEM image of Ni@C (Figure 5.3b), it is seen that the nickel pa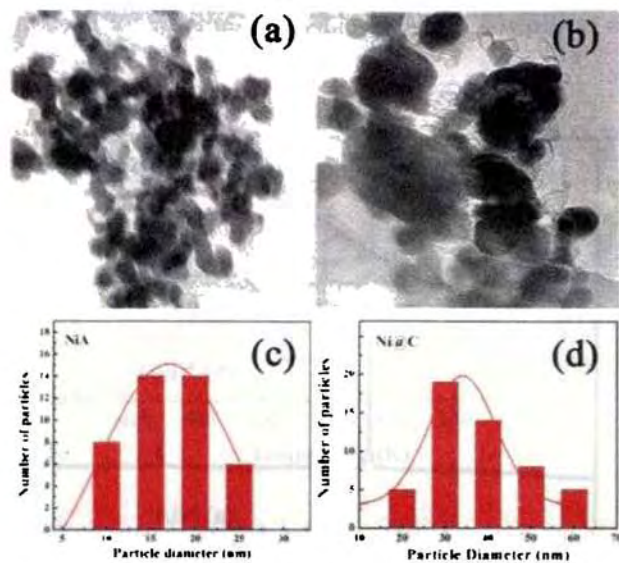rticles of size 20-60 nm are covered with carbon layers. The average size of nickel particles was found to be ∼35 nm. Histogram showing the size distribution of nickel particles in NiA and Ni@C are depicted in Figure 5.3(c,d).

During the initial stages of reaction in aqueous solution, the hydrophilic carboxyl groups of oleic acid get attached to the newly formed elemental metal (nickel) particles [225]. The hydrophobic carbon tails remain pointed outwards from the nickel particle surface, thus preventing it from oxidation. Coating of oleic acid on the nickel surface also inhibit further growth of nickel nanoparticles since the COO^- group prevents the interaction between the neighbouring magnetic nickel grains, thus providing stability to nickel particles against coalescence or agglomeration. At elevated temperatures NiA undergoes pyrolysis. The organic oleic acid coating decomposes, while nickel nanoparticles in the composite grow by coalescence. Nickel particles simultaneously act as catalyst precipitating carbon layers over its surface leading to the formation of stable nickel/carbon core/shell nanostructures [162, 166, 196, 224].

Figure 5.4 depicts the low resolution TEM of Ni@C along with their corresponding energy dispersive spectra and element mapping corresponding to nickel and carbon. The formation of nickel embedded in carbon nanostructures are confirmed from the mapping images.
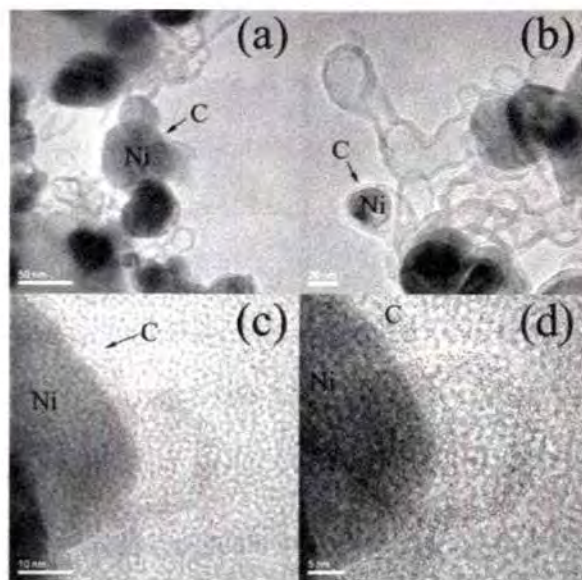
Figure 5.5: (a-b) TEM image, and (c-d) HRTEM image of Ni@C

High resolution TEM (HRTEM) images were analysed (Figure 5.5) to investigate the structure of Ni@C. It revealed the formation of carbon layers over nickel nanoparticles. The average thickness of carbon coating over nickel core is ~5 nm. The composite also contained fibrous carbon structures and hollow carbon shells. These carbon structures over nickel particles protected the highly reactive nickel nanoparticles from oxidation. Once the nickel/carbon core/shell structures are formed, interaction between the neighbouring nickel (core) is minimized which freezes further coalescence of nickel grains thereby controlling their size [185, 201]. It is to be noted that almost all of the nickel nanoparticles formed are effectively encapsulated by carbon layers (Figure 5.3b, 5.4a, 5.5). The spacing between two neighbouring lattice fringes is found to be ~0.34 nm (Figure 5.5c,d) emanating from the curved graphene layers formed by the catalytic activity of nickel. The HRTEM images of Ni@C nanostructure thus confirmed the confinement of nickel nanoparticles within carbon shells. Upto 15 layers of carbon are formed over nickel particles.

Hence, it can be inferred that during annealing, crystallization of the nickel core occurs along with carbonization of oleic acid over the metal surface to form an outer carbon layer [172, 191, 198–200]. The dissolve-diffusion-precipitation model

(DDP Model) [200, 201] suggested for the growth mechanism of metal/carbon core/shell structures can be applied to the present system. The DDP model assumes that the carbon atoms dissolve into the catalyst particle (nickel) and once the particle is supersaturated with carbon, atoms precipitated on metal catalyst forming graphitic layers which occurs at lower temperatures (~ 873 K) [200]. The tubular growth is ceased because of insufficient kinetic energy of the graphitic islands. The experimentally observed results are in agreement with the carbon nanostructure growth reported by Jiao and Seraphin [191].
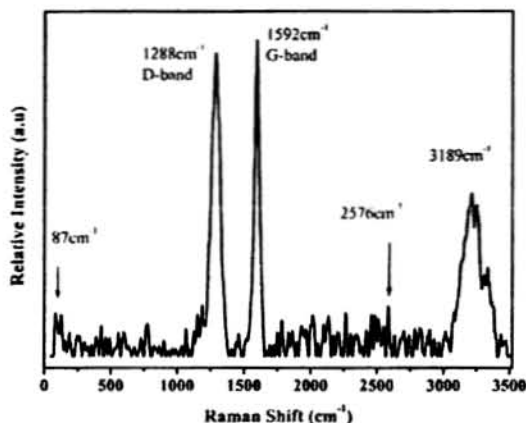
Figure 5.6: Raman spectrum of nickel/carbon nanostructure (Ni@C), $\lambda_{ex}=1064$ nm

Further, information regarding the structure of carbon formed in the system was obtained from the Raman spectrum of Ni@C (depicted in Figure 5.6) at an excitation wavelength of 1064 nm. Raman spectrum revealed two peaks inherent to carbon structures. The G-band (or E_{2g} mode), related to the vibration of sp^2 hybridized carbon in the 2D graphite for ordered carbon species, is at 1592 cm^{-1}.

The Raman breathing mode (D-band or A_{1g} mode) is found at ~ 1288 cm^{-1}[226]. The D-band is highly sensitive to disorders in the carbon materials. A shift in the D-band from the typical values with respect to highly ordered graphitic carbon (G-band: 1592 cm^{-1} and D-band: 1279 cm^{-1}, $\lambda_{ex}=1064$ nm) [175] can be ascribed to the defects (from edges, cracks, dislocations or vacancies), finite size effects and strains developed in the fibrous carbon nanostructures. The bands at 2576 and 3189 cm^{-1} are the overtones of D and G modes. A low intense Raman breathing mode at ~ 87 cm^{-1} is characteristic of a tubular carbon structure.

formed in the sample. Raman results thus agree well with the observed carbon layer structures in the TEM images of Ni@C (Figure 5.3b, 5.4a, and 5.5). The intensity ratio of D to G band is found to be 0.95 indicating the presence of disorder in the system as evident from TEM results.

Formation of magnetic metal@carbon nanostructures are reported at controlled conditions of elevated temperature (>1473 K) and pressure [162, 227]. This requires well fabricated experimental setup with multiple chambers and gas flow inlets equipped with proper cooling system. Sputtering, high pressure chemical vapour deposition or arc discharge processes [43, 44, 228] are some of the techniques used quite often to fabricate carbon nanostructures. This constrains the scalability of the process since many parameters have to be optimized to get the optimal experimental conditions. Here we have obtained highly stable nickel/carbon core/shell nanostructure by the catalytic action of nickel nanoparticles on oleic acid without the application of any external pressure at relatively lower temperature of 873 K.

During heat treatment organic layer undergoes thermal decomposition producing atomic or molecular fragments or radicals of carbon, hydrogen and oxygen. They segregate, diffuse and precipitate over the closest metallic nickel particle surface thereby reducing their surface energy. Nucleation and growth take place through continuous carbon deposition over bare nickel surface. The nickel nanoparticles acts as a catalyst for the growth of carbon layers [229]. Yu'an Huang et al. [230] reported the formation of cage like carbon structures over nickel particle of size less than 40-80 nm in diameter which is in consistent with our results. Earlier reports [54] indicate that the growth rate depends on the catalyst type and is maximum for nickel (nickel>cobalt>iron). Hence this method is most suitable for the encapsulation of nickel due to their superior catalytic activity when compared to other ferromagnetic 3d-transition metals.

5.5 Magnetic properties

Further, the magnetic properties of the surface modified nickel nanoparticles were investigated by measuring the M-H curves at different temperatures (77, 120,

280 and 300 K) with a maximum applied field of 10 kOe. Typical ferromagnetic behaviour was observed for both NiA and Ni@C (Figure 5.7 and 5.8).
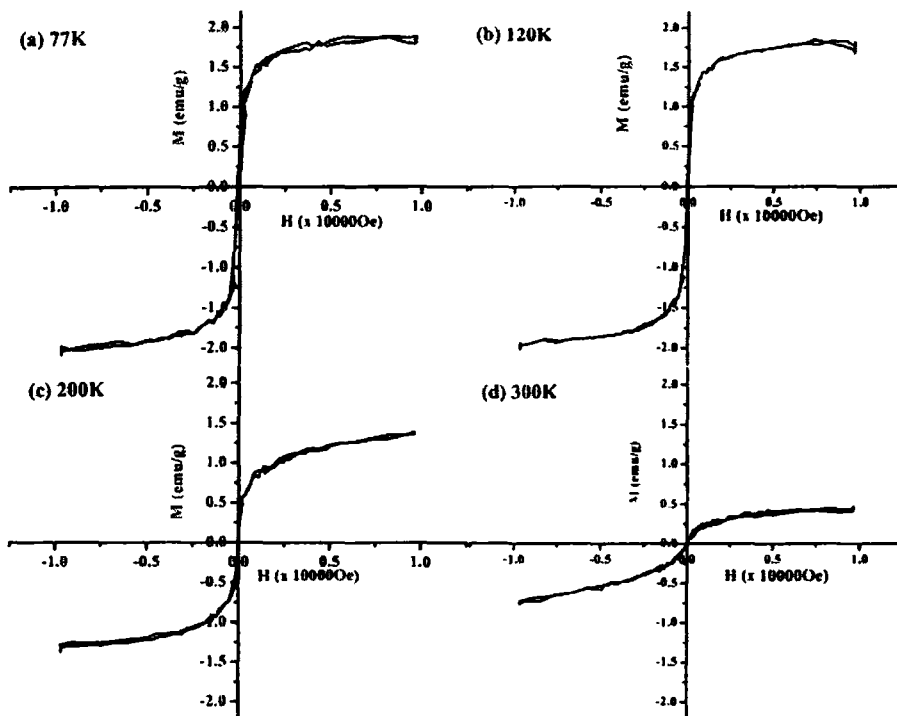
Figure 5.7: Magnetization curves for NiA at (a) 77 K (b) 120 K (c) 200 K and (d) 300 K

The percentage of nickel in NiA determined from ICP-AES analysis was 30.46 wt.% and hence the effective magnetization of nickel in NiA is determined (Table 5.1). The low value of coercivity (<15 Oe at 300 K) indicates the single domain supermparamagnetic nature of the NiA. Lower saturation magnetization is attributed to the finite size effects and amorphous nature of formed nickel particles. Surface effects like spin canting and anisotropy influence the magnetization of oleic acid coated nickel nanoparticles. At reduced particle sizes, as observed from the broad peak in the XRD pattern, the magnetic properties of the surface layers is expected to become increasingly dominant. The high surface to volume ratio, random arrangement of atoms and large number of interfaces, all contribute to higher disorder in the system leading to reduction of magnetic properties.

The M-H loops of Ni@C at different temperatures (Figure 5.8) depict the

intrinsic properties of a ferromagnetic nickel species. Annealing improved the crystallinity simultaneously enhancing the room temperature saturation magnetization to ~23.6 emu/g. The percentage of nickel in the Ni@C nanostructure was estimated to be 43 wt.% from ICP-AES analysis. Taking into account of the magnetic component, the saturation magnetization of Ni@C was estimated to be 54.8 emu/g which is close to the bulk value of nickel (55.4 emu/g)[231].
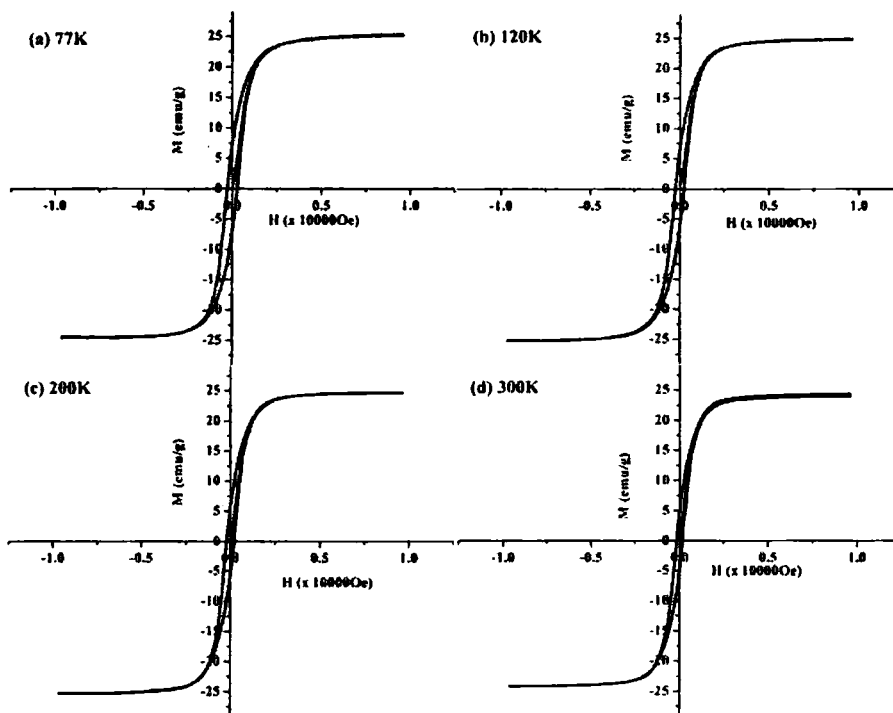
Figure 5.8: Magnetization curves for Ni@C at different temperatures (a) 77 K (b) 120 K (c) 200 K and (d) 300 K

The saturation magnetization (M_s), effective magnetization of nickel (M_{eff}), remanence (M_r) and coercivity (H_c) of passivated nickel nanoparticles at different temperatures are listed in Table 5.1.

The remanance increased from 0.007 to 5.19 emu/g at room temperature. Coercivity depends on factors like magnetocrystalline anisotropy energy, particle morphology, and the surface effects of fine particles. An enhanced coercivity with respect to bulk nickel is observed in Ni@C at all temperatures measured, which is ascribed to the finite size effects [2, 232].

Table 5.1: Hysteresis loop parameters at different temperatures for NiA and Ni@C

T	M_s (emu/g)		M_{eff} (emu/g)		M_r(emu/g)		H_c (Oe)	
(K)	NiA	Ni@C	NiA	Ni@C	NiA	Ni@C	NiA	Ni@C
77	1.87	25.25	6.1	58.7	0.585	7.07	128.6	283
120	1.63	24.93	5.2	57.9	0.289	6.40	40.76	240
200	1.28	24.66	4.1	57.3	0.066	5.86	18.9	210
300	0.42	23.6	1.3	54.8	0.007	5.19	14.6	170

Temperature dependent magnetic properties of passivated nickel nanostructures were also investigated using a SQUID magnetometer. The temperature dependence of magnetization was measured under small DC probe fields (100 and 200 Oe) between 5-300 K using zero-field-cooling (ZFC) and field-cooling (FC) procedures. A λ-shape curve in the ZFC/FC curve (depicted in Figure 5.9a,b) show a superparamagnetic blocking in NiA.
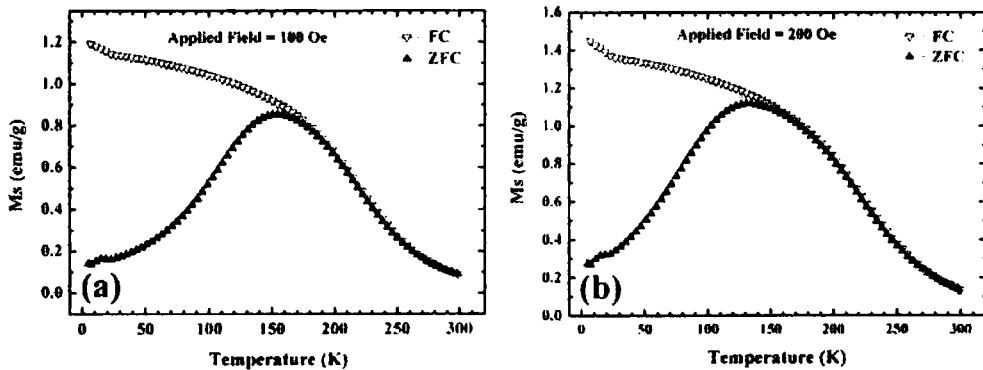
Figure 5.9: ZFC/FC curves of NiA with an applied field of (a) 100 Oe and (b) 200 Oe

At high temperatures the two curves coincides following the Curie-Weiss law. At low temperatures (below ~150 K) the two curves separate out, with the ZFC curve giving a broad maximum, a sure indication of superparamagnetic behavior. The blocking temperature of noninteracting system of nickel nanoparticles were determined from the derivative curves (Figure 5.10a,b).
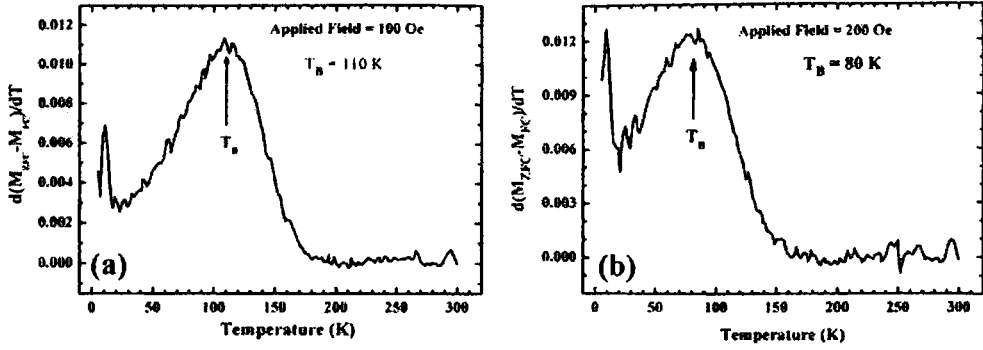
Figure 5.10: Derivative plots showing the blocking temperature with an applied field of (a)100 Oe and (b) 200 Oe

Both M_{ZFC} and M_{FC} are a function of dipole interaction strength, probe field and the particle size distribution of the system. The blocking temperature is given by $T_B = 25KV/k$. For a homogeneous system, the M_{ZFC} and M_{FC} curves follows the Langevin function given by [233]

$$M_{ZFC} = 0 \text{ and } M_{FC} = M_s, \text{ if } T < T_B$$

$$M_{ZFC} = M_{FC} = M_s L\{\tfrac{HV}{T}\}, \text{ if } T > T_B$$

where $L\{HV/T\}$ is the Langevin function [2]. But for an inhomogeneous system, as in the present study, the expression has to be generalized by considering the log normal distribution of grain size. Thus, the magnetization relaxation behavior, level of magnetization and blocking temperature distribution of the system can be determined from the rate of net magnetization reversal at which the particles become unblocked. From the $-d(M_{ZFC} - M_{FC})/dT$ vs T curve (or the T_B distribution curve), the temperature at which T_B distribution peaks can be determined. The bifurcation temperature in the M_{ZFC} curve thus deviates from the T_B so determined.

The blocking temperature of NiA is found to be 110 K with 100 Oe applied field. At a higher field of 200 Oe, the blocking is shifted to 80 K which is consistent with relation for $T_B(H)$ for a noninteracting system given by

$$T_B(H) = T_B(0)[1 - \frac{H}{H_c}]^m \tag{5.1}$$

where $|m|$ can take values between 3/2 and 2 [234]. The broad peak in the ZFC curve is yet another indication regarding the size distribution of magnetic particles in the composite consistent with the TEM results.

The carbon coated nickel particles (Ni@C) possess magnetic properties strikingly different from that of NiA (Figure 5.11). The ZFC/FC curves are found to meet near room temperature indicating the non interacting nature of the nickel particle in the nickel-carbon nanostructures. Ni@C has no signatures of superparamagnetic blocking as evident from the absence of any bifurcation in the ZFC/FC curves. This points towards higher grain size, as evident from the TEM results. These results are consistent with the classical micromagnetic theory (the anisotropy energy is proportional to the volume of single particle and anisotropy constant).
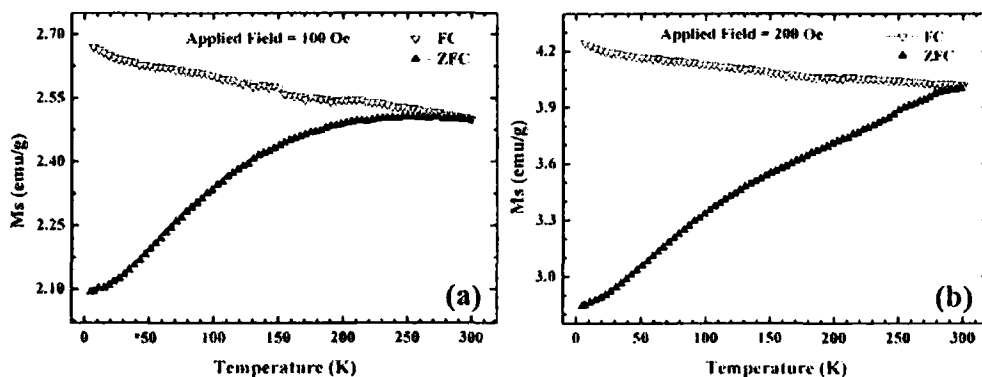
Figure 5.11: ZFC/FC curves at (a)100 Oe and (b)200 Oe for Ni@C

5.6 Microwave absorbing properties

Figure 5.12a shows the variation of real part (ϵ') and imaginary part (ϵ'') of complex permittivity as a function of frequency for Ni@C. ϵ' remained almost a constant ($\sim$11.25) while ϵ'' increased with increase in frequency from 4.2 to 6. Space charge polarization emanating at the nickel carbon interfaces contribute to the high dielectric permittivity in Ni@C nanostructure. The free electrons from nickel core assist the accumulation of charges on the interface while the dielectric shell around nickel reduces the electrical conductivity and limits the eddy current

effects in the Ni@C composite. Moreover, the polarized metal cores act as dipoles at high frequencies[235]. The enhancement in ϵ'' is ascribed to the semi-metallic nature of nickel carbon nanostructures (DC electrical conductivity measured for Ni@C is $\sim 10^{-2}$ S/m).
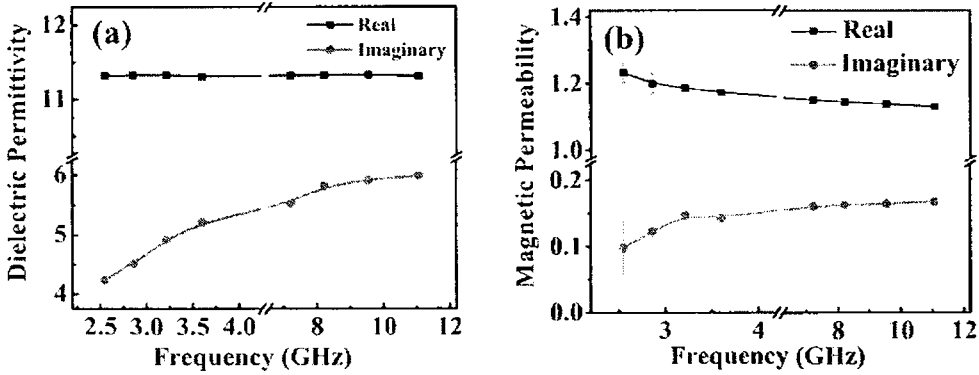
Figure 5.12: (a) Dielectric permittivity and (b) magnetic permeability spectra of Ni@C in the S and X-band

Figure 5.12b shows the frequency dependence of real part (μ') and imaginary part (μ'') of magnetic permeability. Initially there is a decline in μ' in the S-band (1.2 to 1.13) while it is more or less a constant in the X-band. The low value of permeability at high frequencies is expected in core-shell structures due to lower magnetization and slower response to microwave [236]. μ'' is found to increase from 0.09 to 0.16 over the frequency range 2-12 GHz. Primarily, the microwave absorption mechanism is ascribed to the intrinsic magnetic loss of the inclusion due to spin rotation and domain wall displacement resonances [192]. This is caused by the time lag of the magnetization vector behind the external alternative magnetic field. The domain wall motion in nanostructures can be ruled out as the size of the magnetic inclusions are well below their critical diameter ($\sim$55 nm). So the spin rotations ought to contribute to the magnetic loss in the system. though detailed study in this regard needs to be carried out.

The reflection loss for optimum thickness is evaluated from the measured values of ϵ', ϵ'', μ' and μ'' based on the model of a single layer metal backed plane wave absorber proposed by Naito and Suetake [181]. Accordingly, the input impedance (Z_{in}) and hence the reflection loss in decibels is determined.
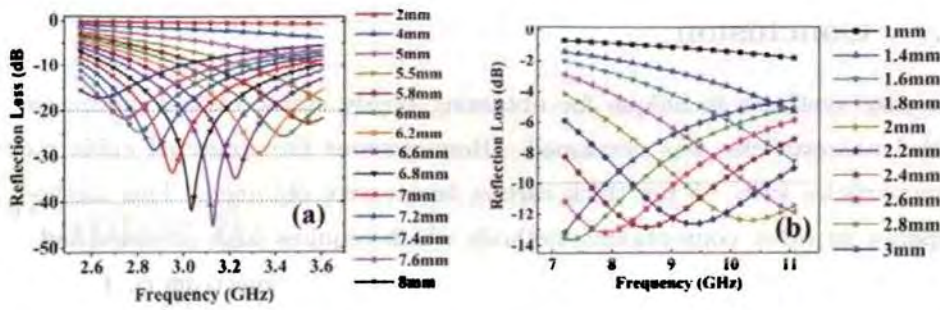
Figure 5.13: Frequency dependence of reflection losses for Ni@C in the (a) S and (b) X-band

Figure 5.13(a, b) shows the reflection loss evaluated using Equation 3.3 and 3.4 in the S and X-band for different absorber layer thicknesses. Reflection loss is found to cross over -10 dB for the absorber with a thickness of 5.8-8 mm in the S-band while it is 2.2-2.6 mm in the X-band. Reflection loss minima of -45 dB is obtained at 3.13 GHz with an absorber thickness of 6.6 mm. This enhancement in microwave absorption is due to CNOs and fibrous carbon structures with nickel nanoparticles as inclusions. Thus, one can make advantage of individual nickel particles for enhanced microwave absorption emanating from the effective anisotropy and dipolar interaction effects between the magnetic domains which may be weak for aggregated magnetic particles. Moreover, the carbon nanostructures formed in the Ni@C composite are interconnected and they form bridges for the mobile charge carriers which can interact with the EM radiation over a short length scale. This increases the electrical loss leading to better impedance matching [181, 214].

The reflection loss minimum is found to shift towards the lower frequency side as the thickness is increased as depicted in Figure 5.13. This can be understood based on the quarter wave principle [182, 214, 237]. When the electromagnetic wave is incident on an absorber backed by a metal plate, a part of it is reflected from the air-absorber interface while some part is reflected from the absorber-metal interface. When the thickness $t = \lambda_0/(4|\epsilon||\mu|)^{1/2}$, where $\lambda_0 = c/f$, these two reflected waves are out of phase by 180° and cancel each other. Since $t \propto 1/f$, the above criterion is satisfied at increased sample thickness for lower frequencies.

5.7 Conclusion

An easy synthesis technique for obtaining highly stable carbon encapsulated nickel nanoparticles was developed. Homogeneous face centered cubic nickel nanoparticles with ~5 nm thick carbon layers were obtained. This method is superior to other conventional methods which requires high pressure and annealing temperatures. The HRTEM images and Raman spectrum confirmed the formation of carbon structures around nickel nanoparticles. The nickel/carbon core/shell nanostructures exhibited a shelf life of more than a year, with high thermal stability and excellent magnetic properties. This synthesis route provides scope for large scale production of nickel/carbon nanostructures. This makes them suitable for use in functionalized drug targeting, as solid lubricants and electromagnetic shield materials. A reflection loss minima less than -10 dB was found for an absorber thickness of 2.2-2.8 mm in the X band. At 3.13 GHz, a minimum reflection loss of -45 dB was obtained for an absorber layer thickness of 6.6 mm. Hence, such hybrid magnetic metal carbon nanostructures can be used as potential candidates for multilayer absorber materials.

Chapter 6

Synthesis of nickel ferrite nanoparticles via different routes and studies on their structural, magnetic and dielectric properties

Properties of materials are substantially modified with reduction in their size. This has been an extensive area of research with regard to the family of ferrites. Nickel ferrite belonging to the class of soft magnetic materials is one such candidate which has wide application potential. In this chapter, nickel ferrite in the nanoregime were prepared by employing both top-down as well as bottom-up approaches. Structural and magnetic properties of these particles were determined using X-ray diffraction, Fourier transform infrared spectrometry and vibrating sample magnetometry. The temperature dependent dielectric properties were examined using an LCR meter. These properties were found to be dependent on size as well as preparative conditions. The enhancement of dielectric parameters with reduction in grain size is in accordance with the Koop's and Maxwell-Wagner dielectric dispersion model.

6.1　Introduction

Novel methodologies for the development of nanoferrites and investigation of their properties has gained much attention owing to their numerous needs for application in areas like magnetic recording media, targeted drug delivery, magnetic resonance imaging, sensors, heterogeneous catalysis, repulsion suspension for use in levitated railway system, ferrofluids, catalysis, magnetic refrigeration, microwave devices and antennas [238–247]. Ferrites have technological importance due to their high frequency applications. They are good dielectric materials whose properties vary with the method of preparation, sintering condition and amount of constituents [19, 248–250]. When size of ferrite particles gets reduced to nanoscale, they exhibit unique properties quite different from their bulk counterparts. This opens up several questions regarding the fundamental physics and chemistry of ferrite materials.
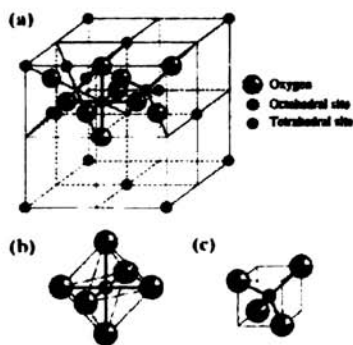
Figure 6.1: (a) Spinel unit cell structure (b) Octahedral interstice (B site: 32 per unit cell, 16 occupied), and (c) tetrahedral interstice (A site: 64 per unit cell, 8 occupied)

Ferrites are well explored in the micron regime [251–253]. They are mixed metal oxides with iron (III) oxides as their main component. Ferrites crystallize in three crystal types [254]: spinel type (with cubic crystal structure and general formula $Me^{2+}Fe_2O_4$ where Me = Fe, Mn, Mg, Ni, Zn, Cd, Co, Cu, Al or a mixture of these, garnet type (with cubic crystal structure and general formula $Ln_3^{3+}Fe_5O_{12}$ where Ln = Y, Sm, Eu, Gd, Tb, Dy, Ho, Er, Tm, or Lu) and magnetoplumbite type (with hexagonal crystal structure and general formula Me^{2+} $Fe_{12}O_{19}$ where Me = Ba or Sr).

Spinel ferrites or ferrospinels as they are called are ferrimagnetic materials named after the mineral spinel, $MgAl_2O_4$ [144, 255, 256] having a general chemical composition $MeO.Fe_2O_3$ where 'Me' is a divalent metal. A unit cell representing the smallest 3D building block of spinel crystal structure is shown in Figure 6.1. The spinel structure is determined primarily by the oxygen ion lattice. The oxygen anions are packed in a face centered cubic arrangement such that there are two kinds of interstitial space between the anions- octahedrally co-ordinated B sites (Figure 6.1b) and tetrahedrally co-ordinated A sites (Figure 6.1c). There are eight formula units of $Me.Fe_2O_4$ in a unit cell. Thus, in a unit cell of 32 oxygen anions, there are 64 tetrahedral sites and 32 octahedral sites. It turns out that out of the 64 tetrahedral sites only 8 are occupied and out of 32 octahedral sites, only 16 are occupied. The exchange interaction between A and B sites is negative and the strongest among the cations, so that the net magnetization results from the difference in magnetic moment between A and B sites.

Factors like ionic radii of the cations, preference of ions to specific sites, Madelung energy, crystal field effects etc. determine the distribution of cations in spinel ferrites. The interesting and useful magnetic and electrical properties of the spinel are governed by the distribution of the Fe and the divalent metal ions among the octahedral and tetrahedral sites of the spinel lattice. According to the occupancy of Fe and Me ions in these sites, spinels can be normal, inverse or mixed. The general cation distribution can be represented as $Me_{\delta}^{2+}Fe_{1-\delta}^{3+}[Me_{1-\delta}^{2+}Fe_{1+\delta}^{3+}]O_4$ where the cations inside brackets are located in octahedral sites and the other outside brackets in tetrahedral sites. For $\delta = 1$, the ferrite form the normal spinel while for $\delta = 0$, it is called inverse spinel. For random distribution $\delta = 1/3$. $ZnFe_2O_4$ and $CdFe_2O_4$ are normal spinels with all the divalent metal cation distributed in the tetrahedral sites. In inverse spinels like $NiFe_2O_4$ and $CoFe_2O_4$, the metallic cation occupies the octahedral sites only with ferric ions equally distributed in the two sites. The lattice constant of ferrites is dependent on the metal-ion content, varying with different metal ions form a cubic side of about 8.3-8.5 A.

Nickel ferrite $(Fe^{3+})_A[Ni^{2+}Fe^{3+}]_B.O_4$ is one of the most important semiconducting ferrimagnetic material with an inverse spinel structure. Considerable attention has been laid towards the study of nanosized nickel ferrite due to their

technological importance [238–247]. Ferrimagnetism in nickel ferrite originates from the magnetic moment of anti-parallel spins between Fe^{3+} ions at tetrahedral sites and Ni^{2+} ions at octahedral sites [144]. Their properties could be tailored by metal substitution. Phase pure nickel ferrite has been studied extensively by several groups [3, 257–261]. Sol-gel pyrolysis, hydrothermal technique, mechanical alloying, co-precipitation technique, electrospinning, reverse micelle technique, plasma deposition method, radio frequency thermal plasma torch technique, pulsed wire discharge and high energy ball milling [19, 20, 261–272] are some of the common synthesis methodologies adopted. Recently Ramalho *et al.* synthesized nickel ferrite powders of crystallite size 120 nm by combustion reaction using urea as fuel [272] while Santi Maensiri *et al.* [248] developed methods to obtain nickel ferrite ($NiFe_2O_4$) nanoparticles using Fe and Ni nitrate precursors and freshly prepared egg white in an aqueous medium.

The strong dependence of the conduction mechanism and dielectric properties of material on the grain size, porosity as well as density are well established. Earlier studies conducted on polycrystalline ferrites [258, 273, 274] have shown the dependence of composition, size and shape on their structural, electrical as well as magnetic properties. Conduction in ferrites is due to hopping of electrons between Fe^{2+} and Fe^{3+} ions over the octahedral sites of the spinel lattice. The magnetic and electrical properties of ferrites are highly sensitive to the cation distribution and microstructure which in turn are sensitive to the synthesis condition. Hence, selection of appropriate process is crucial in order to obtain with desirable properties. Modern research aims at developing simple low temperature techniques for delivering ferrite nanoparticles in large quantities having improved properties than those produced by conventional techniques. Among these, an ideal method would be the one which could be carried out at low temperatures with minimal energy consumption having better yield.

Usually ferrite preparation involves conventional solid state reaction methods, which apart from being cumbersome has serious limitations like requirement of prolonged heating at high temperatures which may result in evaporation of some of the constituents leading to change of the desired stoichiometry. Grinding and milling of the precursor materials can cause loss of some of the materials resulting in nonstoichiometric compositions. Here in this study we have tried

to investigate and compare the structural, magnetic and dielectric properties of ultrafine nickel ferrite particles obtained by autocombustion/sol-gel and ceramic method. The effect of mechanical attrition on various properties of nickel ferrite are also studied.

6.2 Experimental

6.2.1 Synthesis

Nickel ferrite nanoparticles were synthesized by employing both bottom-up and top-down approaches namely sol-gel method, conventional ceramic method and mechanical attrition.

Sol-gel method: Analytical grades of metal precursors, $Fe(NO_3)_3.9H_2O$ (purity >99%, Merck India) and $Ni(NO_3)_2.6H_2O$ (purity >99%, Merck India) were taken in the 2:1 molar ratio and dissolved in minimum quantity of ethylene glycol (25%, AR grade Merck India) at room temperature. The so obtained saturated solution was heated at 333 K to form a wet gel. It was further dried at 373 K which lead to self combustion giving fluffy nano sized nickel ferrite. The sample was homogenized in an high energy ball milling unit (HEBM, model: Fritsch Planetary micromill 'Pulverisette 7') at 200 rpm for 10 min and was labelled as NFEG.

Conventional ceramic method: Oxalic acid ($C_2H_2O_4.2H_2O$, purity >99.5%, Merck India) was allowed to react with ferrous sulphate ($FeSO_4.7H_2O$, purity >99%, Merck India) solution taken in appropriate stoichiometric ratios. The reaction was carried out at 333 K with continuous stirring. The formed precipitate was filtered, thoroughly washed in distilled water and dried at 373 K for 3 h in a hot air oven to obtain ferrous oxalate dyhydrate (FOD). This freshly prepared FOD was then mixed with nickel carbonate ($NiCO_3$, AR grade, Nice India) in 2:1 (Fe:Ni) molar ratio in an agate mortar with acetone (extra pure, Merck India) as the mixing medium. The powder was pre-fired at 773 K for 4 h, again mixed and calcined at 1273 K for 12 h to obtain phase pure nickel ferrite. The sample was labelled as NFCer.

Mechanical attrition using high energy ball milling: Nickel ferrite prepared by both sol-gel and ceramic methods were subjected to HEBM for 180

min. For this the ferrite powder samples were loaded in the mill in 1:10 powder to ball weight ratio and wet milled in toluene medium. The samples were labelled as NFEG180 and NFCer180 respectively for the ball milled NFEG and NFCer samples.

6.2.2   Characterization

XRD pattern was recorded using Rigaku D-max C powder X-ray diffractometer. The SEM images of the synthesized nickel ferrite particles were observed in a JEOL Model JSM - 6390LV. Further, Fourier transform infrared spectrometer (Thermo Nicolete Avatar DTGS) was used to analyse the structure of the metal oxide nanostructures. The room temperature magnetic properties were measured using EG&G PAR 4500 vibrating sample magnetometer. Dielectric measurements of nickel ferrite nanoparticles were carried out in an HP impedance analyzer (4285A) in the frequency range of 100 kHz to 8 MHz. The powder samples were pelletized at a pressure of 5 tonne. They were then held tightly between two circular copper plates (12 mm diameter, thickness ~2 mm) to form a capacitor and placed inside a home-made dielectric cell. The capacitance and loss tangent were measured and recorded by interfacing the impedance analyzer with a personal computer through a GPIB cable IEE488 using LabVIEW (Version 8). Moisture content present. if any, in the samples were removed by heating the pellets in a hot air oven at 373 K for 2 h prior to measurements.

6.3   Structure and morphology

Figure 6.2 shows the XRD pattern of NFEG. NFEG180, NFCer and NFCer180. The diffraction pattern reveals the characteristic peaks of inverse spinel structure corresponding to phase pure nickel ferrite (ICDD 74-2081). The crystallite size of nickel ferrite particles was determined by employing Debye Scherrer's formula. The line broadening of the maximum intense (311) peak clearly shows the effective reduction of grain size induced by HEBM. The crystallite size was found to be 32 nm and 21 nm respectively for NFEG and NFEG180. It showed a 38% reduction in size when subjected to HEBM for 180 min.
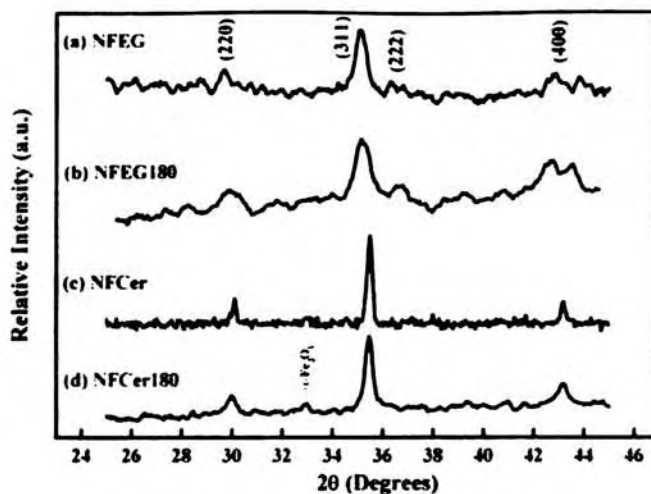
Figure 6.2: XRD patterns of nickel ferrite (a) NFEG (b) NFEG180 (c) NFCer, and (d) NFCer180

The crystallite size of samples prepared by ceramic method was higher than those of sol-gel samples even after milling for 180 min (NFCer: 56 nm, NFCer180: 37 nm). Moreover milling lead to the evolution of α-Fe_2O_3 (indicated in Figure 6.2d) impurity and 33% grain size reduction. Another aspect to be noted here is the ratio of intensity of (222) and (220) plane. This ratio is high for **NFEG** and NFEG180 while (220) plane is hardly seen in the XRD pattern of NFCer or NFCer180. This may be due to the following reason. HEBM reduced the grain size of nickel ferrite. Simultaneously some of the Ni ions get shifted from the B-site to the A-site while an equal number of Fe ions shifts from the A-site to B-site. Thus the percentage of Fe ions in the B-site increases with the reduction in grain size [275]. This could be ascertained by carrying out investigations using Mössbauer studies. Some of the main advantages of non-conventional process are high purity, chemical homogeneity, small and uniform particle size and controlled particle shape [276]. These are looked into by employing electron microscopy techniques.
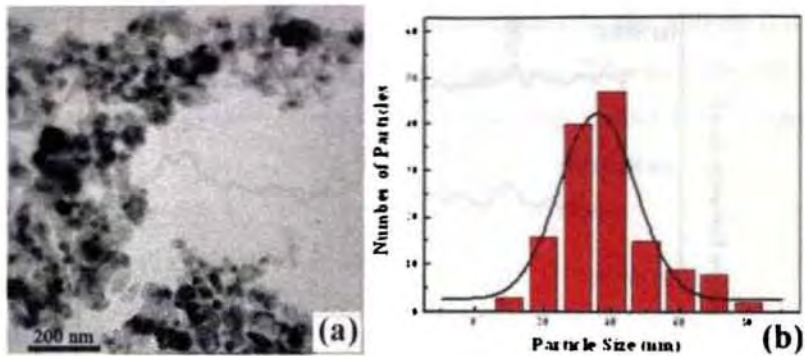
Figure 6.3: (a) TEM image of NFEG and (b) normalized Gaussian fit of grain size distribution

NFEG was subjected to TEM analysis which revealed the average grain size to be 35 nm (Figure 6.3). This is consistent with the particle size estimated from the XRD pattern. The morphology of the nickel ferrite particles NFEG, NFEG180, NFCer and NFCer180 are examined using SEM (Figure 6.4).
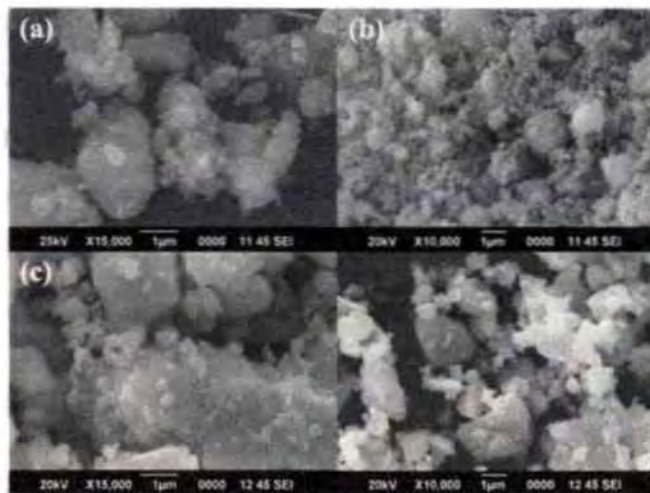
Figure 6.4: SEM images of nickel ferrite particles (a) NFEG (b) NFEG180 (c) NFCer, and (d) NFCer180

HEBM induced reduction in grain size is evident from the SEM images. Sol-gel derived samples (NFEG and NFEG180) possess lower grain size than those obtained by ceramic method (NFCer and NFCer180). This further supports the

XRD results. It clearly dictates the effectiveness of the sol-gel autocombustion method for obtaining finer grains of nickel ferrite particles. Moreover, the particles in NFEG180 have more uniform grains when compared to that of NFCer180.
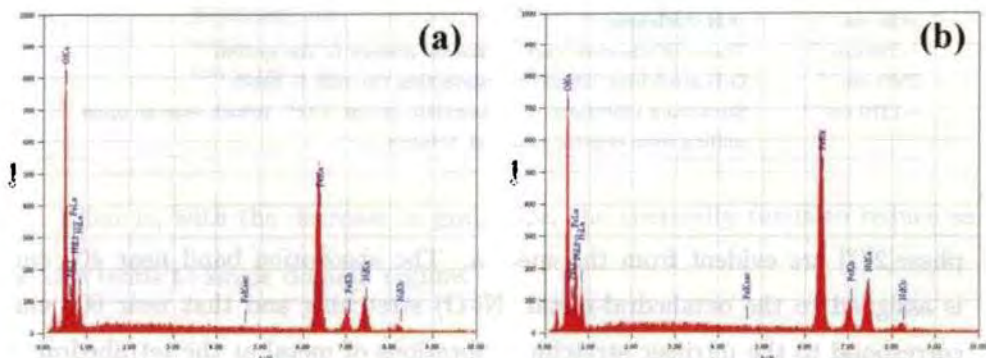
Figure 6.5: Energy dispersive spectrum of (a) NFEG180 and (b) NFCer180
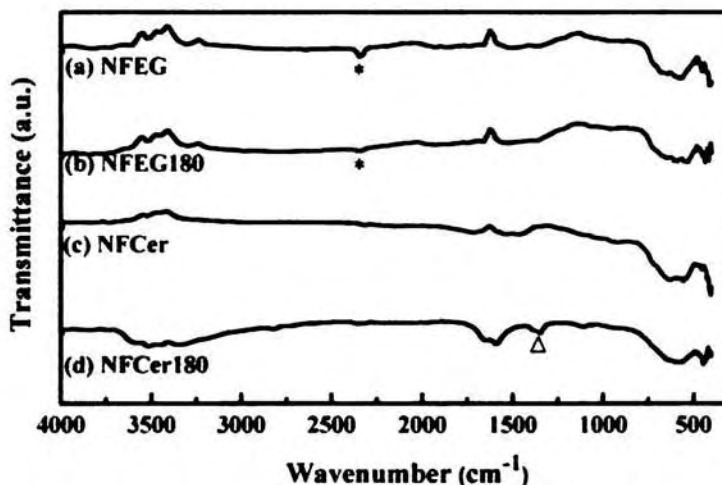
Figure 6.6: FTIR spectrum of nickel ferrite particles (a) NFEG (b) NFEG180 (c) NFCer, and (d) NFCer180

The energy dispersive spectra of selected samples are shown in Figure 6.5. It clearly indicates that Ni:Fe ratio is approximately 1:2. FTIR spectra of nickel ferrite particles are shown in Figure 6.6. The presence of absorption bands corresponding to the tetrahedral and octahedral group complexes within the spinel

Table 6.1: FTIR vibration peaks

Wavenumber	Assignment of peaks
400 cm^{-1}	Octahedral-metal (Ni-O) stretching
600 cm^{-1}	Intrinsic stretching vibrations of metal at tetrahedral site (Fe-O stretching)
1600 cm^{-1}	O-H stretching
~2340 cm^{-1}	Traces of adsorbed carbon dioxide present in the system
3500 cm^{-1}	O-H stretching vibrations interacting through H bonds
~1370 cm^{-1}	Stretching vibrations of carboxylate group (CO^{2-})which emerge upon milling from organic material, toluene

phase[277] are evident from the spectra. The absorption band near 400 cm^{-1} is assigned to the octahedral-metal (Ni-O) stretching and that near 600 cm^{-1} correspond to the intrinsic stretching vibrations of metal at the tetrahedral site (Fe-O stretching).

These vibrations are observed in all the samples (Figure 6.6), typical for pure nickel ferrite [278, 279]. The broad intense band around 3500 cm^{-1} and a less intense band around 1600 cm^{-1} is associated with the O-H stretching vibrations interacting through H bonds emanating from free water molecules. Table 6.1 lists the peaks assigned to different vibrations observed for nickel ferrite.

Absorption peak at ~2340 cm^{-1} (indicated by '*' in Figure 6.6a,b) is due to the presence of traces of carbon dioxide present in the samples formed during combustion. These are seen only in NFEG and NFEG180 while such vibrations are absent in the calcined samples, NFCer and NFCer180. A distinct band at ~ 1370 cm^{-1} in NFCer180 (represented by '$\triangledown$' in Figure 6.6d) indicates the stretching vibrations of carboxylate group (CO_2^-) which emerge upon milling.

6.4 Magnetic properties

The room temperature hysteresis loops of the NFEG and NFCer, and those ball milled for 180 min are shown in Figure 6.7. The corresponding loop parameters determined are tabulated in Table 6.2.

There is a direct correspondence between the duration of milling or the grain size of ferrite particles with their magnetic properties. During the initial stages of ball milling, the grain size decreases and then saturates even after prolonged milling [2, 88]. The change in coercivity of NFEG with milling time is on expected

Table 6.2: Hysteresis loop parameters determined for nickel ferrite nanoparticles

Sample	Magnetization M_s (emu/g)	Coercivity H_c (Oe)	Remanence M_r (emu/g)
NFEG	40	103	6
NFEG180	33	83	4.4
NFCer	42	46	5.1
NFCer180	35	268	8.5

line. That is, with the decrease in grain size, the coercivity tends to reduce as the size tends to single domain regime.
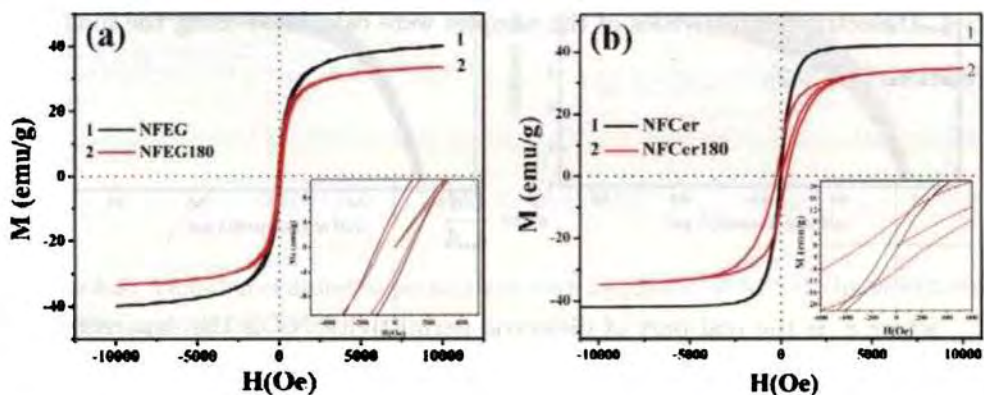
Figure 6.7: M-H curves nickel ferrite samples prepared by different methods (a) Sol-gel and (b) Ceramic method

In the case of NFCer, the grain is far above the critical superparamagnetic limit of ferrite [20] and hence with increase in milling time, the size reduction increases the coercivity. A similar trend is observed with respect to the remanance of the ferrite samples. As mentioned earlier, more light can be thrown on the effect of ball milling on the change in cation redistribution that might occur, by subjecting the samples to Mössbauer studies or neutron diffraction experiments [4, 280].

6.5 Dielectric properties

Although extensive research on the dielectric properties of micron sized ferrite particles have been carried out in the last decades, no much efforts were laid to understand these aspects at the nanoregime, until the advent of novel synthesis techniques. Only recently, the effect of grain size on the dielectric properties of ferrite particles has been investigated by several groups [273, 281]. Proper understanding of these aspects would help in tailoring the properties for obtaining feasible materials for applications. Powder samples were pelletized, dried at 373 K for 2 h and held inside a homemade setup to determine their dielectric properties. Dielectric permittivities of the samples were calculated using the following relations [68, 282].

$$\epsilon^{'} = \frac{Cd}{\epsilon_o A} \tag{6.1}$$

where $\epsilon^{'}$ is the real part of dielectric permittivity, $'C'$ is the capacitance of the capacitor formed by inserting the sample between two metal plates, $'d'$ is the thickness of the sample, ϵ_o the permittivity of free space and $'A'$ is the area of cross section of the sample.

6.5.1 Frequency and temperature dependence of dielectric permittivity

The dependence of dielectric permittivity with frequency or the dielectric dispersion occurs due to several types of polarization mechanisms. This includes electronic, ionic, dipolar or interfacial polarization [282]. The variation of dielectric parameters with frequency was measured at different temperatures and the corresponding plots are shown in Figure 6.8.
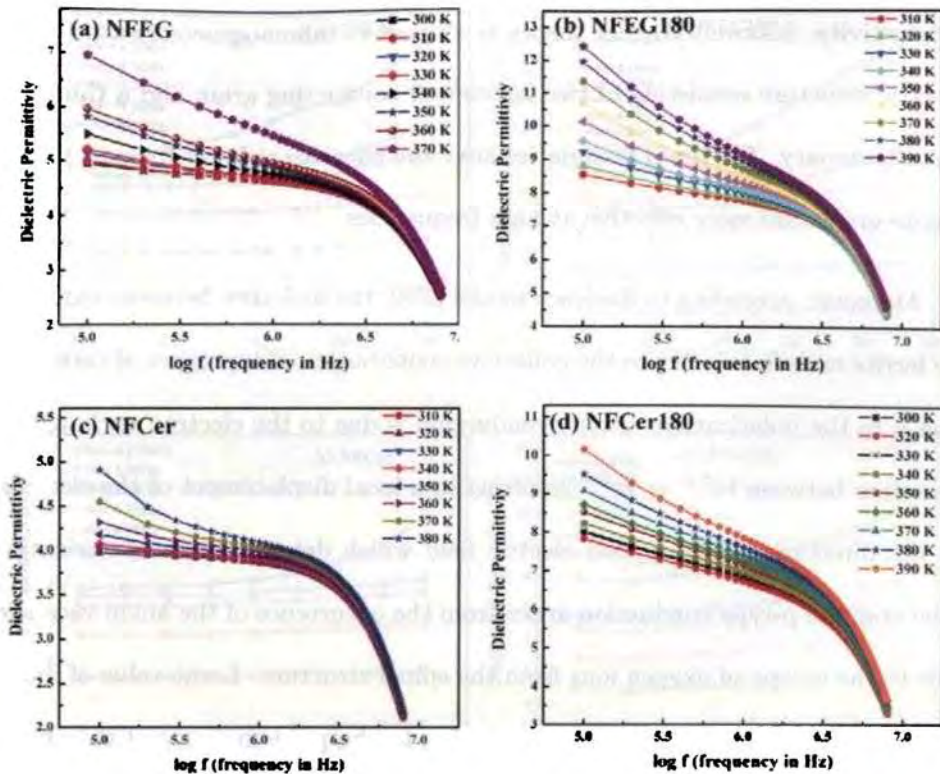
Figure 6.8: Variation of dielectric permittivity with frequency (a) NFEG, (b) NFEG180, (c) NFCer, and (d) NFCer180

Dielectric permittivity is a composition dependent quantity and for ferrites containing ferrous ions in excess, the real part of permittivity normally attains high values at low frequencies while showing a decreasing trend with frequency because excess of ferrous ions leads to high dc conductivity [279]. The observed low frequency dielectric dispersion in ferrites is due to space charge effects [283, 284]. High dielectric permittivity values at lower frequencies were observed for all the samples. This may arise from the dc conductivity of the medium, electronic polarization and interfacial polarization from the heterogeneous structure [285].

As the frequency is increased, the time required for the interfacial charges to be polarized or for the dipoles to arrange is delayed, thus reducing the dielectric permittivity. The dispersion at high frequencies is solely explained by the Maxwell-Wagner model of interfacial polarization and Koop's phenomenological theory [286, 287] of well conducting grains separated by layers of lower

conductivity. Maxwell-Wagner theory is a result of inhomogeneous nature of dielectric structure consisting of two layers-well conducting grain and a thin layer grain boundary. The grain boundaries are more effective at lower frequency while ferrite grains are more effective at high frequencies.

Moreover, according to Rezlescu model [258], the dielectric behavior exhibited by ferrite materials is due to the collective contribution of two types of carriers, p and n to the polarization. n-type conduction is due to the electron exchange interaction between $Fe^{2+} \leftrightarrow Fe^{3+}$ resulting in a local displacement of the electrons in the direction of the applied electric field which determines the polarization. The origin of p-type conduction arises from the occurrence of the anion vacancies due to the escape of oxygen ions from the spinel structure. Large value of dielectric permittivity at lower frequencies is due to the predominance of the species like Fe^{2+} ions, piling up of interfacial dislocations, oxygen vacancies and grain boundary defects. The decrease is rapid at lower frequencies and becomes slow at high frequency.

Temperature dependence of dielectric permittivity of nickel ferrite is also examined. Temperature was varied from 300 to 390 K in steps of 10 K (Figure 6.9). There is a gradual rise in dielectric permittivity due to the increase in interfacial polarization facilitated at higher temperatures [281]. Moreover, the ionic mechanism and drift mobility of charge carriers increases the dielectric permittivity with rise in temperature. In ionic dielectrics, the orientation of the dipoles is facilitated which increases the dielectric permittivity. Chaotic thermal oscillations of molecules are intensified and the degree of orderliness of their orientations is diminished [68].
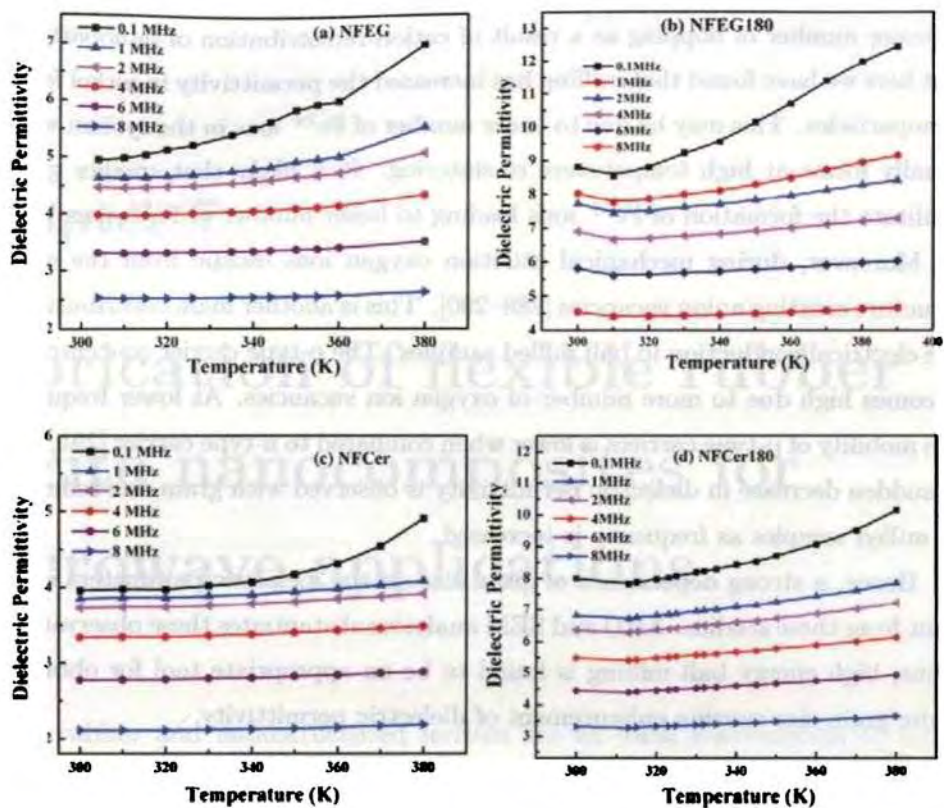
Figure 6.9: Variation of dielectric constant with temperature (a) NFEG, (b) NFEG180, (c) NFCer, and (d) NFCer180

6.5.2 Effect of high energy ball milling on the dielectric permittivity

On comparing the dielectric permittivity of ball milled samples (Figure 6.8 and 6.9), an increase in the permittivity values are observed. The grain size is reduced and hence the number of grain/grain boundary increases. This increases in the number of interfaces formed, which in turn increases the interfacial polarization. It can be seen that ϵ' is increased from 7 to 12.5 in the case of NFEG, while in NFCer, the dielectric permittivity is increased from 5 to 10 after milling for 180 min. Dielectric permittivity of the 180 min milled samples is almost doubled when compared to the pristine ones.

Various researchers found that the $Fe^{2+} \leftrightarrow Fe^{3+}$ hopping is mainly responsible for conduction and suggested a decrease in dielectric permittivity with milling due

to lesser number of hopping as a result of cation redistribution of nanoparticles. But here we have found that milling has increased the permittivity in nickel ferrite nanoparticles. This may be due to lesser number of Fe^{2+} ions in the system which usually forms at high temperature of sintering. It is likely that smaller grains facilitate the formation of Fe^{3+} ions leading to lesser number of Fe^{2+} ions [7].

Moreover, during mechanical attrition oxygen ions escape from the spinel structure creating anion vacancies [288–290]. This is another main contribution to the electrical conduction in ball milled samples. The p-type carrier concentration becomes high due to more number of oxygen ion vacancies. At lower frequency, the mobility of p-type carriers is lower when compared to n-type carrier [291, 292]. A sudden decrease in dielectric permittivity is observed with grain size reduction in milled samples as frequency is increased.

Hence, a strong dependence of grain size on the dielectric parameters is evident from these studies. XRD and SEM analysis substantiates these observations. Thus, high energy ball milling is found to be an appropriate tool for obtaining finite grain size causing enhancement of dielectric permittivity.

6.6 Conclusion

Phase pure nickel ferrite nanoparticles were prepared by different routes namely sol-gel autocombusion method, conventional solid-state reaction method and mechanical attrition by HEBM. Structural and morphology of these particles were systematically analysed employing various analytical tools. XRD and SEM revealed the reduction of grain size with milling. Further, magnetic as well as dielectric properties of the particles were investigated to study the effect of grain size on the ferrite particles. The investigations revealed that sol-gel route followed by HEBM yielded finer particles. Studies confirmed that as the number of grain-grain boundary increases, interfacial polarization enhances the dielectric permittivity of the system. Selecting appropriate synthesis methodology is hence crucial in developing materials for specific applications.

Chapter 7

Fabrication of flexible rubber ferrite nanocomposites for microwave applications

Natural rubber and nanostructured ferrites are an ideal combination to fabricate flexible rubber ferrite nanocomposites. Rubber ferrite nanocomposites can be employed as microwave absorbers and the bandwidth of absorption can be tuned. This chapter discusses the preparation of flexible magnetic nanocomposites by incorporating pre-characterized nickel ferrite nanoparticles in a natural rubber matrix. The processibility and mechanical properties are discussed. Dielectric permittivity of rubber ferrite composites were investigated in the RF frequency regime. The complex dielectric permittivity and magnetic permeability of the composites were measured at different microwave frequencies. A steady increase in dielectric permittivity with increase in filler concentration was observed. Maxwell-Garnett mixture equations were employed to model the effective permittivity and permeability of the composite. Further, reflection loss was estimated by employing the model of single layer absorber backed with a perfect conductor.

7.1 Introduction

The demand for miniaturization of devices has prompted material scientists and engineers towards developing composite materials having multifunctional prop-

erties. These composites consist of two or more constituent materials remaining separate and distinct on a macroscopic level, forming a single component [9]. The constituents in a composite can be categorized as matrix and filler. The matrix surrounds and supports the filler material by maintaining their relative positions, thereby enhancing physical and mechanical properties of the composite. A variety of fillers are available for incorporation in the matrix and the dielectric, mechanical and magnetic properties can be tailored for various applications [62, 69, 160, 293–296]. The polymer matrices commonly used are either plastics or rubbers. Among them natural rubber (NR) is more important because it is a sustainable raw material extracted from the latex of *Hevea Brasilliensis* which produces 99.99% of cis-1, 4 polyisoprene [62]. The chemical structure of NR is as shown in Figure 7.1
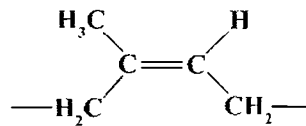
Figure 7.1: Chemical structure of cis 1,4 polyisoprene

NR is widely used not only for its compatibility with fillers but also for its high tensile strength as a result of its outstanding strain induced crystallization [297, 298]. Furthermore, NR is characterized by low hysteresis and low water absorption properties. Raw rubber has a specific gravity of 0.934 and a specific heat of 0.502 at 293 K. Besides that, the specific resistivity of raw rubber is 1×10^{15} to 2×10^{15}ohm.cm [299]. Raw rubber is seldom used in its original state. Rubber manufacture involves addition of rubber many ancillary materials called additives (like vulcanizing agents, accelerators, activators/retarders, antidegradents, fillers, plasticizers etc.) to rubber, thus forming potential materials for articles requiring high mechanical strength. The double bond of polyisoprene in NR is important for sulphur vulcanization. However, these unsaturated sites are reactive to oxygen or ozone consequently degrading the rubber. Hence antioxidants are used to reduce the degradation.

Ferrites of different composition find numerous applications in electronic devices [68, 300–302]. Spinel ferrites, especially nickel ferrite, assumes significance

because of their salient magnetic and dielectric properties at radio and microwave frequencies. They possess high electrical resistivity, mechanical hardness and chemical stability [303] although these properties are size dependent [304]. Nickel ferrite has been widely used in microwave devices and in electromagnetic shields due to its chemical stability, corrosion resistance and high saturation magnetization in addition to its microwave absorbing properties. Significant changes in magnetic and dielectric properties are observed at nanometric dimensions. They find applications in inductor cores, isolators, magnetic recording media, ferrofluids, microwave devices and EMI shields [69–73].

NR composites based on ceramic spinel ferrites have been extensively studied over the last decades [68, 305]. These magnetic rubber composite, otherwise called rubber ferrite composites (RFCs) are significant as far as applications are concerned. Dielectric and magnetic properties of RFCs can be easily tailored by using the right amount of filler in a single shot. Such materials have added functionalities like flexibility, mouldability and tunability of both dielectric and magnetic properties. Incorporation of nano fillers in a polymer matrix will impart reinforcing properties to the matrix [306]. Addition of magnetic fillers modifies the physicomechanical, magnetic as well as dielectric properties of RFCs. Filler addition affects their processability as well since the degree of freedom of rubber chains are decreased due to the interaction and adsorption of non-deformable filler onto the rubber [307]. At room temperature, though there is no physical ageing of NR vulcanisate (glass transition temperature, $T_g = 198$ K or -75 ^oC), there is a mechanical history to the specimen. Although there are several reports on the conduction mechanism in ferrites systems (both at bulk and nanoscales)[68, 305], the studies of their nanocomposites based on NR is scarce.

RFCs can play an important role here in realizing microwave absorbing materials with additional functionalities like elasticity and mouldability aided by lightweight [67, 68, 307]. Tuning the imaginary part of permeability μ'' improves matching, broaden the range of operating frequencies, increase attenuation and reduce the thickness of absorber layer. This can be achieved by using appropriate fillers with optimum magnetic permeability.

Nickel ferrite as a filler fits into the requirement of having the appropriate permeability, low loss and low dc conductivity. High resistivity ($\sim 10^{14}$ times that

of metal) ensures low eddy current loss in high frequency regime [308]. Further, the Curie temperature of nickel ferrite is ~858 K which makes it ideal for high temperature applications. Low coercivity and high saturation magnetization of nickel ferrite are also significant for obtaining good absorption properties. It has been reported that in the nano regime, the dielectric permittivity and magnetic permeability of ferrites gets considerably modified with respect to their ceramic counterparts because of their high surface to volume ratio [68, 300–302]. Hence incorporation of nickel ferrite nanoparticles into a matrix like NR can result in an excellent microwave absorbing material. Moreover, proper understanding of the dielectric and magnetic behaviour of polymer composites at high frequencies will help in engineering new materials for applications.

7.2 Experimental

7.2.1 Synthesis of nickel ferrite nanoparticles

Nickel ferrite particles were synthesized by using a modified sol-gel method [20]. Analytical grade $Fe(NO_3)_3.9H_2O$ (purity >99% AR grade, Merck India) and $Ni(NO_3)_2.6H_2O$ (purity >99% AR grade, Merck India) were taken in a 2:1 molar ratio and dissolved in a minimum amount of ethylene glycol (25% AR grade, Merck India) at room temperature. The saturated solution was heated at 333 ± 5 K for 2 h to form a wet gel. This was further dried at 373 ± 5 K leading to self ignition to produce fluffy nickel ferrite nanoparticles. They were then homogenized in a high energy ball milling unit (Fritsch Planetary micromill 'Pulverisette 7') at 200 rpm for 10 min.

7.2.2 Incorporation of $NiFe_2O_4$ in natural rubber matrix

Pre-characterized nickel ferrite nanoparticles were incorporated in natural rubber (ISNR 5 grade, supplied by Rubber Research Institute of India, Rubber Board, Kottayam) matrix according to a specific recipe (Table 7.1) obtained by extensive experimental iterations. The mixing was first carried out in a Brabender Plasticorder (torque rheometer, model: PL 3S) at 343 K for 10 min at a speed of 50 rpm. This was then homogenized in a two roll mill (15 cm x 33 cm) as per ASTM D 3182(1982).

Table 7.1: Recipe for preparing rubber ferrite nanocomposites

Ingredients	Amount (phr)	Purpose
Natural rubber (ISNR-5)	100	Polymer Base
Zinc Oxide	4	Activator
Stearic Acid	2	Activator
Triphenyl Quinone	1	Antioxidant
CBS*	0.8	Accelerator
Magnetic Nanoparticles	X	Filler
Paraffinic Oil	0.1X, if X$\geq$80	Plasticiser
Sulphur	2.5	Vulcanizing Agent

* n-Cyclohexyl-2-Benzothiazyl Sulphenamide
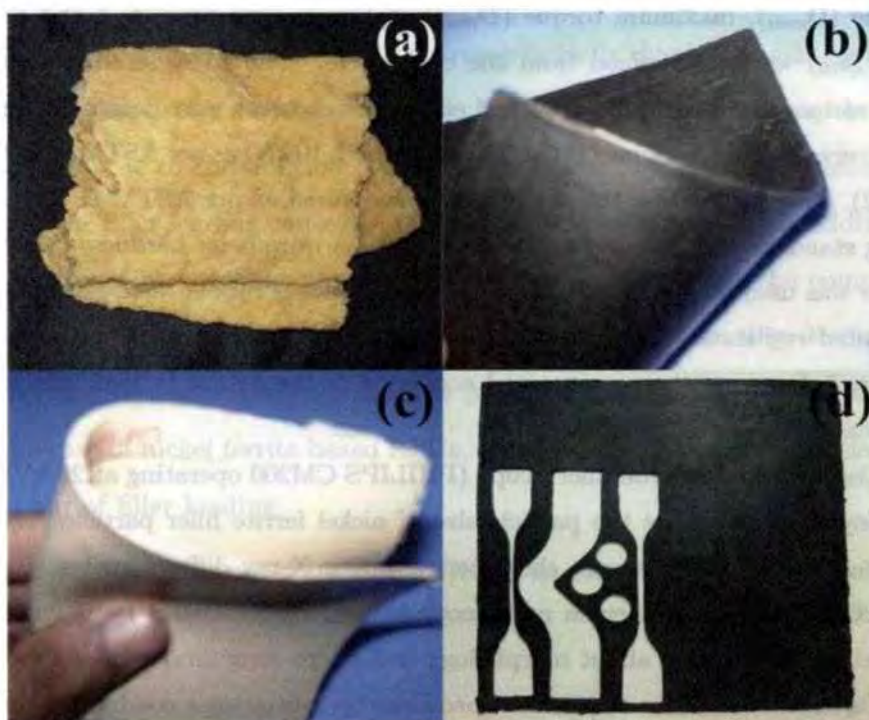
Figure 7.2: (a) Raw natural rubber, (b-d) moulded composite sheets

The mixed compounds were matured for a period of 24 h and the cure characteristics were determined at 423 K. The specimens for testing the physical properties were prepared by compression moulding on an electrically heated hydraulic press having 45 cm x 45 cm platens at a pressure of 140 kg/cm^2 in a standard mould for their respective cure times at 423 K. Natural rubber gum

vulcanisate was labelled as NR0 and RFCs with different percentage of nickel ferrite loading were labelled as NRNFx, where x represents phr of filler (x = 20, 40, 60, 80, 100 and 120 phr - parts per hundred parts by weight of rubber). Figure 7.2 shows the photographs of raw rubber as well as moulded composite sheets.

7.2.3 Characterization

The cure characteristics of the composites were determined using a rubber process analyser (RPA, Alpha-technologies 2000). The cure parameters such as minimum torque (D_{min}), maximum torque (D_{max}), optimum cure time (t_{90}) and scorch time (t_{10}) were determined from the cure curve. The stress-strain properties such as tensile strength, modulus and elongation at break were determined using a universal testing machine (UTM, Shimadzu SPL 10 kN) as per ASTM D 412-98a (2002). Tear strength of the samples were measured as per ASTM D 624(2000) using standard test specimens (Type C). Type A durometer hardness (Shore A) tester was used for measuring the relative hardness of rubber ferrite composites. Rebound resilience (%), the ratio of energy of the indenter after impact to its energy before impact, was measured according to the ASTM D 2632(2001) with vertical rebound resiliometer.

Transmission electron microscopy (PHILIPS CM200 operating at 20 kV) was employed to determine the particle size of nickel ferrite filler particles. Nickel ferrite as well as RFCs were characterized using X-ray diffractometer (Rigaku Dmax-2C). Scanning electron microscope (JEOL JSM - 6390LV) was employed to gather information about morphology and micro structural properties of the fractured surfaces of the tensile test specimens by sputtering a conducting coating over the surface. Thermogravimetric analysis (TGA) was carried out in a Perkin Elmer Pyrex Diamond 6 Instrument in a nitrogen atmosphere at a heating rate of 10 K/min from 313 to 873 K. The room temperature magnetic properties of the composites were studied using a vibrating sample magnetometer (EG & G PAR 4500). The dielectric properties of the RFCs were determined using HP 4285A LCR meter by placing the samples between two circular copper discs of 12 mm diameter to form a capacitor, held inside a homemade dielectric cell in the frequency range 0.1 to 8 MHz in steps of 100 kHz at different temperature

(303-393 K). Complex dielectric permittivity and magnetic permeability were determined with the help of a vector network analyzer in the S (2-4 GHz, Rohde & Schwarz-ZVB4) and X-band (8-12 GHz, Agilent-8510C) by employing the cavity perturbation technique [144, 145].

7.3 Cure characteristics of RFCs

Table 7.2 depicts the variation of cure parameters with loading of nanosized nickel ferrite filler. The cure time is found to decrease initially due to the adsorption of curatives over the active surface of the filler and at higher filler loading the cure time increases due to the dilution effects. Scorch time also showed a decreasing trend since the filler loading causes an increase in heat of mixing due to additional friction imparted by the filler particles [309]. This indicates that the composite takes less time to reach the onset of vulcanization with filler loading. Reduction of scorch time beyond a limit will lead to premature curing of the compounds. But in the case of nickel ferrite based RFCs, the compounds are processable even with 120 phr of filler loading.

From t_{90} and t_{10}, the cure rate index (CRI) was determined using the relation [116]

$$CRI = \frac{100}{t_{90} - t_{10}} \tag{7.1}$$

Figure 7.3 shows the dependence of rate of cure reaction or CRI on the concentration of filler or rubber phase. CRI is found to increase initially with loading (upto 40 phr) suggesting that at lower loadings of nickel ferrite, the filler activates the cure reaction. At higher filler loadings there is a sharp decrease in CRI due to the reduction in the volume fraction of rubber phase.

Table 7.2: Cure characteristics of nickel ferrite filled natural rubber based rubber ferrite nanocomposites

Sample	t_{90} (min)	t_{10} (min)	D_{min} (dNm)	D_{max} dNm
NR0	11.43	5.43	0.11	3.00
NRNF20	8.98	4.04	0.19	3.48
NRNF40	7.87	3.16	0.19	3.70
NRNF60	7.83	2.55	0.16	3.19
NRNF80	14.82	1.84	0.25	2.75
NRNF100	17.65	1.25	0.39	2.90
NRNF120	19.64	1.26	0.22	3.26
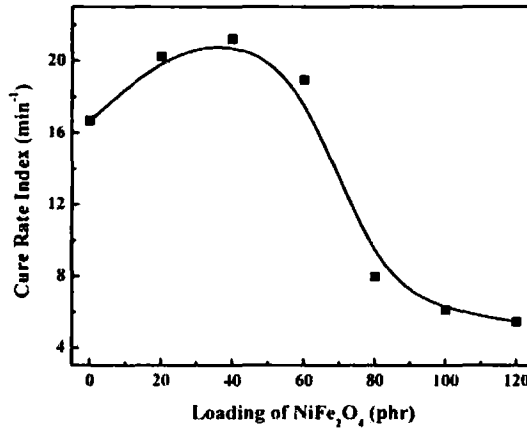
Figure 7.3: Dependence of CRI on nickel ferrite loading in RFCs

The torque values are a direct indication of the polymer-filler interactions. Minimum torque is a measure of the viscosity or stiffness of the compound. Although there is an increase in minimum torque value with loading of nickel ferrite, it does not affect the processability of the compound. The increase in viscosity of the compound with the incorporation of fillers is due to the occlusion of rubber within and between the filler aggregates and immobilization of a layer of elastomer at the surface of the filler [62, 307]. Maximum torque gives information regarding the shear modulus of the fully vulcanized rubber at the vulcanisation temperature. In RFCs, the maximum torque does not decrease substantially because of the porous nature of nano sized filler particles. There is an increase in torque value for RFCs with 20 and 40 phr nickel ferrite loading, but at higher

loadings the maximum torque shows marginal decrease. These results points out that no strong chemical interactions between the filler and matrix takes place in the composite and hence matrix properties are not affected much.

7.4 Mechanical properties

Mechanical properties of the elastomer are a major concern in designing the composite materials for specific applications. Among the different ingredients in the composite, filler plays an important role in delivering the final vulcanizate properties. The filler can be either reinforcing or non-reinforcing, which is decided by the size, size distribution, shape as well as specific surface area [62, 310].
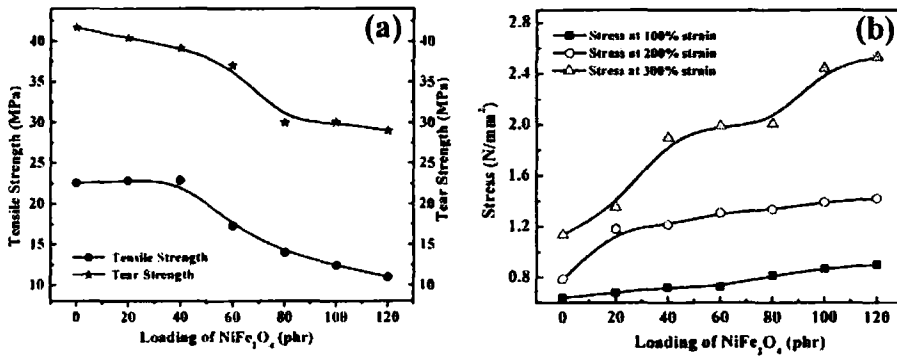
Figure 7.4: Variation of (a) tensile and tear strength and (b) stress at 100%, 200%, and 300% strain

Variation of tensile and tear strength with increase in nickel ferrite loading is depicted in Figure 7.4a. Tensile strength of RFCs is found to reduce with the addition of nickel ferrite above 40 phr. The decrease in tensile strength at higher loadings is due to filler agglomeration and lower volume fraction of rubber. Filler reduces the effective cross-section of the matrix in the composite and they are unable to transfer the stress to the polymer matrix. Moreover, the adsorption of polymer molecular chains on the filler surface reduces the mobility of the polymer segments and results in a rubber shell on the filler surface. This reduced mobility and the rubber shell increase the polymer viscosity and hence the modulus. These factors lead to increase in internal stress at any given external load when

compared to that of the unfilled rubber. The microplastic deformation occurring around the filler particles facilitate damage of the material at lower external load, when compared to the gum vulcanisate. Tear strength (which is a measure of resistance to failure of a material when it is subjected to continuous stretching) is found to decrease with filler loading. For the unfilled rubber tear strength is 41.6 MPa which decreased to 29 MPa with the addition of 120 phr nickel ferrite nanoparticles (30% decrease is noticed). The inclusions of nickel ferrite nanoparticles in between the polymeric chains create stress. Filler loading thus increases the modulus at 100%, 200% and 300% elongations (Figure 7.4b), indicating increase in elasticity of RFC with the incorporation of ferrite nanoparticles.
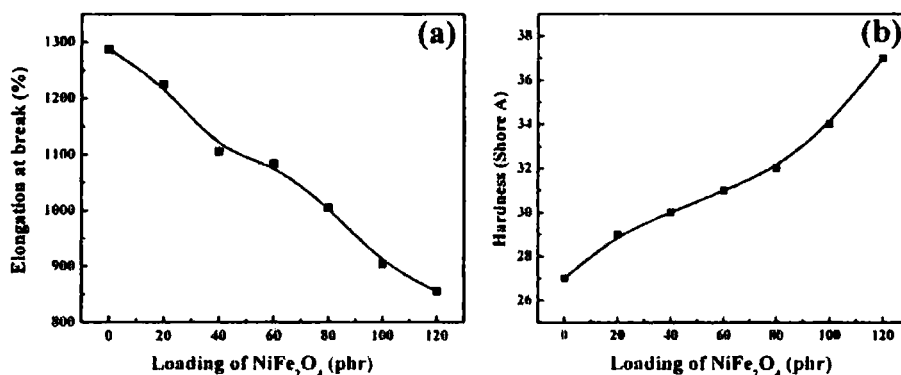
Figure 7.5: Variation of (a) elongation at break, and (b) hardness with filler loading

Elongation at break showed a decreasing trend (Figure 7.5a). Although it is reported that finite size filler can improve the stress bearing capacity of the filler polymer interface, at higher volume fraction of the filler, the interaction between the filler and polymer decreases. This decrease in the elongation at break indicates a reduction in the stress bearing capacity of the composite. The hardness and rebound resilience of the RFCs were measured using standard test methods [62, 110, 111, 311]. Hardness (which is a measure of modulus at low strains) of RFC's is found to increase with loading due to the decrease in mobility of the elastomer matrix (Figure 7.5b).
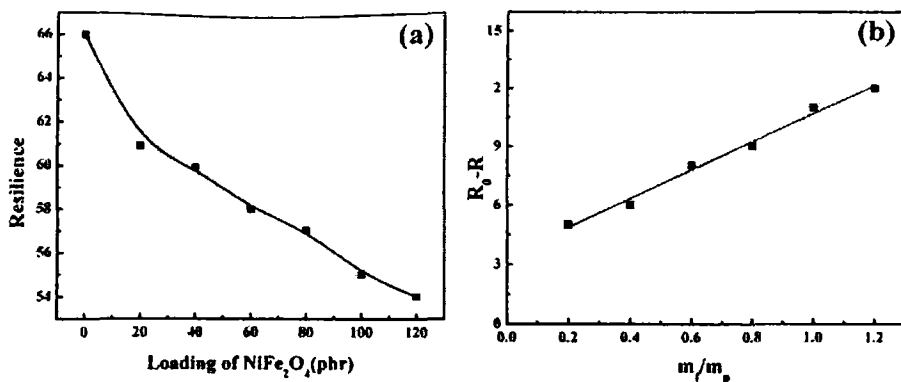
Figure 7.6: (a) Variation of resilience with filler loading, and (b) R_0-R vs m_f/m_p curve

The variation of resilience showed a decreasing trend (Figure 7.6a), which are on expected lines. The filler restricts the mobility and deformability of the matrix macromolecules. The decrease in rebound height with filler loading is related to the mass of the filler (m_f) and polymer (m_p) given by

$$R_0 - R = A\frac{m_f}{m_p} \tag{7.2}$$

where R_o is the rebound height of the gum vulcanisate and R is that of the RFC. From the R_0-R vs m_f/m_p curve, slope of the straight line obtained is 7.28 which is a characteristic constant of the filler (Figure 7.6b).

Although there is a deterioration in the mechanical properties, the composites are not demerited for its elastic applications with the present properties. The obtained physicomechanical properties are adequate for the fabrication of flexible absorber materials with natural rubber as base matrix that has an inherent shock absorbing property. This justifies the preparation of RFCs for static applications from the available base material (NR).

7.5 Structure and morphology

XRD pattern of $NiFe_2O_4$, NRNF80 and NR0 are depicted in Figure 7.7. The characteristic diffraction peaks of $NiFe_2O_4$ (ICDD file No. 01-74-2081) observed in the nickel ferrite powder and composite confirms the formation of pure inverse

spinel structure of the nickel ferrite filler material. From the XRD pattern, average particle size was evaluated using Debye Scherrer's formula [118] and is found to be 32 nm. Diffraction peaks found in NR0 (marked as '*' in Figure 7.7c) are emanating from the unreacted curatives present in the composite. These peaks disappear at higher filler concentration (Figure 7.7b), since characteristic peaks of crystalline nickel ferrite becomes more prominent.
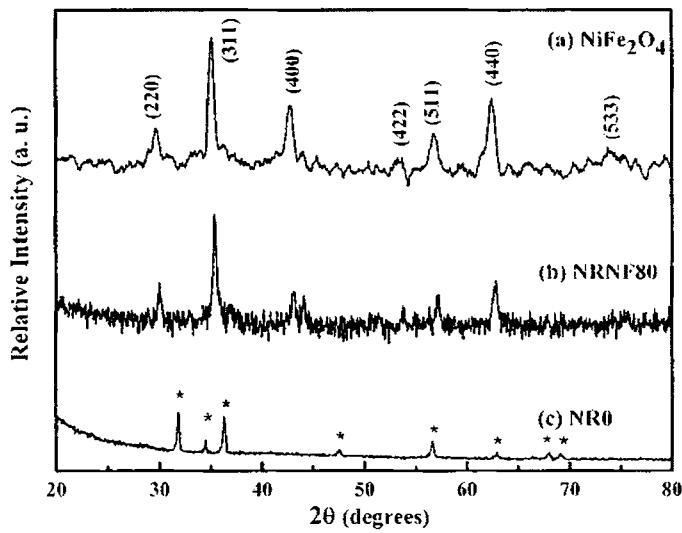
Figure 7.7: X-ray diffraction pattern of (a) $NiFe_2O_4$, (b) NRNF80, and (c) NR0

Size of nickel ferrite particles was determined from the transmission electron micrograph (Figure 6.3). From the normalized Gaussian fit of size distribution, an average particle size of 35 nm was obtained. This is consistent with the particle size estimated from XRD pattern.

Figure 7.8 shows the SEM images of the tensile fracture surfaces of RFCs at different loadings. The large smooth area in NR0 (Figure 7.8a) can be compared with that of the nickel ferrite grains seen in the rough surfaces of RFCs. The images clearly show two distinguishable regions. dark regions is the matrix while the bright patches are the regions of filler particles dispersed in the matrix. The morphology of the composites at different filler loading in the rubber composites indicates the homogenous mixing of the fillers in the composite.
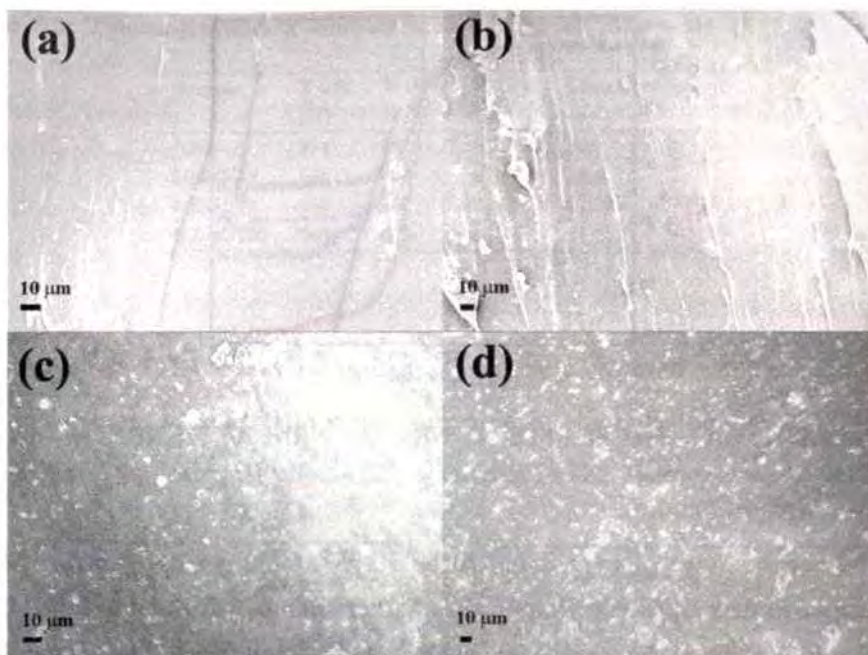
Figure 7.8: SEM images of RFCs (a) NR0 (b) NRNF20 (c) NRNF80 and (d) NRNF120 (Scalebar=10 μm)

At lower loadings (20 phr), rough surfaces with few aggregates due to better rubber-filler interaction is observed. At higher loadings there are filler agglomerations in the composite (seen as bright spots), which may be the reason for the reduction of mechanical properties. Absence of voids around the particles indicates the strong interfacial interaction between the nanoparticles and rubber. This has an important effect on transfer of the local stress [312].

7.6 Thermal studies

The thermal degradation of the cured RFCs were investigated by analyzing the TGA curves. The degradation was recorded when the mass of the sample decreased with temperature. The TGA curves depicted in Figure 7.9 displayed a single step degradation process in all the samples.
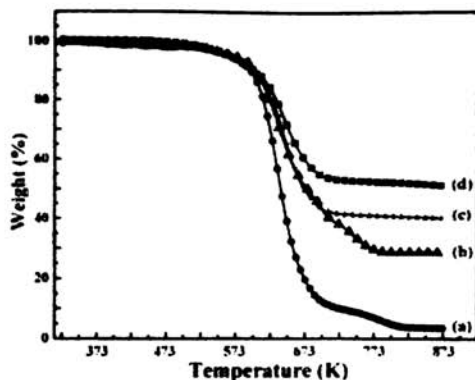
Figure 7.9: TGA curves of RFCs (a) NR0, (b) NRNF20, (c) NRNF80, and (d) NRNF120

The nanocomposites were found to be stable at temperatures below 573 K and began to decompose at temperature higher than 573 K. The weight loss at 873 K is indicative of the residue left in the rubber composites. The temperature at 5% (T-5%), 10% (T-10%) and 30% (T-30%) degradation are given in Table 7.3. T-30% increased from 622 to 650 K with 120 phr loading of nickel ferrite, which confirms the improvement of resistance to thermal degradation. This is due to the presence of metal oxide in the composite which have high thermal stability and can withstand high temperatures ($\sim$ 1173 K). The results reveal that incorporation of nickel ferrite nanoparticles in a rubber matrix can improve the thermal resistance of the RFCs.

The residual char yield at 873 K (which is the fraction of nonvolatile material at 873 K) increases with loading when compared to gum vulcanisate. The formation of char could hinder the out-diffusion in the rubber composites. Therefore, the increase of the char can improve the thermal degradation resistance of RFCs. The enhancement in thermal stability with increase in nickel ferrite nanoparticles in NR evidenced from our study is consistent with earlier reports [313].

7.7   Magnetic properties

The room temperature hysteresis curve of nickel ferrite and RFCs are shown in Figure 7.10a. For nickel ferrite, the hysteresis loop parameters like saturation magnetization (M_s), coercivity (H_c) and magnetic remanence (M_r) are found to

Table 7.3: Thermogravimetric analysis of rubber ferrite composites

Sample	T-5% (K)	T-10% (K)	T-30% (K)	Char Residual at 873 K
NR0	554	595	622	3.5
NRNF20	576	601	636	29.5
NRNF80	**562**	**599**	**641**	**40.5**
NRNF120	569	602	650	51.7

be 44.1 emu/g, 111 Oe and 6.3 emu/g, respectively. A lower value of saturation magnetization of nickel ferrite when compared to the bulk (56 emu/g)[314] can be attributed to finite size effects [29] occurring in the nanoregime.
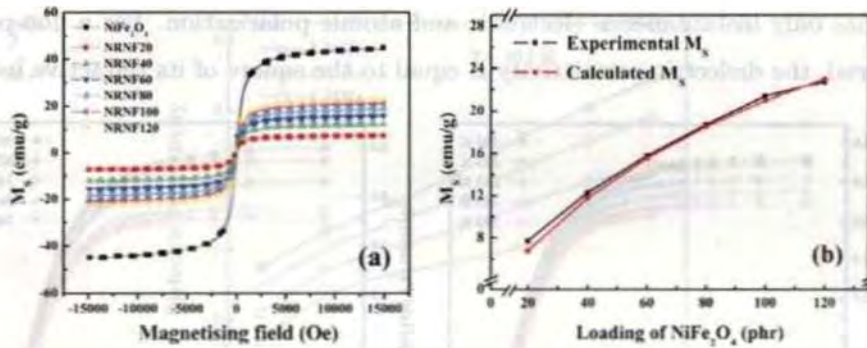
Figure 7.10: Room temperature M-H curve for (a) $NiFe_2O_4$ and RFCs with different loading of nickel ferrite. (b) Variation of M_s with nickel ferrite loading in RFCs

The saturation magnetizations of RFCs are calculated using simple mixture equations [315]

$$M_{composite} = \frac{M_{filler} \times m_{filler}}{m_{composite}} \tag{7.3}$$

where M_{filler} and $M_{composite}$ are the saturation magnetization of the filler and composite respectively. Here $m_{composite}$ is the mass of the composite and m_{filler} the mass of the filler. The calculated M_s is found to be in good agreement with the experimental values as shown in Figure 7.10b. This indicates the non interacting nature of filler with the matrix.

7.8   Dielectric properties

Dielectric dispersion is a cumulative effect of several factors (amount, type and composition of filler; the temperature, frequency, applied voltage, humidity as well as pressure applied during the measurement time) and a consequence of different polarization mechanisms (electronic, ionic, dipole and interfacial polarizations), depending on the frequency of operation.

7.8.1   Dependence of dielectric permittivity of RFCs on frequency

Figure 7.11 (a-d) depicts the variations of dielectric permittivity of RFCs with frequency at temperatures ranging from 303 to 393 K. NR is a non-polar material and has only instantaneous electronic and atomic polarization. For a non-polar material, the dielectric permittivity is equal to the square of its refractive index.
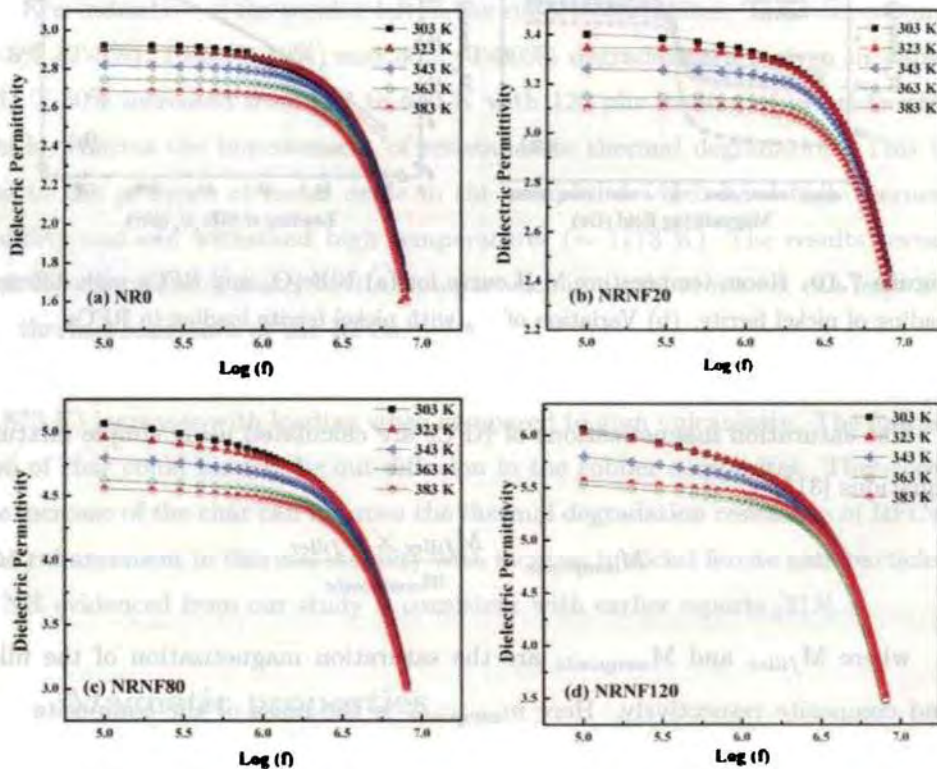
Figure 7.11: Variation of dielectric permittivity with frequency (a) NR0, (b) NRNF20, (c) NRNF80, and (d) NRNF120

NR possesses a refractive index of 1.59 and has a theoretical dielectric permittivity of 2.53 [316]. The experimentally determined room temperature dielectric permittivity of NRNF0 is found to be 2.91 (at f = 0.1 MHz). Deviation from the theoretical value may arise due to the presence of curatives in the gum vulcanizate. Dielectric permittivity decreases rapidly with increasing frequency towards high frequencies. The large value of dielectric permittivity at lower frequencies is attributed to the heterogeneity in the composite [317, 318] which gives rise to interfacial polarization. A summary of room temperature plots of RFCs at different loadings of nano filler is given in Figure 7.12. Similar behavior is observed for all frequencies (2, 4, 6 and 8 MHz). The dielectric permittivity is found to increase with loading while it decreased with increasing frequency.
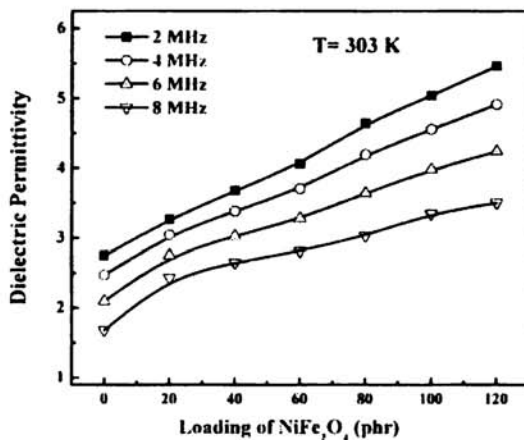
Figure 7.12: Variation of dielectric permittivity with loading of nickel ferrite in the RFCs at 303 K for different frequencies

The electronic polarizations in materials have a relaxation time of 10^{-14}s, and so it will not contribute to the polarization mechanism at radio frequencies. The main mechanism here would therefore be the interfacial polarization. As the frequency of the applied electric field is increased, the orientational polarisation becomes out of phase with the applied field. So, the dipolar motion can no longer follow the rapid vibration in the electric field. Hence the dielectric permittivity of the polymeric materials decreases with increase in applied frequency. This behavior of complex dielectric permittivity ($\epsilon = \epsilon' - j\epsilon''$) can be understood from the Debye model for dielectric relaxation (derived on a molecular basis), given by

$$\epsilon = \epsilon_\infty + \frac{\epsilon_o - \epsilon_\infty}{1 + i\varpi\tau} \qquad (7.4)$$

where ϖ is the angular frequency, ϵ_o is the static dielectric permittivity and ϵ_∞ is the dielectric permittivity at infinite frequency. The real (ϵ') and imaginary (ϵ'') part of dielectric permittivity is given by the relation [282]

$$\epsilon' = \epsilon_\infty + \frac{\epsilon_o - \epsilon_\infty}{1 + (\varpi\tau)^2} \qquad (7.5)$$

$$\epsilon'' = \frac{(\epsilon_o - \epsilon_\infty)\varpi\tau}{1 + (\varpi\tau)^2} \qquad (7.6)$$

Accordingly, the dielectric permittivity decreases with increase in frequency and this decrease is more pronounced at higher frequencies, which is in accordance with the Maxwell-Wagner theory of interfacial polarization and Koop's phenomenological model [282, 286]. As the frequency of applied field increases, interfacial polarization decreases reducing the dielectric permittivity. Thus, by varying the percentage of nickel ferrite alone, the dielectric permittivity of RFCs could be tuned (2.85-6).

7.8.2   Dependence of dielectric permittivity on temperature

Investigating the temperature dependence on the dielectric permittivity of RFCs, it is seen that there is a gradual decrease with temperature (Figure 7.13). Two competing mechanisms namely segmental mobility and thermal expansion of the polymeric material come into play with increase in temperature. The former tends to increase the permittivity while the later reduces it.

At high temperatures thermal expansion occurs in the rubber composite and the ratio of the number of molecules to the effective length of the dielectric diminishes leading to a decrease in effective density of the dielectric material. At this instance, it is to be noted that the linear thermal expansivity of NR is 220 x 10^{-6}/K [62] and hence its volume expansion is 660 parts per million per K. This in turn affects the measurement conditions by increasing the thickness of the formed capacitor, thereby reducing the dielectric permittivity. Differential thermal expansion between the filler and matrix and the resultant disruption of

filler clusters is also one of the reasons for reducing dielectric permittivity with temperature [319].
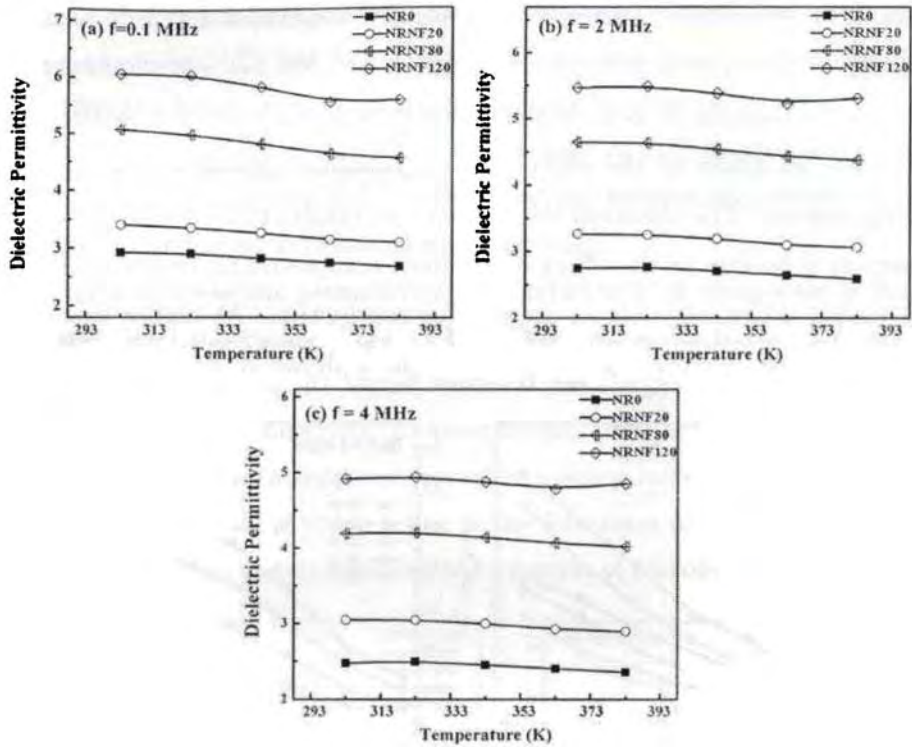
Figure 7.13: Variation of dielectric permittivity of RFCs with temperature at (a) 0.1MHz, (b) 2MHz, and (c) 4MHz

7.8.3 Frequency, loading and temperature dependence on the ac conductivity of RFCs

Different theories namely conduction path theory, tunnel effect theory or electric field radiation theory are employed to explain the electrical conduction in composite materials. The conduction in RFCs largely depends on the type and amount of filler inclusions. The ac conductivity of the samples were evaluated using the relation

$$\sigma_{ac} = 2\pi f \tan \delta \epsilon' \epsilon_o \tag{7.7}$$

where 'f' is the frequency. $\tan \delta$ is the dielectric loss factor, ϵ' is the dielectric permittivity of the medium and ϵ_o is the dielectric permittivity of free space.

The frequency dependence on the ac conductivity of RFCs with different loading of nickel ferrite nanoparticles in the temperature range 300-390 K are plotted in Figure 7.14. Polymeric materials are usually insulators and practically no conductivity is observed in unvulcanized elastomer. NR being a semicrystalline polymer can be thought of as a continuous matrix of amorphous polymer whose properties are modified by the short range crystalline regions which act as the reinforcing centers. The observed low value of ac conductivity in the vulcanized elastomers may be due to the effect of different compounding ingredients added to it for curing which may act as carriers for conduction. At higher frequencies the ac conductivity is increased as seen from plots shown in Figure 7.14a-c.
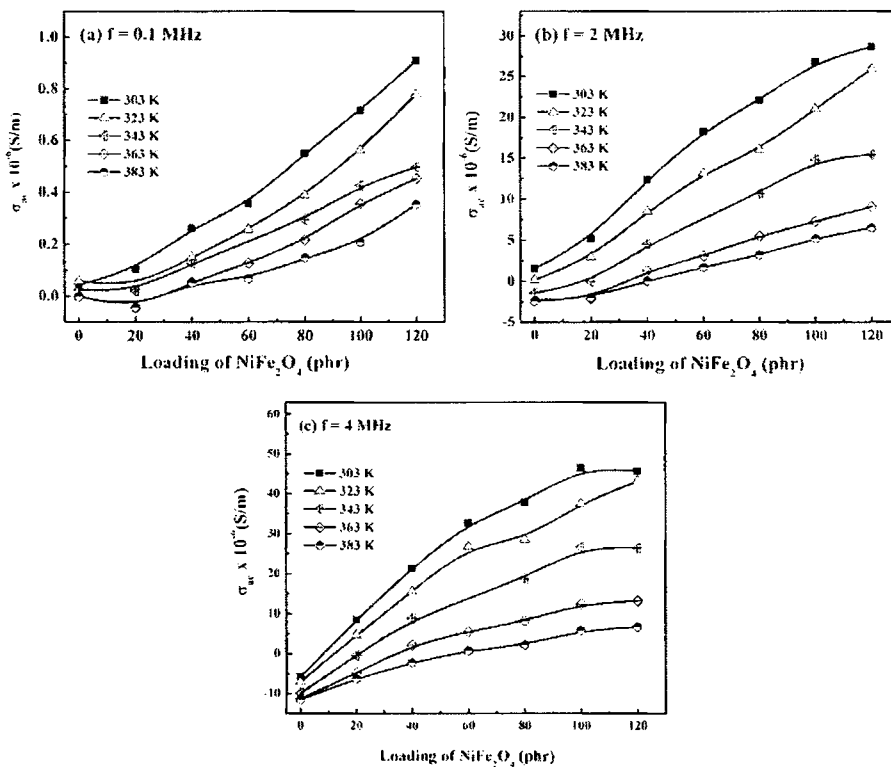
Figure 7.14: Dependence of ac conductivity with filler percentage at different frequencies (a) 0.1 MHz, (b) 2 MHz, and (c) 4 MHz

In the RFCs, the ac conductivity is found to increase with increase in loading of nickel ferrite filler (Figure 7.14) for all frequencies measured. If the conduction is ionic, ion mobility through the crystalline regions will be low and if the

conduction is electronic, the crystalline-amorphous interface will act as tapping regions. This is similar to Maxwell-Wagner two layer models [273, 286, 287]. The hopping of electrons between Fe^{2+} and Fe^{3+} ions on octahedral site and the hole hopping between Ni^{2+} and Ni^{3+} ions in the B site contribute to the conduction in nickel ferrite. At low frequencies, the grain boundaries are more active and hence hopping of electrons between $Fe^{2+} \leftrightarrow Fe^{3+}$ is less. At high frequencies conducting grains are more active and $Fe^{3+} \leftrightarrow Fe^{2+}$ hopping frequencies increase. Hence an increase in conduction is observed with frequency.

Similar to dielectric permittivity, ac conductivity in composites is found to decrease with temperature (Figure 7.15). This may be due to the thermal expansion of polymer matrix. At higher temperatures the polymer density is reduced which reduces the conductivity. At lower loading there are only marginal changes in ac conductivity with temperatures while a sharp increase in the conductivity is observed with loading which is due to the formation of short range conductive paths in the rubber matrix towards the formation of percolation conduction path.
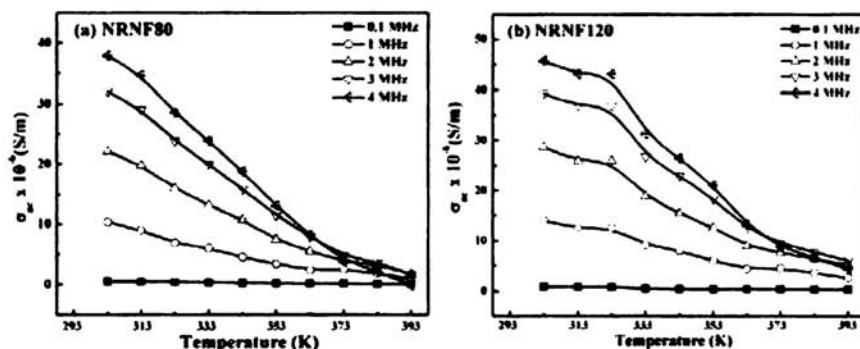
Figure 7.15: Effect of temperature on the ac conductivity at different frequencies for the RFCs (a) NRNF80, and (b) NRNF120

7.9 Microwave absorbing properties

The flexible nanocomposite samples prepared in the form of sheets were cut into rectangular strips of dimension ~ 1 mm x 2 mm x 4 cm. Complex dielectric permittivity ($\epsilon' - i\epsilon''$) and magnetic permeability ($\mu' - i\mu''$) were determined by measuring the shift in resonant frequency and the change in quality factor of a

perturbed microwave cavity by inserting a sample at the maximum electric and magnetic field positions respectively.

7.9.1 Complex dielectric permittivity of the composite

The variation of complex dielectric permittivity of RFCs at different frequencies in the S-band is shown in Figure 7.16. The dielectric permittivity and dielectric loss are found to increase with filler loading. Different types of polarization mechanisms (electronic/ionic/molecular/interfacial)contribute to dielectric permittivity of materials [320]. Electronic and atomic/ionic polarizations occur at optical frequencies [321] while dipolar and interfacial polarizations play a main role at lower frequencies. Since natural rubber is a non-polar material, nickel ferrite plays a prominent role in deciding the permittivity of the composites.
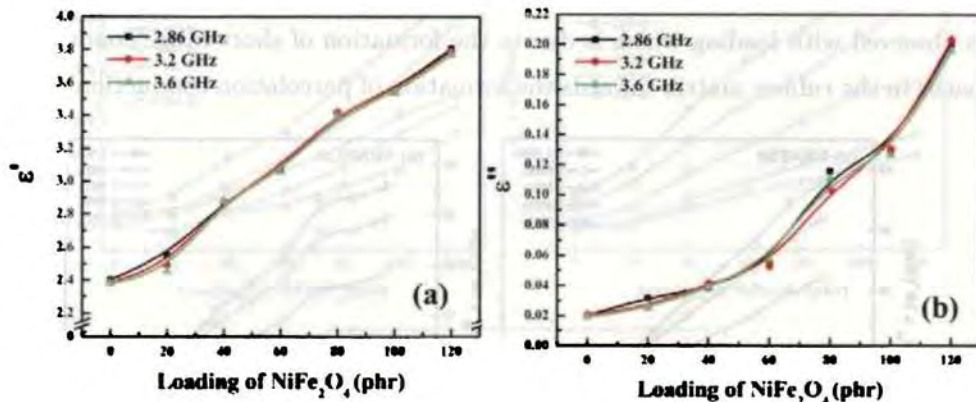
Figure 7.16: Variation of (a)ϵ', and (b)ϵ'' with loading of nickel ferrite

Iron and nickel ions in $NiFe_2O_4$ form electric dipoles with the surrounding O^{2-} and contribute to ϵ' through dipolar polarization. As the weight percentage of nickel ferrite in rubber matrix increases more number of dipoles become available in the composite. This enhances the dielectric permittivity of the composite with higher content of nickel ferrite.

Incorporation of nickel ferrite nanoparticles (NRNF120) increased the dielectric permittivity of the elastomer from 2.38 to 3.8 (Figure 7.16a). This is similar to the results reported in ferrite/EPDM rubber composite [307, 322]. In addition to dipolar polarization, interfacial polarization as well as hopping of electrons

within the grain and across the grain boundaries, contribute to complex dielectric permittivity [323, 324].
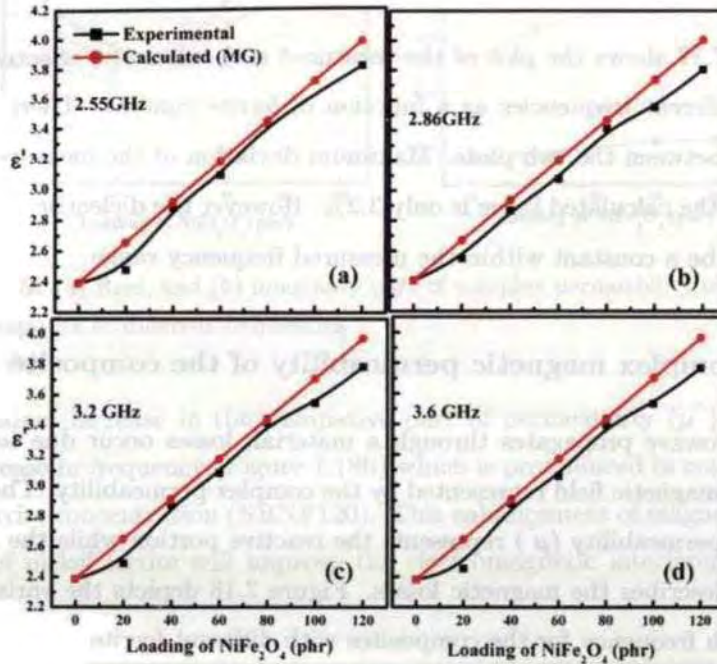
Figure 7.17: Measured and calculated (MG) effective permittivity of rubber ferrite composites at different frequencies (a) 2.55 GHz, (b) 2.86 GHz, (c) 3.2 GHz, and (d) 3.6 GHz

The effective dielectric permittivity (ϵ_{eff}) of the composites is calculated from the two component structure dependent Maxwell-Garnett (MG) mixture equation given by [307, 325],

$$\epsilon_{eff} = \epsilon_m \frac{2\epsilon_m(1 - \nu) + \epsilon_i(1 + 2\nu)}{\epsilon_m(2 + \nu) + \epsilon_i(1 - \nu)} \tag{7.8}$$

Here ϵ_{eff} is the effective permittivity of the composite, ϵ_m is the permittivity of the insulating host medium (NR), ϵ_i is the permittivity of the inclusion (nickel ferrite) and ν is the volume fraction of the inclusion (nickel ferrite). When the permittivity of the inclusion is much higher than the medium, MG theory breaks for all frequencies. By factorizing ϵ_i and applying the condition $\epsilon_i \gg \epsilon_m$, we have [326]

$$\epsilon_{eff} = \epsilon_m \frac{(1 + 2\nu)}{1 - \nu} \qquad (7.9)$$

Figure 7.17 shows the plot of the measured and calculated effective permittivity at different frequencies as a function of ferrite content. There is a good agreement between the two plots. Maximum deviation of the measured permittivity from the calculated value is only 3.2%. However the dielectric permittivity is found to be a constant within the measured frequency range.

7.9.2 Complex magnetic permeability of the composite

When microwave propagates through a material, losses occur due to the time dependent magnetic field represented by the complex permeability. The real part of relative permeability (μ') represents the reactive portion while the imaginary part (μ'') describes the magnetic losses. Figure 7.18 depicts the variation of μ' and μ'' with frequency for the composites with different ferrite concentrations.

The permeability is found to decrease with frequency and increase with filler loading. Permeability dispersion observed in ferrite is due to two magnetization processes: domain wall motion and spin rotation [179]. The permeability μ can be expressed as $\mu = 1 + \chi_{spin} + \chi_{domain}$. But intrinsic rotational susceptibility (χ_{spin}) and domain wall susceptibility (χ_{domain}) in turn is related to the square of saturation magnetization (M_s) [180]. Thus permeability has a direct dependence on M_s. Hence higher value of M_s is one of the reasons for improved permeability for composites with higher filler content. For single domain particles (less than their critical diameter), the main contribution for increased permeability is solely from spin rotation, while the domain wall motion can be neglected. However the composites are found to have lower permeability values when compared to that of pure ferrites. This is because the ferrite grains are embedded in rubber matrix. The nonmagnetic rubber matrix causes a discontinuity in the composite giving way to demagnetizing fields, thus reducing the permeability [326] at low filler content.
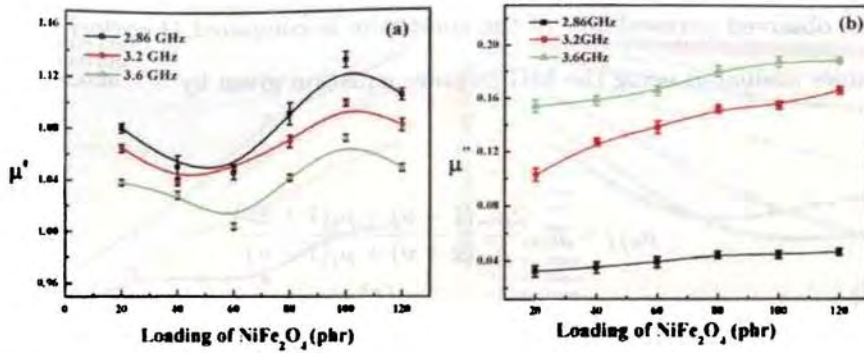
Figure 7.18: (a) Real, and (b) imaginary part of complex permeability of nickel ferrite rubber composite at different frequencies

A gradual increase in the dissipative part of permeability (μ'') is observed with increase in frequency (Figure 7.18b) which is pronounced in composite with higher ferrite concentration (NRNF120). This enhancement of magnetic loss with loading of nickel ferrite will improve the electromagnetic interference shielding effects.
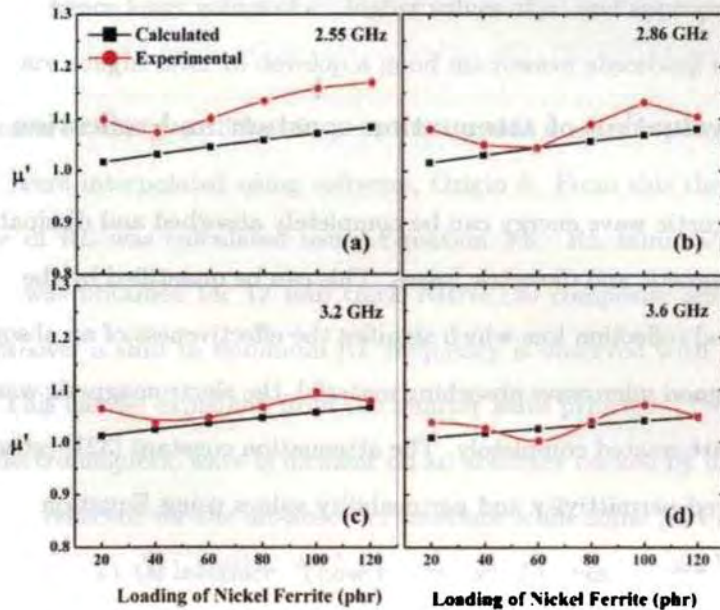
Figure 7.19: Measured and calculated (MG) effective permeability of rubber ferrite composites at different frequencies (a) 2.55 GHz, (b) 2.86 GHz, (c) 3.2 GHz, and (d) 3.6 GHz

The observed permeability of the composite is compared (Figure 7.19) with the values evaluated using the MG mixture equation given by

$$\mu_{eff} = \mu_m \frac{2\mu_m(1 - \nu) + \mu_i(1 + 2\nu)}{\mu_m(2 + \nu) + \mu_i(1 - \nu)} \qquad (7.10)$$

Here μ_{eff} is the effective permeability of the composite, $\mu_m(=1)$ is the permeability of the host medium (natural rubber), μ_i is the permeability of the inclusion (nickel ferrite) and ν is the volume fraction of inclusion (nickel ferrite). The discrepancy between the measured and calculated values is attributed to magnetic interactions occurring between the grains of nickel ferrite. This interaction increases with loading of filler. Also, factors like shape of inclusions, orientation and alignment of moments of inclusions and morphology of the composite affect the frequency response of permeability in a composite [327].

7.9.3   Evaluation of attenuation constant and reflection loss

Electromagnetic wave energy can be completely absorbed and dissipated to heat through magnetic and dielectric losses. This can be quantified by the attenuation constant and reflection loss which signifies the effectiveness of an absorber material. For a good microwave absorbing material, the electromagnetic wave entering should be attenuated completely. The attenuation constant [321] estimated from the measured permittivity and permeability values using Equation 3.2 is plotted in Figure 7.20a.

It is to be noted that at 2.55 GHz the attenuation constant is only 1.4 for NRNF20 whereas a maximum value of $\sim$18 is obtained for NRNF120 at 3.6 GHz. This suggests the improvement in shielding of the RFCs at higher frequencies.
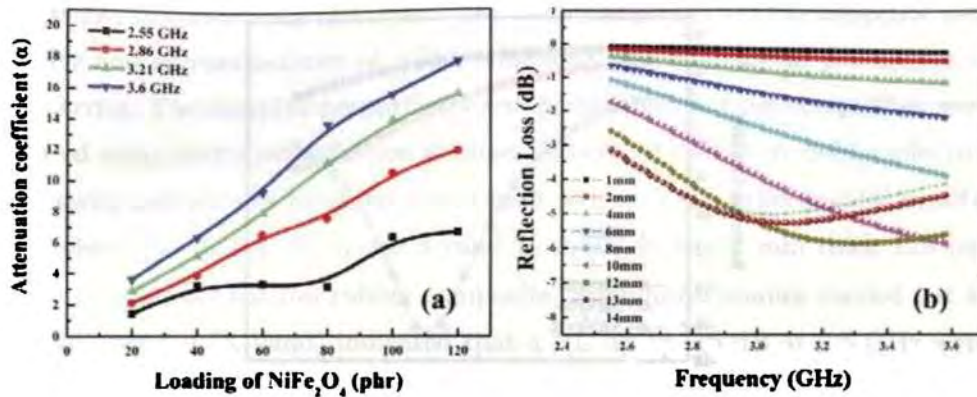
Figure 7.20: (a) Variation of attenuation constant with filler concentration, and (b) variation of reflection loss with thickness in the S-band

As discussed earlier, to obtain low reflection, μ'/ϵ' should be close to unity. But μ' is less than ϵ' at high frequencies constraining the choice of ideal absorber material for the frequency of interest. Improving permeability at high frequencies is difficult and hence lower values of ϵ'', higher values of μ'' and appropriate values of μ' and ϵ' are sought after to develop a good microwave absorbing material.

The measured complex dielectric permittivity and magnetic permeability in the S-band were interpolated using software, Origin 8. From this the frequency dependence of RL was calculated using Equation 3.3. RL minima of -5.9 dB at 3.2 GHz was obtained for 12 mm thick NRNF120 composite sheet (Figure 7.20b). Moreover a shift in minimum RL frequency is observed with increase in thickness. This can be explained from the quarter wave principle [237]. That is, when the electromagnetic wave is incident on an absorber backed by metal plate, a part of it is reflected for the air-absorber interface while some part is reflected from the absorber-metal interface. These two reflected waves are out of phase by 180° and cancel each other at the air absorber interface when the quarter wave thickness criteria [237] is satisfied, given by Equation 3.5. Since $t \propto 1/f$, the above criterion is satisfied at increased sample thickness for lower frequencies.
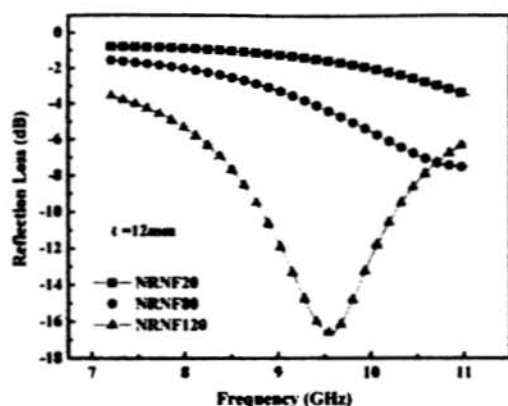
Figure 7.21: Reflection loss evaluated for NRNF20, NRNF80, and NRNF120 with a sheet thickness of 12 mm in the X-band

The X-band permittivity and permeability of selected composites were measured and their corresponding reflection losses were simulated for a thickness of 12 mm. ϵ' is found to be 2.4, 2.9 and 3.7 while ϵ'' is obtained as 0.02, 0.07 and 0.22 respectively for NRNF20, NRNF80 and NRNF120. The measured value of μ' is 1.02, 1.04 and 1.06 whereas μ'' is 0.04, 0.08 and 0.14 respectively for NRNF20, NRNF80 and NRNF120. The reflection loss of the composite is found to depend on the filler concentration. Simulations gave a minimum reflection loss of -16 dB at 9.5 GHz for NRNF120 with an absorber thickness of 12 mm (Figure 7.21). As reported in literature[323], the minimum reflection frequency is found to shift towards lower frequency region with the increase in filler content. Tailoring the complex dielectric permittivity and magnetic permeability of the composites will aid in obtaining improved microwave absorption in the materials based on NR.

7.10 Conclusion

RFCs with different loadings of nanosized nickel ferrite in NR were prepared and moulded into rectangular sheets. Their processability as well as mechanical, thermal, structural and dielectric properties were examined. Though there was a slight deterioration in the reinforcing properties of the composites, the RFCs retained the physicomechanical properties of NR. Filler dispersion in the composite was observed to be uniform. XRD pattern of nickel ferrite and RFCs indicate

phase purity of constituent materials. The electrical properties like dielectric permittivity and ac conductivity of RFCs enhanced with increase in percentage of nickel ferrite. The complex permittivity and permeability of the composites were measured using cavity perturbation method. Maxwell-Garnett model for effective permittivity and permeability was found to fit well with the experimental results. A minimum RL of -5.9 dB in the S-band is obtained for 12 mm thick 120 phr nickel ferrite loaded natural rubber composite. Simulation studies carried out at higher frequencies (X-band) indicated that a RL up to -16 dB at 9.5 GHz were obtained for 12 mm thick NRNF120 composite. These microwave characteristics combined with superlative mechanical properties of natural rubber are desirable for using RFCs as absorbers in the high frequency regime.

Chapter 8

Microwave absorbing properties of ferromagnetic metal/natural rubber nanocomposites

Nanoscale magnetic metal particles embedded in a flexible polymeric material like polyisoprene (natural rubber) permit tailoring of electromagnetic properties of the resulting nanocomposite. This chapter discusses the preparation and characterization of ferromagnetic metal natural rubber nanocomposites. Ferromagnetic metal nanoparticles of Fe, Co and Ni were prepared by the top-down method of high energy ball milling and then they were incorporated in a polymer matrix according to a specific recipe to obtain flexible magnetic nanocomposites. Their dielectric permittivity and magnetic permeability in the different microwave frequencies were investigated using a vector network analyzer by employing a cavity perturbation technique. The reflection losses of the composites with different absorber layer thicknesses were evaluated based on the model of a single layer absorber backed by a perfect conductor. The optimum thickness for a particular operating frequency is determined.

8.1   Introduction

With the proliferation of different communication gadgets and employment of very high frequencies in communication systems (RADAR, mobile phones, wireless LAN, Bluetooth etc.), electromagnetic interference [237, 328] has become a concern of legislators, planners as well as scientists. The development of cost effective flexible electromagnetic wave absorber is one of the alternatives before scientists and engineers in order to mitigate this man made menace [329].

Usually polymer composites are used as electromagnetic wave absorbers. They are made by the incorporation of metal particles or provided with an appropriate coating of metal, in order to tune the matching parameters for enhanced absorption. Once polymer volume predominates in the composite, the filler particles are insulated from one another and their mechanical properties follow those of polymer. But when the filler loading is high, microwave properties are enhanced but mechanical strength degrades. Hence a tradeoff between these two has to be made to obtain a flexible microwave absorbing material.

Natural rubber (NR) is a flexible dielectric material with good mechanical shock absorbing property. Incorporation of ferro/ferri magnetic particles in NR can impart both dielectric permittivity and magnetic permeability to the rubber composites [100, 325]. Magnetic metal inclusions can impart higher magnetic permeability and such metal/polymer composites are of significant interest to the scientific community when compared to conventional composites containing ferrites [325]. But high conductivity of metals limits their use for high frequency applications due to skin effects [159]. This can be overcome by size reduction of metal particles followed by surface modification or incorporation in a nonconducting medium [88, 302].

Emergence of nanotechnology has evolved novel methods of size reduction that has paved way for the fabrication of nanocomposites with superlative absorbing characteristics. Magnetic metal particles have a skin depth of few micrometers in the giga hertz (GHz) range [161, 330]. So reducing the particle size well below this scale and isolating them by an insulating material will help in suppressing the eddy current losses. Nanosized magnetic metal composites based on carbonyl iron[331], hollow nickel spheres [332, 333], Ni-Ag core shell structures[334] and

metal encapsulated in carbon nanotubes [146] have shown enhanced microwave absorbing properties. These magnetic nanostructures have limitations with regard to their scalability and cost.

Metal particles when subjected to high energy ball milling can transform to grains of few tens of nanometers [88] well below their skin depth. Here particle size is controlled by optimizing the duration, speed and medium of milling. Particles of appropriate sizes can thus be prepared and incorporated in to the host matrix to prevent further oxidation. Absorber layer thickness and bandwidth of absorption can be modelled as per the surface impedance equation. This chapter discusses the findings of such an investigation carried out on ferromagnetic metal/rubber nanocomposites.

8.2   Experimental

8.2.1   Synthesis

Ferromagnetic metal powders, Fe (S.D fine-CHEM LTD. BOISAR 401501, Iron (metal) powder, electrolytic-300 mesh LR, Product No.38601), Co(CDH extra pure >99.5%) and Ni (SRL Pvt Ltd, Nickel powder extra pure >99.5%) were subjected to high energy ball milling in a Fritsch Planetary micromill 'Pulverisette 7'. A milling medium of toluene was used to avoid contamination from the milling tools and to minimize the wear. The powder to ball mass ratio was maintained at 1:10. The milling speed was fixed at 500 rpm for 1 h. Earlier studies on ferromagnetic metal powder (α-Fe) [88] indicate that the maximum size reduction is attained during the initial stages of milling time and once an optimum size is attained, reduction in grain size is marginal even after prolonged milling. So the milling time was fixed for 1 h.

These powders were thoroughly characterized and then mixed with natural rubber (ISNR- 5 grade, supplied by Rubber Research Institute of India, Rubber Board. Kottayam) along with appropriate amounts of curatives in a Brabender Plasticorder (model: PL 3S) as per ASTM standards (D 3182-89 2001) according to a specific recipe (Table 8.1) developed by extensive experimental iterations. The samples were labelled as NR0 for gum (unfilled) NR while NRFe80, NRCo80

Table 8.1: Formulation of mixes for preparing ferromagnetic metal natural rubber nanocomposites

Ingredients (phr)	NR0	NRFe80	NRCo80	NRNi80
Natural rubber (ISNR-5)	100	100	100	100
Zinc Oxide	4	4	4	4
Stearic Acid	2	2	2	2
Triphenyl Quinone	1	1	1	1
CBS*	0.8	0.8	0.8	0.8
Filler	-	80 (Vol % 8.6)	80 (Vol % 7.5)	80 (Vol % 7.6)
Sulphur	2.5	2.5	2.5	2.5

*n-Cyclohexyl-2-Benzothiazyl Sulphenamide

Table 8.2: Cure characteristics of metal/rubber nanocomposites

Sample	Maximum torque (dNm)	Minimum torque (dNm)	Cure Time t_{90} (min)	Scorch Time t_{10} (min)	CRI (min^{-1})
NR0	3.001	0.11	11.4	5.4	33.1
NRFe80	4.007	0.14	5.9	2.0	38.0
NRCo80	3.308	0.15	6.9	3.2	51.5
NRNi80	4.050	0.13	8.5	5.1	30.2

and NRNi80 for 80 phr (parts per hundred parts by weight of rubber) of iron, cobalt and nickel nanoparticles filled NR composite respectively.

The compounds were kept to mature for 24 h. Optimum cure time at 150 °C for each samples were determined using rubber process analyzer (RPA, 2000-Alpha technologies). The cure characteristics of filled rubber compound vary with type, size and amount of filler loading [335]. Cure characteristics such as maximum torque, minimum torque, cure time (t_{90}), scorch time (t_{10}) and cure rate index (CRI) were determined prior to moulding of the mixture into sheets (Table 8.2).

The compounds were then compression moulded at 423 K for their respective cure times in an electrically heated hydraulic press. Optimizing the filler loading to 80 phr was done in order to meet the competing requirements of physicomechanical and magnetodielectric properties of the composite. Previous studies on ferrite nanocomposites based on NR have shown a decrease in the mechanical

properties at higher filler loadings, especially above 80 phr [135, 336]. This justifies the selection of the specific composition of filler loadings.

8.2.2 Characterization

Structural analysis of the samples were performed using X-ray diffractometer (Rigaku Dmax-C) using Cu Kα radiation ($\lambda = 1.5418$ Å). The surface morphology of the composites were observed using a field emission scanning electron microscope (FESEM, JSM-6335). Room temperature magnetic measurements of the filler as well as composites were carried out in a vibrating sample magnetometer (EG&G PAR 4500). Complex dielectric permittivity and complex magnetic permeability of the composites were determined by employing cavity perturbation technique using vector network analyzer (S-band: Rohde & Schwarz ZVB4 and X-band: Agilent 8510C). Rectangular strips of the metal rubber nanocomposites were punched out from the composite sheets with appropriate dimensions for characterization. They were then inserted into a rectangular cavity followed by noting the shift in resonant frequency and quality factor.

8.3   Structure and morphology

XRD pattern of 1h ball milled iron (Fe-1h), cobalt (Co-1h) and nickel (Ni-1h) powder are shown in Figure 8.1(a-c). The XRD peaks are compared with the standard values (ICDD file no.: bcc Fe: 85-1410, fcc Co: 15-0806, hcp Co: 05-0727 and fcc Ni: 04-0850). Fe particles are found to be crystalline with bcc structure while Ni particles possess fcc structure. The XRD pattern of cobalt indicates the presence of both fcc and hcp phase of cobalt in the sample (fcc indicated by '∗' and hcp by '#'). The average crystallite size were determined from the Debye Scherrer's formula [117, 118] and is found to be 17±3 nm, 19 nm and 20±4 nm while the lattice parameters were 2.867 Å, 3.511 Å and 2.85 Å for Fe-1h, Co-1h and Ni-1h respectively.
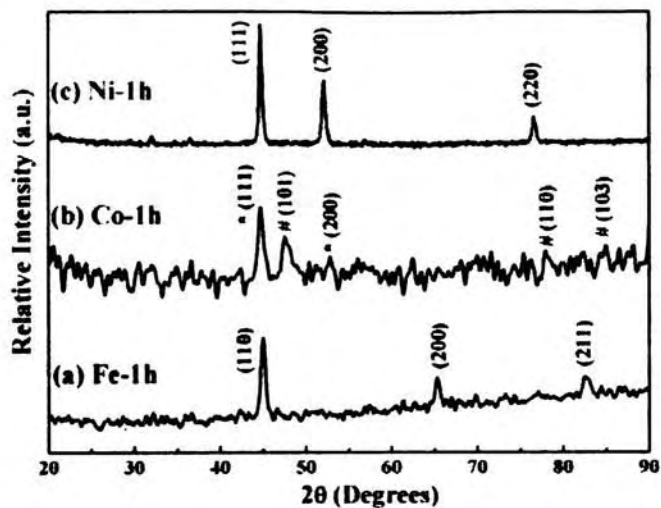
Figure 8.1: XRD pattern of 1 h ball milled metal powder (a) Fe-1h, (b) Co-1h, and (c) Ni-1h
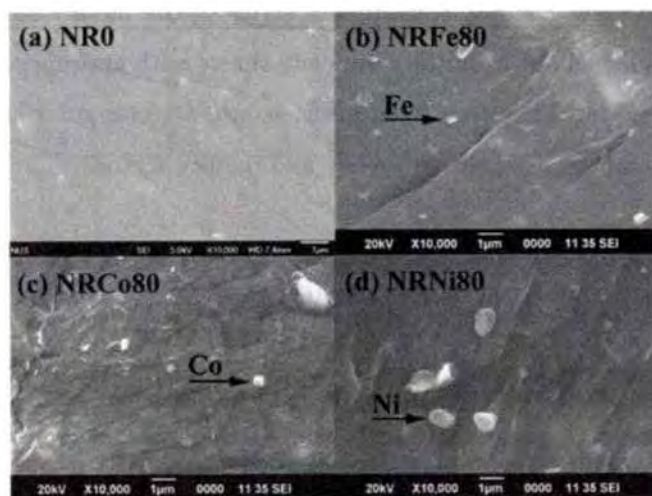
Figure 8.2: SEM images showing the morphology of metal rubber composites (a) NR0, (b) NRFe80, (c) NRCo80, and (d) NRNi80 (isolated grains in the rubber matrix are indicated by arrows)

SEM images of the fractured surface show large smooth area in NR0 when compared to the rough fractured surface of metal/rubber nanocomposites (Figure 8.2). Isolated metal particles are uniformly distributed in the rubber matrix and are indicated by arrows. The skin depths of Fe, Co or Ni are a few micrometers.

Table 8.3: Mechanical properties of metal/rubber nanocomposites

Sample	Tensile strength (MPa)	Tear strength (N/mm)	300% modulus (MPa)	Elongation at break (%)	Hardness (Shore A)	Resilience (%)
NR0	3.001	0.11	11.4	5.4	8.4	33.1
NRFe80	4.007	0.14	5.9	2.0	3.3	38.0
NRCo80	3.308	0.15	6.9	3.2	4.9	51.5
NRNi80	4.050	0.13	8.5	5.1	5.2	30.2

The images reveal that filler grains are far less than the size of their corresponding skin depth [161, 330] and are surrounded by insulating rubber matrix.

8.4 Physicomechanical properites

The properties and performance of a rubber product depend on many factors including the chemical nature of the rubber, the amount and kinds of ingredients incorporated into the rubber compound, processing and vulcanizing conditions, design of the product and service conditions. Among different ingredients, fillers play an important role in determining the final vulcanizate properties. Fillers can be either reinforcing or nonreinforcing. The crucial characteristics that decide the reinforcing capability of the fillers are size, shape, specific surface area and a combination of the size distribution and shape [62].

Mechanical properties namely tensile strength, tear strength, 300% modulus and elongation at break were determined using a Shimadzu, Universal testing machine at a cross head speed of 500 mm/min. Stress-strain measurements were carried out as per ASTM D 412-98a(2002). The hardness and resilience of the composites were also determined. The results are tabulated (Table 8.3). It can be seen that there is only a small change in the tensile as well as tear strength values with loading of 80 phr of ferromagnetic metal nanoparticles, retaining the mechanical properties of NR. 300% modulus as well as elongation at break values are found to increase. The hardness of the composite is improved while rebound resilience is found to decrease with filler incorporation.

8.5 Magnetic properties

The room temperature hysteresis loop of 1h ball milled metal powders and metal rubber nanocomposites (Figure 8.3) show typical ferromagnetic behaviour. The hysteresis loop parameters are given in Table 8.4. The magnetization values of Fe-1h, Co-1h and Ni-1h are lower than their corresponding bulk counterparts (Fe: 218 emu/g, Co: 161 emu/g, Ni: 54.4 emu/g) [2], which may be due to the finite size effects or formation of thin oxide layers by exposure to air. The saturation magnetizations of the metal/rubber nanocomposites are calculated using simple mixture equation given by 7.3. Here $m_{composite}$ (=190.3 g) is the mass of the composite while m_{filler} (=80 g) is the mass of the filler. The maximum deviation of the measured saturation magnetization from those calculated is 4.9%, indicating a good match between the two values. Thus, by knowing the filler magnetization, the magnetic properties of the metal/rubber nanocomposites can be engineered for obtaining the required properties.
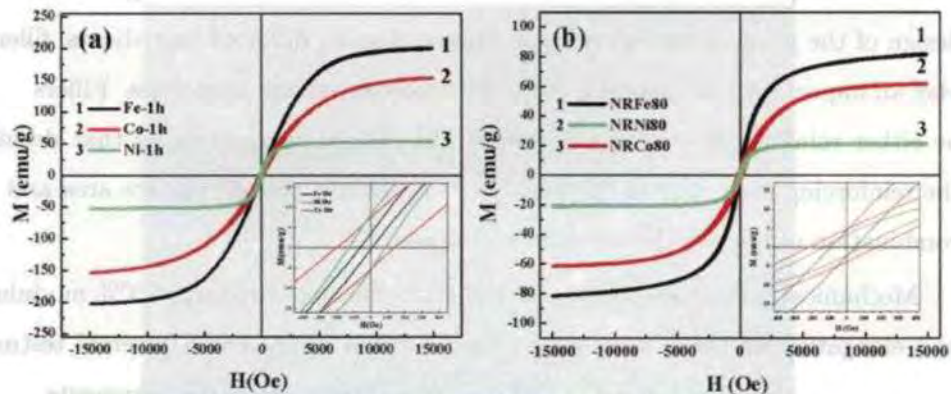
Figure 8.3: Room temperature hysteresis loop of (a) 1 h ball milled Fe/Co/Ni powder and (b) metal/rubber nanocomposites. Inset: Magnified view of M-H loop showing the coercivity of the samples

The coercivity of NRFe80, NRCo80 and NRNi80 are 68, 195 and 108 Oe respectively. The higher value of coercivity observed for NRCo80 is due to the large intrinsic magnetocrystalline anisotropy of cobalt particles [2] when compared to that of iron or nickel. Maximum saturation magnetization and least coercivity

Table 8.4: Observed and calculated magnetization of the composites

Filler	M_{filler} (emu/g)	Composite	M Calculated (emu/g)	M Experimental (emu/g)
Fe-1h	201.65	NRFe80	84.77	82.01
Co-1h	153.85	NRCo80	64.67	61.96
Ni-1h	52.84	NRNi80	22.21	21.13

are observed for NRFe80.

8.6 Microwave absorbing properties

Figure 8.4 (a, b) depicts the variation of real and imaginary part of complex dielectric permittivity of the metal/rubber nanocomposites at different frequencies (S and X-band). For all the three samples (NRFe80, NRNi80 and NRCo80), ϵ' is almost a constant while ϵ'' shows a gradual increase with increase in frequency. It is to be noted that the metal inclusions in an insulating material like NR increased the permittivity of the composite from 2.8 to 6.4 for NRFe80. In the case of NRCo80 and NRNi80, ϵ' is 5 and 4.5 respectively.

Enhancement of effective permittivity in the composite is due to interfacial polarization of free charges from the ultrafine conductive inclusions dispersed in a nonconducting matrix. When an electric field is applied, the free electrons in metal particles move apart and behave like electrically isolated charges near the interface [178, 337–339]. For the same amount of filler loading (in phr), the volume fraction of filler and the number of interfaces are more in NRFe80. This also contributes to the increased value of permittivity in NRFe80. The volume percentage of metal nanoparticles in the composite is well below the percolation threshold (~16 vol%) [340]. Therefore isolated metal nanoparticle inclusions act as minicapacitors giving higher permittivity values. The size of these isolated particles in the rubber matrix is far less than their skin depth (depth of penetration of current at which its value decreases by $(1/e)^{th}$ of its surface value) as evident from the SEM micrographs.
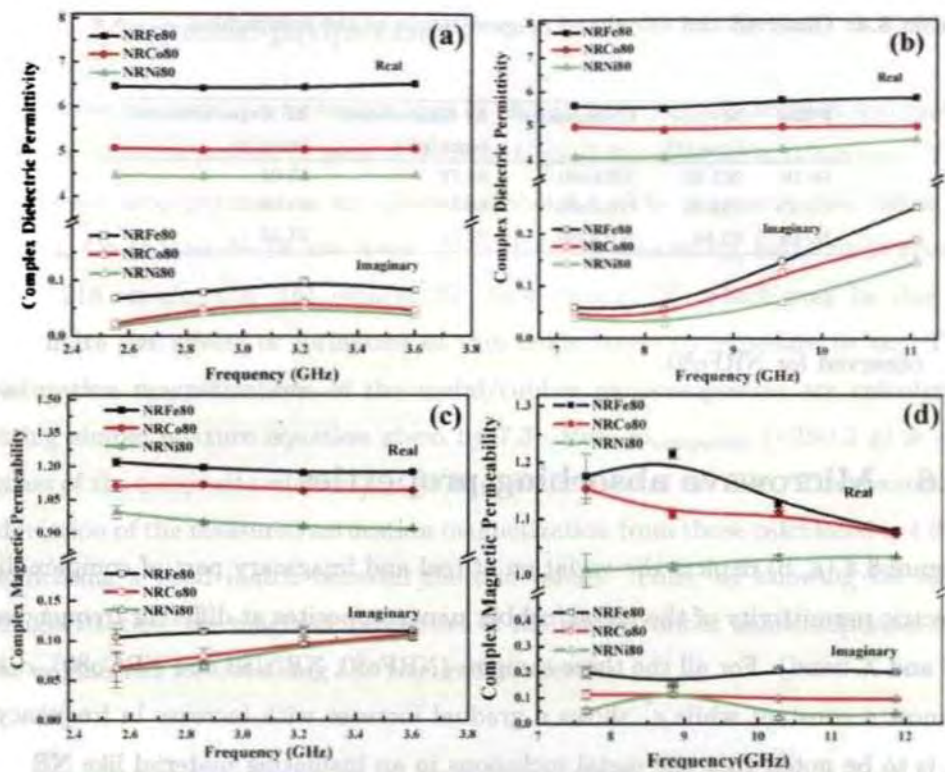
Figure 8.4: Complex dielectric permittivity spectra in the (a) S-band and (b) X-band of metal rubber composites. Complex permeability spectra in the (c) S-band and (d) X-band of metal rubber composite

Due to the presence of insulating rubber in between the metal particles, the mobility of space charges is limited leading to low dielectric loss. In the S-band, a maximum dielectric loss of 0.098 is obtained for NRFe80 at 3.2 GHz. NRCo80 and NRNi80 gave a dielectric loss of 0.059 and 0.05 respectively. In the X-band, the real part of dielectric permittivity (Figure 8.4b) of all the three composites are lower than those found in the S-band consistent with the conventional theories [282]. The imaginary part of dielectric permittivity is enhanced in the X-band indicating improved microwave absorption characteristics at higher frequencies. Microwave dielectric loss may arise from the following mechanisms: DC conductivity/free migration of charge carriers, local regions or local conductivity emanating from grain boundaries and dipole relaxation of defect boundaries [341, 342]. The DC resistivity of the rubber composites is very high and so the

loss due to free migration of charges is vanishingly small at high frequencies. The increased dielectric loss in the X-band is due to the relaxation polarization loss occurring during the oscillation of the dipoles formed around the metal nanoparticle inclusions, which dominates in the high frequency regime.

Other than the space charge polarization, eddy current[343] also affects the electromagnetic properties of the ferromagnetic metal polymer composite. This in turn is dependent on the skin depth of filler inclusion. In the present study, the particles are in the nano regime and thus eddy current effects are vanishingly small. μ' and μ'' of NR is close to 1 and 0 respectively, due to its inherent non-magnetic nature. The complex permeability of the metal rubber composites (NRFe80, NRCo80 and NRNi80) determined at S and X-band are shown in Figure 8.4(c, d). NRFe80 is found to have a maximum permeability of ~ 1.2. Moreover the magnetic loss is increased from 0.1 to 0.2 in the X band. Permeability of a magnetic material has a direct bearing on the saturation magnetization where as it is inversely related to the coercivity of the material [100, 344]. The initial permeability of ferromagnetic materials is given by the relation

$$\mu_i = \frac{M_s^2}{akH_cM_s + b\lambda\xi} \tag{8.1}$$

Here 'a' and 'b' are constants determined by the material composition, λ is the magnetostriction constant, ξ is an elastic strain parameter of crystal, and 'k' is a proportionality coefficient. Thus, for higher values of M_s and lower values of H_c, improved permeability are obtained which in turn enhances the microwave absorption. Both these criterion are satisfied for iron filled composite which thereby give higher permeability.
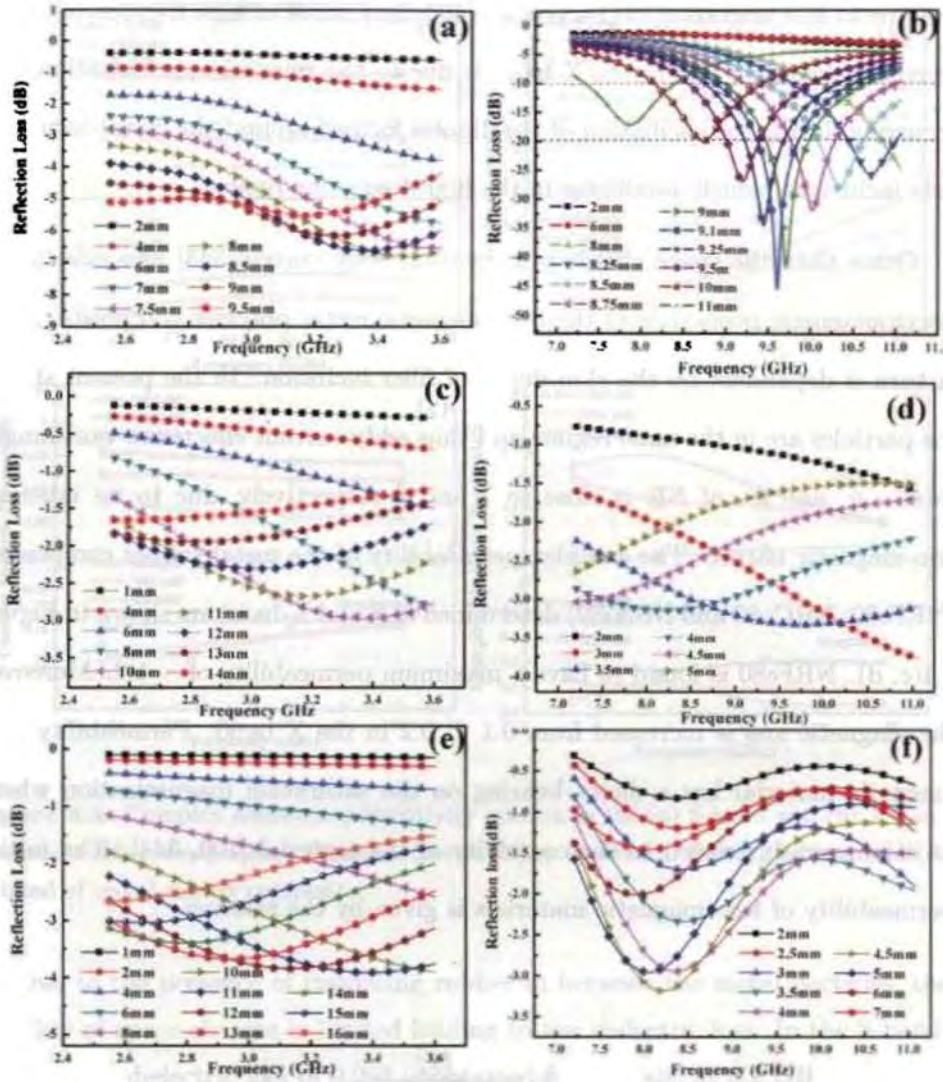
Figure 8.5: Reflection loss curves for metal rubber composites at various absorber thicknesses (a) NRFe80 - S band, (b) NRFe80 - X band, (c) NRCo80 - S band, (d) NRCo80 - X band, (e) NRNi80 - S band and (f) NRNi80 - X band

The effectiveness of a wave absorbing material is determined by parameters like reflection loss and/or transmission loss. A systematic simulation of the reflection loss (RL) of the nanocomposites for different frequency bands and layer thicknesses were carried using the surface impedance equation by considering the single layer metal backed absorber model (Equation 3.3 and 3.4)[181].

Figure 8.5(a-f) depicts the RL at various absorber layer thicknesses (d ~1-16 mm) evaluated in the S and X-bands from the measured complex permittivity and permeability values. NRFe80 gave a RL minimum of -6.8 dB at 3.48 GHz for an absorber thickness of 8 mm in the S-band. In the X-band, NRFe80 gave excellent absorption with RL minima of -45 dB at 9.6 GHz for an absorber thickness of 9.1 mm. The RL over -10dB indicates 90% absorption of electromagnetic energy. -20 dB RL represents energy absorption of 99%. Here for NRFe80, a bandwidth of 1.74 GHz and 510 MHz corresponding to a RL over -10 dB and -20 dB respectively is obtained.

RL for NRNi80 and NRCo80 at different absorber thicknesses were also examined. Both these samples gave RL not more than -4 dB in the frequency bands investigated. A bandwidth of 1.71 GHz below -2 dB is shown for NRNi80 in the X-band, which is insignificant when compared to NRFe80. It is to be noted that increasing the thickness of the absorber material resulted in a shift of RL minima towards lower frequencies (Figure 8.5) consistent with the quarter wave principle [237] i.e.; $d \propto 1/f$ (Equation 3.5). This behaviour is observed in all the samples. Moreover multiresonance peaks were found to be absent in the S and X-band. Investigations carried out by Qing Yuchang *et al.* [342] on the microwave absorbing properties of flake carbonyl iron (55wt%) in epoxy-silicone resin showed a minimum RL of -42.5 dB at 10.6 GHz. Minimum reflectivity of -21.7 dB for 3 mm carbonyl iron/ethylene propylene diene monomer radar absorbing material was reported at 3.54 GHz with 45 vol% of carbonyl iron [345]. In the present study, 8.6 vol% iron/NR nanocomposites gave excellent absorption of electromagnetic wave in the X-band. We have found a decrease in bandwidth with thickness of the absorber (Figure 8.6a). A bandwidth of ~1-2 GHz can be maintained with a thickness of 8.5-11 mm over -10 dB.
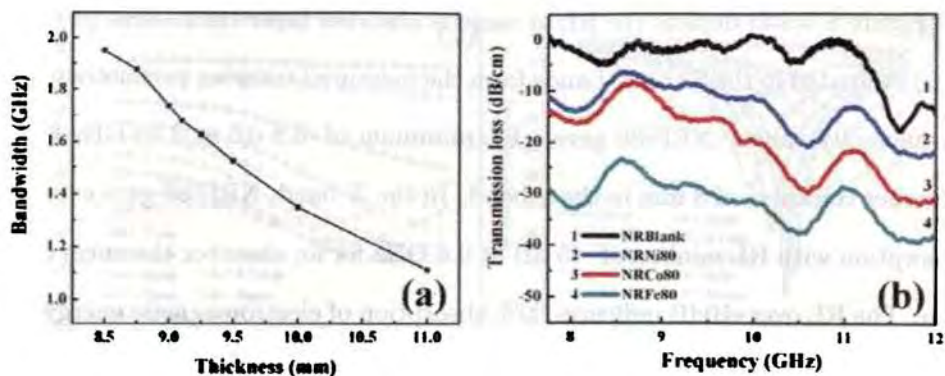
Figure 8.6: (a) Variation of bandwidth with thickness of NRFe80 absorber layer, and (b) transmission loss measured in the X-band

The RL was experimentally determined for 2 mm thick metal/rubber nanocomposites under study and was found to be $\sim$ -2 dB as obtained from simulations. Furthermore, the transmission loss was measured for all the three composites (Figure 8.6b). The effectiveness of iron filled composite was further verified from the lower values of transmission losses (about -30 dB/cm over entire X-band).

Increasing the filler content reduces the matching thickness as well as causes a shift in minimum reflection towards lower frequency. These results are significant for developing multilayer absorbers for using at different frequency bands.

8.7 Conclusion

Mechanical attrition using high energy ball milling was found to be an effective method for obtaining magnetic metal nanoparticles. Flexible NR composite sheets based on Fe/Co/Ni for use as microwave absorbing material were developed. It is found that the mechanical properties of metal rubber nanocomposites are retained. Enhanced dielectric and magnetic properties were obtained for iron filled rubber composites when compared to nickel or cobalt filled nanocomposite. Improved permeability values were found for iron composites are due to higher saturation magnetization and lower coercivity of iron filler particles. RL of -45 dB at 9.5 GHz could be achieved with an absorber thickness of 9.1 mm for iron filled composites. Results point towards the wide possibility of fabricating

cost effective rubber based microwave absorbers with iron nanoparticles as inclusions possessing superlative mechanical properties. Additional functionalities of the composite add value to this widely used and easily available commercial elastomer.

Chapter 9

Conclusions

Nanoscience and nanotechnology is surging ahead with greater pace than antici-
pated and leaving a mark of its own in the day to day life of human beings. This
is an area where materials play a very important role and in particular the size
and shape of particles decides much of its properties. Quantum mechanics was
able to unearth the 'less-understood' at the nano level. Now, with this under-
standing it is possible to tailor various properties of materials namely physical,
mechanical, thermal, optical as well as electrical properties by tuning the size
and shape of particles.

With the advent of nanoscience and nanotechnology, nanostructures, nanocom-
posites and hybrid nanostructures have become very important and they play a
significant role as far as applications are concerned. Magnetism and magnetic
materials have been playing a seminal role right from the civilization days and
will continue to be a dominant one in the days to come. It is a fact that these ma-
terials find places in many areas like in high density data storage, nanoelectronics,
magnetic caloric effect, multiferroics, spintronics or giant magneto resistance.

Oxide form of iron and magnetic metal particles were known for their ferri/
ferro magnetic properties and are increasingly being used. When one wants to
modify the various magnetic characteristics of ferro or ferromagnetic materials,
one has to deal with the adverse effects of finer sizes, visa a vis reactivity, ox-
idation, thermal stability or grain growth. Passivation is a viable alternative
and there can be no other material better than carbon for this purpose. Different
forms of carbon exist and some of them are graphite, diamond, carbon nanotubes,

carbon nano fibres, carbon horns, carbon flowers etc. Latest entry to this family is graphene.

Carbon nano onion or CNOs as they are called, is a very important member of carbon family and has many applications ranging from light emitting devices, optical limiters, solid lubricants, additives for aerospace applications, hydrogen storage devices or fuel cell electrodes. As far as the synthesis of CNOs are concerned, hi-tech techniques like high temperature pyrolysis, thermal ablation, arc discharge or electron beam irradiation based methods are normally employed. If a cost effective method can be adopted for the preparation of CNOs, magnetic metal particles can be embedded in CNO. The advantage of embedding metal nanoparticles in CNO is multifould. Carbon being a good material for dielectrics, and embedding magnetic metal nanoparticles in CNO will impart the required magnetic characteristics, they can be useful material for microwave absorbing applications. The nonlinear optical properties of magnetic metal embedded hybrid nanostructures will also be of interest both from a fundamental perspective and an application point of view.

Natural rubber is abundantly available in the state of Kerala and value addition to this naturally occurring resource will be always an alternative proposition by fabricating composites based on natural rubber and nanoparticles of ferri/ferromagnetic materials. Natural rubber based magnetic nanocomposite are also candidate materials for microwave absorption because they can be moulded into desired shape, fabricated in the form of gaskets and moreover, their mechanical and electromagnetic properties can be modified by incorporating fillers like precipitated silica or carbon black. This particular investigation was carried out with these objectives in mind and the following are the summary of this work. There exist scope for improvement which are highlighted in this chapter.

Metallic iron is an important magnetic material and the nanoform of iron is investigated in great detail. When the size of iron particles become finer and finer, it is prone to atmospheric oxidation and pasisvation is highly essential. Passivation of iron nanoparticles with oleic acid provides the repulsive energy to prevent agglomeration. The effect of thermal annealing on the hybrid structures prepared by novel techniques was carried out and it has been found that the resultant material formed is stable iron-carbon nanocomposites. A saturation magnetization

of 113 emu/g was obtained for the iron-carbon nanocomposite with no observable oxide phase. The Raman spectra revealed typical D and G fingerprint bands emanating from the carbon matix. Optimized carbon coating over the magnetic metal nanoparticles is highly desirable in minimising the eddy current loss of these materials with higher Snoek's limit. Restricting the particle size of the magnetic material well below the skin depth and passivating with a dielectric layer of carbon embodiments an ideal structure. This helps in manipulating the complex dielectric permittivity as well as complex magnetic permeability, which in turn can tune the microwave absorbing properties. Attempts were made to study the variation of dielectric permittiviy and magnetic permeability at microwave frequencies and hence determine their reflection loss to understand the effectiveness of the absorbing properties of the nanostructures. The passivated magnetic iron nanoparticles were found to possess good impedance matching which lead to the enhancement of microwave absorption. Iron-carbon nanostructures gave a reflection loss minimum of -18 dB with an absorber layer thickness of $\sim$ 2 mm in the X-band.

Similarly, experiments were carried out to prepare highly stable cobalt and nickel nanoparticles. As in the case of iron nanoparticles, cobalt and nickel nanoparticles were synthesized by in situ passivation with oleic acid. Thermal treatment of oleic acid passivated cobalt nanoparticles at different temperatures were examined using transmission electron microscope. The results revealed the evolution of carbon nano onions which was really exciting (shown in the front cover of this thesis). A growth mechanism for the evolution of CNOs was also proposed. Though the observance of CNO in cobalt nanostructure was a serendipity, it worked out to be a very cost effective method and the evaluation of various properties revealed that the quality of CNO thus prepared are superlative. Such nanostructures previously reported required hi-tech experimental conditions. This was a cost effective and scalable technique and a patent is filed for this process. The optical limiting properties of cobalt encapsulated within the graphitic shells were examined using open aperture z-scan techniques. The numerical fits of the open aperture experiments were found to fit well with the two photon absorption mechanism. Cobalt/carbon nanostructures were found to possess superlative microwave absorbing properties in the X- band with a reflection

of -16 dB having an absorber thickness of 1.75 mm.

Highly stable nickel/carbon hybrid nanostructures were also successfully fabricated. These contained nickel/carbon core/shell nanostructures, hollow carbon nano onions and carbon nano fibres. The magnetic properties of these passivated nickel nanoparticles were investigated using SQUID magnetometer. In the case of nickel/carbon nanostructures, the microwave absorbing properties were comparatively good with respective to iron or cobalt nanostructures. It gave a reflection loss minima of -45 dB at 3.13 GHz with a thickness of 6.6 mm. The loss was over -10 dB within a thickness range of 5.8-8 mm in the S-band where as it was over -10 dB for a thickness of 2.2-2.6 mm in the X-band. One can also think of tuning carbon coating thicknesses for attaining the perfect impedance matching criteria. The very fact that high quality CNO could be fabricated using controlled thermal annealing of cobalt-oleic acid protocols prompts one to ponder whether such non-magnetic nanostructures of Cu or Pt-CNOs could be fabricated? Such structures are also important because of the uniqueness of Cu-CNO combinations.

The catalytic property of 3d-transition metal particles were employed to fabricate highly stable magnetic metal carbon nanostructures. The shelf life of carbon passivated magnetic metal nanoparticles was excellent which promises the usability of these nanostructures in devices. The percentage of magnetic constituent in the composite can be optimized for tuning the magnetic and dielectric properties in order to improve the impedance matching. Moreover, a thorough study employing in situ TEM experiments to unravel the reaction kinetics relating the evolution of carbon layers over metal nanostructures can be carried out in future. The presence of any traces of oxide contamination can be closely looked into by employing techniques like X-ray photoelectron spectroscopy on the system.

Investigations on the structural and magnetic properties of nickel ferrite nanoparticles, obtained by different synthesis routes were also carried out. It was found that the dielectric properties could be tuned with respect to their grain size. The obtained results were very well correlated with the conventional dielectric dispersion models. The effect of high energy ball milling on the cation redistribution that may occur can be investigated in ferrite nanoparticles can further be studied by employing techniques like Mossbauer spectroscopy, neutron diffraction or X-ray photo electron spectroscopy. The gas sensing properties of nanoferrites

have not been investigated in this thesis. There exist scope for research in this regard which can be carried out by appropriately tuning the composition of the materials.

The main drawback of magnetic nanoparticles for device fabrication is that they are difficult to be moulded into complex shapes which make it less effective for structures in movable parts. This issue was thoughtfully tackled by fabricating natural rubber-nickel ferrite nanocomposites. Recipe for mixing was formulated by extensive experimental iterations and composites were moulded and cut into desired shape. The percentage of filler particle (nickel ferrite) was varied and the cure and their physicomechanical and microwave absorbing properties were studied. Flexible magnetic composites sheets were developed possessing good microwave absorbing properties. From the experimental results of the complex dielectric permittivity and magnetic permeability, a reflection loss minimum of -16 dB was obtained at 9.5 GHz for 12 mm thick 120 phr nickel ferrite loaded natural rubber nanocomposite. Preliminary work to improve the bandwidth as well as to enhance the mechanical strength was carried out by formulating a recipe with precipitated silica or carbon black as additional filler along with nickel ferrite in natural rubber. These results are not included in the thesis to avoid deviation from the main theme.

Magnetic metal nanoparticles like iron, cobalt or nickel well below their skin depth were also incorporated in natural rubber for the fabrication of ferromagnetic metal rubber nanocomposite based microwave absorbers. Metal nanoparticles of Fe/Co/Ni were prepared by the top-down approach of high energy ball milling. Iron filled rubber composite gave best results in X-band of the microwave spectrum. A reflection loss minimum of -45 dB at 9.5 GHz could be achieved for a layer thickness of 9 mm. Hence quality sheets of natural rubber nanocomposites with desired physicomechanical as well as microwave absorbing properties were fabricated which provides value addition to the easily available raw material in the state of Kerala, India.

An experimental set-up for measuring the complex dielectric permittivity and complex magnetic permeability employing cavity perturbation technique was made operational during the course of this investigation. A completely automated microwave measurement set-up using virtual instrument software, Lab-

VIEW could be designed for data acquisition and evaluation of reflection loss. Transmission/Reflection method can also be optimized to measure the reflection loss in the samples.

There are many grey areas in this investigation too. As discussed earlier, miniaturization is the sole concern of materials engineers and researchers. To reduce the device size with improved compatibility and with existing technologies, one can think of fabricating microwave absorbers with novel nanostructures like nanotubes or nanowires. Initial work on magnetic metal nanowires have been carried out in the laboratory which gave encouraging results. To assure flexibility and tunability of properties heterostructures can be fabricated. An emulsion consisting of magnetic particles, with the right curatives in a rubber latex carrier along with pigments like TiO_2 or precipitated silica could be a stealth paint. For this, elaborative studies need to be carried out with regard to their microwave absorption characteristics in the various microwave bands. Prior to fabrication, extensive theoretical studies could also be performed for optimizing the material combination and thickness to save time and money. Such paints with stealth properties combined with thermal stability could find place in aerospace applications. These studies could not be conducted here because of time constrains. However, some initial studies on latex-ferrite films were carried out.
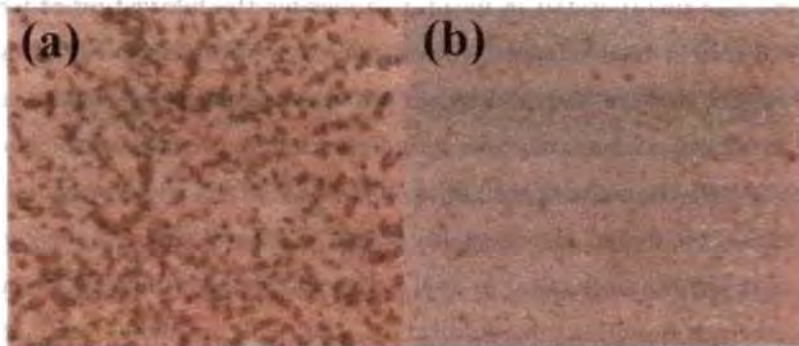

Figure 9.1: Optical microscope images of magnetic thin films of latex-ferrite composite casted on glass substrate (a) uncured films and (b) cured films

Aqueous ferrofluid of iron oxide was prepared and mixed with rubber latex. Thin films were obtained by spin coating the mixture (Figure 9.1a). Films were

also coated after the addition of curatives in a specified recipe (Figure 9.1b). This gave agglomeration free magnetic films while those coated without curatives lead to the agglomeration of ferrite particles forming fractal like structures. However not much was gathered on these structures and this is an area where more fundamental insights need to be de derived and perhaps can be linked to its morphology. This can be carried out as an extension of the present investigation. Metal-CNO nanostructures exhibiting excellent nonlinear optical properties can be a good optical limiter if these structures can be spun on to appropriate substrates. For the evaluation of microwave absorbing properties of emulsions, a separate set-up can be fabricated and the data can be modelled using appropriate theories. Even thin films on various substrates and such multilayered films along with ferroelectric layers will give rise to multiferroic nanostructures. This is a futuristic proposition.

One wonders whether there is any room for disorder in any scientific investigation! The very fact that there is convergence in ones research at some point of his/her work, because of serendipity, is a sort of 'order-out of disorder' phenomenon. Though it sounds philosophical, there are many parallels for this in the day to day life too. If the evolution of a cost effective process for the fabrication of cobalt-carbon nano onions is a serendipity, then this is also an 'order in disorder'. Perhaps it is the amount of 'disorder' that determines order in any phenomenon. Hypothetically speaking, if Alexander the Great had met with Gymnosophist who was meditating in the Himalayas, the Gymnosophist would have commented, "If your motive is linear, I am looking at infinity" which is nonlinear and replete with opportunities. This work too has close parallels in this context and this investigation and its outcome is only a small seed which needs nurturing and can be nucleated and controlled as in self assembly. So linear structures and order from nonlinear structures and disorder can be evolved!

Bibliography

[1] Stephen Blundell. *Magnetism in Condensed Matter*. Oxford University press, Oxford, 2003.

[2] BD Cullity and CD Graham. *Introduction to Magnetic Materials*. Second edition. IEEE Press, John Wiley and Sons, New Jersey, 2009.

[3] Umit Özgür. Yahya Alivov, and Hadis Morkoc. *J Mater Sci: Mater Electron*, 20:789, 2009.

[4] Soshin Chikazumi. *Physics of Magnetism*. John Wiley and Sons Inc, USA, 1964.

[5] CSSR Kumar and J Hormes. *Nanofabrication Towards Biomedical Applications-Techniques, Tools Applications, and Impact*. WILEY -VCH Verlag GmbH Co. KGaA, 2005.

[6] Hari Singh Nalwa. *Nanostructures Materials and Nanotechnology*. Academic Press, California USA, 2002.

[7] VRK Murthy and B Viswanathan. *Ferrite Materials, Science and Technology*. Narosa Publishing House, New Delhi, 1962.

[8] RD McMichael, RD Shull, LJ Swartzendruber, and LH Bennett. *J Magn Magn Mater*, 111:29, 1992.

[9] PM Ajayan, LS Schadler, and PV Braun. *Nanocomposite Science and Technology*. Wiley CH Publischers Verlag, GmbH Co. KGaA, Weinhein, 2003.

[10] Irena Ban, Miha Drofenik, and Darko Makovec. *J Magn Magn Mater*, 307:250, 2006.

[11] Charles J O'Connor, Candace T Seip. Everett E Carpenter, Sichu Li, and Vijay T John. *J Magn Magn Mater*, 277:350, 2004.

[12] Kenneth S Suslick, Mingming Fang, and Taeghwan Hyeon. *J Am Chem Soc*, 118:11960, 1996.

[13] R Abu Mukh-Qasem and A Gedanken. *J Colloid Inter Sci*, 284:489, 2005.

[14] Charles P Gibson and Kathy J Putzer. *Science*, 267:1338, 1995.

[15] K Bridger, J Watts, M Tadros, X Gang, SH Liou, and CL Chien. *J Appl Phys*, 61:3323, 1987.

[16] C Salling, S Schultz, I McFayden, and M Ozaki. *IEEE Trans Magn*, 27:5184, 1991.

[17] Takafumi Seto, Kenji Koga, Hiroyuki Akinag, Fumiyoshi Takano, Takaaki Orii, and Makoto Hirasawa. *J Nanoparticle Res*, 8:371, 2006.

[18] Q Ou, T Tanaka, M Mesko, A Ogino, and M Nagatsu. *Diamond and Related Materials*, 17:664, 2008.

[19] N Sivakumar, A Narayanasamy, N Ponpandian, J-M Greneche, K Shinoda, B Jeyadevan, and K Tohji. *J Phys D: Appl Phys*, 39:4688, 2006.

[20] Mathew George, Asha Mary John, Swapna S Nair, PA Joy, and M R Anantharaman. *J Magn Magn Mater*, 302:190, 2006.

[21] Man-Sung Yim and François Caron. *Prog Nucl Energy*, 48:2, 2006.

[22] Hugh O Pierson. *Handbook of Carbon, Graphite, Diamond and Fullerenes: Properties, Processing and Applications*. Noyes Publications, USA, 1993.

[23] HW Kroto, JR Heath, SC O'Brien, RF Curl, and RE Smalley. *Nature*, 318:162, 1985.

[24] W Krätschmer, LD Lamb, K Fostiropoulos, and DR Huffman. *Nature*, 347:354, 1990.

[25] D Ugarte. *Nature*, 359:707, 1992.

[26] PM Ajayan and S Iijima. *Nature*, 361:333, 1993.

[27] S Seraphin, D Zhou, J Jiao, JC Withers, and R Loufty. *Nature*, 362:503, 1993.

[28] RS Ruff, DC Lorents, B Chan, R Malhotra, and S Subramoney. *Science*, 259:346, 1993.

[29] SA Majetich, JO Artman, ME McHenry, NT Nuhfer, and SW Staley. *Phys Rev B*, 48:16845, 1993.

[30] VP Dravid, JJ Host, MH Teng, B Elliott, J Hwang, DL Johnson, TO Mason, and JR Weertman. *Nature*, 374:602, 1995.

[31] HJ Huang, SH Yang, and G Gu. *J Phy Chem B*, 102:3420, 1998.

[32] VA Davydov, AV Rakhmanina, V Agafonov, B Narymbetov, JP Boudou, and H Szwarc. *Carbon*, 42:261, 2004.

[33] VA Davydov, AV Rakhmanina, JP Boudou, A Thorel, H Allouchi, and V Agafonov. *Carbon*, 44:2015, 2006.

[34] H Pan, W Chen, YP Feng, W Jia, and J Linb. *J Phys Chem*, 88:223106, 2006.

[35] Philip Moriarty. *Rep Prog Phys*, 64:297, 2001.

[36] Iijima Sumio. *Nature*, 354:56, 1991.

[37] L Joly-Pottuz, B Vacher, T Le Mogne, JM Martin, T Mieno, CN He, and NQ Zhao. *Tribol Lett*, 29:213, 2008.

[38] L Joly-Pottuz, N Matsumoto, H Kinoshita, B vacher, M Belin, and G Montagnac et al. *Tribol Inter*, 41:69, 2008.

[39] Cun Li, Xiaogang Yang, Baojun Yang, Yan Yan, and Yitai Qian. *Mater Chem Lett*, 103:427, 2007.

[40] Hosun Lee, TD Kang, Kay Hyeok An, Dong Jae Bae, and Young Hee Lee. *Jpn J Appl Phys*, 42:5880, 2003.

[41] N Sano, H Wang, I Alexandrou, M Chhowalla, KBK Teo, and GAJ Amaratunga et al. *J Appl Phys*, 92:2783, 2002.

[42] Y Saito, T Yoshikawa, M Inagaki, M Tomita, and T Hayashi. *Chem Phys Lett*, 204:277, 1993.

[43] XH Chen, M Deng, JX Wang, HS Yang, GT Wu, and XB Zhang. *Chem Phys Lett*, 336:201, 2001.

[44] VL Kuznetsov, AL Chuvilin, YV Butenko, IY Malkov, and VM Titov. *Chem Phys Lett*, 222:343, 1994.

[45] D Jason Palmer. *Materials Today*, 10:9, 2007.

[46] Jiyoung Chang, Byung-Kwon Min, Jongbaeg Kim, Sang-Jo Lee, and Liwei Lin. *Smart Mater Struct*, 18:065017, 2009.

[47] Seiji Akita, Yoshikazu Nakayama, Syotaro Mizooka, Yuichi Takano, Takashi Okawa, Yu Miyatake, Sigenori Yamanaka, and Masashi Tsuji. *Appl Phys Lett*,

[48] Kaylene Atkinson, Siegmar Roth, Michael Hirscher, and Dr Werner Grnwald. *Fuel Cells Bulletin*, 4:9, 2001.

[49] Panapoy M, Supattanapalapol S, and Ksapabutr B. *2nd IEEE International Nanoelectronics Conference (INEC 2008)*, page 452, 2008.

[50] P Burattin, M Che, and C Louis. *J Phys Chem B*, 104(45):10482, 2000.

[51] KAS Fernando, MJ Smith, BA Harruff, WK Lewis, EA Guliants, and CE Bunker. *J Phys Chem C*, 113(2):500, 2009.

[52] SC Tsang, V Caps, I Paraskevas, D Chadwick, and D Thompsett. *Angew Chem Int Ed*, 43:5645, 2004.

[53] XG Zhu, XW Wei, and S Jiang. *J Mater Chem*, 17:2301, 2007.

[54] J Kang, P Nash, J Li, C Shi, and N Zhao. *Nanotechnology*, 20:235607, 2009.

[55] Debasis Bera, Suresh C Kuiry, Matthew McCutchen, Arnold Kruize, Helge Heinrich, Meyya Meyyappan, and Sudipta Seal. *Chem Phys Lett*, 386:364, 2004.

[56] Zhipeng Cheng, Fengsheng Li, Yi Yangm Yi Wang, and Weifan Chen. *Mater Lett*, 62:2003, 2008.

[57] Peter Reiss, Myriam Protire, and Liang Li. *Small*, 5:154, 2009.

[58] PJF Harris and SC Tsang. *Chem Phys Lett*, 293:53, 1998.

[59] TN Narayanan, AP Reena Mary, MM Shaijumon, Lijie Ci, PM Ajayan, and MR Anantharaman. *Nanotechnology*, 20:055607, 2009.

[60] S Subramoney. *Adv Mater*, 10(15):1157, 2003.

[61] CG Williams. *J Chem Soc*, 15:110, 1867.

[62] CM Blow and C Hepburn. *Rubber Technology and Manufacture*. Buttlerworths.

[63] A Ansarifar, N Ibrahim, and M Bennett. *Rubber Chem Technol*, 78:793, 2005.

[64] Rodrguez, L Ibarra, and I Mora. *J Appl Poly Sci*, 106:973, 2007.

[65] A Nsarifar, N Ibrahim, and M Bennett. *Rubber Chem Technol*, 78:793, 2005.

[66] JM Dadck. *French Patent*, page 1 135734, 1995.

[67] MR Anantharaman, KA Malini, S Sindhu, EM Mohammed, SK Date, SD Kulkarni, PA Joy, and Philip Kurian. *Bull Mater Sci*, 21(6):623, 2001.

[68] MR Anantharaman, S Sindhu, S Jagatheesan, KA Malini, and Philip Kurian. *J Phys D: Appl Phys*, 32(15):1801, 1999.

[69] S Sindhu, MR Anantharaman, Bindu P Thampi, KA Malini, and Philip Kurian. *Bull Mater Sci*, 25(7):599, 2002.

[70] RH Kodama, AE Berkowitz, EJ McNiff, and S Foner. *Phys Rev Lett*, 77:394, 1996.

[71] B Martinez, T Obradors, Ll Balcells, A Rounanet, and C Monty. *Phys Rev Lett*, 80:181, 1998.

[72] J Ding, T Reynolds, WF Miao, PG McCormick, and R Street. *Appl Phys Lett*, 65:3135, 1994.

[73] J Ding, WF Miao, R Street, and PG McCormick. *J Alloys Compds*, 281:32, 1998.

[74] DDL Chung. *Carbon*, 39:279, 2001.

[75] David K Cheng. *Field and Wave electromagnetic*. Pearson Education.

[76] Jun Wang and Werner J Blau. *J Opt A: Pure Appl Opt*, 11:024001, 2009.

[77] TN Narayanan, S Sandeep, MM Shaijumon, Lijie Ci, PM Ajayan, Reji P, and MR Anantharaman. *Nanotechnology*, 20(28):285702, 2009.

[78] SS Harilal, CV Bindhu, VPN Nampoori, and CPG Vallabhan. *J Appl Phys*, 86(3):1388, 1999.

[79] FZ Henari, WJ Blau, LR Milgrom, G Yahioglu, D Philips, and JA Lacey. *Chem Phys Lett*, 267:229, 1997.

[80] SR Mishra, HS Rawat, SC Mehendale, KC Rustagi, AK Sood, Ranjini Bandyopadhyay, A Govindaraj, and CNR Rao. *Chem Phys Lett*, 317:510, 2000.

[81] J Wang and WJ Blau. *Phys Chem C*, 112:2298, 2008.

[82] Richard C Hollins. *Curr Opin Solid State Mater Sci*, 4:189, 1999.

[83] DG McLean, RL Sutherland, MC Brant, and DM Brandelik. *Opt Lett*, 18:858, 1993.

[84] Jun Wang and Werner J Blau. *J Opt A: Pure Appl Opt*, 11:024001, 2009.

[85] R Philip, G Ravindra Kumar, N Sandhyarani, and T Pradeep. *Phys Rev B*, 62:13160, 2000.

[86] PV Kamat, M Flumiani, and GV Hartland. *J Phys Chem B*, 102:3123, 1998.

[87] Dhirendra Bahadur, Satish Vitta, and Om Prakash. *Inorganic Materials, recent advances.* Narosa Publishing House, Mumbai India, 2004.

[88] Vijutha Sunny, TN Narayanan, US Sajeev, PA Joy, D Sakthi Kumar, Yasuhiko Yoshida, and MR Anantharaman. *Nanotechnology,* 17:4765, 2006.

[89] T Kameyama, K Sakanaka, A Motoe, T Tsunoda, T Nakanaga, NI Wakayama, H Takeo, and K Fukuoda. *J Mater Sci,* 25:1058, 1990.

[90] V Sepelàk, D Baabe, and KD Becker. *J Mater Synth Process,* 8:333, 2000.

[91] Min Nie, Kai Sun, and Dennis Desheng Meng. *J Appl Phys,* 106:054314, 2009.

[92] Urs O Hafeli and Gayle J Pauer. *J Magn Magn Mater,* 194:76, 1999.

[93] Jhunu Chatterjee, Yousef Haik, and Ching-Jen Chen. *J Magn Magn Mater,* 246:382, 2002.

[94] QA Pankhurst, J Connolly, SK Jones, and J Dobson. *J Magn Magn Mater,* 246:382, 2002.

[95] Vijutha Sunny, D Sakthi Kumar, Yasuhiko Yoshida, Magdalena Makarewicz, Wojciech Tabis', and MR Anantharaman. *Carbon,* 48:1643, 2010.

[96] J Park, V Privman, and E Matijevic. *J Phys Chem B,* 105:11630, 2001.

[97] DK Kim, Y Zhang, W Voit, KV Rao, and M Muhammed. *J Magn Magn Mater,* 225:30, 2001.

[98] L Vayssières, C Chanèac, E Tronc, and JP Jolivet. *J Colloid Interface Sci,* 205:205, 1998.

[99] C Jeffrey Brinker and George W Scherer. *Sol-gel Science.* Academic Press, California, 1990.

[100] Vijutha Sunny, Philip Kurian, P Mohanan, PA Joy, and MR Anantharaman. *J Alloys Compd,* 489:297 303, 2010.

[101] Dong-Hwang Chen and Xin-Rong He. *Mater Res Bull,* 36(7-8):1369, 2001.

[102] AC Pierre. *Ceram Bull,* 70:1281, 1991.

[103] B Stahl, NS Gajbhiye, G Wilde, D Kramer, J Ellrich, M Ghafari, H Hahn, H Gleiter, J Weibmuller, R Wurshum, and P Schlossmacher. *Adv Mater,* 14:24, 2002.

[104] DH Chen and XR He. *Mater Res Bull,* 36:1369, 2001.

[105] MA Ahmed, N Okasha, and S I El-Dek. *Nanotechnology*, 19:065603, 2008.

[106] M Singh and SP Sud. *J Mater Sci Eng*, 83:180, 2001.

[107] A Lakshman, KH Rao, and RG Mendiratta. *J Magn Magn Mater*, 250:92, 2002.

[108] C Suryanarayana, G H Chen, and FHS Froes. *Scr Metall*, 26:1727, 1992.

[109] Vishu Shah. *Handbook of Plastic Testing Technology*. John Wiley and Sons, New York, 1984.

[110] Roger Brown. *Physical Testing of Rubber*. 3rd Edition, Chapmann & Hall, London, 1996.

[111] John S Dick. *Rubber Technology Compounding and Testing for Performance*. Hanser Publishers, Munich, 2001.

[112] Z Bartha, P Erdos, and J Maits. *Int Polym Sci Technol*, 10:T/50, 1983.

[113] NV Zakharenko and FB Yremchuk. *Int Polym Sci Technol*, 12:T/23, 1985.

[114] HP Schreiber and Olguin. *Polym Eng Sci*, 23:129, 1983.

[115] GCN Lee and JR Purdon. *Polym Eng Sci*, 9:360, 1969.

[116] G Mathew, RP Singh, NR Nair, and S Thomas. *J Mater Sci*, 38:2469, 2003.

[117] BD Cullity. *X-ray Diffraction*. Addison-Wesley Publishing Company Inc, 1959.

[118] C Suryanarayana and M Grant Norton. *X-Ray Diffraction*. Plenum Press, New York, 1998.

[119] Linda C Sawyer and David T Grubb. *Polymer Microscopy*. 2nd Edition Chapman Hall, London, 1987.

[120] Watt M. *Principle and Practice of Electron Microscopy*. Cambridge University Press, Cambridge, 1997.

[121] A Subramanian and LD Marks. *Ultramicroscopy*. 98:151, 2004.

[122] CH Lin, PC Kuo, JL Pan, and DR Huang. *J Appl Phys*, 79 (8):6035, 1996.

[123] Joachin Nolte. *ICP Emission Spectroscopy: A Practical Guide*. Wiley-VCH Verlag GmbH & Co, 2003.

[124] Brian Smith. *IR Spectral Interpretation - A Systematic Approach*. CRC press, 1999.

[125] E Smith and G Dent. *Modern Raman Spectroscopy: A Practical Approach.* John Wiley & Sons Ltd, 2005.

[126] Skoog Douglass A, F James Holler, and Timothy A Nieman. *Principles of Instrumental Analysis.* 5th Editon Philadelphia, Harcourt, 1998.

[127] JJ Pankov. *Optical Processes in Semiconductors.* Printice-Hall, New Jersey USA, 1971.

[128] Simon Foner. *Rev Sci Instrum,* 30:548, 1959.

[129] Joseph A Pesch. *Rev Sci Instrum,* 54:480, 1983.

[130] RV Krishnan and A Banerjee. *Rev Sci Instrum,* 70:85, 1999.

[131] Hong-Chang Yang and Tamkang. *J Sci Eng,* 6(1):9, 2003.

[132] JC Denardin, AL Brandl, M Knobel, P Panissod, AB Pakhomov, H Liu, and XX Zhang. *Phys Rev B,* 65:064122, 2002.

[133] Aparna Roy ANDV Srinivas, S Ram, and JA De Toro. *J Appl Phys,* 100:094307, 2006.

[134] JL Dormann and D Fiorani. *J Magn Magn Mater,* 140-144:415, 1995.

[135] EM Mohammed and MR Anantharaman. *J Instrum Soc India,* 32 (3):165, 2002.

[136] Debye P. *Polar Molecules.* Dover Publication, New York, 1929.

[137] AM Nicolson and G Ross. *IEEE Trans Instrum Meas,* IM-19(4):377, 1970.

[138] WB Weir. *Proc IEEE,* 62(1):33 36, 1974.

[139] James Baker-Jarvis, Eric J Vanzura, and William A Kissick. *IEEE Trans Micro Theory Tech,* 38(8):1096, 1990.

[140] HA Bethe and J Schwinger. *Cornell Univ NRDC Rep,* D1-117, 1943.

[141] A Parkash, JK Vaid, and A Mansingh. *IEEE Trans Microw Theory Tech,* MTT-27:791, 1979.

[142] SH Chao and IEEE Trans. *Microw. Theory Tech.* MTT-33:519, 1985.

[143] DC Dube, MT Lanagan, JH Kim, and SJ Jang. *J Appl Phys,* 63(7):2466, 1988.

[144] B Viswanathan and VRK Murthy. *Ferrite Materials Science and Technology.* Springer-Verlag, London, 1990.

[145] Anjali Verma and Dinesh C Dube. *IEEE Trans Instrum Meas*, 54:2120, 2005.

[146] TN Narayanan, Vijutha Sunny, MM Shaijumon, PM Ajayan, and MR Anantharaman. *Electrochem Solid-State Lett*, 12(4):K21, 2009.

[147] Mi Lin, Yong Wnag, and Mohammed N Afsar. *Infrared and Millimeter Waves and 13th International Conference on Terahertz Electronics*, page 62, Williamsburg VA, 2005.

[148] RL Sutherland. *Hand book of nonlinear optics*. 2nd Edition. Marcel Dekker Inc, New York, 2003.

[149] M Sheik-Bahae, AA Said, TH Wei, DJ Hagann, and Van Stryland. *IEEE J Quanta Electro*, 26:760, 1990.

[150] Robert W Boyd. *Nonlinear Optics*, volume 2nd edition. Academic press, CA USA, 2003.

[151] L Nicolais and G Carotenuto. *Metal-polymer nanocomposites*, volume 2nd edition. John Wiley & Sons Inc, New Jersy, 2005.

[152] SR Rudge, TL Kurtz, CR Vessely, LG Catterall, and DL Williamson. *Biomaterials*, 21:1411, 2000.

[153] DL Huber. *Small*, 12:482, 2009.

[154] WL Zhoua, EE Carpenter, J Lin, A Kumbhar, J Sims, and CJ O'Connor. *Eur Phys, J D* 16:289, 2001.

[155] EE Carpenter. *J Magn Magn Mater*, 225:17, 2001.

[156] KS Suslick, S Choe, A Cichowlas, and MW Grinsta. *Nature*, 353:414, 1991.

[157] G Kataby, M Cojocaru, R Prozorov, and A Gedanken. *Langmuir*, 15:1703, 1999.

[158] G Kataby, A Ulman, R Prozorov, and A Gedanken. *Langmuir*, 14:1512, 1998.

[159] JL Snoek. *Physica (Amsterdam)*, 14:207, 1948.

[160] VB Bregar. *IEEE Trans Magn*, 40(3):1679, 2001.

[161] S Sugimoto, T Maeda, D Book, T Kagotani, K Inomata, M Homma, H Ota, Y Houjou, and R Sato. *J Alloys Compd*, 330-332:301, 2002.

[162] AA El-Gendi, EMM Ibrahim, VO Khavrus, Y Krupskaya, S Hampel, A Leonhardt, B Behner, and R Klingeler. *Carbon*, 47:2821, 2009.

[163] G Xing, S Jia, and Z Shi. *New Carbon Mater*, 22:337, 2007.

[164] RF Pacheco, M Arruebo, C Marquina, R Ibarra, and JAJ Santamara. *Nanotechnology*, 17:4765, 2006.

[165] J Qiu, Y Li, Y Wang, Y An, Z Zhao, Y Zhou, and W Li. *Fuel Process Technol*, 86:267, 2004.

[166] J Huo, H Song, and X Chen. *Carbon*, 42:3177, 2004.

[167] C Saiyasombat, N Petchsang, IM Tang, and JH Hodak. *Nanotechnology*, 19:085705, 2008.

[168] L Zhang, R He, and HC Gu. *Appl Surf Sci*, 253:2611, 2006.

[169] N Wu, L Fu, M Su, M Aslam, KC Wong, and PD Vinayak. *Nano Lett*, 4:383, 2004.

[170] T Enz, M Winterer, B Stahl, S Bhattacharya, G Miehe, K Foster, C Fasel, and H Hahn. *J Appl Phys*, 99:044306, 2006.

[171] B Wei, M Shima, RPati, SK Nayak, DJ Singh, R Ma, Y Li, Y Bando, S Nasu, and PM Ajayan. *Small*, 2(6):804, 2006.

[172] J Wang, DTang, X Liu, and Z Zhen. *J Mater Chem*, 17:1597, 2007.

[173] A Kleibert, F Bulut, W Rosellen, K H Meiwes-Broer, J Bansmann, and M Getzlaff. *J Phys: Confer Series*, 211:012017, 2010.

[174] L Yan, S Shen, W Li, and X Wang. *J Appl Polym Sci*, 101:4211, 2006.

[175] V Mennellaa, G Monacob, L Colangeli, and E Bussoletti. *Carbon*, 33(2):115, 1995.

[176] XG Lui, B Li, DY Geng, WB Cui, F Yang, ZG Xie, DJ Kang, and ZD Zhang. *Carbon*, 47:470, 2009.

[177] HR Rechenberg, JAH Coaquira, C Marquina, B Garca-Landa, MR Ibarra, AM Benito, W Maser, E Muoz, and MT Martnez. *J Magn Magn Mater*, 226-230:1930, 2001.

[178] LX Lian, LJ Deng, M Han, W Tang, and SD Feng. *J Appl. Phys*, 101:09M520, 2007.

[179] JP Bouchaud and PG Zerah. *J Appl Phys*, 67:5512, 1989.

[180] T Nakamura. *J Magn Magn Mater*, 168 (3):285, 1996.

[181] Y Naito and K Suetake. *IEEE Trans Micro Theory Techn*, MTT-19:65, 1971.

[182] D Parker. *IEEE Trans Micro Theory Techn*, 50(3):1039, 2002.

[183] B Zhang, Y Feng, J Xiong, Y Yang, and H Lu. *IEEE Trans Magn*, 42(7):1778, 2006.

[184] YX Yang, RK Singh, and PA Webley. *Adsorption*, 119(14):265, 2008.

[185] T Hyeon. *Chem Commun*, page 927, 2003.

[186] Michael A Zalich, Vincent V Baranauskas, Judy S Riffle, Martin Saunders, and Timothy G St. Pierre. *Chem Mater*, 18:2648, 2006.

[187] Yang Xu, Meena Mahmood, Zhongrui Li, Enkeleda Dervishi, Steve Trigwell, Vladimir P Zharov, and et al. *Nanotechnology*, 19:135102, 2008.

[188] Garry P Glaspell, Paul W Jagodzinski, and A Manivannan. *J Phys Chem B*, 108:9604, 2004.

[189] Satoshi Tomita, Masahiro Hikita, Minoru Fujii, Shinji Hayashi, Kensuke Akamatsu, Shigehito Deki, and Hidehiro Yasuda. *J Appl Phys*, 88(9):5452, 2000.

[190] YD Zhang, JI Budnick, WA Hines, SA Majetich, and EM Kirkpatrick. *App Phys Lett*, 76(1):94, 2000.

[191] Jun Jiao and Supapan Seraphin. *App Phys Lett*, 83(5):2442, 1998.

[192] J Jankovskis. *J Magn Magn Mater*, 304:e492, 2006.

[193] Julio Osuna, Dominique de Caro, Catherine Amiens, and Bruno Chaudret. *J Phys Chem*, 100:14571, 1996.

[194] Vijutha Sunny and MR Anantharaman. *Indian Complete Patent Application No*, CHE:294, 2008.

[195] ZP Huang, DZ Wang, JG Wen, M Sennett, H Gibson, and ZF Ren. *Appl Phys A*, 74:387, 2002.

[196] MA Ermakova, D Yu Ermakov, LM Plyasova, and GG Kuvshinov. *Catal Lett*, 62:93, 1999.

[197] R Tsu, JH Gonzalez, and IC Hernandez. *Solid State Commun*, 27:507, 1978.

[198] SC Tsang, V Caps, I Paraskevas, D Chadwick, and D Thompsett. *Angew Chem Int Ed*, 43:5645, 2004.

[199] K Kosugi, JM Bushiri, and N Nishi. *Appl Phys Lett*, 111:1753, 2004.

[200] S Tomita, M Hikita, M Fujii, A Hayashi, and K Yamamoto. *Chem Phys Lett*, 316:361, 2000.

[201] F Ding, A Rosèn, EEB Campbell, LKL Falk, and K Bolton. *J Phys Chem B*, 110:7666, 2006.

[202] Takeo Oku, Gnter Schmid, and Katsuaki Suganuma. *J Mater Chem*, 8:2113, 1998.

[203] Yuri Koltypin, Asuncion Fernandez, T Cristina Rojas, Juan Campora, Pilar Palma, and Ruslan Prozorov et al. *Chem Mater*, 11:1331, 1999.

[204] E Cattaruzza, F Gonella, G Mattei, P Mazzoldi, D Gatteschi, and C Sangregorio et al. *Appl Phys Lett*, 73(9):1176, 1998.

[205] Y Lin, S Taylor, H Li, SKA Fernando, L Qu, W Wang, and et al. *J Mater Chem*, 14:527, 2004.

[206] L Guo, Q Huang, XY Li, and S Yang. *Phys Chem Chem Phys*, 3:1661, 2001.

[207] Y He, X Li, and MT Swihart. *Chem Mater*, 17(5):1017, 2005.

[208] AP Weber, M Seipenbusch, and GJ Kasper. *Nanoparticle Res*, 5:293, 2003.

[209] TN Narayanan, MM Shaijumon, Lijie Ci, PM Ajayan, and MR Anantharaman. *Nano Res*, 1:465, 2008.

[210] S Sugimoto, K Okayama, S Kondo, H Ota, M Kimura, Y Yoshida, H Nakamura, D Book, T Kagotani, and M Homma. *Mater Trans JIM*, 39:1080, 1998.

[211] YB Feng, T Qiu, CY Shen, and XY Li. *Mater Trans JIM*, 42(3):36, 2006.

[212] KM Lim, MC Kim, KA Lee, and CG Park. *IEEE Trans Magn*, 39:1836, 2003.

[213] XG Liu, ZQ Ou, DY Geng, Z Han, ZG Xie, and ZD Zhang. *J Phys D: Appl Phys*, 42:155004, 2009.

[214] Qinglei Liu, Di Zhang, Tongxiang Fan, Jiajun Gu, Yoshinari Miyamoto, and Zhixin Chen. *Carbon*, 46(3):461, 2008.

[215] A Sarkar, S Kapoor, G Yashwant, HG Salunke, and T Mukherjee. *J Phys Chem B*, 109:7203, 2005.

[216] Aparna Roy, V Srinivas, S Ram, JA De Toro, and U Mizutani. *Phys Rev B*, 71:184443, 2005.

[217] DS Sidhaye, T Bala, S Srinath, H Srikanth, P Pankaj, and M Sastry et al. *J Phys Chem C*, 113:3426, 2009.

[218] V Tzitzios, G Basina, M Gjoka, V Alexandrakis, V Georgakilas, and D Niarchos et al. *Nanotechnology*, 17:3750, 2006.

[219] J Qiu, Y Li, Y Wang, Z Zhao, Y Zhou, and Y Wang. *Nanotechnology*, 83:615, 2004.

[220] J Qiu, Y Li, Y Wang, Z Zhao, and Y Zhou et al. *Fuel Process Technol*, 86:267, 2004.

[221] J Geng, DA Jefferson, and BFG Johnson. *Chem Commun*, page 2442, 2004.

[222] F Barroso-Bujans, JLG Fierro, S Rojas, Sànchez-Cortes S, Arroyo M, and López-Manchado MA. *Carbon*, 45(8):1669, 2007.

[223] Y Liu, J Ling, W Li, and X Zhang. *Nanotechnology*, 15:43, 2004.

[224] Y Koltypin, A Fernandez, TC Rojas, J Campora, P Palma, and R Prozorov et al. *Chem Mater*, 11:1331, 1999.

[225] JG Yang, YL Zhou, T Okamoto, T Bessho, S Satake, and R Ichino et al. *Chem Lett*, 35:1190, 2006.

[226] I Calizo, AA Balandin, W Bao, F Miao, and CN Lau. *Nano Lett*, 7(9):2645, 2007.

[227] ZH Wang, CJ Choi, BK Kim, JC Kim, and ZD Zhang. *Carbon*, 41:1751, 1995.

[228] PZ Si, ZD Zhang, DY Geng, CY You, XG Zhao, and WS Zhang. *Carbon*, 41:247, 2003.

[229] C Singh, MSP Shaffer, KKK Koziol, IA Kinloch, and AH Windle. *Chem Phys Lett*, 372:860, 2003.

[230] Y Huang, Z Xu, Y Yang, T Tang, R Huang, and J Shen. *J Phys Chem C*, 113:6533, 2009.

[231] Wohlfarth EP. *Ferromagnetic Materials*. North-Holland.

[232] JH Hwang, VP Dravid, MP Teng, JJ Host, BR Elliott, and DL Johnson et al. *J Mater Res*, 12:1076, 1997.

[233] Jing Ju Lu and Huei Li Huang. *Chine J Phys*, 38:L97, 2000.

[234] V Singh, MS Seehra, and J Bonevich. *J Appl Phys*, 103:07D524, 2008.

[235] R Ravindran, K Gangopadhyay, S Gangopadhyay, N Mehta, and N Biswas. *Appl Phys Lett*, 89:263511, 2006.

[236] B Lu, XL Dong, H Huang, XF Zhang, XG Zhu, JP Lei, and JP Sun. *J Magn Magn Mater*, 320:1106, 2008.

[237] Baoshan Zhang, Yong Feng, Jie Xiong, Yi Yang, and Huaixian Lu. *IEEE Trans Magn*, 42(7):1778, 2006.

[238] Adriana P Herrera, Maricarmen RodriGuez, Madeline Torres-Lugo, and Carlos Rinaldi. *J Mater Chem*, 18:855, 2008.

[239] Palash Gangopadhyay, Sbastien Gallet, Edith Franz, Andr Persoons, and Thierry Verbiest. *IEEE Trans Magn*, 41(10):4194, 2005.

[240] R Jurgons, C Seliger, A Hilpert, L Trahms, S Odenbach, and C Alexiou. *J Phys Condens Matter*, 18:s2893, 2006.

[241] PY Lee, K Ishizaka, H Suematsu, W Jiang, and KYatsui. *J Nanoparticle Research*, 8:29, 2006.

[242] CV Gopal Reddy, SV Manorama, and VJ Rao. *J Mat Sci Lett*, 19:775, 2000.

[243] K Arshaka, KTwomey, and D Egan. *Sensors*, 2:50, 2002.

[244] N Iftimie, E Rezlescu, PD Popa, and N Rezlescu. *J Optoelectron Adv Mater*, 8(3):1016, 2006.

[245] CPL Rubinger, DX Gouveia, JF Nunes, CCM Salgueiro, MPF Graca JAC Paiva, P Andre, and LC Costa. *Microwave Opt Technol Lett*, 49(6):1341, 2007.

[246] Jian Lu, Shuli Ma, Jiayu Sun, Chunchao Xia, Chen Liu, Zhiyong Wang, Xuna Zhao, Fabao Gao, Qiyong Gong, Bin Song, Xintao Shuai, Hua Ai, and Zhongwei Gu. *Biomaterials*, 30:2919, 2009.

[247] Masahiro Yamaguchi, Ki Hyeon Kim, and Shinji Ikedaa. *J Magn Magn Mater*, 304:208, 2006.

[248] Santi Maensiri, Chivalrat Masingboon, Banjong Boonchomb, and Supapan Seraphin. *J Magn Magn Mater*, 56:797, 2007.

[249] S Chkoundali S Ammar, N Jouini, F Fievet, P Molinie, M Danot, F Villain, and J-M Greneche. *J Phys: Condens Matter*, 16:4357, 2004.

[250] Remesh Peelamedu, Craig Grimes, Dinesh Agrawal, Rustum Roy, and Purushotham Yadoji. *J Mater Res*, 18(10):2292, 2003.

[251] Suman and N D Sharma. *Indian J Pure Appl Phys*, 45:549, 2007.

[253] F Kenfack and H Langbein. *Chin Phys Lett*, 19:269, 2002.

[254] J Smit and HPJ Wijn. *Ferrites*. Philips Technical Library.

[255] EJW Verwey and EL Heilmann. *J Chem Phys*, 15(4):174, 1947.

[256] Babita Baruwati, K Madhusudan Reddy, Sunkara V Manorama, Rajnish K Singh, and Om Parkash. *Appl Phys Lett*, 85(14):2833, 2004.

[257] GP Joshi, NS Saxena, R Mangal, A Mishra, and TP Sharma. *Bull Mater Sci*, 26(4):387, 2003.

[258] E Rezlescu, N Iftimie, PD Popa, and N Rezlesc. *J Phys Conf Ser*, 15:51, 2005.

[259] GB McGarvey and DG Owen. *J Mat Sci*, 33:35, 1998.

[260] TK Kundu and S Mishra. *Bull Mater Sci*, 31(3):507, 2008.

[261] Jae-Gwang Lee, Hi Minlee, and Chul Sung Kim. *J Magn Magn Mater*, 900:177, 1998.

[262] KJ Davis, KO Grady, and S Morup. *J Magn Magn Mater*, 149:14, 1995.

[263] J Ding, WM Miao, PG McCormick, and R Street. *Appl Phys Lett*, 67:3804, 1995.

[264] J Ding, PG McCormick, and R Street. *J Magn Magn Mater*, 171:309, 1997.

[265] V Sepèlak, A Buchal, and KD Becker. *Mater Sci Forum*, 862:278, 1998.

[266] W Roos. *J Am Ceram Soc*, 63:601, 1980.

[267] SE Jacobo and MA Blesa. *J Mater Sci*, 32:1025, 1997.

[268] Christy R Vestal and Z John Zhang. *Int J of Nanotechnology*, 1:240, 2004.

[269] Y Shi, J Ding, X Liu, and J Wang. *J Magn Magn Mater*, 205:249, 1999.

[270] Yoshiaki Kinemuchi, Kazuhiro Ishizaka, Hisayuki Suematsu, Weihua Jiang, and Kiyoshi Yatsui. *Thin Solid Films*, 407:109, 2002.

[271] Hongxia Wang, Faling Zhang, Wei Zhang, Xianjie Wang, Zhe Lu, Zhengnan Qian, Yu Suia, Dawei Dong, and Wenhui Su. *J Cryst Growth*, 293:169, 2006.

[272] MAF Ramalho, L Gama, SG Antonio, CO Paiva-Santos, EJ Miola, RHGA Kiminami, and ACFM Costa. *J Mater Sci*, 42:3603, 2007.

[273] E Veena Gopalan, KA Malini, D Sakthi Kumar, Yasuhiko Yoshida, IA Al-Omari, S Saravanan, and MR Anantharaman. *J Phys.: Conden Matter*, 21:146006, 2009.

[274] Tadanori Hashimoto, Tetsuya Yamada, and Toshinobu Yoko. *J Appl Phys*, 80(6):3184, 1996.

[275] John Jacob, M Abdul Khadar, Anil Lonappan, and K T Mathew. *Bull Mater Sci*, 31:847, 2008.

[276] A Dias and UTL Buono. *J Mater Sci*, 21:3278, 1997.

[277] Waldron RD. *Phys Rev*, 99:1727, 1955.

[278] Masoud Salavati-Niasari, Fatemeh Davar, and Tahmineh Mahmoudi. *Polyhedron*, 28:1455, 2009.

[279] M Mouallem-Bahout and O Pena S Bertrand. *J Solid State Chem*, 178:1080, 2005.

[280] Vladimir Sepèlak, Ingo Bergmann, Armin Feldhoff, Paul Heitjans, Frank Krumeich, and Dirk Menzel et al. *J Phys Chem C*, 111:5026, 2007.

[281] E Veena Gopalan, KA Malini, S Saravanan, D Sakthi Kumar, Yasuhiko Yoshida, and MR Anantharaman. *J Phys D: Appl Phys*, 41:185005, 2008.

[282] Tareev B. *Physics of Dielectric Materials*. Mir Publishers.

[283] Mathew George, Swapna S Nair, KA Malini, PA Joy, and MR Anantharaman. *J Phys D: Appl Phys*, 40:1593, 2007.

[284] BP Rao and KH Rao. *J Mate Sci*. 32:6049, 1997.

[285] NE Hill, WE Vaughan, AH Price, and M Davies. *Dielectric properties and molecular behaviour*. Van-Nostrand reinhold company.

[286] Koops C G. *Phys Rev*, 83:121, 1951.

[287] KW Wagner. *Ann Physics*, 40:817, 1913.

[288] GF Goya and HR Rechenberg. *J Magn Magn Mater*, 203:141, 1999.

[289] N Ponpandian and A Narayanasamy. *J Appl Phys*, 92:2770, 2002.

[290] Rezlescu N and Rezlescu E. *Phys. Status Solidi(a)*, 59:575, 1974.

[291] H Ismael, MK El Nimr, AM Abou El Ata, MA El Hiti, MA Ahmed, and AA Murakhow. *J Magn Magn Mater*, 150:403, 1995.

[292] MA El Hiti, MA Ahmed, MM Mosaad, and SM Attia. *J Magn Magn Mater*,

[293] Mingzhong Wu, Huahul He, Zhensheng Zhao, and Xi Yao. *J Phys D: Appl Phys*, 33:2927, 2000.

[294] N Sombatsompop, S Thongsang, T Markpin, and E Wimolmala. *J Appl Poly Sci*, 93:2119, 2004.

[295] Changshu Xiang, Yubai Pan, Xuejian Liu, Xingwei Sun, Xiaomeni Shi, and Jingkun Guo. *Appl Phys Lett*, 87:123103, 2005.

[296] I Nedkov, L Milenova, and N Dishovsky. *IEEE Trans MAG*, 30(6):4545, 1994.

[297] Shigeyuki Toki, Igors Sics, Shaofeng Ran, Lizhi Liu, and Benjamin S Hsiao. *Polymer*, 44:6003, 2003.

[298] M Arroyo, MA López-Manchado, JL Valentn, and J Carretero. *Compos Sci Technol*, 67:1330, 2007.

[299] Werner Hofmann. *Rubber Technology Handbook*. Oxford University Press.

[300] S Kolev, A Yanev, and I Nedkov. *Phys Status Solidi(c)*, 3(5):1308, 2006.

[301] NN Al-Moayed, MN Afsar, UA Khan, S McCooey, and M Obol. *IEEE Trans Magn*, 44(7):1768, 2008.

[302] G Viau, F Fievet-Vincent, F Fievet, PToneguzzo, F Ravel, and O Acher. *J Appl Phys*, 81(6):2749, 1997.

[303] Ronald F Soohoo. *IEEE Trans Mag.* 4(2):118, 1968.

[304] RH Kodama. *J Magn Magn Mater*, 200:359, 1999.

[305] KA Malini, EM Mohammed, S Sindhu, PA Joy, SK Date, SD Kulkarni, P Kurian, and MR Anantharaman. *J Mater Sci*, 36:5551, 2001.

[306] C Piña-Hernndez, L Hernndez, LM Flores-Vlez, LF del Castillo, and O Domnguez. *J Mater Eng Perform*, 16(1):470, 2007.

[307] KH Prema, Philip Kurian, MR Anantharaman, MN Suma, and Manoj Joseph. *J Mater Eng Perform*, 40:331, 2008.

[308] AJ Baden Fuller. *Ferrites at Microwave Frequencies*. Peter Peregrinus Ltd.

[309] VG Geethamma, R Joseph, and S Thomas. *Bull Mater Sci*, 55(4):583, 1995.

[310] SH Bidkar, AG Patil, UR Kapadul, and DG Hundiwale. *Inter J Polymeric Materials*, 55:135, 2006.

[311] Vishu Shah. *Handbook of Plastic Testing Technology*. John Wiley and Sons.

[312] Zhanhu Guo, Hongfei Lin, Amar B Karki, Suying Wei, David P Young, Sung Park, John Willis, and Thomas H Hahn. *Polym Degrad Stab*, 68:2551, 2008.

[313] Hanu LG, Simon GP, and Cheng YB. *Polym Degrad Stab*, 91:1373, 2006.

[314] V Šepelǎk, K Tk ov, VV Boldyrev, S Wi?mann, and KD Becker. *Physica B*, 617:234, 1997.

[315] E Muhammad Abdul Jamal, PA Joy, Philip Kurian, and MR Anantharaman. *Mater Sci Eng B*, 156:24, 2009.

[316] Maya Jacob, KT Varughese, and Sabu Thomas. *J Mater Sci*, 41:5538, 2006.

[317] MB Kothale, KK Patankar, SL Kadam, VL Mathe, AV Rao, and BK Chougule. *Mater Chem Phys*, 77:691, 2002.

[318] Omprakash S Upadhyay, Devendrakumar. *Bull Mater Sci*, 19:513, 1996.

[319] ZM Elimat, AM Zihlif, and G Ragosta. *J Phys D: Appl Phys*. 41:165408, 2008.

[320] Jian Liang Xie, Mangui Han, Liang Chen, Renxiong Kuang, and Longjiang Deng. *J Magn Magn Mater*, 314(1):37, 2007.

[321] AN Yusoff, MH Abdullah, SH Ahmad, SF Jusoh, AA Mansor, and SAA Hamid. *J Appl Phys*, 92:876, 2002.

[322] Feng Yongbao, Qiu Tai, Shen Chunying, and Li Xiaoyun. *Microwave Conference Proceedings, APMC 2005. Asia-Pacific Conference Proceedings*, 2:4, 2005.

[323] Haitao Zhao, Xudong Sun, Changhui Mao, and Jun Du. *Physica B*, 404:69, 2009.

[324] Zhang Haijun, Liu Zhichao, Yao Xi. Zhang Liangying, and Wu Mingzhong. *Mater Sci Eng B*, 97:160, 2003.

[325] Mingzhong Wu, Haijun Zhang, Xi Yao, and Liangying Zhang. *J Phys D: Appl Phys*, 34:889, 2001.

[326] Kenneth Bober, Robert H Giles, and Jerry Waldman. *Int J Infrared Millimeter Waves*, 18 (L):101, 1997.

[327] MY Koledintseva, PC Ravva, RE DuBroff, JL Drewniak, and KN Rozanov. *Proc IEEE Int Symp Electromag Compat*, 1:169, 2005.

[328] Neelakanta PS and Park JC. *IEEE Trans Microwave Theory Tech*, 43(6):1381,

[329] Xiaoling Yu, Gang Lin, Duanming Zhang, and Huahui He. *Materials Design*, 27:700, 2006.

[330] Wen Fu-Sheng, Qiao Liang, Zhou Dong, Zuo Wen-Liang, Yi Hai-Bo, and Li Fa-Shen. *Chin Phy B*, 17(6):2263, 2008.

[331] Huang Yao-Qing, HOU Zhi-Ling, SONG Wei-Li, Yuan Jie, and Cao Mao-Sheng. *Chin Phy B*, 26(5):057701, 2009.

[332] Yida Deng, Ling Zhao, Bin Shen, Lei Liu, and Wenbin Hua. *J Appl Phy*, 100:014304, 2006.

[333] Zhenguo An, Shunlong Pan, and Jingjie Zhang. *J Phys Chem C*, 113:2715, 2009.

[334] Chung-Che Lee and Dong-Hwang Chen. *Appl Phy Lett*, 90:193102, 2007.

[335] H Ismail, N Rosnah, and HD Rozman. *Polymer*, 38(16):4059, 1997.

[336] KA Malini, EM Mohammed, S Sindhu, P Kurian, and MR Anantharaman. *Rubber and Composites*, 31(10):449, 2002.

[337] L Zhen, YX Gong, JT Jiang, and WZ Shao. *J Appl Phys*, 104:034312, 2008.

[338] N Bowler N. *IEEE Trans Dielectr Electr Insul*, 13:703, 2006.

[339] SS Kim, ST Kim, JM Ahn, and KH Kim. *J Magn Magn Mater*, 271:39, 2004.

[340] H Scher and R Zallen. *J Chem Phys*, 53:3759, 1970.

[341] K Bethe and J Verweel. *IEEE Trans Mag*, 5:474, 1969.

[342] Qing Yuchang, Zhou Wancheng, Luo Fa, and Zhu Dongmei. *J Magn Magn Mater*, 321(1):25, 2009.

[343] Sung-Soo Kim, Sun-Tae Kim, Yeo-Choon Yoon, and Kyung-Sub Leeb. *J Appl Phys*, 97:10F905, 2005.

[344] Ruitao Lv, Feizu Kang, Jialin Gu, Xuchun Gui, Jinquan Wei, Kunlin Wang, and Dehai Wu. *Appl Phy Lett*, 93:223105, 2008.

[345] Feng Yongbao, Qiu Tai, Li Xiaoyun, and Shen Chunying. *Journal of Wuhan University of Technology-Mater Sci Ed*, 22(2):266, 2007.